



**HAL**  
open science

# Regulation, activation, and deactivation of soluble guanylate cyclase and NO-sensors

Olga Petrova

► **To cite this version:**

Olga Petrova. Regulation, activation, and deactivation of soluble guanylate cyclase and NO-sensors. Biochemistry, Molecular Biology. Université Paris Saclay (COMUE), 2017. English. NNT : 2017SACLX113 . tel-01713240

**HAL Id: tel-01713240**

**<https://pastel.hal.science/tel-01713240>**

Submitted on 20 Feb 2018

**HAL** is a multi-disciplinary open access archive for the deposit and dissemination of scientific research documents, whether they are published or not. The documents may come from teaching and research institutions in France or abroad, or from public or private research centers.

L'archive ouverte pluridisciplinaire **HAL**, est destinée au dépôt et à la diffusion de documents scientifiques de niveau recherche, publiés ou non, émanant des établissements d'enseignement et de recherche français ou étrangers, des laboratoires publics ou privés.

# Regulation, activation, and deactivation of soluble guanylate cyclase and NO-sensors

Thèse de doctorat de l'Université Paris-Saclay  
préparée à l'Ecole Polytechnique

École doctorale n°573 : Interfaces : approches interdisciplinaires,  
fondements, applications et innovation.  
Spécialité de doctorat : Biologie

Thèse présentée et soutenue à Palaiseau le **19 décembre 2017**, par

**Mme Olga Petrova**

Composition du Jury :

Jérôme SANTOLINI Chercheur CEA – HDR Laboratoire Stress Oxydant et Détoxication, CEA	Président
François BONTEMS Chercheur CNRS – HDR Virologie Structurale, Institut Pasteur	Rapporteur
Christophe GUIGNABERT Chercheur INSERM – HDR HAP: Physiopathologie et Innovation Thérapeutique, Univ. Paris-Sud	Rapporteur
Hélène MUNIER-LEHMANN Chercheuse Institut Pasteur – HDR Chimie et Biocatalyse : Biochimie et Criblage, Institut Pasteur	Examinatrice
Roberto MOTTERLINI Chercheur INSERM – HDR Institut Mondor de Recherche Biomédicale	Examineur
Michel NEGRERIE Chercheur INSERM – HDR Laboratoire d'Optique et Biosciences, Ecole Polytechnique	Directeur de thèse



## *Acknowledgements*

---

I want to thank many individuals whose kind support and help turned my work into this thesis.

First of all I would like to thank François Hache for approving my candidature as a doctoral student and paving the way for me to join the Laboratory for Optics and Biosciences.

I owe my deepest gratitude to my supervisor Michel Négrerie who offered me the possibility to work in this topic. I was lucky to be a student of Michel, as he is a good teacher and never stopped encouraging me on my way, in moments of disappointment and of success. Without his continuous optimism concerning this work, enthusiasm, encouragement, and support this study would not have been completed.

I also express my warmest gratitude to Isabelle Lamarre who guided me through the technical issues of biochemistry and cell biology. Her contribution to my knowledge has been essential during this work. Jean-Christophe Lambry helped us in molecular dynamics simulation for what I am very grateful to him.

This thesis would not have been possible without our collaborators:

Jessica Wales (from the University of Arizona Cancer Center, Tucson (USA)) made an experiment with a common idea that helped us to interpret some results. Catherine Grillon and Fabienne Fasani (from Center for Molecular Biophysics, Orléans) helped us to design and perform the experiment with angiogenic cells. The proteins that we used in the experiments were purified and provided by Dr. Emil Martin (Internal Medicine, University of Texas, Houston, USA), Dr. Colin Andrew (Eastern Oregon University, USA) and Dr. Pierre Nioche (Université Paris Descartes, Laboratoire de Toxicologie et Signalisation Cellulaire). Special thanks to Dr. Colin Andrew and all coauthors for the joint effort that resulted in a publication and to Dr. Pierre Nioche for attending the seminar of my third year as a reviewer of my thesis.

I would like to thank the committee presented at my defense Hélène Munier-Lehmann, Jérôme Santolini, Christophe Guignabert, François Bontems and Roberto Moterlini for their rational criticism and advices.

It is a pleasure to thank those who made my life easier during my work in the LOB. Particularly, many thanks to Olivier Ramodiharilafy for his immense assistance in instructing me in the laboratory space. I could address him on all questions concerning what and where to find, whom to ask and how to use. He was constantly close to the student environment, always supporting us and providing advice.

Antigoni Alexandrou is very open and positive person, always was ready to help me on all issues. Thank you for discussing my work at the seminar and on pre-defense. Your comments helped me to improve the presentation.

Also thanks to Ursula Liebl, Hannu Myllykallio, Marten Vos, Chiara Stringari and Laura Antonucci for their valuable inputs.

It was a pleasure to communicate with Ernan Roitman and Pascal Preira. Pascal, thank you for your nice vocal skills: it was a pleasure to listen to you while we worked together in the biochemical lab.

I am grateful secretaries Christelle Francais and Laure Lachapelle for their help to foreign students to simplify life in the laboratory and in general in France.

I was happy to work in a wonderful team of creative and unique students: Pierre Sournia, Thuy Hoang, Marlen Kruse, Carolina Villamil Franco, Chao Yu, Xiujun Zheng, Bastian Geissler, Paul Stroe, Lamiae Abdeladim, Joséphine Morizet, Mayla Salman and Ravi Teja Raavi.

The greatest thanks to my close friends Lipsa Nag and Marco Schmid, I can not imagine my journey in the laboratory without them, they supported me in all my endeavors. And of course, I am grateful to my close russian friends Gulfina Frolova, Anna Karatovsaya and Ramil Allayarov for their significant contribution to my psychological condition during my stay in France, despite many kilometers between us.

I owe my deepest gratitude to my (grand) mother and father for having raised such daughter, and to my sister and brother (in law) thanks to whom I am in France.

---

## **Regulation, activation, and deactivation of soluble guanylate cyclase and NO-sensors**

### CONTENT

---

Acknowledgements .....	iii
Résumé .....	3
<b>I – INTRODUCTION</b>	
1 – Signal transduction .....	5
2 – The NO – cGMP – sGC signaling pathway .....	5
3 – Bibliography .....	8
<b>II – SOLUBLE GUANYLATE CYCLASE: THE ENDOGENOUS NITRIC OXIDE RECEPTOR</b>	
1 – Involvement of Guanylate cyclase in physiological processes .....	12
2 – Guanylate cyclase structure and molecular functioning .....	22
3 – Guanylate cyclase pharmacology .....	35
4 – Objectives of the present study .....	44
5 – Bibliography .....	45
<b>III – SEARCHING AN EXOGENOUS INHIBITOR OF GUANYLATE CYCLASE</b>	
1 – Aims and Methodology .....	60
2 – Materials and methods .....	60
3 – Results of the screening of natural compounds .....	65
4 – Interaction of inhibitors with sGC .....	75
5 – Analogues of the identified compounds .....	85
6 – Properties of the inhibitors .....	89
7 – Inhibition of angiogenesis .....	95
8 – Conclusion .....	97
9 – Bibliography .....	97
<b>IV – THE MECHANISM OF ACTION OF sGC ACTIVATORS</b>	
1 – Methodology .....	102
2 – Materials and methods .....	103
3 – Quantifying the activation .....	107
4 – Mechanism of action of sGC activators .....	113
5 – Conclusion .....	123

6 – Bibliography.....	123
<b>V – CONTROL OF DIATOMICS BINDING BY BACTERIAL NO-SENSORS</b>	
1 – Ligand dynamics .....	128
2 – Materials and methods.....	130
3 – L16A mutant of the NO-sensor from <i>Alcaligenes xylosoxydans</i> .....	133
4 – Dioxygen binding to the NO-sensor from <i>Thermoanaerobacter tengcongensis</i> .....	142
5 – Conclusion.....	152
6 – Bibliography.....	152
<b>VI – OVERVIEW AND PERSPECTIVES .....</b>	<b>157</b>
<b>VII – ANNEXES</b>	
A – List of abbreviation.....	161
B – Principles of Surface plasmon resonance imaging .....	163
C – Principles and methods of time-resolved absorption spectroscopy.....	166
D – Molecular dynamics simulation – CHARMM .....	170
E – Bibliography .....	172

---

**Titre :** Régulation, activation et désactivation de la guanylate cyclase soluble et de senseurs du NO.

**Mots clés :** Guanylate cyclase soluble, transduction du signal, nitric oxide, cyclic GMP, allostérie, activateurs et inhibiteurs de la guanylate cyclase, spectroscopie d'absorption transitoire.

**Résumé :** Cette thèse est consacrée à la régulation de la guanylate cyclase soluble (sGC), le récepteur endogène du monoxyde d'azote (NO) chez les mammifères qui est impliqué dans la transduction du signal. La voie de signalisation NO/sGC/cGMP est impliquée dans de nombreux processus physiologiques et pathologiques, dont la régulation de la pression artérielle et l'angiogenèse associée aux tumeurs. L'enzyme sGC est activée par la fixation du NO sur son hème et catalyse la formation du cGMP à partir du GTP. Alors que la sGC est présente dans de nombreuses cellules de mammifères, le domaine hémique bactérien homologue (H-NOX) est impliqué dans la détection du NO et la régulation du métabolisme. Il n'existe à l'heure actuelle (janvier 2018) qu'un seul médicament qui cible la sGC : il s'agit d'un activateur utilisé pour traiter l'hypertension artérielle pulmonaire.

Le travail expérimental de cette thèse est constitué de trois parties :

- 1- La recherche d'inhibiteurs de la sGC.
- 2- L'étude du mécanisme d'activation de la sGC par la molécule médicament riociguat.
- 3- L'étude du contrôle de la dynamique du NO par des senseurs de NO bactériens.

Un objectif important de cette thèse est la découverte d'inhibiteurs de la sGC pour ralentir la progression tumorale. Le criblage de 300 composés naturels d'une chimiothèque, par mesure de l'activité de la sGC purifiée, a révélé six inhibiteurs actifs ( $IC_{50} = 0.2 - 1 \mu M$ ). Deux autres composés naturels, l'hypéricine et l'hypocrelline, qui avaient été utilisés dans des cellules mais jamais avec la sGC purifiée, se sont avérés être des inhibiteurs. Ces huit molécules inhibent aussi la sGC cellulaire des cellules HUVEC en culture.

Par spectroscopie, nous montrons que deux inhibiteurs agissent en oxydant l'hème alors que les autres inhibiteurs sont des effecteurs allostériques qui ne se fixent ni sur l'hème, ni sur le site catalytique ou sur le site des activateurs. Nous avons ainsi découvert une nouvelle classe de composés pharmacologiques ciblant la voie de signalisation NO/cGMP.

Plusieurs de ces composés ont été testés sur des cultures de cellules endothéliales, modèles pour l'angiogenèse, qui développent des néo-vaisseaux. A une concentration de  $10 \mu M$  l'hypéricine bloque l'angiogenèse de ces cellules modèles.

Nous avons ensuite étudié par spectroscopie d'absorption résolue en temps la transition structurale induite dans la sGC par l'activateur riociguat, un médicament indiqué pour l'hypertension artérielle pulmonaire, en synergie avec le CO. L'hypothèse de travail était que le riociguat facilite la rupture de la liaison Fe-His de l'hème, ce que nous ne pouvons pas montrer par spectroscopie d'absorption à l'équilibre du fait des spectres trop peu différenciés. L'idée directrice a été d'identifier les espèces moléculaires activées et non activées grâce à leur spectres transitoires après photodissociation du CO. Cette technique nous a permis de démontrer des changements de coordination de l'hème, notamment que le riociguat induit la rupture de la liaison Fe-His au niveau de l'hème, à l'instar du NO, l'activateur naturel de la sGC.

Deux états allostériques distincts de la sGC induits par le riociguat existent en présence du CO ayant les coordinations 6c-hème et 5c-hème. Nous montrons que ces activateurs allostériques possèdent une efficacité différente indépendamment de leur affinité pour la sGC. Cette efficacité peut être calculée par le rapport des espèces transitoires mesurées.

Nous avons évalué le composé naturel isoliquiritigénine qui est commercialisé comme activateur de la sGC mais n'a jamais été testé sur la sGC purifiée. Nous montrons qu'il s'agit en réalité d'un inhibiteur de la sGC, aussi bien purifiée que dans des cellules HUVEC. Une hypothèse est l'activation de la phosphodiesterase PDE5 qui dégrade le cGMP produit par la sGC, faisant ainsi apparaître une apparente activation de la sGC.

Dans un second projet consacré au contrôle de l'affinité des gaz par les senseurs du NO, nous avons mesuré la dynamique des ligands diatomiques CO, NO et O<sub>2</sub> sur 12 ordres de grandeur temporelle pour le type sauvage et un mutant du transporteur bactérien du NO, le cytochrome c' de *Alcaligenes xylosoxidans* (AXCP). Remarquablement, la simple mutation Leu16Ala augmente l'affinité pour le CO d'un facteur 10<sup>8</sup>, celle du NO 10<sup>6</sup>, et rend cette protéine réactive à O<sub>2</sub>. Ces affinités pour l'hème de L16A-AXCP sont les plus élevées jamais mesurées.

Dans le cas de CO et NO, la recombinaison géminée après photodissociation a une amplitude de ~100 % tandis que la recombinaison bimoléculaire n'est pas détectable, ce qui indique que ces deux ligands diatomiques ne peuvent pas sortir de la protéine. Des simulations de dynamique moléculaire ont démontré que le CO dissocié est contraint de rester à 4 Å du Fe<sup>2+</sup> dans le mutant L16A du fait d'une rotation d'un groupe propionate de l'hème. Cette conformation est induite par la chaîne Ala16, contrairement au type sauvage Leu16, et affecte les trois ligands de l'hème CO, NO et O<sub>2</sub>. Cette contrainte augmente considérablement la probabilité de liaison de CO et NO au fer de l'hème. Ce mécanisme constitue un nouveau mode de contrôle de l'affinité d'un ligand diatomique.

La protéine senseur H-NOX de la bactérie *Thermoanaerobacter tengcongensis* (*Tt* H-NOX) est homologue au domaine senseur hémique de la sGC et son rôle n'est pas connu, bien qu'elle fixe avec une très forte affinité le NO et O<sub>2</sub>. Pour comprendre son fonctionnement en présence de ces deux ligands, nous avons mesuré la dynamique de O<sub>2</sub> après photodissociation par spectroscopie d'absorption transitoire sur 12 ordres de grandeur temporelle, en variant la concentration de O<sub>2</sub>.

Nous avons mis en évidence deux processus : la photo-oxydation de l'hème à l'échelle picoseconde après la photo-dissociation de O<sub>2</sub> est prépondérante par rapport à la simple recombinaison de O<sub>2</sub>. Cependant l'hème revient à son état réduit à l'échelle μs. Cette réduction a lieu simultanément à la recombinaison bimoléculaire de O<sub>2</sub> (5 μs). L'accepteur d'électrons dans la poche de l'hème reste à identifier. Ainsi la conformation particulière de l'hème de la protéine senseur *Tt* H-NOX, notamment sa distortion, lui confère des propriétés redox que ne possèdent pas les autres protéines homologues.

Ces résultats confirment l'hypothèse que *Tt* H-NOX n'est sans doute pas un senseur de O<sub>2</sub> ou de NO *stricto sensu* mais un senseur redox.

Nous nous sommes intéressés à la régulation de la guanylate cyclase et des senseurs de NO, en nous efforçant de faire le lien entre les propriétés biochimiques des protéines et de leurs effecteurs allostériques avec leur comportement dynamique, notamment les changements de coordination de l'hème qui constituent un relai intramoléculaire à la transduction du signal.

## CHAPTER I

### INTRODUCTION

#### 1 – Signal transduction

The capability of cells to receive various signals and to respond accordingly is an essential property of multicellular organisms. Signals arriving from outside the cell regulate processes that determine cell survival, their ability for division and differentiation, functional activity or death. Various molecular events and biochemical transformations occur within the cell when triggered by external chemical or physical signals.

Signals are induced by the binding of first messengers such as extracellular factors, hormones, cytokines or neurotransmitters to specific receptors that can either be allosteric transmembrane proteins or channels which, upon ligand interaction allow signals to pass in the form of small ion movement.

Complex signal transduction involves the coupling of ligand-receptor interactions at the cell surface to many intracellular events involving specialized proteins. These events imply the formation of *second messengers* such as (not exhaustively) 3',5'-cyclic adenosine monophosphate (cAMP), 3',5'-cyclic guanosine monophosphate (cGMP), inositol trisphosphate, diacylglycerol, the gaseous molecules NO, CO and H<sub>2</sub>S. Second messengers may activate phosphorylation of tyrosine kinases, serine, or threonine kinases that change conformation and activate downstream proteins in the signaling chain that leads to the formation of the primary or secondary cell response.

In the last two decades, signal transduction in pathological processes has become one of the most important subject of modern drug research due to the numerous possibilities of identifying targets. Activation or inhibition of diverse signaling pathways at different steps leads to diverse physiological responses, such as cell proliferation, death, differentiation, and metabolism [1]. One major example of the actively studied signaling pathway is NO – cGMP signaling, which is involved in the regulation of many physiological and pathological processes. Violation of at least one of the intermediate link in this signaling pathway can lead to disorders such as cardio [2], immune [3], neurodegenerative [4, 5] and metabolic diseases [6].

#### 2 – The NO – sGC – cGMP signaling pathway

Nitric oxide (NO) is a highly reactive gas produced by organisms, ranging from bacteria to humans, and is crucial in various biological functions [7]. NO participates in intercellular signaling in the central and peripheral nervous systems. NO inhibits the growth and

multiplication of many types of pathogenic organisms [8], inhibits mitosis of human cells [9], has an anticoagulant activity [10], impedes leukocyte adhesion to the vascular endothelium and prevents platelet aggregation. NO also promotes tracheal smooth muscle relaxation of bronchi [11] and blood vessels [12].

The first known physiological target of NO is the enzyme soluble guanylate cyclase (sGC), which contains a heme iron cofactor necessary for sGC activation. NO interacts not only with metal groups but also with thiols and oxides, affects proteins, lipids, sugars, and nucleic acids [13]. The preferred reactions depend on the concentration of the NO in cells and on the reaction rates. For example, the fastest reaction rates are observed with superoxide ions forming peroxynitrite ( $\text{ONOO}^-$ ), a powerful oxidant that can modify proteins and lipids by nitration. For some heme proteins, reaction rates of NO with the central heme iron can be very high. NO signaling is linked to the general redox state of the cell and can affect several signaling pathways. The ubiquitous action of NO explains why it has both protective and harmful effects. For example, in some cases, NO can promote or inhibit apoptosis [14], kill tumors, or increase the potential for metastasis or vascularization [15], or trigger ischaemic preconditioning in the heart and mediate effects of preconditioning [13, 16].

The generation of NO in human cells occurs through the enzymatic oxidation of L-arginine to citrulline catalyzed by NO-synthase. The endothelial NO-synthase (eNOS) is crucial to generating NO in endothelial cells of a cardiovascular system, which is responsible for vasorelaxation, replication of smooth-muscle cells and inhibition of platelet adhesion [17]. Production of NO by neuronal NO-synthase (nNOS) [18] was first discovered in neuronal cells as a neurotransmitter, particularly in nonadrenergic noncholinergic nerves [19]. In peripheral nerves, NO is an actor of the relaxation of vascular and non-vascular smooth muscles. It relaxes sphincters in the gut, mediates relaxation of the corpus cavernosum causing penile erection, relaxes the bladder and urethra and alters responses in airways [13]. Inducible NOS (iNOS) was first detected in the mechanism of macrophage phagocytosis [20]. iNOS is not expressed in healthy quiescent cells, but only in response to inflammatory stimuli. Once expressed, it generates larger amounts of NO than eNOS and nNOS and its activity is not dependent on intracellular calcium and activation of calmodulin, contrary to eNOS and nNOS.

Although the enzyme sGC and second messenger cGMP were identified in the 1960s [21, 22], the complete outline of the NO – cGMP signaling pathway has been understood only in the last 20 years. After the discovery of cAMP in 1958 [23] and its physiological role, scientists began searching other relevant nucleotides: 6 years later, cGMP was discovered in the urine of rats [24].

Guanylate cyclase was found in mammalian cells in 1969 [21], but only in 1977, it was shown that exogenous NO gas and NO donors like nitroglycerin and nitroprusside activate sGC from rat liver and bovine tracheal smooth muscle [25, 26]. In 1980 Furchgott

and Zawadzki demonstrated the existence of a substance produced by the endothelium that was required to mediate relaxation of blood vessels, the so-called "endothelium-derived relaxing factor" (EDRF) [27]. It was later determined that the substance EDRF is endogenous nitric oxide [28, 29]. Research into its functions led to the Nobel Prize in 1998 awarded to Robert F. Furchgott, Louis J. Ignarro, and Ferid Murad for discovering the role of nitric oxide as a cardiovascular signaling molecule [30-32].

The action of NO in vasodilation starts with NO synthesis by eNOS and its diffusion from endothelial cells through the membrane of smooth muscle cells to bind to NO-specific receptor sGC, leading to synthesis of the second messenger cGMP. After sGC activation, subsequent steps of signaling pathways take place triggered by increasing the concentration of cGMP. There are three known targets for cGMP, which mediate signal transduction: cGMP-dependent protein kinase [33], cGMP-gated ion channels [34], and cGMP-regulated phosphodiesterase [35], (described in CHAPTER II).

In this work, we are interested in the NO signaling pathway involving sGC, subsequent partner proteins, and second messengers intervening especially in blood vessel relaxation. The complete biochemistry of the NO signaling pathway will be described in CHAPTER II. The functioning of the endogenous NO-receptor sGC is crucial in several diseases and this thesis is focused on the activation and deactivation mechanisms of sGC and cognate NO-sensors at the molecular level.

The present thesis is organized as follows. CHAPTER II is devoted to the description of the action and the role of sGC, both at the cellular and the molecular levels. The literature on this subject is extremely large and our overview, albeit as complete as possible, is necessarily non-exhaustive. The end of CHAPTER II is devoted to a review of existing activators and inhibitors of sGC. For a better reading, we chose to describe the experimental methods at the beginning of each chapter, but deeper descriptions of particular methods, not necessary to understand the results, are placed at the end (CHAPTER VII). The discovery of new exogenous inhibitors of guanylate cyclase will be described in CHAPTER III. CHAPTER IV is devoted to the identification of the mechanism of action of allosteric sGC activators, one of which is already commercialized as a drug. The control of NO affinity and dynamics is crucial for homologous and non-homologous bacterial NO-sensors. Thus, a complete understanding of the NO-receptors functioning requires the study of the dynamics of diatomic binding (CO, NO, O<sub>2</sub>) to their heme site, that will be discussed in CHAPTER V. As a general conclusion, we will link the dynamic properties of these proteins to their allosteric and biochemical properties.

### 3 – Bibliography

1. King, M. W. Mechanisms of Cellular Signal Transduction. *Medcal Biochemistry* **1996**.
2. Buys, E.; Sips, P. New Insights into the Role of Soluble Guanylate Cyclase in Blood Pressure Regulation. *Current opinion in nephrology and hypertension* **2014**, *23*, 135-142.
3. Nagy, G.; Clark, J. M.; Buzás, E. I.; Gorman, C. L.; Cope, A. P. Nitric oxide, chronic inflammation and autoimmunity. *Immunol Lett.* **2007** *111*, 1-5.
4. Jaffrey, S. R.; Snyder, S. H. Nitric Oxide: A Neural Messenger. *Annual Review of Cell and Developmental Biology* **1995**, *11*, 417-440.
5. Bredt, D. S.; Snyder, S. H. Nitric oxide: a physiologic messenger molecule. *Annu Rev Biochem.* **1994**, *63*, 175-195.
6. Chin, C.-H.; Tsai, F.-C.; Chen, S.-P.; Wang, K.-C.; Chang, C.-C.; Pai, M.-H.; Fong, T.-H. YC-1, a potent antithrombotic agent, induces lipolysis through the PKA pathway in rat visceral fat cells. *European Journal of Pharmacology* **2012**, *689*, 1-7.
7. Rószter, T. The Biology of Subcellular Nitric Oxide. **2012**.
8. Hon, W. M.; Lee, K. H.; Khoo, H. E. Nitric Oxide in Liver Diseases. *Annals of the New York Academy of Sciences* **2002**, *962*, 275-295.
9. Murillo-Carretero, M.; Ruano, M. J.; Matarredona, E. R.; Villalobo, A.; Estrada, C. Antiproliferative effect of nitric oxide on epidermal growth factor-responsive human neuroblastoma cells. *J Neurochem* **2002** *83*, 119-131.
10. Irokawa, M.; Nishinaga, M.; Ikeda, U.; Shinoda, Y.; Suematsu, M.; Gouda, N.; Ishimura, Y.; Shimada, K. Endothelial-derived nitric oxide preserves anticoagulant heparan sulfate expression in cultured porcine aortic endothelial cells. *Atherosclerosis* **1997**, *135*, 9-17.
11. Joos, G. F. Potential usefulness of inhibiting neural mechanisms in asthma. *Monaldi Arch Chest Dis* **2000** *55*, 411-414.
12. Ignarro, L. J.; Cirino, G.; Casini, A.; Napoli, C. Nitric Oxide as a Signaling Molecule in the Vascular System: An Overview. *Journal of Cardiovascular Pharmacology* **1999**, *34*, 879-886.
13. Vallance, P.; Leiper, J. Blocking NO synthesis: how, where and why? *Nat Rev Drug Discov* **2002**, *1*, 939-950.
14. Moncada, S.; Erusalimsky, J. D. Does nitric oxide modulate mitochondrial energy generation and apoptosis? *Nat Rev Mol Cell Biol* **2002**, *3*, 214-220.
15. Lala, P. K.; Chakraborty, C. Role of nitric oxide in carcinogenesis and tumour progression. *The Lancet Oncology* **2001**, *2*, 149-156.
16. Nandagopal, K.; Dawson, T. M.; Dawson, V. L. Critical Role for Nitric Oxide Signaling in Cardiac and Neuronal Ischemic Preconditioning and Tolerance. *Journal of Pharmacology and Experimental Therapeutics* **2001**, *297*, 474-478.
17. Matthys, K. E.; Bult, H. Nitric oxide function in atherosclerosis. *Mediators of Inflammation* **1997**, *6*, 3-21.
18. Alderton, W. K.; Cooper, C. E.; Knowles, R. G. Nitric oxide synthases: structure, function and inhibition. *Biochemical Journal* **2001**, *357*, 593-615.
19. Garthwaite, J.; Charles, S. L.; Chess-Williams, R. Endothelium-derived relaxing factor release on activation of NMDA receptors suggests role as intercellular messenger in the brain. *Nature* **1988**, *336*, 385-8.

20. Hibbs, J. B.; Taintor, R. R.; Vavrin, Z.; Rachlin, E. M. Nitric oxide: A cytotoxic activated macrophage effector molecule. *Biochemical and Biophysical Research Communications* **1988**, 157, 87-94.
  21. White, A. A.; Aurbach, G. D. Detection of guanyl cyclase in mammalian tissues. *Biochimica et Biophysica Acta (BBA) - Enzymology* **1969**, 191, 686-697.
  22. Smith, M.; Drummond, G. I.; Khorana, H. G. Cyclic Phosphates. IV.1 Ribonucleoside-3',5' Cyclic Phosphates. A General Method of Synthesis and Some Properties. *Journal of the American Chemical Society* **1961**, 83, 698-706.
  23. Rall, T. W.; Sutherland, E. W. Formation of a cyclic adenine ribonucleotide by tissue particles. *J. Biol. Chem.* **1958**, 232, 1065-1076.
  24. Ashman, D. F.; Lipton, R.; Melicow, M. M.; Price, T. D. Isolation of adenosine 3',5'-monophosphate and guanosine 3',5'-monophosphate from rat urine. *Biochemical and Biophysical Research Communications* **1963**, 11, 330-334.
  25. Arnold, W. P.; Mittal, C. K.; Katsuki, S.; Murad, F. Nitric oxide activates guanylate cyclase and increases guanosine 3':5'-cyclic monophosphate levels in various tissue preparations. *Proceedings of the National Academy of Sciences of the United States of America* **1977**, 74, 3203-3207.
  26. Schultz, K.-D.; Schultz, K.; Schultz, G. Sodium nitroprusside and other smooth muscle-relaxants increase cyclic GMP levels in rat ductus deferens. *Nature* **1977**, 265, 750-751.
  27. Furchgott, R. F.; Zawadzki, J. V. The obligatory role of endothelial cells in the relaxation of arterial smooth muscle by acetylcholine. *Nature* **1980**, 288(5789) 373-376.
  28. Moncada, S.; Palmer, R. M.; Higgs, E. A. The discovery of nitric oxide as the endogenous nitrovasodilator. *Hypertension* **1988**, 12, 365-372.
  29. Ignarro, L. J.; Buga, G. M.; Wood, K. S.; Byrns, R. E.; Chaudhuri, G. Endothelium-derived relaxing factor produced and released from artery and vein is nitric oxide. *Proceedings of the National Academy of Sciences of the United States of America* **1987**, 84, 9265-9269.
  30. Murad, F. Discovery of some of the biological effects of nitric oxide and its role in cell signaling (Nobel lecture). *Angew. Chem. Inter. Ed.* **1999**, 38, 1857-1868.
  31. Ignarro, L. J. Nitric Oxide: A Unique Endogenous Signaling Molecule in Vascular Biology (Nobel Lecture). *Angew. Chem. Inter. Ed.* **1999**, 38, 1882-1892.
  32. Furchgott, R. F. Endothelium-Derived Relaxing Factor: Discovery, Early Studies, and Identification as Nitric Oxide (Nobel Lecture). *Angew. Chem. Inter. Ed.* **1999**, 38, 1870-1880.
  33. Lohmann, S. M.; Vaandrager, A. B.; Smolenski, A.; Walter, U.; De Jonge, H. R. Distinct and specific functions of cGMP-dependent protein kinases. *Trends in Biochemical Sciences* **1997**, 22, 307-312.
  34. Zagotta, W. N.; Siegelbaum, S. A. Structure and Function of Cyclic Nucleotide-Gated Channels. *Annual Review of Neuroscience* **1996**, 19, 235-263.
  35. Degerman, E.; Belfrage, P.; Manganiello, V. C. Structure, Localization, and Regulation of cGMP-inhibited Phosphodiesterase (PDE3). *Journal of Biological Chemistry* **1997**, 272, 6823-6826.
-



---

## CHAPTER II

### SOLUBLE GUANYLATE CYCLASE: THE ENDOGENOUS NITRIC OXIDE RECEPTOR

#### SYNOPSIS

---

<b>1 – Involvement of Guanylate cyclase in physiological processes.....</b>	<b>12</b>
1.1 – Smooth muscle relaxation.....	12
1.2 – Platelet aggregation and disaggregation .....	14
1.3 – Apoptosis .....	15
A – NO as a pro-apoptotic inducer.....	16
B – NO as an anti-apoptotic modulator.....	16
1.4 – Tumor progression and angiogenesis.....	17
1.5 – Proliferation and differentiation of cells .....	19
A – Inhibition of cell proliferation .....	19
B – Enhanced proliferation.....	19
C – Differentiation.....	20
1.6 – Neuronal communication.....	20
1.7 – Inflammation.....	21
<b>2 – Guanylate cyclase structure and molecular functioning.....</b>	<b>22</b>
2.1 – Structure of sGC .....	22
2.2 – The heme coordination .....	26
2.3 – Electronic and chemical properties of nitric oxide .....	29
2.4 – Guanylate cyclase biochemistry .....	31
2.4.1 – cGMP-dependent protein kinases.....	32
2.4.2 – Other targets of cGMP.....	33
2.4.3 – Kinetics of GTP and NO binding to sGC.....	34
<b>3 – Guanylate cyclase pharmacology .....</b>	<b>35</b>
3.1 – Activators of Guanylate cyclase .....	35
3.1.1 – Heme-dependent sGC allosteric activators .....	35
3.1.2 – Heme-independent sGC activators .....	38
3.1.3 – Isoliquiritigenin .....	39
3.2 – Inhibitors of guanylate cyclase .....	40
3.2.1 – Heme-oxidizing inhibitors.....	40
3.2.2 – Inhibitors which bind to sGC catalytic domain.....	41
<b>4 – Objectives of the present study .....</b>	<b>44</b>
<b>5 – Bibliography .....</b>	<b>45</b>

## **1 – Involvement of Guanylate cyclase in physiological processes**

The soluble guanylate cyclase (sGC) is the primary nitric oxide (NO) receptor in mammals and the central component of the NO-signaling pathway. The functioning of this endogenous NO-receptor is crucial in several diseases and we focused here on the study of activation and deactivation mechanisms of sGC, which are directly linked with pathological processes.

sGC is located in many cells, tissues and organs. This fact indicates involvement of NO-sGC-cGMP signaling pathway in a wide regulation of intracellular metabolism: regulation of blood pressure (smooth muscle relaxation and vasodilation) [1, 2], platelet aggregation and disaggregation [3], apoptosis [4], signaling in tumor cell proliferation (angiogenesis) [5, 6], immune response [7], proliferation, and differentiation of cells [8], plasticity, communication between neurons [9, 10], and in inflammation [11, 12]. Because of its very wide involvement, we will describe in this first part the role of sGC in several (but not all) physiological processes, then its molecular properties, ending this part with the objectives of the present study. The experimental details are given at the beginning of each chapter.

### **1.1 – Smooth muscle relaxation**

Smooth muscle relaxation (vasodilation) in cardiovascular system through the NO-sGC-cGMP pathway is a significant and historical feature of NO signaling [2, 13]. The research of NO as signaling molecule was conducted after the discovery of Endothelium-derived relaxing factor (EDRF) by Robert Furchgott in 1980 [14]. He showed the ability of endothelial cells to generate and release a labile substance that produced relaxation of the underlying smooth muscle in the vascular segment. Later, Ignarro and Murad conducted a series of experiments to determine whether EDRF released from artery could activate guanylate cyclase and thereby account for elevated cyclic GMP levels in response to acetylcholine or bradykinin [15, 16]. It was shown that activation of sGC by EDRF was heme-dependent, like its activation by nitric oxide. In 1988 the fact that EDRF is NO was revealed [15, 17].

Vasodilation signaling starts from the binding of first messengers (acetylcholine, bradykinin) present in blood flow to their receptors (G proteins) incorporated within the membrane of endothelial cells (EC, monocellular layer inside wall of the artery) (Figure 1). This binding causes activation of inositol trisphosphate (IP<sub>3</sub>) system, where IP<sub>3</sub> binds to Ca<sup>2+</sup> channels of the endoplasmic reticulum that releases Ca<sup>2+</sup> ions to the cytosol. This event induces the binding of Ca<sup>2+</sup>/calmodulin complex to the enzyme NO-synthase and triggers the synthesis of NO from L-arginine to L-citrulline. Then, NO very easily diffuses through the cell membrane to reach its sGC receptor in the smooth muscle cells surrounding the artery.

The sGC catalyzes the formation of cGMP from GTP leading to cGMP-dependent protein kinases (PKG) activation in smooth muscle cells. Phosphodiesterase 5 (PDE-5) is the enzyme which regulate intracellular cGMP level by catalyzing the hydrolytic cleavage of the 3' phosphodiester bond of the cyclic nucleotides. PKG causes reuptake of  $\text{Ca}^{2+}$  and the opening of calcium-activated potassium channels in smooth muscle membrane. The fall in concentration of  $\text{Ca}^{2+}$  in the cytoplasm ensures that the myosin light-chain kinase can no longer phosphorylate the myosin molecule, thereby stopping the cross-bridge cycle and leading to relaxation of the smooth muscle cell [18].

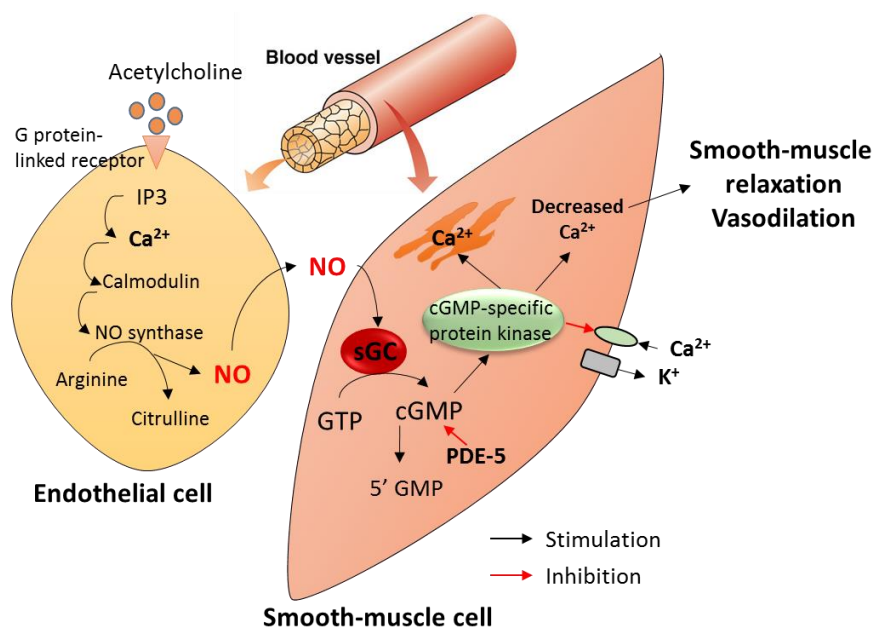


**Figure 1.** Smooth muscle cell relaxation and subsequent vasodilation controlled by the NO – cGMP – sGC pathway. NO is produced in endothelial cells and diffuses through the cell membrane to the smooth-muscle cell to activate sGC. Then sGC catalysis cGMP formation from GTP, which activates in turn PKG and induces smooth muscle relaxation. IP3: inositol trisphosphate, NO: nitric oxide, sGC: soluble guanylate cyclase, PDE-5: phosphodiesterase 5. Modified scheme is taken from [19].

Impairment of the NO-cGMP signaling pathway in arteries is implicated in cardiovascular diseases, including systemic arterial and pulmonary hypertension (PAH), coronary artery disease, peripheral vascular disease, and atherosclerosis [20, 21]. Pulmonary hypertension is an increase of blood pressure in lung vasculature (in the pulmonary artery, pulmonary vein, or pulmonary capillaries) due to narrowing of blood vessels connected to and within the lungs. The affected blood vessels become stiffer and thicker, in a process known as fibrosis. Unregulated vasoconstriction makes harder for the heart to pump blood through the lungs. The increased workload of the heart causes hypertrophy of the right ventricle, making the heart less able to pump blood through the lungs, and therefore, the right ventricular muscle cannot get enough oxygen to meet its needs [22].

The pathology of PAH results from pulmonary endothelial cell dysfunction or injury accompanied by dysregulation of various signaling pathways, including decreased production of NO, prostacyclin and increased levels of endothelin-1, thromboxane A2 and serotonin [23]. The oxidative stress can also lead to superoxide anions reaction with nitric oxide to generate peroxynitrite which oxidizes and uncouples eNOS thereby impairing NO synthesis and causing uncoupled eNOS to generate reactive oxygen species. Thus oxidative stress results in oxidation of heme group of sGC, which renders it less responsive to NO and can result in dissociation of heme from sGC [23]. Oxidative stress also leads to atherosclerosis, an inflammatory disease where arterial lesions are formed via a complex process involving platelet adhesion, leukocyte infiltration and activation and intimal migration and proliferation of smooth muscle cells.

### 1.2 – Platelet aggregation and disaggregation

The NO-sGC-cGMP pathway in platelet activation has been investigated for more than 30 years. It appeared that NO and cGMP play both a stimulatory and an inhibitory role in platelet activation depending on cAMP activity [3, 24, 25]. The levels of free cytosolic cAMP and cGMP are controlled by their synthesis through adenylate cyclase (AC) and sGC (Figure 2).

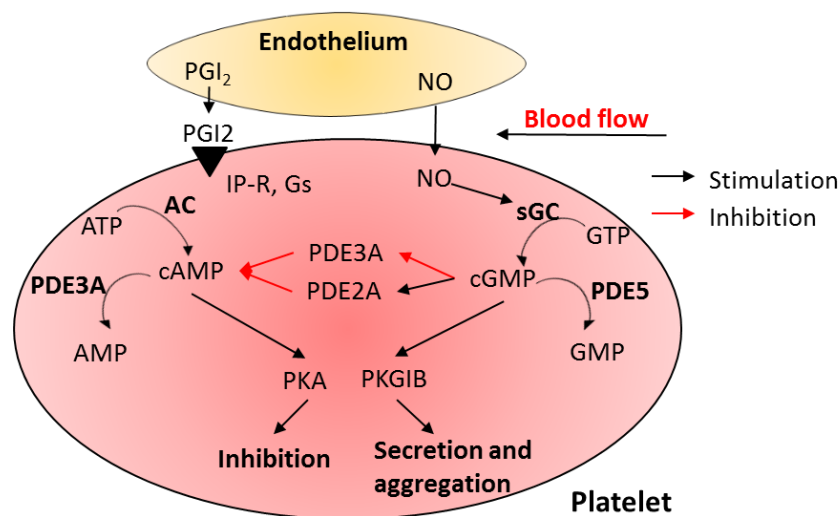


**Figure 2.** NO-sGC-cGMP signaling pathway in platelets. The intact endothelium releases prostaglandin I<sub>2</sub> (PGI<sub>2</sub>) and nitric oxide (NO) to activate adenylate cyclase (AC) and soluble guanylyl cyclase (sGC), leading to the formation of cAMP and cGMP, correspondingly. cAMP phosphorylates phosphokinase A (PKA), which inhibits granule release, adhesion, and aggregation of platelets, and cGMP phosphorylates phosphokinase G (PKG), which is responsible for secretion and aggregation of platelets. cGMP controls the activity of cAMP through inhibition of PDE3A and activation of PDE2A. Modified scheme is taken from [26].

The intact endothelial cells inhibit platelet activation by producing nitric oxide, endothelial-ADPase and prostacyclin, where endothelial-ADPase degrades the platelet

activator ADP. Resting platelets maintain active calcium efflux via a cyclic AMP-activated calcium pump. Intracellular calcium concentration determines platelet activation status driving platelet conformational change and degranulation. The two signaling systems cAMP and cGMP work together for controlling inhibition or activation of granule release, adhesion, and aggregation of platelets.

Adenylate cyclase located in platelets is activated by G-protein-coupled receptor signaling. Binding of prostacyclin (prostaglandin I<sub>2</sub>) from endothelial cells to its IP receptor on the platelet surface activates the intracellular receptor-linked stimulatory G-protein (G<sub>s</sub>). G<sub>s</sub> is turned into its active GTP-bound form, G<sub>s</sub>-GTP which binds to adenylate cyclase and stimulates the synthesis of cAMP from ATP. Increase of cAMP production promotes the efflux of calcium and reduces its intracellular availability for platelet activation.

Soluble guanylate cyclase is abundantly present in platelets and is activated by NO synthesized in platelets or diffused through the platelets membrane from endothelium. The second messenger cGMP synthesized by sGC from GTP activates the cGMP-dependent protein kinases G (PKG) and also inhibits phosphodiesterase 3 (PDE3), an enzyme that destroys cyclic adenosine monophosphate (cAMP). cAMP activates the protein kinase A (PKA), a known platelet aggregation inhibitor. Subsequent substrate phosphorylation results in the inactivation of small G-proteins of the Ras and Rho families, inhibition of the release of Ca<sup>2+</sup> from intracellular stores, and modulation of actin cytoskeleton dynamics. cAMP and cGMP are both degraded by phosphodiesterases, which might restrict signaling to specific subcellular compartments. An emerging principle of cyclic nucleotide signaling in platelets is the high degree of interconnection between activating and cAMP/cGMP-dependent inhibitory signaling pathways at all levels, including cAMP/cGMP synthesis and breakdown, and PKA/PKG-mediated substrate phosphorylation. Consequently, defects in cAMP/cGMP pathways might contribute to platelet hyperactivity in cardiovascular diseases [26].

### **1.3 – Apoptosis**

Dysregulated apoptosis plays a critical role in the development of a number of pathologies, including tumorigenesis and chemoresistance. NO may have both pro- and anti-apoptotic properties depending on cell lines, the background redox state of the cell, the amount of generated NO and the isoform of nitric oxide synthase (NOS). For instance, protective effects in stroke seem to be mediated by eNOS (vascular), whereas harmful effects are due to NO from nNOS activity (neuronal toxicity) [27, 28]. At low concentrations, NO seems to be anti-apoptotic, in part through inhibition of caspase activity by means of nitrosation, whereas at higher concentrations, it can indirectly activate caspases [29, 30].

### **A – NO as a pro-apoptotic inducer**

NO induces biochemical characteristics of apoptosis in several cell types: macrophages, thymocytes, pancreatic islets, certain neurons, and tumor cells [31]. Although the precise mechanism that determines the cellular sensitivity to NO-induced apoptosis is not clearly understood, the pro-apoptotic effects of NO on these cells seem to be independent (but not all) of the cGMP accumulation through the activation of soluble guanylate cyclase.

Activation of NO-cGMP apoptotic signaling pathway occurs in the case of high concentrations of NO or peroxynitrite that revealed the induction of cytotoxicity against tumor cells and surrounding tissues via cytochrome c release from mitochondria, p53 accumulation and JNK/SAPK activation [31] [32, 33]. The induction of apoptosis can be blocked by the inhibition of soluble guanylyl cyclase with ODQ or the cGMP-dependent protein kinase G inhibitor KT5822 [34]. Activation of sGC induce apoptosis in cardiomyocytes, human colon cells [35], pulmonary artery smooth muscle cells [36], and neuronal cells [37].

### **B – NO as an anti-apoptotic modulator**

The mechanism underlying the NO-mediated anti-apoptotic effects may be cell-type specific with multiple pathways in hepatocytes, human B lymphocytes, endothelial cells, splenocytes eosinophils and cells derived from rat adrenal medulla (PC12) [31]. For example, NO (5 – 100  $\mu$ M) blocks apoptosis in PC12 cells via the NO/cGMP/PKG pathway [38] and inhibits hepatocyte apoptosis, both through cGMP-dependent interruption of apoptotic signaling and direct inhibition of caspase activity [39].

Inhibition of apoptosis by NO produced by sGC activation may be associated with the induction of heat shock protein 70 (Hsp 70) response, suppression of Bax expression, induction of protective pathways through the induction of heme oxygenase and cyclooxygenase. It may involve up-regulation of intracellular antioxidant systems, especially glutathione, inhibit caspase 3-like enzymes via S-nitrosylation or through a cGMP dependent mechanism, both leading to inactivation of caspases [40]. It has been shown that the signaling pathway by which NO prevents apoptosis in cardiomyocytes includes the up-regulation of an inhibitor (p21 waf1) which acts on the important cyclin-dependent kinase 2 (A/cdk2) [41]. Inhibitors of NOS down-regulate the serine/threonine kinase (Akt) survival pathway and inhibit phosphorylation of cAMP-responsive element-binding protein (CREB) via cGMP associated with decreased Bcl-2 expression in cerebellar neurons [42], whereas exposure to NO donors increases cGMP in cardiomyocytes, neural and pancreatic cell lines [40].

Figure 3 shows several possibilities of the NO–cGMP–PKG involvement in the apoptosis pathways of the ovarian cancer cells which express all key components of the NO–cGMP–PKG signaling pathway, including three isoforms of NOS, providing an endogenous source of NO [43]. Besides, cancer cells continuously produce NO at low physiological

levels, activating the sGC and elevating cGMP levels sufficiently enough to cause continuous high-level activation of PKG. Such sGC/cGMP basal activity regulates p53 expression and promotes cell survival in part through regulation of caspase-3. Another regulating mechanism goes through the cGMP/PKG-I $\alpha$  signaling pathway which maintains the expression of certain inhibitors of apoptosis proteins (such as c-IAP1, livin, survivin, anti-apoptotic Bcl-2 family member Mcl-1) which decrease activity of caspase-3 and promote cell survival. In all cases, hyperactivated PKG-I $\alpha$  increases inhibitors of apoptosis proteins and resistance to apoptosis [44].

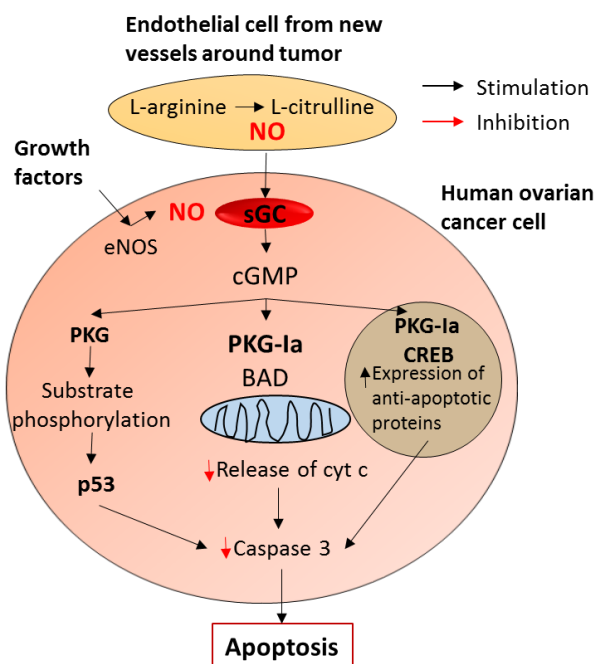


**Figure 3.** Involvement of NO–cGMP–PKG in apoptosis pathways in ovarian cancer cells. sGC (soluble guanylate cyclase), NO (nitric oxide), cGMP (cyclic guanosine monophosphate), PKG-I $\alpha$  (protein kinase G type Ia), eNOS (endothelial nitric oxide synthase), cyt c (cytochrome c), BAD (Bcl-2-associated death promoter protein), CREB (cAMP response element-binding protein, cellular transcription factor), p53 (cellular tumor antigen). Modified scheme is taken from [44].

### 1.4 – Tumor progression and angiogenesis

The role of NO – cGMP signaling in tumor biology has been extensively studied during the last three decades and it has been shown that NO exhibits a paradoxical and diverse role in many cancer types, as we have seen for apoptosis.

The effect of NO in the regulation of cell survival and cell death in many cancer types can be either cGMP-dependent or cGMP-independent. The first mechanism, cGMP-dependent works through activation of soluble guanylate cyclase by NO. The second mechanism, cGMP-independent is mediated by reactive nitrogen species that are produced as a result of the interaction of NO with dioxygen (O $_2$ ), oxygen reactive species or superoxide radicals ( $\bullet$ O $^{2-}$ ) [45]. The NO-cGMP signaling is involved in resistance to apoptosis in human

melanoma [46], suppresses apoptosis in ovarian cancer cells [47], prostate cancer cells [48], bone cancer [49], head and neck cancer cells [50], and in some cases mediates angiogenesis with endothelial cells [51]. Endothelial NOS, sGC and PKG participate in anti-apoptotic and pro-angiogenic effects of PI3K/Akt pathway (phosphatidylinositol 3-kinase / protein kinase B). This pathway plays an essential role in promoting angiogenesis or tumor vascularization [44]. For example, the presence of active sGC in the chicken chorioallantoic membrane (CAM) was detected during the days of maximal angiogenesis [51]. Inhibition of sGC decreased neovascularization in the CAM and sGC activation promoted the formation of neovessels. *In vitro*, pharmacological activation of sGC or adenovirus-mediated sGC gene transfer promoted endothelial cell proliferation and migration, whereas sGC inhibition blocked tube-like network formation. In addition, sGC inhibition blocked the migratory response to vascular endothelial cell growth factor [51]. These results have directly motivated our study described in CHAPTER III.

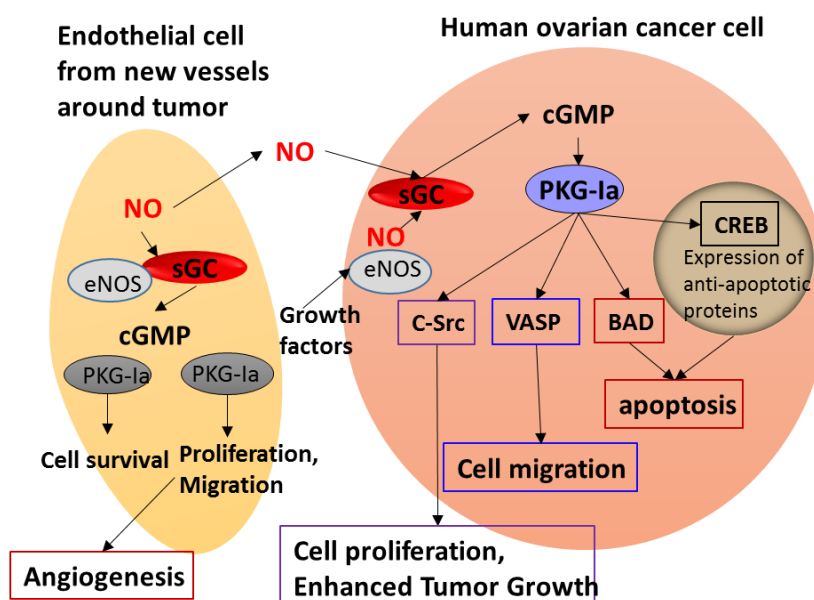


**Figure 4.** Cellular model of the involvement of the NO/cGMP/PKG-I $\alpha$  signaling pathway in promoting chemoresistance, tumor growth, angiogenesis, and apoptosis of ovarian cancer. The simplified scheme is taken from [44]. eNOS: endothelial nitric oxide synthase, sGC: soluble guanylate cyclase, cGMP: cyclic guanosine monophosphate, PKG-I $\alpha$  – splice variant of phosphokinase G, C-Src – proto-oncogene tyrosine-protein kinase, VASP – vasodilator-stimulated phosphoprotein, BAD: B-cell lymphoma 2 associated death promoter protein, CREB: cyclic adenosine monophosphate response element-binding protein.

A cellular model of the involvement of the NO/cGMP/PKG-I $\alpha$  signaling pathway in promoting chemoresistance, tumor growth, angiogenesis, and apoptosis of ovarian cancer is shown in Figure 4. The low physiological level of NO activates sGC, elevating cGMP levels that enhance the activation of PKG-I $\alpha$  splice variant of PKG. Additional NO can be produced

by endothelial cells after their invasion into the tumor by providing new blood vessels. PKG- $\alpha$  phosphorylates several downstream proteins leading to enhanced cell proliferation, contributing to chemoresistance in ovarian cancer cells and increased cell migration and invasion. We presented here a simplified scheme of the NO-sGC-cGMP signaling pathway in tumor progression and angiogenesis, although the mechanisms are more complicated and have much more intermediate steps that can be found in reference [52].

### **1.5 – Proliferation and differentiation of cells**

The major effect exerted by NO on cell proliferation in normal and tumor cell types is the arrest of cell cycle progression and subsequent inhibition of the proliferative processes [53]. From another side, there are a large number of studies showing the stimulatory action of NO on cell proliferation. The decisive factor is the actual concentration of NO. For example, proliferation increases at low concentration of NO in the micromolar or sub-molar range but decreases for NO concentration in millimolar range [54]. An overview of the proliferation inhibition by NO in different types of normal and tumor cells is presented in [53].

#### **A – Inhibition of cell proliferation**

Soluble guanylate cyclase is the primary target of NO in cell proliferation, inducing the rise in the concentration of cGMP as demonstrated in vascular smooth muscle [55] and endothelial cells [56], and glial cerebellar cells [57]. cGMP-dependent down-regulation of proto-oncogene N-Myc is critical for the NO-induced proliferative arrest and for neuronal differentiation induced by NO in SK-N-BE neuroblastoma cells [58]. Inhibition of cell proliferation mediated by inducible NOS (through interferon IFN $\gamma$  stimulation) correlates with a rise in cGMP in liver stellate cells [59] and vascular smooth muscle cells [60]. Activation of sGC stimulates production of cGMP and dependent protein kinase (PKG) leading to subsequent phosphorylation of vasodilator-stimulated phosphoprotein, inhibition of Raf1, and therefore decreases signaling by the mitogen-activated protein kinases pathway [53].

#### **B – Enhanced proliferation**

Stimulatory action of exogenous NO on the proliferation of different cultured cells is described in [54]. The molecular mechanisms underlying the proliferative action of NO $\bullet$  at low concentration are not yet well understood. However, it was demonstrated that NO in concentration up to 100  $\mu$ M induces proliferation of bovine coronary venule endothelial cells [61], umbilical vein endothelial cells [62], cardiomyocytes [63], myoblasts [64] and cancer cells such as ovarian carcinoma [65], pancreatic tumor [66] and pheochromocytoma PC12 cells [67] via cGMP signaling pathway.

### **C – Differentiation**

NO signaling system also participates in the differentiation of mouse and human progenitor cells in bone marrow by suppressing the activity of NO synthases [68] and embryonic stem cells (ESC) into cardiomyocytes [69]. Some studies indicate that the NOS-1 isoform is expressed in both mouse and human ESC and mRNA and protein levels fall to basal level as ESC differentiate. Stem cells express low level of protein kinase G [70] and do not express enzymatically active NO receptor sGC, but sGC  $\alpha 1$ ,  $\alpha 2$ , and  $\beta 1$  levels increase during cell differentiation which lead to a robust increase in NO-inducible intracellular cGMP levels. Slow-release of NO donor provided a modest increase in the differentiation of mouse and human ES cells into myocardial cells [71]. Activation of sGC by BAY 41-2272 or YC-1 caused a 3- to 4-fold increase in the mRNA expression of the cardiac specific transcription factor (Nkx2.5) and cardiac markers myosin light chain 2 and major histocompatibility complex [69]. Some plant compounds have an effect on in stem cells differentiation via the NO-cGMP signaling system. For example the flavonoid icariin from *Herba Epimedii* [72] induces differentiation of mouse ESC into cardiomyocytes by elevating the cAMP/cGMP ratio and upregulates the endogenous generation of NO during the early stages of cardiac development. The angiogenesis inhibitor Genistein, phytoestrogen found predominantly in soy stimulates osteoblastic differentiation in bone marrow culture [73] and the polyphenol curcumin induces differentiation of stem cells via modulation of the NO pathway [74].

### **1.6 – Neuronal communication**

Depending on the brain region and nitric oxide concentration, NO can both stimulate and inhibit the release of a particular transmitter. Being a multifunctional messenger in the central nervous system, it regulates primarily the release of glutamate, which then modulates the release of various other transmitters in several brain regions, such as the hippocampus, the striatum, the hypothalamus and the locus coeruleus.

NO signaling pathway in neuronal communication involves soluble guanylyl cyclase and cGMP, but increase of cGMP can also arise independently of NO via activation of membrane-bound particulate guanylyl cyclase by natriuretic peptides. We will only describe the NO-dependent pathway in neuronal communication presented in Figure 5. The targets of cGMP are cGMP-dependent protein kinases (PKG), cyclic nucleotide hydrolyzing phosphodiesterases and cyclic nucleotide-gated (CNG) cation channels. The neuronal NOS (nNOS) is abundantly expressed throughout the central nervous system and represents the principal source of NO in many neurons [10]. It is a  $\text{Ca}^{2+}$ /calmodulin-regulated enzyme, which can be activated by  $\text{Ca}^{2+}$  influx via N-methyl-D-aspartate (NMDA) receptors [9]. Endothelial NOS expression is confined to endothelial cells but NO released within the cerebral vasculature is able to transmit signal to axons located in close proximity [75]. NO stimulates cGMP synthesis within glutamatergic neurons (Figure 5).

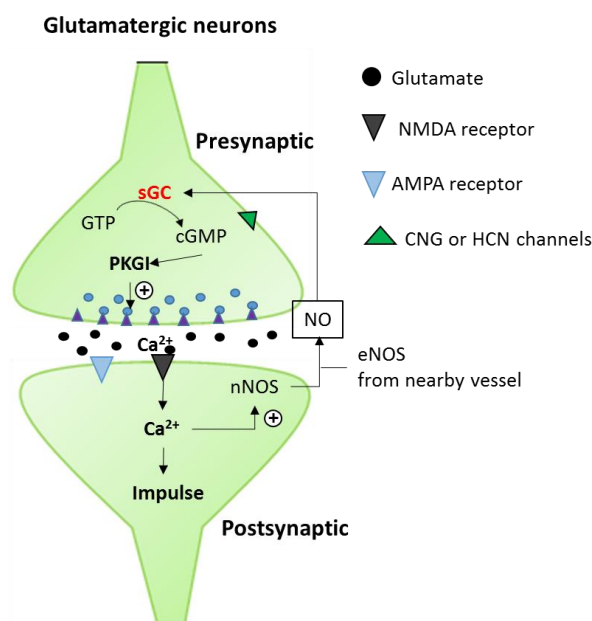


**Figure 5.** NO – cGMP – sGC signaling pathway in a glutamatergic synapse. Modified scheme is taken from [9].

Nitric oxide (NO) generated postsynaptically by  $\text{Ca}^{2+}$ /calmodulin-activated neuronal NO synthase (nNOS) and derived from eNOS in nearby vessels diffuses to the presynaptic terminal, where it activates sGC. Depending on the NO concentration, glutamate release is either enhanced or decreased, resulting in either enhanced or decreased activation of postsynaptic NMDA or AMPA/kainate receptors on cholinergic neurons followed by enhanced or decreased acetylcholine release. The resulting increase of the intracellular second messenger cGMP activates various receptors, including the cGMP-dependent protein kinase I (PKGI). Through phosphorylation of its substrates, PKGI leads to an increase in presynaptic transmitter release [9]. This action is thought to involve clustering of vesicular proteins and proteins of the docking/fusion machinery in the presynaptic membrane (purple triangles) at the release sites. In addition, cGMP may modulate transmitter release by activating presynaptic ion channels regulated by cyclic nucleotides (CNG and HCN channels) [10].

### 1.7 – Inflammation

Inflammation involves complex signaling pathways such as increasing blood flow, cytokine interaction and the recruitment of a number of cell types that can lead to oxidative stress, cell death, angiogenesis and neurogenesis [11]. The role of NO in inflammation is complicated because at high concentration it is cytotoxic and proinflammatory but has opposite effect at low concentration. For example, inducible NOS is synthesized by macrophages and other immune cells produce NO in the micromolar range. At such

concentration, NO induces oxidative damage of DNA and modifications of protein structure and function that can lead to cell death. In contrast, NO produced by endothelial NOS, which is constantly present in the cell at nanomolar concentrations has an anti-inflammatory effect [12]. NO acts at low concentration and the level of cGMP is regulated by specific enzymes phosphodiesterases (PDEs) which convert cGMP to GMP. Thereby, intracellular level of cGMP is regulated by both sGC activity and PDE. Several PDE inhibitors have been found and used as therapeutic agents as they increase cyclic nucleotide levels, enhancing NO-cGMP signalization [76]. Selective PDE5 inhibitors sildenafil (Viagra, Pfizer) and vardenafil (Levitra, Bayer) and the PDE4 inhibitor ibudilast increase levels of cGMP/cAMP in the brain and have a protective effect, including improved memory in aged rats [77] and mice [78], decreased cell damage in the event of ischemic cerebrovascular injury [79], and protection of multiple sclerosis patients from neurodegeneration [11]. The sildenafil enhancing effect of cGMP is also useful in the treatment of pulmonary hypertension and congestive heart failure. It may promote ischemia-induced angiogenesis and immune regulation [12].

## 2 – Guanylate cyclase structure and molecular functioning

### 2.1 – Structure of sGC

Guanylate cyclase exists in the cells as a membrane-spanning form (particulate GC, pGC without heme and not activated by NO) and a soluble form (sGC activated by NO). Both pGC and sGC form cGMP but involved in different cGMP signaling pathways. The ratio between these two forms of the enzyme depends on tissues. Soluble and particulate GC encoded by separate genes and differ not only in the localization but also in activity and regulation mechanism. The 3 types of particulate guanylate cyclase are activated by different regulators: atrial natriuretic factor, the natriuretic peptide of the brain and intestinal peptide, guanylin [80]. Only sGC possess a heme cofactor, and we have only worked on this protein.

Although sGC is the endogenous NO receptor constitutively expressed in the cytoplasm of many mammalian cells, the 3D X-ray structure of the entire protein has not yet been determined, because of the difficulty of obtaining crystals. But in the last decade, several teams have been able to obtain the crystal structures of isolated sGC domains from different organisms [81, 82] and then to reconstruct the sGC full structure using a template obtained by cryo-electromicroscopy [132]. Soluble guanylate cyclase consists of two subunits (Figure 6): the catalytic  $\alpha$ -subunit harboring the GTP binding site and the regulatory  $\beta$ -subunit, which contains the heme prosthetic group necessary for NO stimulation.

In humans, several isoforms of sGC exist,  $\alpha 1$ ,  $\alpha 2$ ,  $\beta 1$  and  $\beta 2$  [83] where subunits  $\alpha 1/\alpha 2$  share 46% sequence identity whereas  $\beta 1/\beta 2$  subunits share 41% sequence identity. Isoform  $\alpha 1\beta 1$  (also called GC1) is the most studied and the role of other isoforms is not well understood, although the  $\alpha 2\beta 1$  (GC2) complex is located in neural cells. Extensive

biochemical and kinetic analysis of both GC1 and GC2 does not reveal any significant difference especially regarding NO sensitivity and the enzymatic regulation of the isoforms appears to be similar [84]. The cloned  $\beta$ 1 subunit of guanylate cyclase from human, bovine and rat sources contains 619 amino acids and has a molecular mass of approximately 70 kDa [85]. The  $\alpha$ 1 subunit contains 690-717 amino acids and has a molecular mass of 77-82 kDa. Each subunit comprises two modular domains: the N-terminal and the C-terminal catalytic domain (Figure 6).

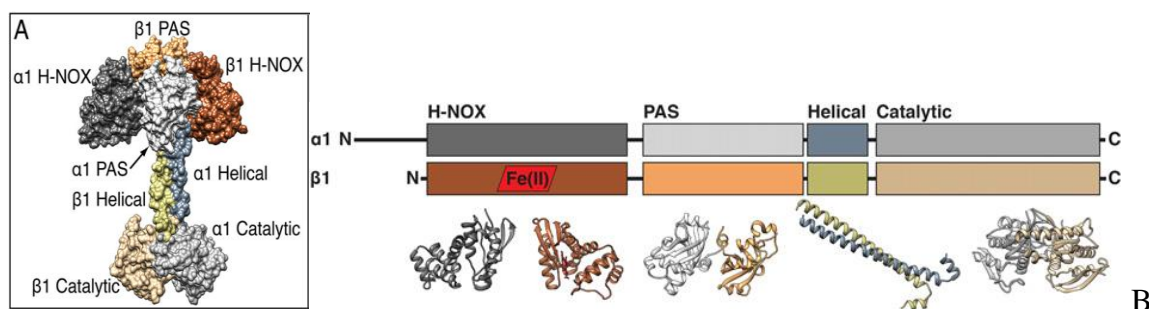


**Figure 6.** (A) The higher-order domain architecture of sGC obtained by electron microscopy. The individual structures of each domain were inserted in the overall envelope of sGC obtained by cryo-electron microscopy. (B) X-ray crystallographic models of sGC domains.  $\alpha$ 1 domains are shown in shades of gray, and  $\beta$ 1 domains are shown in color. The H-NOX domain of the  $\beta$ 1 subunit contains the heme cofactor, shown in red. The H-NOX structures are modeled from a standalone *Nostoc sp.* PCC 7120 H-NOX domain (PDB: 2O09). The PAS and helical domains are modeled on individual domain truncations. The PAS domain is based on the PAS domain from *Manduca sexta* (PDB: 4GJ4), and the helical domain is based on the  $\beta$ 1 *R. norvegicus* structure (3HLS). The catalytic domain is the *Homo sapiens*  $\alpha$ 1 $\beta$ 1 crystal structure (PDB: 3UVJ). Images are taken from [80].

The C-terminal domains of both subunits combine to form a heterodimeric catalytic domain. Both sGC subunits include three distinct regulatory and structural domains: N-terminal H-NOX (heme-containing NO/oxygen-binding) domain, a PAS (Per/Arnt/Sim)-like domain, and the  $\alpha$ -helical region capable of forming coiled coils. Only the  $\beta$  subunit binds ferrous heme iron liganded with the histidine 105 residue (His-105). The corresponding region of the  $\alpha$  subunit may have a similar structure, but lacks critical heme-binding residues [86].

The PAS and helical domains are responsible for heterodimerization and signal transmission [81]. The C termini of  $\alpha$  and  $\beta$  subunits constitute the catalytic domain with the cyclase active site formed at the subunit interface [87]. Bradley G. Fritz [88] and William Montfort [82] first modeled domain–domain contacts among the H-NOX, PAS, and coiled-coil domains by using chemical cross-linking of a truncated form of *Manduca sexta* sGC (*Ms* sGC-NT) (Figure 7). This protein lacks the  $\alpha$ 1 H-NOX domain and both cyclase domains but responds to gaseous ligands and stimulators in a similar manner to full-length sGC. Amine–amine and amine–carboxylate chemical crosslinks were introduced into the recombinant

protein and identified by high-resolution tandem mass spectrometry [134], showing that the coiled-coil domain was indeed formed from parallel helices. The  $\alpha 1$  H-NOX and PAS domains were in contact with the  $\beta 1$  H-NOX domain and with the coiled-coil domain as shown in Figure 10.

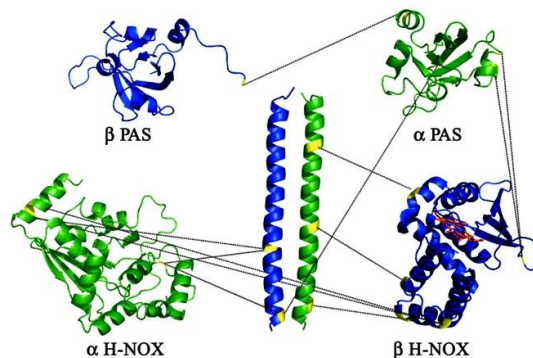


**Figure 7.** Model of domain contacts and intermolecular cross-links for  $\alpha 1$  and  $\beta 1$  subunits of *Ms* sGC-NT derived from chemical cross-linking and small-angle X-ray scattering. Nine cross-links were found between the coiled-coil and other domains in *Ms* sGC NT protein, eight of these were between the  $\alpha 1$  and  $\beta 1$  strands. Five additional cross-links were found between the other domains, four of which were between  $\alpha 1$  and  $\beta 1$  subunits. The image is taken from reference [88].

Interaction of NO with the sGC induces several discrete conformational changes in the enzyme, spanning from the N-terminal H-NOX domain to the C-terminal catalytic output domain. When NO binds to heme of sGC, the bond between the heme iron and the proximal histidine is broken (Figure 8). This cleavage is the very first event of the molecular switch from NO binding to cGMP release.

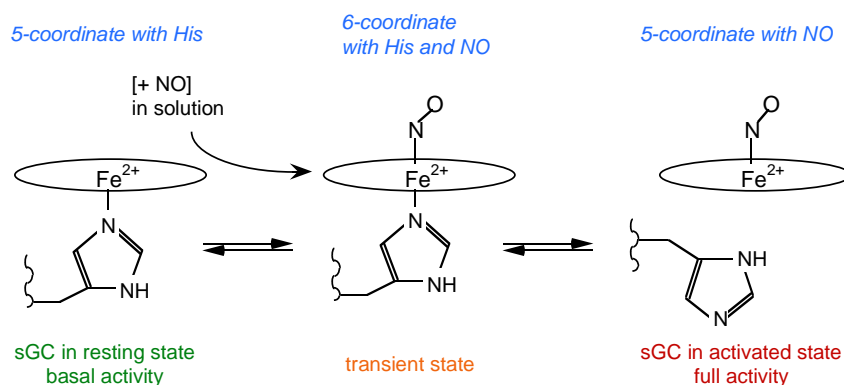


**Figure 8.** Mechanism of sGC activation by NO binding to the iron in the heme of  $\beta$  H-NOX domain. In resting state, iron is 5 coordinate with His ( $\text{Fe}^{2+}$ -5c-His). When NO binds to the heme of sGC, iron forms very short-time species  $\text{Fe}^{2+}$ -6c-NO-His as a transient state and then the covalent bond between the heme iron and the proximal histidine is broken forming  $\text{Fe}^{2+}$ -5c-NO leading to conformational changes and activation of sGC.

However, the entire mechanism of sGC functioning from this cleavage is not yet fully revealed. The discovery and crystal structure determination of prokaryotic homologs H-NOX

domain of sGC [141, 142] makes a valuable contribution to the understanding of sGC functioning.

The link between NO signaling in humans and bacterial NO sensing mechanism was first detected by Nioche *et al.* [89] and Pellicena *et al.* [90] independently in 2004. They proved that some bacteria have a NO sensing or NO-binding heme protein (SONO or H-NOX), which share 15 – 40% sequence identity with the human H-NOX domain of sGC. This protein was identified in bacteria across many phyla, including *Proteobacteria*, *Firmicutes*, *Bacteroidetes*, *Cyanobacteria*, and *Thermotogae* [91]. There are now over 250 known bacterial species that contain H-NOX proteins, but certain species, such as *Actinobacteria* or *Bacilli* lack H-NOX genes, although they produce NO [92]. Many other types of NO sensors exist and it is currently unknown what evolutionary processes govern the presence of H-NOX genes and associated signaling pathways.

The first crystal structure of H-NOX family member shown in Figure 9 was obtained from *Thermoanaerobacter tengcongensis* (Tt H-NOX).

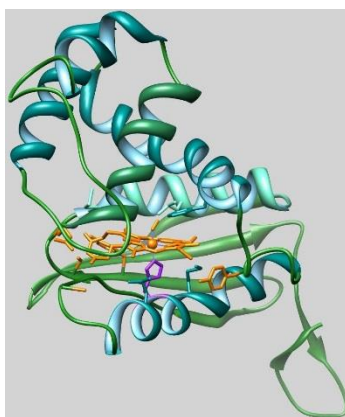


**Figure 9.** 3D model of the NO-sensing bacterial protein from *Thermoanaerobacter tengcongensis* (Tt-H-NOX). His-102 residue and heme prosthetic group are displayed in purple and yellow accordingly. The figure is generated using CHIMERA.

The heme cofactor is deeply buried between the two subdomains (helical N-terminal and C-terminal) and the central iron is coordinated axially to a conserved His residue on  $\alpha$ -helix [92]. The model of heme binding domain (H-NOX) of the human sGC was created based on the crystal structure of the prokaryotic H-NOX protein of *Thermoanaerobacter tengcongensis* (Figure 10).

The heme prosthetic group in the ferrous Fe(II) state is capable of coordinating several diatomic gas ligands O<sub>2</sub>, NO, and CO [92]. Consequently, a variety of gas-binding hemoproteins exist with very diverse properties toward gases. For example, the H-NOX domain of sGC is highly selective for NO and does not bind O<sub>2</sub>, whereas Tt-H-NOX has a very large affinity for O<sub>2</sub>.

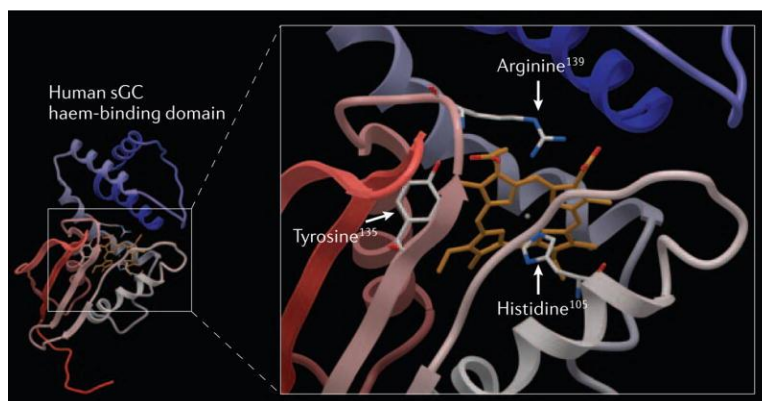


**Figure 10.** Model of the heme-binding domain (H-NOX) of the human soluble guanylate cyclase (sGC),  $\beta$ -subunit. Amino acids residues corresponding to the coordination of the heme are shown on the right with an enlarged view. The histidine-105 and the axial ligand are located perpendicularly to the heme. Arginine-139 and tyrosine-135 constitute the sGC heme binding motif. The image is taken from reference [93].

The discrimination between NO and CO in 5c-His heme proteins is governed by their electronic configurations. NO possesses an unpaired electron whereas CO has a pair of electrons, resulting in a high enthalpic barrier for CO binding but a negligible one for NO [94, 95]. This difference results in the possibility for NO to bind to  $\text{Fe}^{2+}$  positioned out-of the heme plane (domed heme) [96], but in the need for CO to wait for favorable fluctuations of the heme to become close to an in-plane conformation [95]. The reason is a weak trans effect by CO. Binding of NO results in at least a 200-fold increase in sGC activity compared with only a 4-fold increase stimulated by CO.

The crystal structure of  $\text{O}_2$ -binding H-NOX proteins from an obligate anaerobe *Thermoanaerobacter tengcongensis*, showed that the tyrosine residue forms a direct H-bond with the heme-bound  $\text{O}_2$  in the distal pocket of the heme. The H-bonding network is absent in the distal heme pocket of the NO-selective H-NOX proteins, including sGC and is instead replaced by non-hydrogen bonding, hydrophobic residues [97]. The hypothesis of importance the tyrosine residue in the heme pocket for  $\text{O}_2$  binding was not confirmed, because the introducing a Tyr residue into full-length sGC did not confer  $\text{O}_2$  binding [98, 99].

Subsequent mutagenesis studies of H-NOX proteins have revealed additional elements that are responsible for discrimination against  $\text{O}_2$  binding: heme distortion, heme pocket conformation, and protein dynamics [99-101]. A detailed explanation can be found in reference [99].

## 2.2 – The heme coordination

In heme proteins, the coordination of the central metal ion is essential for triggering and controlling the activation mechanisms by specifically altering the heme conformation,

and thus the protein conformation upon binding various ligands. Ligands chemically bound to the metal ion may attract or donate electrons to the bond and change the electron density at the ion level which in turn affects the proximal axial bond. The number of such ligating atoms surrounding a central metal ion is designated as the coordination number of the metal ion. The metal ions may be coordinated to either nitrogen, oxygen or sulfur atoms belonging to amino acid residues. Iron is the most frequent metal in proteins, located in the heme, consisting of a large heterocyclic organic porphyrin made of four pyrrolic groups joined together by methine bridges (Figure 11).

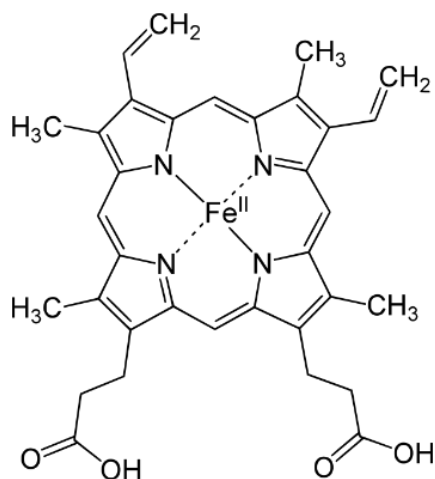


**Figure 11.** Iron-protoporphyrin, heme B group of hemoglobin, myoglobin and other heme proteins.

In sGC, the NO-induced activation depends on the presence of the reduced  $\text{Fe}^{2+}$  heme moiety and its removal abolishes any activation. The central ferrous iron of the prosthetic group is coordinated between the four pyrrole nitrogens and the axial ligand histidine-105, building a penta-coordinated histidyl-heme complex. Binding of NO to this complex results in the formation of a hexa-coordinated histidine-heme-NO intermediate that rapidly decays into a penta-coordinated nitrosyl-heme complex with a rate constant approximately  $5 \text{ s}^{-1}$  [102]. The cleavage of the heme-histidine bond is the molecular switch that leads to a ~200-fold activation of sGC [93]. A detailed mechanism of sGC activation by NO is described in the next section.

Heme has diverse roles as electron transfer (cytochrome c),  $\text{O}_2$  transport, and storage (Hb and Mb), and  $\text{O}_2$  catalysis (NOS, peroxidase). Iron in the ferrous state ( $\text{Fe}^{2+}$ ) is extremely reactive and very easily oxidizes to ferric form ( $\text{Fe}^{3+}$ ). The rate of oxidation is modulated by the protein structure surrounding the heme which may even preclude  $\text{O}_2$  binding, like in sGC.

Back in 1984, Ignarro showed that alterations of the chemical structure of protoporphyrin IX changed the activation of sGC purified from bovine lung [103]. Hydrophobic side chains at positions 2 and 4 and vicinal propionic acid residues at positions

6 and 7 of the porphyrin ring were essential for maximal enzyme activation (increase of  $V_{\max}$  and affinities  $K_M$  for GTP). These experiments [103] demonstrated the importance of the porphyrin ring conformation and proximal His ligation for the enzyme activation. Similarly, metalloporphyrins inhibited enzymatic activity and ferroprotoporphyrin IX ( $K_i = 350$  nM), zinc-protoporphyrin IX ( $K_i = 50$  nM) and manganese-protoporphyrin IX ( $K_i = 9$  nM) were competitive with protoporphyrin IX. The reconstructed sGC kept its basal activity but did not respond to NO [103]

Heme may bind the biologically important diatomic molecules NO, CO, and O<sub>2</sub>. Soluble guanylate cyclase containing heme is activated by NO in a reversible manner. In resting state of sGC, iron has 5-coordinate with His-105 (Figure 12a). When NO binds to the distal side of sGC, it exerts a strong repulsive trans effect on the proximal His-iron bond and Fe has 6-coordinate with His and NO (Figure 12b). This transient effect leads to disrupt the bond between the less tightly bound His-105 and iron, producing 5 coordinate-NO species (Figure 12c).

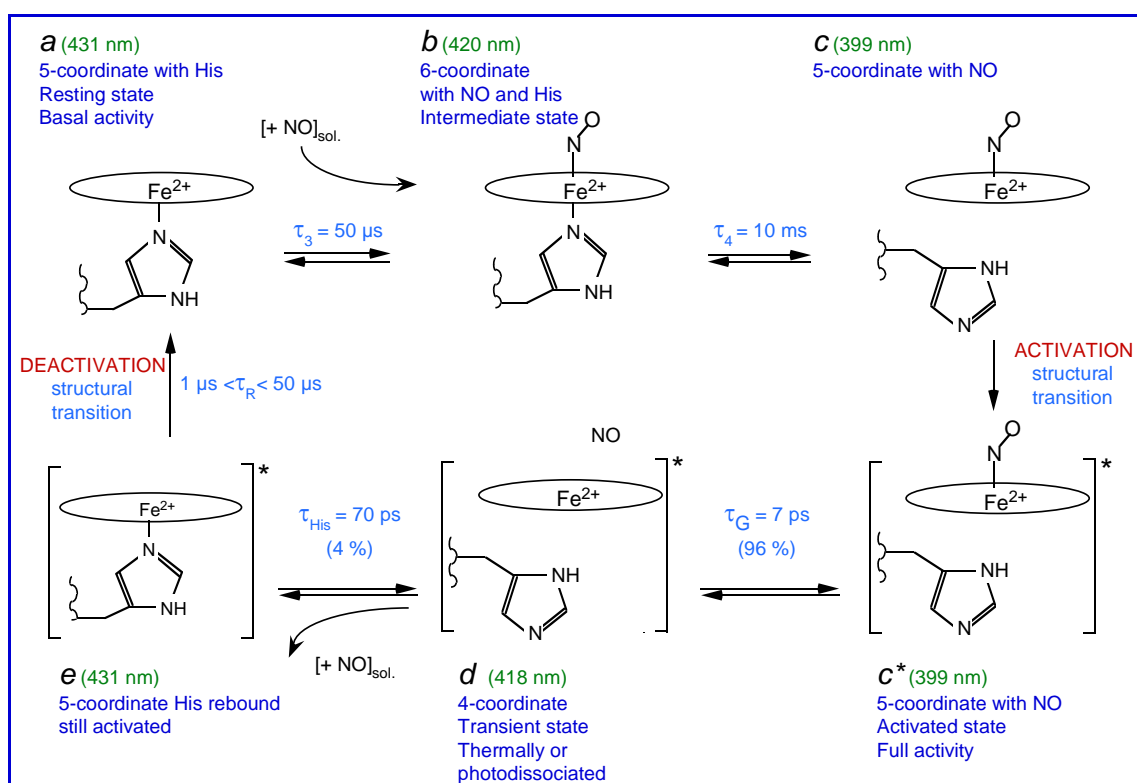


**Figure 12.** Model of sGC activation by NO, with the corresponding heme coordination states. The time constants are given for each transition. The corresponding maximum of the Soret absorption band is indicated in green. \*The star for the three species at the bottom means that sGC is activated.

In the 5-coordinate states (with His or NO) the central iron is displaced out of the heme plane towards the coordinating ligand (Figure 12d). In the 5-coordinate state with NO,

His-105 is detached and structural constraints are relaxed, inducing a conformational change in the entire protein which is responsible for the increased catalytic activity.

Several models published in the past 15 years include a state with NO bound at the proximal side of the heme, replacing His-105. This hypothesis originates from the similarity with the bacterial NO-transporter cytochrome c' from *Alcaligenes xylosoxidans* (see CHAPTER V), which also forms a 5-coordinate complex with NO, and whose crystal structure revealed NO bond at the proximal side [104]. However, such a heme conformation was never demonstrated for sGC and it is only a working hypothesis.

### 2.3 – Electronic and chemical properties of nitric oxide

Although NO is known as a toxic gas at high concentration, its biological role as a messenger comes from its special chemical properties. NO binding to proteins is determined by its paramagnetism (possessing an unpaired electron) and its uncharged nature that is especially important in determining NO selective interactions. The unpaired electron of •NO requires another unpaired electron, which explains the rich chemistry of •NO with other radical species. This also explains why •NO is relatively unreactive to many molecules in biology, but NO reacts at appreciable rates with transition metals like  $\text{Fe}^{2+}$  [105].

The molecular orbital diagram of NO (Figure 13) shows three electrons in antibonding  $\sigma^*$  and  $\pi^*$  orbitals and eight electrons in bonding orbitals. The unpaired electron occupying the highest energy level (HOMO) is in antibonding  $\pi^*$  orbital.

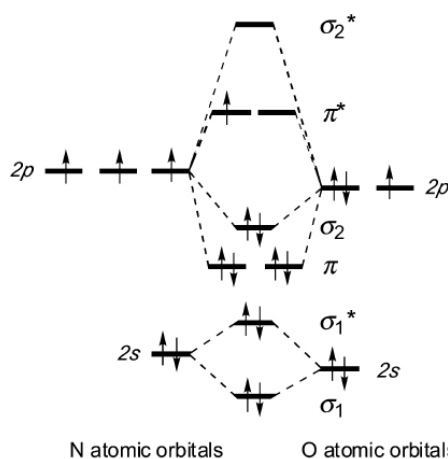
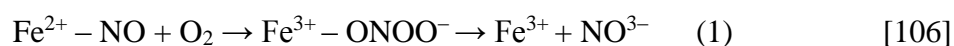


**Figure 13.** Molecular orbital diagram of NO

Now I will focus on •NO reaction with transition metals whose electrons (both paired and unpaired) only partially occupy  $d$  orbitals. These orbitals can accommodate up to 10 electrons and in general can be closely spaced in energy, depending on the arrangement of ligands around the metal. Thus, transition metals attract unpaired electrons and share electrons to make a bond. In particular •NO and  $\text{O}_2$  both form bonds with transition metals, which differ from an organic covalent bond and is called a coordinate bond. The more widespread

transition metal which bonds •NO is iron in either the ferrous (Fe<sup>2+</sup>) or ferric (Fe<sup>3+</sup>) state. The dissociation of •NO from ferroheme proteins is in general much slower than for ferriheme proteins [105]. The iron in many hemoproteins is redox active and can participate in one-electron redox reactions with •NO, which can easily be oxidized to become nitrosonium ion (NO<sup>+</sup>) or reduced to nitroxide (NO<sup>-</sup>). For example, the reaction with oxyferrohemoglobin to form nitrate (NO<sub>3</sub><sup>-</sup>) and ferriheme is biologically important:



The reaction of O<sub>2</sub> with the ferrous heme-NO complexes of hemoglobin and myoglobin are relatively slow and proceed at rates that basically match their rates of heme Fe<sup>2+</sup>-NO dissociation [107]. Therefore, NO dissociation from the ferrous heme is the initial and rate-limiting step for the overall oxidation. In these cases, NO dissociation allows O<sub>2</sub> to bind to the ferrous heme and form a heme Fe<sup>2+</sup>-O<sub>2</sub> complex, which then reacts rapidly with NO forming peroxynitrite and ferriheme (reaction 1).

For sGC, it is known that the heme does not exhibit a measurable affinity for O<sub>2</sub> despite having a vacant axial position on the heme [108]. This is in contrast to other hemoproteins with a Fe<sup>2+</sup>-proximal His linkage, including globins and heme-containing oxygenases [109]. The electron density on the ferrous heme in sGC is significantly lowered relative to the ferrous heme of other hemoproteins. This decrease in the electron density is due to the weak Fe<sup>2+</sup>-proximal His bond that weakens the Fe<sup>2+</sup>-O<sub>2</sub> bond strength as a result of diminished electron donation from iron to O<sub>2</sub> [110]. The lack of affinity for O<sub>2</sub> allows sGC to function as a selective NO-sensor even in the presence of high concentrations of O<sub>2</sub> and prevents oxidation of ferrous heme by O<sub>2</sub>.

The ability of proteins to carry out oxidation-reduction reactions depends also on its reduction potential (E<sub>h</sub>). For example, the reduction potential of truncated version of sGC, Ms sGC-NT1 (E<sub>h</sub> = 234 mV) is 206 mV more positive than that of myoglobin (E<sub>h</sub> = 28 mV) [111] and 67 mV more positive than that of the oxygen-binding Tt H-NOX protein (E<sub>h</sub> = 167 mV) [100], both of which function as ferroheme proteins. Myoglobin has a partially polar heme pocket and a relatively not distorted heme, even when bound to NO [112]. The H-NOX proteins have very hydrophobic heme pockets [113, 114], which favor neutral ferrous heme, but are also highly distorted [100, 115]. The mutations leading to a decreased level of heme distortion also lead to decreased reduction potentials at different pH [115]. A homology model of the Ms sGC β H-NOX domain [116] suggests that sGC has an even more hydrophobic pocket than Tt H-NOX, which is consistent with the more positive midpoint potential and its invariance with pH [110]. The more positive the potential, the greater the affinity for electrons and tendency to be reduced.

Additional factors that prevent the heme oxidation are: the heme environment of protein, and particularly the characteristics of the heme-thiolate bond, heme distortion, heme pocket access, active site residues, and the influence of bound cofactor or substrate [107].

The heme  $\text{Fe}^{3+} - \text{NO}$  complexes are also quite stable for some proteins (catalase, horse radish peroxidase, cytochrome c peroxidase) and not stable for others (guanylate cyclase, metmyoglobin, methemoglobin, cytochrome c) [106].



Among the three redox forms of NO ( $\text{NO}^-$ ,  $\text{NO}^\bullet$ ,  $\text{NO}^+$ ), only the uncharged NO radical ( $\text{NO}^\bullet$ ) has been shown to significantly activate soluble guanylate cyclase [117]. This can explain the absence of reduction properties of NO for  $\text{Fe}^{3+}$  for sGC.

Having small size and hydrophobicity, nitric oxide goes through the cell membranes by diffusion without any support of carriers. However, NO has a very short half-life, for example, the consumption of NO by erythrocytes and the half-life of NO in the vascular lumen are approximately 2 ms. Reacting with radicals, as well as transition metal centers and oxygen in physiological conditions, the lifetime of NO mainly depends on the relative abundance of  $\text{O}_2$ . Thus, the extravascular half-life of free NO ranges from 0.09 to  $> 2$  s, depending on  $\text{O}_2$  concentration and distance from the vessel [118].

## 2.4 – Guanylate cyclase biochemistry

The NO–cGMP–sGC signaling pathway starts from the formation of NO by oxidation of L-arginine to L-citrulline in the presence of  $\text{O}_2$ , catalyzed by nitric oxide synthase (NOS) in the presence of the cofactor NADPH as an electron donor (Figure 14).

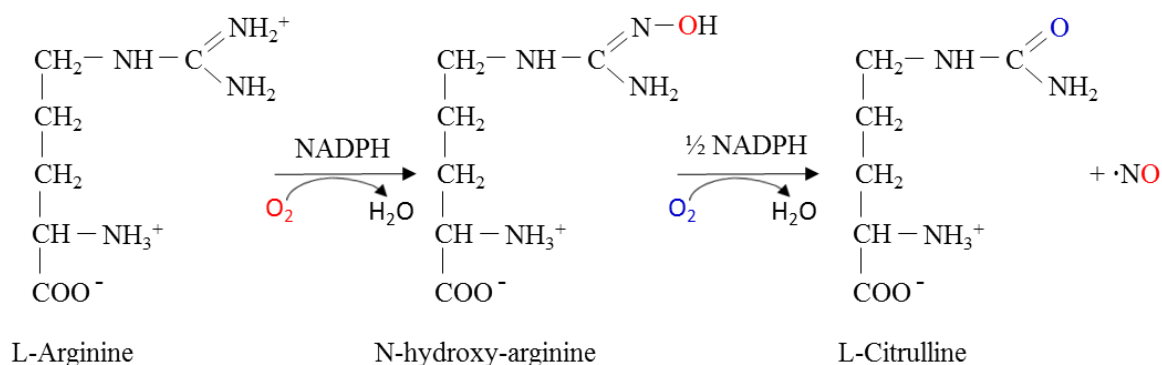


**Figure 14.** Formation of NO by oxidation of L-arginine to L-citrulline via two successive monooxygenation reactions producing N-hydroxy-arginine as an intermediate. One of the guanidine nitrogens of L-arginine is oxidized by molecular oxygen to NO, catalyzed by NO-synthase with electron transfer from the cofactor NADPH. Two moles of  $\text{O}_2$  and 1.5 moles of NADPH are consumed per mole of NO formed.

Among three isoforms of NOS, endothelial, neuronal and inducible (eNOS, nNOS, and iNOS), both eNOS and nNOS are constitutively expressed whereas iNOS is induced by immunostimulatory signals [119].

Newly synthesized NO activates the cytosolic sGC, leading to conversion of GTP to cGMP (Figure 15), which in turn activates cGMP-dependent protein kinase (PKG). cGMP can also signal via PKG-independent mechanisms by activating cyclic nucleotide-gated (CNG) channels, hyperpolarization-activated cyclic nucleotide-gated (HCN) channels, or by modulating various phosphodiesterases (PDE) (Figure 16).

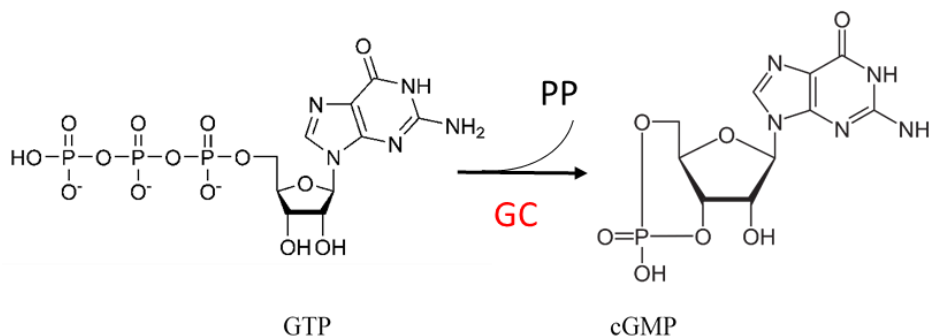


**Figure 15.** Synthesis of cGMP from GTP catalyzed by guanylate cyclase (SGC).

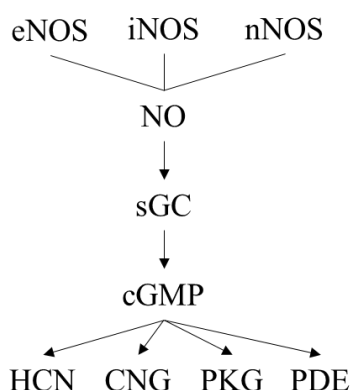


**Figure 16.** NO – cGMP signaling pathways. Nitric oxide (NO) is generated by endothelial (eNOS), neuronal (nNOS), and inducible (iNOS) NO synthase and activates the cytosolic soluble guanylyl cyclase (sGC), leading to a rise of intracellular cGMP. Signaling goes through the cGMP-dependent protein kinase G (PKG) pathway. cGMP also signal via cGK-independent mechanisms, e.g., by activating cyclic nucleotide-gated (CNG) channels, hyperpolarization-activated cyclic nucleotide-gated (HCN) channels, or by modulating various phosphodiesterases (PDE). Modified scheme is taken from [9].

### 2.4.1 – cGMP-dependent protein kinases

Two families of cGMP-dependent protein kinases (PKG) have been found in mammals: the cytosolic PKG type I and the membrane-bound PKG type II. (There exist  $\alpha$  and  $\beta$  isoforms of the cytosolic PKG type I [120]). Both PKG are homodimers, with each subunit

containing a N-terminal domain mediating homodimerization, a regulatory domain binding to cGMP and a catalytic domain phosphorylating the serine/threonine side chains on substrate proteins [120]. Normally, PKGI is involved in cardiovascular homeostasis through NO–cGMP –sGC signaling pathway and PKGII plays a role in the particular guanylate cyclase-derived cGMP-mediated electrolyte transport and bone formation. The two forms of PKG have different localization, for example, PKGI is highly expressed in smooth muscle cells, platelets, fibroblasts, and less expressed in vascular endothelium and cardiomyocytes. PKGII is more specific for renal cells, exocrine cells in distal airways, the gastrointestinal tract, salivary glands, chondrocytes and some brain nuclei, and relatively absent in the cardiovascular system. PKGI participates in smooth muscle relaxation and in the regulation of vascular tone, reducing cytosolic  $Ca^{2+}$  levels, inhibiting RhoA signaling and phosphorylating of myosin binding protein. Changes in PKGI activity play a role in the pathological vascular remodeling process in pulmonary arterial hypertension [120].

#### **2.4.2 – Other targets of cGMP**

##### ***Cyclic nucleotide-gated ion channels***

There are two types of ion channel proteins which are regulated by cyclic nucleotides. The cyclic nucleotide-gated ion channels (CNGs) and the hyperpolarization-activated cyclic nucleotide-gated ion channels (HCNs). The activation of the channels regulates the flow of ions across the plasma membrane (membrane hyperpolarization) in response to binding of cGMP and cAMP. The CNGs have a higher affinity for cGMP while HCNs are more selective to cAMP [121].

##### ***Phosphodiesterases***

Phosphodiesterases (PDEs) are the enzymes which regulate intracellular cGMP and cAMP levels by catalyzing the hydrolytic cleavage of the 3' phosphodiester bond of the cyclic nucleotides. PDEs are divided into 11 families according to the substrate affinity and selectivity, sequence homology and regulatory mechanisms. PDE1, PDE2, and PDE11 bind cyclic GMP and cyclic AMP with equal affinity; PDE5, PDE6 and PDE9 are highly selective for cGMP; PDE3 and PDE10 are cyclic GMP sensitive but cyclic AMP-selective. In this way, cAMP can compete with cGMP for the binding site of phosphodiesterases, thereby there is a cross talk between intracellular cAMP and cGMP levels. For example, PDE3, a crucial regulator of myocardial contractility, binds with high affinity to both cAMP and cGMP but catalyzes cAMP at a higher rate. Therefore cGMP acts as a competitive inhibitor of cAMP hydrolysis. For the NO–cGMP signaling pathway, PDE5 is a crucial enzyme that hydrolyzes cGMP to GMP. It is known that the PDE5 lowers cGMP concentration leading to smooth muscle contraction while inhibition of the enzyme prolongs vasorelaxation, making PDE5 an important pharmaceutical target for drug development for the cardiovascular system [122].

### 2.4.3 – Kinetics of GTP and NO binding to sGC

Different forms of sGC catalyze the conversion of GTP to cGMP at different rates depending upon the species. Apparent Michaelis constant  $K_{mGTP}$  for the substrate GTP for the basal and fully activated forms of different species of sGC have been determined in the ranges 90 – 300  $\mu\text{M}$  and 40 – 250  $\mu\text{M}$ , respectively (Table 1). Our experiment on expressed human  $\alpha_1\beta_1$  sGC showed  $K_{mGTP} = 130 \mu\text{M}$  with maximum reaction rate of 182 picomoles cGMP/picomoles sGC/min in presence of 300  $\mu\text{M}$  of the NO-donor sodium nitroprusside (SNP). Under *in vivo* conditions within smooth muscle cells, the concentration of GTP is in excess  $[\text{GTP}] > 1 \text{ mM}$  [123]. The dissociation constant ( $K_D$ ) for GTP = 326  $\mu\text{M}$  for catalytic domain of human of  $\alpha_1\beta_1$  sGC [124].

Although sGC functions in the intracellular environment containing 20 – 40  $\mu\text{M}$   $\text{O}_2$  and up to 10 nM NO during NO synthesis [125], the sGC heme is not susceptible to oxidation by  $\text{O}_2$ . Only CO and NO bind to the reduced sGC heme and form complexes that are characterized by an absorbance maximum at 423 nm and 399 nm, respectively.

**Table 1.** Kinetic parameters of GTP binding to guanylate cyclase

Protein	Km GTP, $\mu\text{M}$		Vmax, mol/min/mg		Sources of NO	Reference
	Basal sGC	With NO	Basal sGC	With NO		
Human sGC	234 $\pm$ 16	69 $\pm$ 6	6.3 pM	41 pM	DEA/NO, 10 $\mu\text{M}$	[126]
Human $\alpha_1\beta_1$ sGC	-	130	-	182 pM	SNP, 300 $\mu\text{M}$	This work
Human recombinant sGC	90	49.8	58.6 nM	11.6 nM	NOC-12 100 $\mu\text{M}$	[127]
Rat sGC $\alpha_1\beta_1$	300	250	0.1 $\pm$ 0.02 $\mu\text{M}$	21.9 $\pm$ 1.3 $\mu\text{M}$	SNP, 10 $\mu\text{M}$	[128]
Rat $\alpha_1\beta_1$ sGC	130 $\pm$ 20	44 $\pm$ 2	-	-	DEA/NO, 1000 $\mu\text{M}$	[129]
Bovine lung sGC	180	43	22 nM	1330 nM	NOC-12, 100 $\mu\text{M}$	[130]
$\alpha_1\beta_1$	-	212 $\pm$ 41	-	3.8 $\pm$ 1 nM	DEA/NO, 100 $\mu\text{M}$	[131]

A model for sGC activation and NO consumption has been predicted in [125]. NO triggers the cGMP formation rate over a concentration range of 5 – 100 nM, with Hill coefficients between 1.1 and 1.5. The activation of sGC (half-life = 1 – 2 s) is much more rapid than deactivation (50 s) [125]. NO binds to the heme of sGC at a diffusion-controlled rate to form an initial 6-coordinate complex, which rapidly converts to a 5 coordinate ferrous nitrosyl complex [132]. Dissociation of NO from the heme is relatively slow (0.0007  $\text{s}^{-1}$ )

[133] which would suggest that the sGC heme-NO complex has a  $K_D = 10 - 100$  pM. Another experiment shows that NO binds to the heme ( $k_{on} = 1.4 \times 10^8 \text{ M}^{-1}\text{s}^{-1}$  at 4 °C) to form a 6-coordinate ferrous-nitrosyl intermediate, which then converts to the final 5-coordinate species via iron histidine bond cleavage in a NO concentration-dependent fashion ( $k_{6c-5c} = 2.4 \times 10^5 \text{ M}^{-1}\text{s}^{-1}$  at 4 °C) [134]. Bimolecular NO binding at 20 °C to 5c-His:  $k_{6c} = 1 \times 10^8 \text{ M}^{-1}\text{s}^{-1}$  and conversion 6c-NO  $\rightarrow$  5c-NO:  $k_{5c} = 0.5 \times 10^6 \text{ M}^{-1}\text{s}^{-1}$  [135]. In contrast, CO binds to the sGC heme with a fast on-rate ( $3.58 \times 10^4 \text{ M}^{-1}\text{s}^{-1}$ ) and a fast off-rate ( $3.5 \text{ s}^{-1}$ ) at 10 °C leading to  $K_D = 97 \text{ }\mu\text{M}$ . Time-resolved measured bimolecular association rates of CO  $k_{on} = 0.075 \pm 0.01 \times 10^6 \text{ M}^{-1}\text{s}^{-1}$  for full length of sGC and  $k_{on} = 0.83 \pm 0.1 \times 10^6 \text{ M}^{-1}\text{s}^{-1}$  for isolated  $\beta 1$  H-NOX domain at 20 °C [136].

### 3 – Guanylate cyclase pharmacology

Soluble guanylate cyclase can be activated not only by NO (or NO donors) but also by nitrosothiols and carbon monoxide (CO). Nitrosothiols are not present in high enough concentration *in vivo* to act as messengers in signaling [137] and CO activates only ~5 fold sGC in contrast with NO which activates sGC 400-fold [138], [108]. However, CO in synergy with artificial activator can activate sGC to levels similar that of the NO-stimulated enzyme [139].

#### 3.1 – Activators of Guanylate cyclase

There are two classes of allosteric modulators that increase sGC activity: stimulators (Table 2) and activators (Table 3) arbitrarily named by Bayer's researchers after their mode of action. sGC stimulators can function without NO or CO, or synergistically with NO or CO by stabilizing the ligand-heme complex, provided the heme group is intact in the ferrous state [140]. The activity of sGC stimulators depends on the reduced ( $\text{Fe}^{2+}$ ) heme being present in the prosthetic group of sGC. In distinction to stimulators, sGC activators primarily activate sGC when the enzyme is devoid of heme which has been oxidized. They bind to the unoccupied heme pocket and replace the weakly bound oxidized heme [140] leading to the protein active conformation.

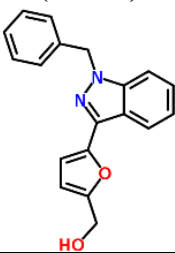
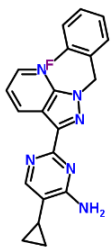
##### 3.1.1 – Heme-dependent sGC allosteric activators

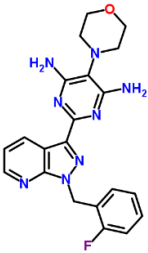
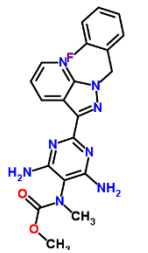
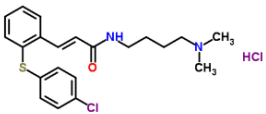
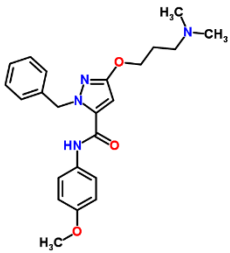
**YC-1.** The first NO-independent, heme-dependent sGC stimulator YC-1, a synthetic benzylindazole derivative, was described by Japanese scientists S. Yoshina et al. in 1978 [141]. The characterization 20 years later demonstrated that YC-1 was a relatively weak stimulator of sGC and had side effects. The activating effect of YC-1 depends on the reduced prosthetic heme moiety of sGC and its removal or oxidation abolishes YC-1 induced sGC activation. The molecular mechanism of YC-1 activation and its binding site were subject to controversy. Based on homology between the catalytic domain of adenylate cyclase and sGC,

it was suggested that YC-1 might bind to the catalytic domain of sGC, activating the enzyme by a mechanism that is comparable to forskolin-induced activation of adenylate cyclases [93]. From another side, spectroscopic studies demonstrated that YC-1-induced alterations of the CO-heme bond that was observed in heme-containing fragments of the  $\beta$ -subunit in the absence of the catalytic domain. Due to crosstalk between the mechanisms of NO and YC-1 mediated sGC activation, this hypothesis is attractive. The search for novel indazole derivatives as more potent sGC stimulators led to identification of pyrazolopyridine BAY 41-2272 and BAY 41-8543, CMF-1571 and A-350619 [142].

**BAY 41-2272 and BAY 41-8543.** These two activators work in synergy with CO like YC-1. It was shown that removal of the prosthetic heme moiety of sGC or its oxidation by ODQ strongly diminished BAY 41-2272 / 41-8543-induced sGC activation. BAY 41-2272 inhibits platelet aggregation ( $IC_{50} = 36$  nM), induces relaxation of phenylephrine-precontracted rabbit aorta rings ( $IC_{50} = 304$  nM), reduces proliferation in smooth muscle and decreases mean arterial blood pressure in hypertensive rats [142]. Compared to YC-1, BAY 41-2272 does not inhibit phosphodiesterases [143], has greater potency (by 20-fold) and specificity for sGC. BAY 41-8543 relaxes vessels and inhibits platelet aggregation *in vitro* at nM concentrations [143]. *In vivo*, it decreases blood pressure and reduces thrombosis [144].

**Table 2.** Heme-dependent sGC stimulators, hypothesized to have the same binding site.

sGC stimulator	Action	Reference
<p><b>Benzylindazole (YC -1)</b></p> 	<p><math>EC_{50}</math> for purified sGC: 20 <math>\mu</math>M  <math>IC_{50}</math> for relaxation of rabbit aortic rings: 10 <math>\mu</math>M  <math>IC_{50}</math> for collagen-induced aggregation of washed human platelets: 12 <math>\mu</math>M</p>	<p>[93, 145-148]</p>
<p><b>Pyrazolopyridine (BAY41-2272)</b></p> 	<p><math>EC_{50}</math> for purified sGC: 0.3 <math>\mu</math>M  <math>IC_{50}</math> for relaxation of rabbit aortic rings: 0.3 <math>\mu</math>M  <math>IC_{50}</math> for relaxation of sheep pulmonary artery rings: 0.15 <math>\mu</math>M  <math>IC_{50}</math> for relaxation of rat anococcygeus muscle: 0.15 <math>\mu</math>M  <math>IC_{50}</math> for collagen-induced aggregation of washed human platelets: 0.04 <math>\mu</math>M  <math>IC_{50}</math> for relaxation of rat basilar artery: 0.07 <math>\mu</math>M</p>	<p>[149-153]</p>

<p><b>BAY (41-8543)</b></p> 	<p>EC<sub>50</sub> for purified sGC: 1 μM. IC<sub>50</sub> for relaxation of rabbit aortic rings: 0.2 μM.</p>	<p>[143, 144, 154, 155]</p>
<p><b>Riociguat (BAY 63-2521)</b></p> 	<p>Concentration dependently stimulates sGC activity up to 73-fold <i>in vitro</i> from 0.1 to 100 μM. IC<sub>50</sub> for reduction of coronary perfusion pressure in the rat heart Langendorff: 0.01-1 μM. IC<sub>50</sub> for vasoconstriction in isolated mouse lungs: 0.01 μM.</p>	<p>[140, 150, 156, 157]</p>
<p><b>A-350619</b></p> 	<p>EC<sub>50</sub> for purified sGC: 30 μM. Relaxation of corpus cavernosum with an EC<sub>50</sub> of 80 μM. (10 μM in combination with sodium nitroprusside).</p>	<p>[128, 158, 159]</p>
<p><b>CFM-1571</b></p> 	<p>Weak activation of purified sGC. Synergizes strongly with NO. IC<sub>50</sub> for collagen-induced aggregation of washed human platelets: 2.8 μM. Preclinical studies have been stopped.</p>	<p>[93, 160]</p>

**BAY 63-2521.** Riociguat (BAY 63-2521, commercial name Adempas, Bayer). This is the first commercial drug of the class of sGC stimulators that treats two forms of pulmonary hypertension: chronic thromboembolic and pulmonary arterial hypertension. Riociguat was the result of pharmacokinetic optimization of pyrimidine precursors (BAY 41-8543 and BAY 41-2272) [150]. It stimulates sGC activity up to 73-fold *in vitro* in the concentration range 0.1 to 100 μM [156]. Like YC-1, Riociguat requires the presence of a reduced sGC heme, which may be deficient during oxidative stress such as in pulmonary arterial hypertension. It

possesses vasodilatory properties similar to BAY 41-8543 both *in vitro* and *in vivo*. At concentration 0.01 – 1  $\mu\text{M}$ , the compound reduces coronary perfusion pressure in the rat heart Langendorff preparation without affecting left ventricular pressure and heart rate [157]. It inhibits contraction of rabbit aortic rings, rabbit contraction saphenous artery rings and strips of rabbit corpus cavernosum. It promotes vasorelaxation in arteries isolated from nitrate-tolerant rabbit, decreases acute pulmonary vasoconstriction in isolated mouse lungs at a concentration of 0.01  $\mu\text{M}$ . At concentrations up to 10  $\mu\text{M}$  it does not inhibit the cGMP-specific PDEs [140].

**A-350619.** A-350619 activates sGC in synergy with NO or CO like YC-1. Oxidation of the sGC heme moiety by ODQ reduced its effectiveness of stimulating sGC. Based on findings that A-350619 and YC-1 did not have additive effects on sGC activation when combined, it was proposed a common binding site for both activators. A-350619 relaxes cavernosum smooth muscle *in vitro* and induces a sustained increase in skin blood flow *in vivo* [142].

**CFM-1571.** CFM-1571 is a heme-dependent activator of sGC ( $EC_{50} = 5.49 \mu\text{M}$ ) [160]. It does not activate adenylyl cyclase, does not inhibit phosphodiesterases and has minimal inhibition of iNOS (25%) and nNOS (17%). Inhibits collagen-stimulated platelet aggregation *in vitro* ( $IC_{50} = 2.84 \mu\text{M}$ ) [93].

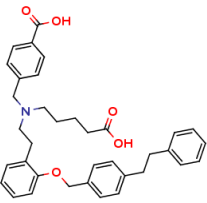
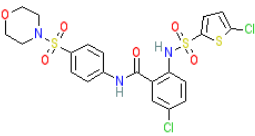
### 3.1.2 – Heme-independent sGC activators

Two compounds founded the novel class of NO- and heme-independent sGC activators, cinaciguat (BAY 58-2667) and ataciguat (HMR 1766) (Table 3). These two chemical structures do not have similarity and showed completely different characteristics to any of the heme-dependent sGC stimulators. The activation of sGC by BAY 58-2667 and HMR 1766 was even stronger after oxidation or removal of the prosthetic heme group of sGC. Both of them act in oxidized sGC devoid of by binding in the sGC heme pocket and mimicking the heme group and promoting the active sGC conformation. Clinical development of HMR 1766 and BAY 58-2667 has been stopped due to their low bioavailability and low potency [118].

**BAY 58-2667.** BAY 58-2667 (cinaciguat) is the most potent NO-independent sGC activator due to its ability to activate sGC with  $EC_{50}$  and  $K_D$  values in the low nanomolar range. This compound produces an additive, not synergistic effect with NO donors. Oxidation or removal of the prosthetic heme group potentiates BAY 58-2667-induced enzyme activation. BAY 58-2667 is able to mimic the spatial structure of the sGC heme and relax blood vessels with a potency that is several orders of magnitude greater than the NO donors sodium nitroprusside (SNP) and 3-morpholinopyridone. The compound reduces coronary perfusion pressure in the rat Langendorff heart preparation and, like its predecessors BAY 41-2272 and BAY 41-8543 [93, 161].

**HMR 1766.** Similarly to BAY 58-2667, competition between HMR-1766 (ataciguat) and porphyrinic heme site ligands was observed. It was suggested that HMR1766 might be capable of activating both the heme-containing and the heme-deficient form of sGC [110].

**Table 3.** Heme-independent sGC activators which replace the deficient heme.

sGC stimulator	Action	Reference
<p><b>Cinaciguat (BAY 58-2667)</b></p> 	<p>37-fold activation of purified rat sGC (200-fold activation when this preparation is fully oxidized/heme-free). EC<sub>50</sub> for heme-free/oxidized sGC: 10 nM. K<sub>d</sub> for oxidized sGC: 1 nM. IC<sub>50</sub> for relaxation of rabbit saphenous artery: 0.4 nM. IC<sub>50</sub> for relaxation of pig coronary artery: 0.5 nM. IC<sub>50</sub> for relaxation of dog femoral vein: 3.6 nM.</p>	<p>[154, 161-163]</p>
<p><b>Ataciguat (HMR 1766)</b></p> 	<p>50-fold activation of purified bovine sGC (90-fold activation when this preparation is fully oxidized). EC<sub>50</sub> for purified bovine sGC: 0.51 μM. IC<sub>50</sub> for relaxation of rat thoracic aorta: 5.9 μM. 1.2 μM and 0.4 μM (without/with ODQ). IC<sub>50</sub> for relaxation of pig coronary artery: 1.2 μM. IC<sub>50</sub> for relaxation of human corpus cavernosum: 10 μM.</p>	<p>[86, 164]</p>

### 3.1.3 – Isoliquiritigenin

Isoliquiritigenin (ILQG) is a flavonoid isolated from *Dalbergia odorifera T.*, which induces vascular smooth muscle relaxation in rat aorta via activation of the sGC–cGMP pathway [165, 166]. The effect of isoliquiritigenin and YC-1 was measured in the presence of sGC inhibitor ODQ on the tension in endothelial-free rat aortic rings. Both compounds induced a concentration-dependent relaxation with EC<sub>50</sub> of YC-1 1.9 μM and of isoliquiritigenin 9.4 μM. The inhibitor of sGC ODQ (30 μM) suppressed the effect of YC-1 but not of ILQG. These results suggest that the effects of YC-1 are due to stimulation of sGC, whereas the effects of isoliquiritigenin are rather related to inhibition of phosphodiesterase activity [166]. ILQG (1 – 1000 μM) is able to significantly reduce the contractile responses to acetylcholine and histamine. It relaxes guinea-pig trachea through a multiple of intracellular actions, including sGC activation, inhibition of PDEs, and associated activation of the cGMP/PKG signaling cascade, leading to the opening of [K<sup>+</sup>] channels and [Ca<sup>2+</sup>] decrease through PKG-dependent mechanism and thus to tracheal relaxation [167].

On the other hand, ILQG may be effective in preventing diabetic complications through inhibiting rat lens aldose reductase ( $IC_{50}$  of 0.32  $\mu\text{M}$ ) and sorbitol accumulation in human red blood cells ( $IC_{50}$  of 2  $\mu\text{M}$ ) [168]. ILQG may inhibit mono- and diphenolase tyrosinase activities ( $IC_{50}$  of 8.1  $\mu\text{M}$ ) [169] and may induce cell cycle arrest and cell growth inhibition in particular prostate cancer cell lines [170]. ILQG also induces apoptosis of human gastric cancer MGC-803 cells through increasing the intracellular free calcium concentration and decreasing the mitochondrial transmembrane potential) [171]. These effects of ILQG do not involve sGC.

### 3.2 – Inhibitors of guanylate cyclase

Enhancement of the activity of NO-sGC-cGMP system in proliferation, angiogenesis, and tumor formation motivates the search for specific allosteric inhibitors of sGC, which might serve as a basis for the creation of new drugs, able to selectively inhibit this activity. Such inhibitors are absent. All inhibitors of sGC known so far can be divided into two types depending on their mechanism of action:

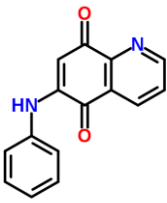
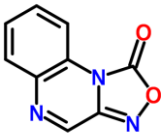
- 1) compounds which oxidize heme moiety of sGC (Table 4);
- 2) compounds which bind to sGC catalytic domain (Table 5).

#### 3.2.1 – Heme-oxidizing inhibitors

The first generation of sGC inhibitors features methylene blue and LY83583, one of the oldest reported inhibitors (Table 4). These inhibitors, however, are non-specific to sGC and work by generating superoxide, which causes deactivation of NO [172, 173]. Methylene blue (MB) acts as a powerful oxidant of ferrous iron bound to various enzymes either in heme or non-heme forms. Inhibition of cGMP production in endothelial cells was measured in presence ( $IC_{50} = 5.8 \mu\text{M}$ ) and absence ( $IC_{50} = 0.4 \mu\text{M}$ ) of superoxide dismutase (SOD). Inhibition of purified sGC is achieved by MB  $IC_{50} = 60 \mu\text{M}$  and maximal inhibition of 72% at 1 mM [174]. LY-83583 reduces platelet-endothelial cell adhesion and acetylcholine-induced vasorelaxation [85], stimulates glucose transport independent of the cGMP pathway [175] and inhibits the olfactory cyclic nucleotide-gated ion [176].

**Table 4.** Inhibitors of sGC which oxidizes the heme and prevent NO binding.

sGC inhibitors	Mechanism of action	Reference
<p><b>Methylene blue</b></p> 	<p>Nonspecific. Oxidizes the heme moiety.</p> <p>cGMP formation from endothelial cells: <math>IC_{50} = 0.4 \mu\text{M}</math>.</p> <p>Purified sGC: <math>IC_{50} = 60 \mu\text{M}</math> and maximal inhibition of 72% at 1 mM.</p>	<p>[174]</p>

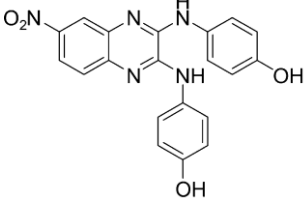
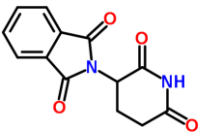
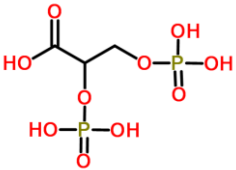
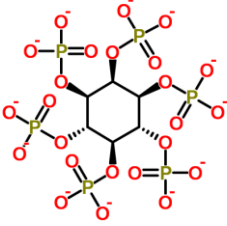
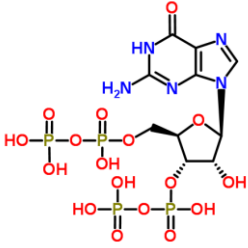
<p><b>LY-83583</b></p> 	<p>Nonspecific. Oxidizes the heme moiety.</p> <p>sGC inhibition in human platelets: IC<sub>50</sub> = 2 μM.</p> <p>Inhibition of leukotriene synthesis in guinea pig lung and rat peritoneal cells: IC<sub>50</sub>=1.8 μM.</p>	<p>[177-180]</p>
<p><b>ODQ</b></p> 	<p>Nonspecific. Oxidizes the heme moiety.</p> <p>Highly selective, irreversible, heme-site inhibitor, competitive with NO.</p> <p>Complete inactivation of sGC in 10 minutes at 0.3 μM ODQ.</p> <p>S-nitroso-glutathione-enhanced sGC activity in mouse cerebellum homogenates: IC<sub>50</sub> = 80 nM</p> <p>Purified sGC: IC<sub>50</sub> = 20 nM</p>	<p>[181, 182]</p>
<p><b>NS-2028</b></p> 	<p>Nonspecific. Oxidizes the heme moiety.</p> <p>Inhibition of purified bovine lung sGC with IC<sub>50</sub> values of 30 and 200 nM for basal and NO-stimulated sGC.</p> <p>S-nitroso-glutathione-enhanced sGC activity in mouse cerebellum homogenates: IC<sub>50</sub> = 17 nM.</p> <p>Does not inhibit particulate guanylate cyclase or adenylate cyclase.</p>	<p>[183]</p>

The most studied inhibitors with oxidation properties of the sGC heme are ODQ (1-H[1,2,4]oxadiazolo[4,3-a]quinoxalin-1-one) and its analog NS-2028, 4.7 fold more potent than ODQ [183]. They induce heme-iron oxidation which preclude NO binding and leaves only basal sGC activity [183, 184] and are nonspecific for sGC. Some experiments based on circular dichroism showed that sGC might have an allosteric binding site for ODQ [183]. It is still an open question whether ODQ causes sGC oxidation through intramolecular transfer or via an outer sphere mechanism by binding to a site remote from the heme iron.

### 3.2.2 – Inhibitors which bind to sGC catalytic domain

Inhibitors binding to sGC catalytic domain include nonspecific quinoxaline derivative (D12), thalidomide and specific organic phosphates and GTP analogs (Table 5). D12 is a newly characterized inhibitor of sGC, which shares some structural features with ODQ. It binds to the catalytic domain of sGC, locking the enzyme in its basal conformation, either making sGC not activatable by NO or blocking GTP binding [185]. Acting in the micromolar range, D12 may also inhibit particulate GC but not the related adenylate cyclase [173, 185].

**Table 5.** Inhibitors which bind to sGC catalytic domain

sGC inhibitors	Parameters and conditions	Reference
<p><b>D12, quinoxaline derivative</b></p> 	<p>Nonspecific. Allosteric regulation of sGC catalytic domain. Shares some structural features with OQD. Purified sGC: IC<sub>50</sub> = 19-34 μM. [NO] = 10 nM, [GTP] = 1 mM. sGCcat domain: KD = 11 μM. Full-length sGC: KD = 19.4 ± 2.1 μM. Inhibits particulate GC.</p>	<p>[173, 185]</p>
<p><b>Thalidomide</b></p> 	<p>Nonspecific. Binds to catalytic domain of sGC. Inhibits pro-angiogenic functions in endothelial cell cultures treated with 75 mg·mL<sup>-1</sup> of thalidomide and incubated for 8 h.</p>	<p>[173, 186]</p>
<p><b>2,3 – BPG (2,3-bisphosphoglyceric acid)</b></p> 	<p>Specific. GTP-competitive. sGC from bovine lung: Ki = 108 μM.</p>	<p>[187]</p>
<p><b>IHP (inositol hexakisphosphate)</b></p> 	<p>GTP-competitive. sGC from bovine lung: Ki = 9.7 μM.</p>	<p>[188]</p>
<p><b>G-tetra-P (Guanosine tetraphosphate)</b></p> 	<p>Specific. GTP-competitive. Rat lung sGC: Ki = 10 μM</p>	<p>[188]</p>

<p><b>Dial GTP (2'3'-dialdehyde derivative of GTP)</b></p> 	<p>Specific. GTP-competitive. Rat lung sGC: <math>K_i = 1 \mu\text{M}</math>.</p>	<p>[188]</p>
<p><b>P-P-P (Inorganic triphosphate)</b></p>	<p>Specific. GTP-competitive. Rat lung sGC: <math>K_i = 4 \mu\text{M}</math></p>	<p>[188]</p>

Another interesting molecule, thalidomide, a well-known approved drug, currently used for cancer treatment, showed inhibition of sGC which might be responsible for its anti-angiogenesis effects [186]. Molecular modeling and docking supported binding of the thalidomide to the catalytic domain of sGC [186]. Thalidomide is almost not studied compound for sGC activity but it may open new opportunities for the development of sGC inhibitors.

Biologically active organic phosphates could regulate the sGC activities and alter the sensitivity of the enzyme to NO. Among these sGC-inhibiting compounds 2,3-bisphosphoglyceric acid (2,3-BPG), inositol hexakisphosphate (IHP), phosphoribosyl pyrophosphate, and ATP. It is assumed that 2,3-BPG and IHP can block the activity in a competitive manner with GTP, while ATP suppresses the activity in competitive and non-competitive manners, but the mechanisms are not fully understood [187]. Other examples of phosphates are GTP analogs: G-tetra-P (Guanosine tetraphosphate), dial GTP (2'3'-dialdehyde derivative of GTP), and P-P-P (Inorganic tripolyphosphate) [188]. They inhibit purified sGC from rat lung in a competitive manner with GTP.

More studies are needed to fully understand the mechanisms of guanylate cyclase activation and deactivation.

### 3.3 – Inhibitors of the NO-sGC-cGMP signaling pathway

Inhibitors of NO signaling pathway include, for instance, inhibition of the three isoforms of NOS. This approach has some difficulties in achieving isoform specificity and in targeting to specific cells. The most interest was focused on iNOS and nNOS inhibitors. The problem of such inhibitors is that some compounds are selective for one or other isoform *in vivo*, but do not show real selectivity at enzyme level. For example, 7-nitroindazole (7-NI) is a selective inhibitor of nNOS, but in reality, it inhibits all three NOS isoforms [30]. Another

inhibitor of iNOS is aminoguanidine, it can be 10 fold selective over eNOS and 5 fold selective over nNOS [189].

Other compounds such as substrate analogs, dimerization inhibitors, and cofactor blockers present also a potential problem of selectivity [189]. The first described inhibitors of NOS were analogs of L-arginine, bis-isothioureas, which compete with arginine for the binding site. Despite their selectivity for iNOS over eNOS, their development as drugs was stopped by toxic effects [190]. The highly selective iNOS inhibitor 1400W has been developed and its selectivity was 10,000-fold for iNOS over eNOS and at least 30-fold for iNOS compared with nNOS [191]. However this compound is toxic for animals and human. Successful inhibitor of iNOS was Astra-Zeneca compound AR-C102222, spiroquinazalone derivative [192], with  $IC_{50}$  of 0.04  $\mu$ M. *In vivo*, it is effective in reducing inflammation in a standard oedema model and decreases adjuvant induced arthritis in rats [189]. There are also dimerization inhibitors that block the formation of both the arginine and the cofactor tetrahydrobiopterin-binding sites and produce an inhibitor–monomer complex. But such inhibitors prevent calmodulin binding to iNOS and they are not specific [189]. A significant number of NOS inhibitors were described [193] and some of them have a good potential for experimental and clinical applications.

Another target for inhibition of NO-signaling pathway is phosphodiesterase type 5 (PDE5). There are inhibitors of PDE5, which metabolize cGMP exclusively, lowers systemic and pulmonary artery pressure under physiological conditions in animals and humans [194]. Some are described in Section 2.1.2.

In spite of the large variety of targets of NO-signaling inhibition, it is difficult to find a specific inhibitor for a particular NOS or PDE without additional inhibition of other NOS or PDE isoforms. Acting on the sGC may avoid the suppression of other signaling pathways where NOS or PDE isoforms are required, but in return, the same NO-cGMP pathway may also be impacted in non targeted cells. In this thesis, we largely focused on the study of sGC direct inhibition.

#### **4 – Objectives of the present study**

We saw that soluble guanylate cyclase and the NO – cGMP – sGC signaling pathway participate in the regulation of numerous processes. While sGC is present in many mammalian cells, its homologous bacterial domain (H-NOX) is involved in NO detection and metabolism regulation of bacteria and possibly in biofilm formation. The selective inhibition or activation of an actor in the NO – cGMP – sGC pathway would have major effects in controlling these physiological processes.

No allosteric inhibitors of sGC were reported so far, but only non-specific compounds which can interact with other cellular targets. In the CHAPTER III we report the discovery of

allosteric exogenous sGC inhibitors. We screened a library of natural compounds and evaluated the inhibition of hypericin and of its cognate molecule hypocrellin A. The selected compounds could either be directly used as tools to study pathways involving sGC or serve as lead compounds for future drug design.

For curing cardiovascular diseases, in particular pulmonary hypertension, sGC activators and stimulators were developed in the last two decades, based on the template molecule YC-1, the very first active compound discovered. There is only one sGC-targeting drug on the market, the compound BAY 63-2521 (commercialized as Adempas<sup>®</sup>) against pulmonary hypertension and part of my research (CHAPTER IV) is focused on the understanding of its activating mechanism on sGC. This study included both biochemistry and spectroscopic techniques.

Not only mammalian cells but also bacterial cells possess NO receptors. However, the former must detect endogenous NO whereas the latter must detect exogenous NO from the environment. Consequently the NO concentration range is not necessarily the same and the protein sensitivity must be adapted to its function. Since NO binds to the heme, a straightforward mean of modulating the range of detection is to change side-chains on the NO pathway to and from the heme. This is demonstrated by time-resolved spectroscopy in the first part of CHAPTER V in which we describe a new way of dramatically increasing the affinity for gaseous ligands. In the second part of CHAPTER V we analyzed the dynamics of O<sub>2</sub> binding to a bacterial sensor domain whose function is still unknown. The identified properties are discussed as clues to its function.

## 5 – Bibliography

1. Buys, E.; Sips, P. New Insights into the Role of Soluble Guanylate Cyclase in Blood Pressure Regulation. *Current opinion in nephrology and hypertension* **2014**, 23, 135-142.
2. Ignarro, L. J.; Cirino, G.; Casini, A.; Napoli, C. Nitric Oxide as a Signaling Molecule in the Vascular System: An Overview. *Journal of Cardiovascular Pharmacology* **1999**, 34, 879-886.
3. Zhang, G.; Xiang, B.; Dong, A.; Skoda, R. C.; Daugherty, A.; Smyth, S. S.; Du, X.; Li, Z. Biphasic roles for soluble guanylyl cyclase (sGC) in platelet activation. *Blood* **2011**, 118, 3670-3679.
4. Schonhoff, C. M.; Gaston, B.; Mannick, J. B. Nitrosylation of cytochrome c during apoptosis. *J Biol Chem.* **2003** 278, 18265.
5. Fraser, M.; Chan, S. L.; Fiscus, R. R.; Tsang, B. K. Regulation of p53 and suppression of apoptosis by the soluble guanylyl cyclase/cGMP pathway in human ovarian cancer cells. *Oncogene* **2006**, 25, 2203–2212
6. Blaise, G. A.; Gauvin, D.; Gangal, M.; Authier, S. Nitric oxide, cell signaling and cell death. *Toxicology* **2005**, 208 (2), 177 - 192.
7. Nagy, G.; Clark, J. M.; Buzás, E. I.; Gorman, C. L.; Cope, A. P. Nitric oxide, chronic inflammation and autoimmunity. *Immunol Lett.* **2007** 111, 1-5.
8. Bian, K.; Murad, F. What is next in nitric oxide research? From cardiovascular system to cancer biology. *Nitric Oxide* **2014**, 43, 3-7.

9. Feil, R.; Kleppisch, T. NO/cGMP-dependent modulation of synaptic transmission. *Handb Exp Pharmacol* **2008**, 529-60.
10. Prast, H.; Philippu, A. Nitric oxide as modulator of neuronal function. *Progress in Neurobiology* **2001**, 64, 51-68.
11. Raposo, C.; Luna, R. L.; Nunes, A. K.; Thome, R.; Peixoto, C. A. Role of iNOS-NO-cGMP signaling in modulation of inflammatory and myelination processes. *Brain Res Bull* **2014**, 104, 60-73.
12. Rizzo, N. O.; Maloney, E.; Pham, M.; Luttrell, I.; Wessells, H.; Tateya, S.; Daum, G.; Handa, P.; Schwartz, M. W.; Kim, F. Reduced NO-cGMP signaling contributes to vascular inflammation and insulin resistance induced by high-fat feeding. *Arterioscler Thromb Vasc Biol* **2010**, 30, 758-65.
13. Hobbs, A. J. Soluble guanylate cyclase: the forgotten sibling. *Trends in Pharmacological Sciences* **1997**, 18, 484-491.
14. Furchgott, R. F.; Zawadzki, J. V. The obligatory role of endothelial cells in the relaxation of arterial smooth muscle by acetylcholine. *Nature* **1980**, 288(5789) 373-376.
15. Ignarro, L. J.; Buga, G. M.; Wood, K. S.; Byrns, R. E.; Chaudhuri, G. Endothelium-derived relaxing factor produced and released from artery and vein is nitric oxide. *Proceedings of the National Academy of Sciences of the United States of America* **1987**, 84, 9265-9269.
16. Murad, F. Discovery of some of the biological effects of nitric oxide and its role in cell signaling (Nobel lecture). *Angew. Chem. Inter. Ed.* **1999**, 38, 1857-1868.
17. Moncada, S.; Palmer, R. M.; Higgs, E. A. The discovery of nitric oxide as the endogenous nitrovasodilator. *Hypertension* **1988**, 12, 365-372.
18. Shami, P. J.; Moore, J. O.; Gockerman, J. P.; Hathorn, J. W.; Misukonis, M. A.; Weinberg, J. B. Nitric oxide modulation of the growth and differentiation of freshly isolated acute non-lymphocytic leukemia cells. *Leukemia Research* **1995**, 19, 527-533.
19. Lasker, G. F.; Pankey, E. A.; Kadowitz, P. J. Modulation of Soluble Guanylate Cyclase for the Treatment of Erectile Dysfunction. *Physiology* **2013**, 28, 262-269.
20. Tsai, E. J.; Kass, D. A. Cyclic GMP signaling in cardiovascular pathophysiology and therapeutics. *Pharmacology & Therapeutics* **2009**, 122, 216-238.
21. Pacher, P.; Beckman, J. S.; Liaudet, L. Nitric Oxide and Peroxynitrite in Health and Disease. *Physiological reviews* **2007**, 87, 315-424.
22. Budhiraja, R.; Tuder, R. M.; Hassoun, P. M. Endothelial Dysfunction in Pulmonary Hypertension. *Circulation* **2004**, 109, 159-165.
23. Stasch, J. P.; Pacher, P.; Evgenov, O. V. Soluble Guanylate Cyclase as an Emerging Therapeutic Target in Cardiopulmonary Disease. *Circulation* **2011**, 123, 2263-73.
24. Li, Z.; Xi, X.; Gu, M.; Feil, R.; Ye, R. D.; Eigenthaler, M.; Hofmann, F.; Du, X. A Stimulatory Role for cGMP-Dependent Protein Kinase in Platelet Activation. *Cell* **2003**, 112, 77-86.
25. Marjanovic, J. A.; Li, Z.; Stojanovic, A.; Du, X. Stimulatory roles of nitric oxide synthase 3 and guanylyl cyclase in platelet activation. *Journal of Biological Chemistry* **2005**.
26. Smolenski, A. Novel roles of cAMP/cGMP-dependent signaling in platelets. *Journal of Thrombosis and Haemostasis* **2012**, 10, 167-176.
27. Huang, Z.; Huang, P. L.; Panahian, N.; Dalkara, T.; Fishman, M. C.; Moskowitz, M. A. Effects of cerebral ischemia in mice deficient in neuronal nitric oxide synthase. *Science* **1994**, 265, 1883-5.
28. Dawson, V. L.; Dawson, T. M. Nitric oxide in neurodegeneration. *Prog Brain Res* **1998**, 118, 215-29.

29. Kim, P. K.; Kwon, Y. G.; Chung, H. T.; Kim, Y. M. Regulation of caspases by nitric oxide. *Ann N Y Acad Sci* **2002**, 962, 42-52.
30. Vallance, P.; Leiper, J. Blocking NO synthesis: how, where and why? *Nat Rev Drug Discov* **2002**, 1, 939-950.
31. Choi, B. M.; Pae, H. O.; Jang, S. I.; Kim, Y. M.; Chung, H. T. Nitric oxide as a pro-apoptotic as well as anti-apoptotic modulator. *J Biochem Mol Biol* **2002**, 35, 116-26.
32. Taimor, G.; Hofstaetter, B.; Piper, H. M. Apoptosis induction by nitric oxide in adult cardiomyocytes via cGMP-signaling and its impairment after simulated ischemia. *Cardiovasc Res* **2000**, 45, 588-94.
33. Shimojo, T.; Hiroe, M.; Ishiyama, S.; Ito, H.; Nishikawa, T.; Marumo, F. Nitric oxide induces apoptotic death of cardiomyocytes via a cyclic-GMP-dependent pathway. *Exp Cell Res* **1999**, 247, 38-47.
34. Loweth, A. C.; Williams, G. T.; Scarpello, J. H. B.; Morgan, N. G. Evidence for the involvement of cGMP and protein kinase G in nitric oxide-induced apoptosis in the pancreatic B-cell line, HIT-T15. *FEBS Letters* **1997**, 400, 285-288.
35. Soh, J. W.; Mao, Y.; Kim, M. G.; Pamukcu, R.; Li, H.; Piazza, G. A.; Thompson, W. J.; Weinstein, I. B. Cyclic GMP mediates apoptosis induced by sulindac derivatives via activation of c-Jun NH2-terminal kinase 1. *Clin Cancer Res* **2000**, 6, 4136-41.
36. Chiche, J. D.; Schlutsmeier, S. M.; Bloch, D. B.; de la Monte, S. M.; Roberts, J. D., Jr.; Filippov, G.; Janssens, S. P.; Rosenzweig, A.; Bloch, K. D. Adenovirus-mediated gene transfer of cGMP-dependent protein kinase increases the sensitivity of cultured vascular smooth muscle cells to the antiproliferative and pro-apoptotic effects of nitric oxide/cGMP. *J Biol Chem* **1998**, 273, 34263-71.
37. Li, Y.; Maher, P.; Schubert, D. Requirement for cGMP in nerve cell death caused by glutathione depletion. *J Cell Biol* **1997**, 139, 1317-24.
38. Kim, Y.-M.; Chung, H.-T.; Kim, S.-S.; Han, J.-A.; Yoo, Y.-M.; Kim, K.-M.; Lee, G.-H.; Yun, H.-Y.; Green, A.; Li, J.; Simmons, R. L.; Billiar, T. R. Nitric Oxide Protects PC12 Cells from Serum Deprivation-Induced Apoptosis by cGMP-Dependent Inhibition of Caspase Signaling. *The Journal of Neuroscience* **1999**, 19, 6740-6747.
39. Kim, Y.-M.; Talanian, R. V.; Billiar, T. R. Nitric oxide inhibits apoptosis by preventing increases in caspase-3-like activity via two distinct mechanisms. *Journal of Biological Chemistry* **1997**, 272, 31138-31148.
40. Blaise, G. A.; Gauvin, D.; Gangal, M.; Authier, S. Nitric oxide, cell signaling and cell death. *Toxicology* **2005**, 208, 177-192.
41. Maejima, Y.; Adachi, S.; Ito, H.; Nobori, K.; Tamamori-Adachi, M.; Isobe, M. Nitric oxide inhibits ischemia/reperfusion-induced myocardial apoptosis by modulating cyclin A-associated kinase activity. *Cardiovascular Research* **2003**, 59, 308-320.
42. Ciani, E.; Guidi, S.; Bartesaghi, R.; Contestabile, A. Nitric oxide regulates cGMP-dependent cAMP-responsive element binding protein phosphorylation and Bcl-2 expression in cerebellar neurons: implication for a survival role of nitric oxide. *Journal of Neurochemistry* **2002**, 82, 1282-1289.
43. Leung, E. L.; Fraser, M.; Fiscus, R. R.; Tsang, B. K. Cisplatin alters nitric oxide synthase levels in human ovarian cancer cells: involvement in p53 regulation and cisplatin resistance. *British Journal of Cancer* **2008**, 98, 1803-1809.
44. Wong, J. C.; Fiscus, R. R. *Protein Kinase G-Ia Hyperactivation and VASP Phosphorylation in Promoting Ovarian Cancer Cell Migration and Platinum Resistance*. Ovarian Cancer - A Clinical and Translational Update., 2013.

45. Mujoo, K.; Sharin, V. G.; Martin, E.; Choi, B.-K.; Sloan, C.; Nikonoff, L. E.; Kots, A. Y.; Murad, F. Role of soluble guanylyl cyclase–cyclic GMP signaling in tumor cell proliferation. *Nitric Oxide* **2010**, *22*, 43-50.
46. Grimm, E. A.; Ellerhorst, J.; Tang, C.-H.; Ekmekcioglu, S. Constitutive intracellular production of iNOS and NO in human melanoma: possible role in regulation of growth and resistance to apoptosis. *Nitric Oxide* **2008**, *19*, 133-137.
47. Leung, E. L.; Wong, J. C.; Johlfs, M. G.; Tsang, B. K.; Fiscus, R. R. Protein Kinase G Type I $\alpha$  Activity in Human Ovarian Cancer Cells Significantly Contributes to Enhanced Src Activation and DNA Synthesis/Cell Proliferation. *Molecular Cancer Research* **2010**, *8*, 578-591.
48. Cai, C.; Chen, S. Y.; Zheng, Z.; Omwancha, J.; Lin, M. F.; Balk, S. P.; Shemshedini, L. Androgen regulation of soluble guanylyl cyclase[ $\alpha$ ]1 mediates prostate cancer cell proliferation. *Oncogene* **2006**, *26*, 1606-1615.
49. Menéndez, L.; Juárez, L.; García, V.; Hidalgo, A.; Baamonde, A. Involvement of nitric oxide in the inhibition of bone cancer-induced hyperalgesia through the activation of peripheral opioid receptors in mice. *Neuropharmacology* **2007**, *53*, 71-80.
50. Park, S.-W.; Lee, S.-G.; Song, S.-H.; Heo, D.-S.; Park, B.-J.; Lee, D.-W.; Kim, K.-H.; Sung, M.-W. The effect of nitric oxide on cyclooxygenase-2 (COX-2) overexpression in head and neck cancer cell lines. *International Journal of Cancer* **2003**, *107*, 729-738.
51. Pyriochou, A.; Beis, D.; Koika, V.; Potytarchou, C.; Papadimitriou, E.; Zhou, Z.; Papapetropoulos, A. Soluble Guanylyl Cyclase Activation Promotes Angiogenesis. *Journal of Pharmacology and Experimental Therapeutics* **2006**, *319*, 663-671.
52. Wong, J. C.; Fiscus, R. R. Protein Kinase G-I $\alpha$  Hyperactivation and VASP Phosphorylation in Promoting Ovarian Cancer Cell Migration and Platinum Resistance. In *Ovarian Cancer - A Clinical and Translational Update*, Díaz-Padilla, I. n., Ed. InTech: Rijeka, 2013; p Ch. 12.
53. Villalobo, A. Nitric oxide and cell proliferation. *FEBS Journal* **2006**, *273*, 2329-2344.
54. Villalobo, A. Enhanced Cell Proliferation Induced by Nitric Oxide. *Dynamic Cell Biology, Global Science Books* **2007**, *1*, 60-64.
55. Garg, U. C.; Hassid, A. Nitric oxide-generating vasodilators and 8-bromo-cyclic guanosine monophosphate inhibit mitogenesis and proliferation of cultured rat vascular smooth muscle cells. *Journal of Clinical Investigation* **1989**, *83*, 1774-1777.
56. Yang, W. D.; Ando, J.; Korenaga, R.; Toyooka, T.; Kamiya, A. Exogenous Nitric Oxide Inhibits Proliferation of Cultured Vascular Endothelial Cells. *Biochemical and Biophysical Research Communications* **1994**, *203*, 1160-1167.
57. Garg, U. C.; Devi, L.; Turndorf, H.; Goldfrank, L. R.; Bansinath, M. Effect of nitric oxide on mitogenesis and proliferation of cerebellar glial cells. *Brain Research* **1992**, *592*, 208-212.
58. Ciani, E.; Severi, S.; Contestabile, A.; Bartesaghi, R.; Contestabile, A. Nitric oxide negatively regulates proliferation and promotes neuronal differentiation through N-Myc downregulation. *Journal of Cell Science* **2004**, *117*, 4727-4737.
59. Kawada, N.; Seki, S.; Kuroki, T.; Inoue, M. Regulation of stellate cell proliferation by lipopolysaccharide: role of endogenous nitric oxide. *Journal of gastroenterology and hepatology* **1998**, *13 Suppl*, S6-13.
60. Nunokawa, Y.; Tanaka, S. Interferon- $\gamma$  inhibits proliferation of rat vascular smooth muscle cells by nitric oxide generation. *Biochemical and Biophysical Research Communications* **1992**, *188*, 409-415.

61. Ziche, M.; Parenti, A.; Ledda, F.; Dell'Era, P.; Granger, H. J.; Maggi, C. A.; Presta, M. Nitric oxide promotes proliferation and plasminogen activator production by coronary venular endothelium through endogenous bFGF. *Circ Res* **1997**, 80, 845-52.
62. Luczak, K.; Balcerzyk, A.; Soszynski, M.; Bartosz, G. Low concentration of oxidant and nitric oxide donors stimulate proliferation of human endothelial cells in vitro. *Cell Biol Int* **2004**, 28, 483-6.
63. Lepic, E.; Burger, D.; Lu, X.; Song, W.; Feng, Q. Lack of endothelial nitric oxide synthase decreases cardiomyocyte proliferation and delays cardiac maturation. *Am J Physiol Cell Physiol* **2006**, 291, C1240-6.
64. Ulibarri, J. A.; Mozdziak, P. E.; Schultz, E.; Cook, C.; Best, T. M. Nitric oxide donors, sodium nitroprusside and S-nitroso-N-acetylpencillamine, stimulate myoblast proliferation in vitro. *In Vitro Cell Dev Biol Anim* **1999**, 35, 215-8.
65. Bechtel, K. M.; Bonavida, B. Inhibitory effects of 17beta-estradiol and progesterone on ovarian carcinoma cell proliferation: a potential role for inducible nitric oxide synthase. *Gynecol Oncol* **2001**, 82, 127-38.
66. Hajri, A.; Metzger, E.; Vallat, F.; Coffy, S.; Flatter, E.; Evrard, S.; Marescaux, J.; Aprahamian, M. Role of nitric oxide in pancreatic tumour growth: in vivo and in vitro studies. *Br J Cancer* **1998**, 78, 841-9.
67. Bal-Price, A.; Gartlon, J.; Brown, G. C. Nitric oxide stimulates PC12 cell proliferation via cGMP and inhibits at higher concentrations mainly via energy depletion. *Nitric Oxide* **2006**, 14, 238-46.
68. Michurina, T.; Krasnov, P.; Balazs, A.; Nakaya, N.; Vasilieva, T.; Kuzin, B.; Khrushchov, N.; Mulligan, R. C.; Enikolopov, G. Nitric Oxide Is a Regulator of Hematopoietic Stem Cell Activity. *Molecular Therapy* **2004**, 10, 241-248.
69. Krumenacker, J. S.; Katsuki, S.; Kots, A.; Murad, F. Differential expression of genes involved in cGMP-dependent nitric oxide signaling in murine embryonic stem (ES) cells and ES cell-derived cardiomyocytes. *Nitric Oxide* **2006**, 14, 1-11.
70. Mujoo, K.; Krumenacker, J. S.; Murad, F. Nitric oxide-cyclic GMP signaling in stem cell differentiation. *Free radical biology & medicine* **2011**, 51, 2150-2157.
71. Mujoo, K.; Sharin, V. G.; Bryan, N. S.; Krumenacker, J. S.; Sloan, C.; Parveen, S.; Nikonoff, L. E.; Kots, A. Y.; Murad, F. Role of nitric oxide signaling components in differentiation of embryonic stem cells into myocardial cells. *Proceedings of the National Academy of Sciences* **2008**, 105, 18924-18929.
72. Zhu, D.-Y.; Lou, Y.-J. Icariin-mediated expression of cardiac genes and modulation of nitric oxide signaling pathway during differentiation of mouse embryonic stem cells into cardiomyocytes in vitro. *Acta Pharmacol Sin* **2006**, 27, 311-320.
73. Pan, W.; Quarles, L. D.; Song, L.-H.; Yu, Y.-H.; Jiao, C.; Tang, H.-B.; Jiang, C.-H.; Deng, H.-W.; Li, Y.-J.; Zhou, H.-H.; Xiao, Z.-S. Genistein stimulates the osteoblastic differentiation via NO/cGMP in bone marrow culture. *Journal of Cellular Biochemistry* **2005**, 94, 307-316.
74. Mujoo, K.; Nikonoff, L. E.; Sharin, V. G.; Bryan, N. S.; Kots, A. Y.; Murad, F. Curcumin induces differentiation of embryonic stem cells through possible modulation of nitric oxide-cyclic GMP pathway. *Protein & Cell* **2012**, 3, 535-544.
75. Garthwaite, G.; Bartus, K.; Malcolm, D.; Goodwin, D.; Kollb-Sielecka, M.; Dooldeniya, C.; Garthwaite, J. Signaling from blood vessels to CNS axons through nitric oxide. *J Neurosci* **2006**, 26, 7730-40.
76. Puzzo, D.; Privitera, L.; Leznik, E.; Fa, M.; Staniszewski, A.; Palmeri, A.; Arancio, O. Picomolar amyloid-beta positively modulates synaptic plasticity and memory in hippocampus. *J Neurosci* **2008**, 28, 14537-45.

77. Prickaerts, J.; van Staveren, W. C.; Sik, A.; Markerink-van Ittersum, M.; Niewohner, U.; van der Staay, F. J.; Blokland, A.; de Vente, J. Effects of two selective phosphodiesterase type 5 inhibitors, sildenafil and vardenafil, on object recognition memory and hippocampal cyclic GMP levels in the rat. *Neuroscience* **2002**, 113, 351-61.
78. Baratti, C. M.; Boccia, M. M. Effects of sildenafil on long-term retention of an inhibitory avoidance response in mice. *Behav Pharmacol* **1999**, 10, 731-7.
79. Wakita, H.; Tomimoto, H.; Akiguchi, I.; Lin, J. X.; Ihara, M.; Ohtani, R.; Shibata, M. Ibudilast, a phosphodiesterase inhibitor, protects against white matter damage under chronic cerebral hypoperfusion in the rat. *Brain Res* **2003**, 992, 53-9.
80. Campbell, M. G.; Underbakke, E. S.; Potter, C. S.; Carragher, B.; Marletta, M. A. Single-particle EM reveals the higher-order domain architecture of soluble guanylate cyclase. *Proceedings of the National Academy of Sciences* **2014**, 111, 2960-2965.
81. Underbakke, E. S.; Iavarone, A. T.; Marletta, M. A. Higher-order interactions bridge the nitric oxide receptor and catalytic domains of soluble guanylate cyclase. *Proceedings of the National Academy of Sciences of the United States of America* **2013**, 110, 6777-6782.
82. Montfort, W. R.; Wales, J. A.; Weichsel, A. Structure and Activation of Soluble Guanylyl Cyclase, the Nitric Oxide Sensor. *Antioxidants & Redox Signaling* **2017**, 26(3), 107-121.
83. Mayer, B.; Koesling, D. cGMP signalling beyond nitric oxide. *Trends in Pharmacological Sciences* **2001**, 22, 546-548.
84. Mergia, E.; Koesling, D.; Friebe, A. Genetic mouse models of the NO receptor 'soluble' guanylyl cyclases. *Handb Exp Pharmacol* **2009**, 33-46.
85. Koesling, D.; Herz, J.; Gausepohl, H.; Niroomand, F.; Hinsch, K.-D.; Mülsch, A.; Böhme, E.; Schultz, G.; Frank, R. The primary structure of the 70 kDa subunit of bovine soluble guanylate cyclase. *FEBS Letters* **1988**, 239, 29-34.
86. Gileadi, O. Structures of soluble guanylate cyclase: implications for regulatory mechanisms and drug development. *Biochemical Society Transactions* **2014**, 42, 108-113.
87. Winger, J. A.; Marletta, M. A. Expression and characterization of the catalytic domains of soluble guanylate cyclase: interaction with the heme domain. *Biochemistry* **2005**, 44, 4083-90.
88. Fritz, B. G.; Roberts, S. A.; Ahmed, A.; Breci, L.; Li, W.; Weichsel, A.; Brailey, J. L.; Wysocki, V. H.; Tama, F.; Montfort, W. R. Molecular Model of a Soluble Guanylyl Cyclase Fragment Determined by Small-Angle X-ray Scattering and Chemical Cross-Linking. *Biochemistry* **2013**, 52, 1568-1582.
89. Nioche, P.; Berka, V.; Vipond, J.; Minton, N.; Tsai, A.-L.; Raman, C. S. Femtomolar Sensitivity of a NO Sensor from *Clostridium botulinum*. *Science* **2004**, 306, 1550-1553.
90. Pellicena, P.; Karow, D. S.; Boon, E. M.; Marletta, M. A.; Kuriyan, J. Crystal structure of an oxygen-binding heme domain related to soluble guanylate cyclases. *Proceedings of the National Academy of Sciences of the United States of America*. **2004**, 101, 12854-12859.
91. Karow, D. S.; Pan, D.; Tran, R.; Pellicena, P.; Presley, A.; Mathies, R. A.; Marletta, M. A. Spectroscopic Characterization of the Soluble Guanylate Cyclase-like Heme Domains from *Vibrio cholerae* and *Thermoanaerobacter tengcongensis*. *Biochemistry*. **2004**, 43, 10203-10211.
92. Plate, L.; Marletta, M. A. Nitric Oxide-Sensing H-NOX Proteins Govern Bacterial Communal Behavior. *Trends in biochemical sciences* **2013**, 38.
93. Evgenov, O. V.; Pacher, P.; Schmidt, P. M.; Haskó, G.; Schmidt, H. H. H. W.; Stasch, J.-P. NO-independent stimulators and activators of soluble guanylate cyclase: discovery and therapeutic potential. *Nature reviews. Drug discovery*. **2006**, 5, 755-768.

94. Tsai, A.-L.; Berka, V.; Martin, E.; Olson, J. S. A “sliding scale rule” for selectivity among NO, CO, and O<sub>2</sub> by heme protein sensors. *Biochemistry*. **2011**, 51, 172-186.
95. Andrew, C. R.; Petrova, O. N.; Lamarre, I.; Lambry, J.-C.; Rappaport, F.; Negrerie, M. The Dynamics Behind the Affinity: Controlling Heme-Gas Affinity via Geminate Recombination and Heme Propionate Conformation in the NO Carrier Cytochrome c'. *ACS Chemical Biology*. **2016**, 11, 3191-3201.
96. Kruglik, S. G.; Yoo, B. K.; Franzen, S.; Vos, M. H.; Martin, J. L.; Negrerie, M. Picosecond primary structural transition of the heme is retarded after nitric oxide binding to heme proteins. *Proc Natl Acad Sci USA*. **2010**, 107, 13678-83.
97. Ma, X.; Sayed, N.; Beuve, A.; van den Akker, F. NO and CO differentially activate soluble guanylyl cyclase via a heme pivot-bend mechanism. *The EMBO Journal*. **2007**, 26, 578-588.
98. Martin, E.; Berka, V.; Bogatenkova, E.; Murad, F.; Tsai, A. L. Ligand selectivity of soluble guanylyl cyclase: effect of the hydrogen-bonding tyrosine in the distal heme pocket on binding of oxygen, nitric oxide, and carbon monoxide. *J Biol Chem* **2006**, 281, 27836-45.
99. Plate, L.; Marletta, M. A. Nitric Oxide-Sensing H-NOX Proteins Govern Bacterial Communal Behavior. *Trends in biochemical sciences* **2013**, 38, 10.1016/j.tibs.2013.08.008.
100. Olea, C.; Boon, E. M.; Pellicena, P.; Kuriyan, J.; Marletta, M. A. Probing the function of heme distortion in the H-NOX family. *ACS Chem Biol* **2008**, 3, 703-10.
101. Weinert, E. E.; Plate, L.; Whited, C. A.; Olea, C.; Marletta, M. A. Determinants of Ligand Affinity and Heme Reactivity in H-NOX Domains. *Angewandte Chemie (International ed. in English)* **2010**, 49, 720-723.
102. Martin, E.; Berka, V.; Tsai, A. L.; Murad, F. Soluble Guanylyl Cyclase: The Nitric Oxide Receptor. In *Methods in Enzymology*, Academic Press: 2005; Vol. 396, pp 478-492.
103. Ignarro, L. J.; Ballot, B.; Wood, K. S. Regulation of soluble guanylate cyclase activity by porphyrins and metalloporphyrins. *J Biol Chem* **1984**, 259, 6201-7.
104. Lawson, D. M.; Stevenson, C. E. M.; Andrew, C. R.; Eady, R. R. Unprecedented proximal binding of nitric oxide to heme: implications for guanylate cyclase. *The EMBO Journal* **2000**, 19, 5661-5671.
105. Lancaster, J. R. Nitric oxide: a brief overview of chemical and physical properties relevant to therapeutic applications. *Future Science OA* **2015**, 1.
106. Cooper, C. E. Nitric oxide and iron proteins. *Biochim Biophys Acta* **1999**, 1411, 290-309.
107. Tejero, J.; Santolini, J.; Stuehr, D. J. Fast Ferrous Heme-NO Oxidation in Nitric Oxide Synthases. *The FEBS journal* **2009**, 276, 4505-4514.
108. Stone, J. R.; Marletta, M. A. Soluble Guanylate Cyclase from Bovine Lung: Activation with Nitric Oxide and Carbon Monoxide and Spectral Characterization of the Ferrous and Ferric States. *Biochemistry* **1994**, 33, 5636-5640.
109. Makino, R.; Park, S. Y.; Obayashi, E.; Iizuka, T.; Hori, H.; Shiro, Y. Oxygen binding and redox properties of the heme in soluble guanylate cyclase: implications for the mechanism of ligand discrimination. *J Biol Chem* **2011**, 286, 15678-87.
110. Hoffmann, L. S.; Schmidt, P. M.; Keim, Y.; Schaefer, S.; Schmidt, H. H.; Stasch, J. P. Distinct molecular requirements for activation or stabilization of soluble guanylyl cyclase upon haem oxidation-induced degradation. *Br J Pharmacol* **2009**, 157, 781-95.
111. Ding, X. D.; Weichsel, A.; Andersen, J. F.; Shokhireva, T. K.; Balfour, C.; Pierik, A. J.; Averill, B. A.; Montfort, W. R.; Walker, F. A. Nitric oxide binding to the ferri- and ferroheme states of nitrophorin 1, a reversible NO-binding heme protein from the saliva of the blood-sucking insect, *Rhodnius prolixus*. *Journal of the American Chemical Society* **1999**, 121, 128-138.

112. Schreiter, E. R.; Rodriguez, M. M.; Weichsel, A.; Montfort, W. R.; Bonaventura, J. S-nitrosylation-induced conformational change in blackfin tuna myoglobin. *J Biol Chem* **2007**, 282, 19773-80.
113. Nioche, P.; Berka, V.; Vipond, J.; Minton, N.; Tsai, A. L.; Raman, C. S. Femtomolar sensitivity of a NO sensor from *Clostridium botulinum*. *Science*. **2004**, 306, 1550-3.
114. Pellicena, P.; Karow, D. S.; Boon, E. M.; Marletta, M. A.; Kuriyan, J. Crystal structure of an oxygen-binding heme domain related to soluble guanylate cyclases. *Proc Natl Acad Sci U S A* **2004**, 101, 12854-9.
115. Olea, C.; Kuriyan, J.; Marletta, M. A. Modulating Heme Redox Potential Through Protein-Induced Porphyrin Distortion. *Journal of the American Chemical Society* **2010**, 132, 12794-12795.
116. Hu, X.; Murata, L. B.; Weichsel, A.; Brailey, J. L.; Roberts, S. A.; Nighorn, A.; Montfort, W. R. Allostery in recombinant soluble guanylyl cyclase from *Manduca sexta*. *J Biol Chem* **2008**, 283, 20968-77.
117. Dierks, E. A.; Burstyn, J. N. Nitric oxide (NO), the only nitrogen monoxide redox form capable of activating soluble guanylyl cyclase. *Biochem Pharmacol* **1996**, 51, 1593-600.
118. Thomas, D. D.; Liu, X.; Kantrow, S. P.; Lancaster, J. R. The biological lifetime of nitric oxide: Implications for the perivascular dynamics of NO and O(2). *Proceedings of the National Academy of Sciences of the United States of America* **2001**, 98, 355-360.
119. Stuehr, D. J. Mammalian nitric oxide synthases. *Biochimica et Biophysica Acta (BBA) - Bioenergetics* **1999**, 1411, 217-230.
120. Chen, C.-N.; Watson, G.; Zhao, L. Cyclic guanosine monophosphate signalling pathway in pulmonary arterial hypertension. *Vascular Pharmacology* **2013**, 58, 211-218.
121. Kaupp, U. B.; Seifert, R. Cyclic nucleotide-gated ion channels. *Physiol Rev* **2002**, 82, 769-824.
122. Rybalkin, S. D.; Yan, C.; Bornfeldt, K. E.; Beavo, J. A. Cyclic GMP Phosphodiesterases and Regulation of Smooth Muscle Function. *Circulation Research* **2003**, 93, 280-291.
123. Ignarro, L. J.; Degnan, J. N.; Baricos, W. H.; Kadowitz, P. J.; Wolin, M. S. Activation of purified guanylate cyclase by nitric oxide requires heme. Comparison of heme-deficient, heme-reconstituted and heme-containing forms of soluble enzyme from bovine lung. *Biochim Biophys Acta* **1982**, 718, 49-59.
124. Mota, F.; Allerston, C. K.; Hampden-Smith, K.; Garthwaite, J.; Selwood, D. L. Surface plasmon resonance using the catalytic domain of soluble guanylate cyclase allows the detection of enzyme activators. *Bioorganic & Medicinal Chemistry Letters* **2014**, 24, 1075-1079.
125. Condorelli, P.; George, S. C. In vivo control of soluble guanylate cyclase activation by nitric oxide: a kinetic analysis. *Biophys J* **2001**, 80, 2110-9.
126. Ramanathan, S.; Mazzalupo, S.; Boitano, S.; Montfort, W. R. Thrombospondin-1 and angiotensin II inhibit soluble guanylyl cyclase through an increase in intracellular calcium concentration. *Biochemistry* **2011**, 50, 7787-99.
127. Emmons, T. L.; Mathis, K. J.; Shuck, M. E.; Reitz, B. A.; Curran, D. F.; Walker, M. C.; Leone, J. W.; Day, J. E.; Bienkowski, M. J.; Fischer, H. D.; Tomasselli, A. G. Purification and characterization of recombinant human soluble guanylate cyclase produced from baculovirus-infected insect cells. *Protein Expression and Purification* **2009**, 65, 133-139.
128. Miller, L. N.; Nakane, M.; Hsieh, G. C.; Chang, R.; Kolasa, T.; Moreland, R. B.; Brioni, J. D. A-350619: a novel activator of soluble guanylyl cyclase. *Life Sci* **2003**, 72, 1015-25.
129. Denninger, J. W.; Schelvis, J. P. M.; Brandish, P. E.; Zhao, Y.; Babcock, G. T.; Marletta, M. A. Interaction of Soluble Guanylate Cyclase with YC-1: Kinetic and Resonance Raman Studies. *Biochemistry* **2000**, 39, 4191-4198.

130. Mathis, K. J.; Emmons, T. L.; Curran, D. F.; Day, J. E.; Tomasselli, A. G. High yield purification of soluble guanylate cyclase from bovine lung. *Protein Expr Purif* **2008**, 60, 58-63.
131. Koglin, M.; Behrends, S. Biliverdin IX is an endogenous inhibitor of soluble guanylyl cyclase. *Biochemical Pharmacology* **2002**, 64, 109-116.
132. Derbyshire, E. R.; Marletta, M. A. Biochemistry of soluble guanylate cyclase. *Handb Exp Pharmacol* **2009**, 17-31.
133. Kharitonov, V. G.; Russwurm, M.; Magde, D.; Sharma, V. S.; Koesling, D. Dissociation of nitric oxide from soluble guanylate cyclase. *Biochem Biophys Res Commun* **1997**, 239, 284-6.
134. Zhao, Y.; Brandish, P. E.; Ballou, D. P.; Marletta, M. A. A molecular basis for nitric oxide sensing by soluble guanylate cyclase. *Proceedings of the National Academy of Sciences* **1999**, 96, 14753-14758.
135. Yoo, B. K.; Lamarre, I.; Martin, J. L.; Rappaport, F.; Negrerie, M. Motion of proximal histidine and structural allosteric transition in soluble guanylate cyclase. *Proc Natl Acad Sci U S A* **2015**, 112, E1697-704.
136. Yoo, B. K.; Lamarre, I.; Martin, J. L.; Negrerie, M. Quaternary structure controls ligand dynamics in soluble guanylate cyclase. *J Biol Chem*. **2012**, 287, 6851-9.
137. Denninger, J. W.; Marletta, M. A. Guanylate cyclase and the ·NO/cGMP signaling pathway. *Biochimica et Biophysica Acta (BBA) - Bioenergetics* **1999**, 1411, 334-350.
138. Ingi, T.; Cheng, J.; Ronnett, G. V. Carbon Monoxide: An Endogenous Modulator of the Nitric Oxide–Cyclic GMP Signaling System. *Neuron* **1996**, 16, 835-842.
139. Stones, J. R.; Marletta, M. A. Synergistic activation of soluble guanylate cyclase by YC-1 and carbon monoxide: implications for the role of cleavage of the iron-histidine bond during activation by nitric oxide. *Chemistry & Biology* **1998**, 5, 255-261.
140. Dasgupta, A.; Bowman, L.; D'Arsigny, C. L.; Archer, S. L. Soluble Guanylate Cyclase: A New Therapeutic Target for Pulmonary Arterial Hypertension and Chronic Thromboembolic Pulmonary Hypertension. *Clinical Pharmacology & Therapeutics* **2015**, 97, 88-102.
141. Yoshina, S.; Tanaka, A.; Kuo, S. C. Studies on heterocyclic compounds. XXXVI. Synthesis of furo[3,2-c]pyrazole derivatives. (4) Synthesis of 1,3-diphenylfuro[3,2-c]pyrazole-5-carboxaldehyde and its derivatives. *Yakugaku zasshi: Journal of the Pharmaceutical Society of Japan* **1978**, 98, 272–279.
142. Stasch, J.-P.; Becker, E. M.; Alonso-Alija, C.; Apeler, H.; Dembowski, K.; Feurer, A.; Gerzer, R.; Minuth, T.; Perzborn, E.; Pleis zlig, U.; Schröder, H.; Schroeder, W.; Stahl, E.; Steinke, W.; Straub, A.; Schramm, M. NO-independent regulatory site on soluble guanylate cyclase. The first biochemical and pharmacological characterization of BAY 41–2272 as a novel NO-independent but haem-dependent stimulator of sGC. *Nature* **2001**, 212–215.
143. Stasch, J.-P.; Alonso-Alija, C.; Apeler, H.; Dembowski, K.; Feurer, A.; Minuth, T.; Perzborn, E.; Schramm, M.; Straub, A. Pharmacological actions of a novel NO-independent guanylyl cyclase stimulator, BAY 41-8543: in vitro studies. *British Journal of Pharmacology* **2002**, 135, 333-343.
144. Stasch, J.-P.; Dembowski, K.; Perzborn, E.; Stahl, E.; Schramm, M. Cardiovascular actions of a novel NO-independent guanylyl cyclase stimulator, BAY 41-8543: in vivo studies. *British Journal of Pharmacology* **2002**, 135, 344-355.
145. Wu, C. C.; Ko, F. N.; Kuo, S. C.; Lee, F. Y.; Teng, C. M. YC-1 inhibited human platelet aggregation through NO-independent activation of soluble guanylate cyclase. *Br J Pharmacol* **1995**, 116, 1973-8.

146. Russwurm, M.; Mergia, E.; Mullershausen, F.; Koesling, D. Inhibition of deactivation of NO-sensitive guanylyl cyclase accounts for the sensitizing effect of YC-1. *J Biol Chem* **2002**, *277*, 24883-8.
147. Lee, Y.-C.; Martin, E.; Murad, F. Human recombinant soluble guanylyl cyclase: Expression, purification, and regulation. *Proceedings of the National Academy of Sciences of the United States of America* **2000**, *97*, 10763-10768.
148. Friebe, A.; Mullershausen, F.; Smolenski, A.; Walter, U.; Schultz, G.; Koesling, D. YC-1 potentiates nitric oxide- and carbon monoxide-induced cyclic GMP effects in human platelets. *Mol Pharmacol* **1998**, *54*, 962-7.
149. Straub, A.; Stasch, J.-P.; Alonso-Alija, C.; Benet-Buchholz, J.; Ducke, B.; Feurer, A.; Fürstner, C. NO-Independent stimulators of soluble guanylate cyclase. *Bioorganic & Medicinal Chemistry Letters* **2001**, *11*, 781-784.
150. Stasch, J. P.; Becker, E. M.; Alonso-Alija, C.; Apeler, H.; Dembowski, K.; Feurer, A.; Gerzer, R.; Minuth, T.; Perzborn, E.; Zlig, U. P.; Schröder, H.; Schroeder, W.; Stahl, E.; Steinke, W.; Straub, A.; Schramm, M. NO-independent regulatory site on soluble guanylate cyclase. The first biochemical and pharmacological characterization of BAY 41-2272 as a novel NO-independent but haem-dependent stimulator of sGC. *Nature* **2001**, 212-215.
151. Bischoff, E.; Stasch, J.-P. Effects of the sGC Stimulator BAY 41-2272 Are Not Mediated by Phosphodiesterase 5 Inhibition. *Circulation* **2004**, *110*, e320-e321.
152. Evgenov, O. V.; Ichinose, F.; Evgenov, N. V.; Gnoth, M. J.; Falkowski, G. E.; Chang, Y.; Bloch, K. D.; Zapol, W. M. Soluble guanylate cyclase activator reverses acute pulmonary hypertension and augments the pulmonary vasodilator response to inhaled nitric oxide in awake lambs. *Circulation* **2004**, *110*, 2253-9.
153. Teixeira, C. E.; Priviero, F. B.; Todd, J., Jr.; Webb, R. C. Vasorelaxing effect of BAY 41-2272 in rat basilar artery: involvement of cGMP-dependent and independent mechanisms. *Hypertension* **2006**, *47*, 596-602.
154. Schmidt, P.; Schramm, M.; Schroder, H.; Stasch, J. P. Mechanisms of nitric oxide independent activation of soluble guanylyl cyclase. *Eur J Pharmacol* **2003**, *468*, 167-74.
155. Straub, A.; Benet-Buchholz, J.; Fröde, R.; Kern, A.; Kohlsdorfer, C.; Schmitt, P.; Schwarz, T.; Siefert, H.-M.; Stasch, J.-P. Metabolites of Orally Active NO-Independent Pyrazolopyridine Stimulators of Soluble Guanylate Cyclase. *Bioorganic & Medicinal Chemistry* **2002**, *10*, 1711-1717.
156. Schermuly, R. T.; Stasch, J.-P.; Pullamsetti, S. S.; Middendorff, R.; Müller, D.; Schlüter, K.-D.; Dingendorf, A.; Hackemack, S.; Kolosionek, E.; Kaulen, C. Expression and function of soluble guanylate cyclase in pulmonary arterial hypertension. *European Respiratory Journal*. **2008**, *32*, 881-891.
157. Stasch, J. P.; Hobbs, A. J. NO-independent, haem-dependent soluble guanylate cyclase stimulators. *Handb Exp Pharmacol* **2009**, 277-308.
158. Zhang, H. Q.; Xia, Z.; Kolasa, T.; Dinges, J. A concise synthesis of ortho-substituted aryl-acrylamides—potent activators of soluble guanylyl cyclase. *Tetrahedron letters* **2003**, *44*, 8661-8663.
159. Nakane, M. Soluble guanylyl cyclase: physiological role as an NO receptor and the potential molecular target for therapeutic application. *Clinical chemistry and laboratory medicine* **2003**, *41*, 865-870.
160. Selwood, D. L.; Brummell, D. G.; Budworth, J.; Burtin, G. E.; Campbell, R. O.; Chana, S. S.; Charles, I. G.; Fernandez, P. A.; Glen, R. C.; Goggin, M. C. Synthesis and biological evaluation of novel pyrazoles and indazoles as activators of the nitric oxide receptor, soluble guanylate cyclase. *Journal of medicinal chemistry* **2001**, *44*, 78-93.

161. Stasch, J.-P.; Schmidt, P.; Alonso-Alija, C.; Apeler, H.; Dembowski, K.; Haerter, M.; Heil, M.; Minuth, T.; Perzborn, E.; Pleiss, U.; Schramm, M.; Schroeder, W.; Schröder, H.; Stahl, E.; Steinke, W.; Wunder, F. NO- and haem-independent activation of soluble guanylyl cyclase: molecular basis and cardiovascular implications of a new pharmacological principle. *British Journal of Pharmacology* **2002**, 136, 773-783.
162. Schmidt, P. M.; Schramm, M.; Schroeder, H.; Wunder, F.; Stasch, J. P. Identification of residues crucially involved in the binding of the heme moiety of soluble guanylate cyclase. *J Biol Chem* **2004**, 279, 3025-32.
163. Stasch, J. P.; Schmidt, P. M.; Nedvetsky, P. I.; Nedvetskaya, T. Y.; H, S. A.; Meurer, S.; Deile, M.; Taye, A.; Knorr, A.; Lapp, H.; Muller, H.; Turgay, Y.; Rothkegel, C.; Tersteegen, A.; Kemp-Harper, B.; Muller-Esterl, W.; Schmidt, H. H. Targeting the heme-oxidized nitric oxide receptor for selective vasodilatation of diseased blood vessels. *J Clin Invest* **2006**, 116, 2552-61.
164. Schindler, U.; Strobel, H.; Schonafinger, K.; Linz, W.; Lohn, M.; Martorana, P. A.; Rutten, H.; Schindler, P. W.; Busch, A. E.; Sohn, M.; Topfer, A.; Pistorius, A.; Jannek, C.; Mulsch, A. Biochemistry and pharmacology of novel anthranilic acid derivatives activating heme-oxidized soluble guanylyl cyclase. *Mol Pharmacol* **2006**, 69, 1260-8.
165. Yu, S. M.; Kuo, S. C. Vasorelaxant effect of isoliquiritigenin, a novel soluble guanylate cyclase activator, in rat aorta. *Br J Pharmacol.* **1995**, 114, 1587-94.
166. Wegener, J. W.; Nawrath, H. Differential effects of isoliquiritigenin and YC-1 in rat aortic smooth muscle. *European Journal of Pharmacology.* **1997**, 323, 89-91.
167. Liu, B.; Yang, J.; Wen, Q.; Li, Y. Isoliquiritigenin, a flavonoid from licorice, relaxes guinea-pig tracheal smooth muscle in vitro and in vivo: role of cGMP/PKG pathway. *Eur J Pharmacol* **2008**, 587, 257-66.
168. Aida, K.; Tawata, M.; Shindo, H.; Onaya, T.; Sasaki, H.; Yamaguchi, T.; Chin, M.; Mitsuhashi, H. Isoliquiritigenin: a new aldose reductase inhibitor from glycyrrhizae radix. *Planta Med.* **1990**, 56, 254-8.
169. Nerya, O.; Vaya, J.; Musa, R.; Izrael, S.; Ben-Arie, R.; Tamir, S. Glabrene and isoliquiritigenin as tyrosinase inhibitors from licorice roots. *J Agric Food Chem.* **2003**, 51, 1201-7.
170. Kanazawa, M.; Satomi, Y.; Mizutani, Y.; Ukimura, O.; Kawauchi, A.; Sakai, T.; Baba, M.; Okuyama, T.; Nishino, H.; Miki, T. Isoliquiritigenin Inhibits the Growth of Prostate Cancer. *European Urology.* **2003**, 43, 580-586.
171. Ma, J.; Fu, N. Y.; Pang, D. B.; Wu, W. Y.; Xu, A. L. Apoptosis induced by isoliquiritigenin in human gastric cancer MGC-803 cells. *Planta Med.* **2001**, 67, 754-7.
172. Dierks, E. A.; Burstyn, J. N. The Deactivation of Soluble Guanylyl Cyclase by Redox-Active Agents. *Archives of Biochemistry and Biophysics* **1998**, 351, 1-7.
173. Sousa, E. H. S.; Lopes, L. G. d. F.; Gonzalez, G.; Gilles-Gonzalez, M.-A. Drug discovery targeting heme-based sensors and their coupled activities. *Journal of Inorganic Biochemistry* **2017**, 167, 12-20.
174. Mayer, B.; Brunner, F.; Schmidt, K. Inhibition of nitric oxide synthesis by methylene blue. *Biochemical Pharmacology* **1993**, 45, 367-374.
175. Leinders-Zufall, T.; Zufall, F. Block of Cyclic Nucleotide-gated Channels in Salamander Olfactory Receptor Neurons by the Guanylyl Cyclase Inhibitor LY 83583. *J. Neurophysiol.* **1995**, 74, 2759 - 2762
176. Prasad, R. K.; Behrooz, A.; Ismail-Beigi, F. LY-83583 Stimulates Glucose Transporter-1-Mediated Glucose Transport Independent of Changes in cGMP Levels. *Eur. J. Pharmacol.* **1999**, 366, 101 - 109

177. Mulsch, A.; Luckhoff, A.; Pohl, U.; Busse, R.; Bassenge, E. LY 83583 (6-anilino-5,8-quinolinedione) blocks nitrovasodilator-induced cyclic GMP increases and inhibition of platelet activation. *Naunyn Schmiedebergs Arch Pharmacol* **1989**, 340, 119-25.
178. Fleisch, J. H.; Haisch, K. D.; Spaethe, S. M.; Rinkema, L. E.; Cullinan, G. J.; Schmidt, M. J.; Marshall, W. S. Pharmacologic analysis of two novel inhibitors of leukotriene (slow reacting substance) release. *Journal of Pharmacology and Experimental Therapeutics* **1984**, 229, 681-689.
179. Luond, R. M.; McKie, J. H.; Douglas, K. T. A direct link between LY83583, a selective repressor of cyclic GMP formation, and glutathione metabolism. *Biochem Pharmacol* **1993**, 45, 2547-9.
180. Mulsch, A.; Busse, R.; Liebau, S.; Forstermann, U. LY 83583 interferes with the release of endothelium-derived relaxing factor and inhibits soluble guanylate cyclase. *J Pharmacol Exp Ther* **1988**, 247, 283-8.
181. Garthwaite, J.; Southam, E.; Boulton, C. L.; Nielsen, E. B.; Schmidt, K.; Mayer, B. Potent and selective inhibition of nitric oxide-sensitive guanylyl cyclase by 1H-[1,2,4]oxadiazolo[4,3-a]quinoxalin-1-one. *Mol Pharmacol* **1995**, 48, 184-8.
182. Schrammel, A.; Behrends, S.; Schmidt, K.; Koesling, D.; Mayer, B. Characterization of 1H-[1,2,4]oxadiazolo[4,3-a]quinoxalin-1-one as a heme-site inhibitor of nitric oxide-sensitive guanylyl cyclase. *Mol Pharmacol* **1996**, 50, 1-5.
183. Olesen, S.-P.; Drejer, J.; Axelsson, O.; Moldt, P.; Bang, L.; Nielsen-Kudsk, J. E.; Busse, R.; Mülsch, A. Characterization of NS 2028 as a specific inhibitor of soluble guanylyl cyclase. *British Journal of Pharmacology* **1998**, 123, 299-309.
184. Zhao, Y.; Brandish, P. E.; DiValentin, M.; Schelvis, J. P.; Babcock, G. T.; Marletta, M. A. Inhibition of soluble guanylate cyclase by ODQ. *Biochemistry* **2000**, 39, 10848-10854.
185. Mota, F.; Gane, P.; Hampden-Smith, K.; Allerston, C. K.; Garthwaite, J.; Selwood, D. L. A new small molecule inhibitor of soluble guanylate cyclase. *Bioorg Med Chem* **2015**, 23, 5303-10.
186. Majumder, S.; Rajaram, M.; Muley, A.; Reddy, H. S.; Tamilarasan, K. P.; Kolluru, G. K.; Sinha, S.; Siamwala, J. H.; Gupta, R.; Ilavarasan, R.; Venkataraman, S.; Sivakumar, K. C.; Anishetty, S.; Kumar, P. G.; Chatterjee, S. Thalidomide attenuates nitric oxide-driven angiogenesis by interacting with soluble guanylyl cyclase. *British Journal of Pharmacology* **2009**, 158, 1720-1734.
187. Suzuki, T.; Suematsu, M.; Makino, R. Organic phosphates as a new class of soluble guanylate cyclase inhibitors. *FEBS Letters* **2001**, 507, 49-53.
188. Brandwein, H. J.; Lewicki, J. A.; Waldman, S. A.; Murad, F. Effect of GTP Analogues on Purified Soluble Guanylate Cyclase. *The Journal of Biological Chemistry* **1982**, 257, 1309-1311.
189. Corbett, J. A.; McDaniel, M. L. The Use of Aminoguanidine, a Selective iNOS Inhibitor, to Evaluate the Role of Nitric Oxide in the Development of Autoimmune Diabetes. *Methods* **1996**, 10, 21-30.
190. Garvey, E. P.; Oplinger, J. A.; Tanoury, G. J.; Sherman, P. A.; Fowler, M.; Marshall, S.; Harmon, M. F.; Paith, J. E.; Furfine, E. S. Potent and selective inhibition of human nitric oxide synthases. Inhibition by non-amino acid isothiouras. *Journal of Biological Chemistry* **1994**, 269, 26669-26676.
191. Garvey, E. P.; Oplinger, J. A.; Furfine, E. S.; Kiff, R. J.; Laszlo, F.; Whittle, B. J.; Knowles, R. G. 1400W is a slow, tight binding, and highly selective inhibitor of inducible nitric-oxide synthase in vitro and in vivo. *Journal of Biological Chemistry* **1997**, 272, 4959-4963.
192. Beaton, H.; Hamley, P.; Nicholls, D. J.; Tinker, A. C.; Wallace, A. V. 3, 4-Dihydro-1-isoquinolinamines: a novel class of nitric oxide synthase inhibitors with a range of isoform selectivity and potency. *Bioorganic & medicinal chemistry letters* **2001**, 11, 1023-1026.
193. Vítěček, J.; Lojek, A.; Valacchi, G.; Kubala, L. Arginine-Based Inhibitors of Nitric Oxide Synthase: Therapeutic Potential and Challenges. *Mediators of Inflammation* **2012**, 2012, 318087.

194. Baliga, R. S.; Zhao, L.; Madhani, M.; Lopez-Torondel, B.; Visintin, C.; Selwood, D.; Wilkins, M. R.; MacAllister, R. J.; Hobbs, A. J. Synergy between natriuretic peptides and phosphodiesterase 5 inhibitors ameliorates pulmonary arterial hypertension. *American journal of respiratory and critical care medicine* **2008**, 178, 861-869.

---



---

## CHAPTER III

### SEARCHING AN EXOGENOUS INHIBITOR OF GUANYLATE CYCLASE

#### SYNOPSIS

---

<b>1 – Aims and Methodology .....</b>	<b>60</b>
<b>2 – Materials and methods.....</b>	<b>60</b>
2.1 – The GreenPharma library .....	60
2.2 – Activity and inhibition of purified sGC ( <i>in vitro</i> ) .....	60
2.3 – Enzyme-linked immunosorbent assay .....	61
2.4 – Culture of HUVEC cells.....	61
2.5 – Activity and inhibition of sGC in HUVEC cells.....	62
2.6 – Surface plasmon resonance imaging .....	62
2.6.1 – Injected compounds.....	63
2.7 – Cross-linking of an activator analog (IWP-854) .....	63
2.8 – Inhibition of angiogenesis by identified compounds .....	64
<b>3 – Results of the screening of natural compounds .....</b>	<b>65</b>
3.1 – Screening of the GreenPharma library .....	65
3.2 – Inhibition by the identified compounds of sGC purified and in HUVEC.....	68
3.3 – Inhibition of sGC in HUVEC cells.....	70
3.4 – Cross-effect of NO with the identified inhibitors on sGC activity in HUVEC.....	72
3.5 – Cross-effect of inhibitors with NO and BAY 41-2272 on sGC activity .....	73
<b>4 – Interaction of inhibitors with sGC.....</b>	<b>75</b>
4.1 – Inhibition of purified sGC by hypericin .....	75
4.1.1 – Competition of hypericin with the substrate GTP.....	75
4.2 – Kinetics of inhibitors binding.....	78
4.2.1 – Hypericin binding to purified sGC.....	78
4.2.2 – Hypocrellin binding to purified sGC.....	81
4.2.3 – GreenPharma compounds binding to sGC and bacterial H-NOXs .....	83
<b>5 – Analogues of the identified compounds.....</b>	<b>85</b>
5.1 – Analogues of HTANQ.....	86
<b>6 – Properties of the inhibitors.....</b>	<b>89</b>
6.1 – Heme-oxidized properties of the inhibitors.....	89
6.2 – Comparison of the identified inhibitors.....	92
<b>7 – Inhibition of angiogenesis .....</b>	<b>95</b>
<b>8 – Conclusions .....</b>	<b>97</b>
<b>9 – Bibliography .....</b>	<b>97</b>

---

## 1 – Aims and Methodology

Chapter III is devoted to the discovery of new active compounds for guanylate cyclase and their binding mechanism. First, we screened 300 natural compounds from Greenpharma library for inhibition effect of purified sGC. Having found six inhibitors and several analogues of two of these compounds, we measured their half maximal inhibitory concentration for both purified sGC and sGC in human umbilical vein endothelial cultured cells (HUVEC). Furthermore, we also evaluated the inhibition of hypericin and of its cognate molecule hypocrellin A, which are photoactive agents in cancer therapy. The compounds with better inhibition ability were tested to inhibit the formation of vessels on human skin microvascular endothelial cells (HSkMEC). Using different methods like immunoenzymatic assay, competitor cross-linking and Surface Plasmon Resonance (SPR), we could exclude sites of guanylate cyclase where the inhibitors do not bind. We showed that the inhibitors do not compete for NO and BAY 41-2272 binding sites. Hypericin does not compete for GTP binding site. Two inhibitors oxidize the heme of guanylate cyclase. The discovered compounds could either be directly used as tools or serve as lead compounds for drug design.

## 2 – Materials and methods

Purified full-length recombinant human  $\alpha 1\beta 1$  sGC was purchased from Alexis (ALX-201-177). Human umbilical vein endothelial cells (HUVEC) isolated from normal vein was from Gibco. Purified hypericin and hypocrellin were obtained from Invitrogen and the activator BAY 41-2272 was purchased from Enzo. The chemical library containing 320 natural compounds was purchased from Greenpharma company and individual inhibitors from Ambinter.

### 2.1 – The GreenPharma library

The Greenpharma chemical library comprises 320 natural compound of various structures from plants, bacteria and fungi. It does not contain amino acids, peptides, nucleic acids, long fatty chains and metals. To search for potential inhibitors of guanylate cyclase, we selected a subset of 300 chemically diverse and drug-like natural compounds from plants and fungi from Greenpharma. We excluded substances with a low molecular weight (lower than 350 g/mol) and low hydrophobicity. Each compound from the library was first tested at the concentration of 20  $\mu$ M for its effect on purified sGC catalytic activity by direct assay of its product cGMP.

### 2.2 – Activity and inhibition of purified sGC (*in vitro*)

Activity measurements were carried out on purified sGC as previously described [1] with minor modifications. All compounds from Greenpharma library, hypericin, hypocrellin

and the activator BAY41-2272 were diluted in DMSO to the desired concentration of stock solution. Purified sGC was resuspended in TEA buffer (triethanolamine 25 mM, NaCl 10 mM, DTT 1 mM, pH 7.4). Selected compounds at increasing concentration (0.1 – 200  $\mu$ M) were mixed with sGC at 100 nM and incubated overnight at 4 °C in the dark. When investigating the cross-effect of BAY41-2272, this activator was mixed together with inhibitors. The final concentration of DMSO was < 2.5%. Then sGC (25 nM final) was incubated in assay buffer (100  $\mu$ L final volume) for 10 minutes at 37 °C. The assay buffer composition was: TEA 100 mM, pH 7.4, DTT 1 mM, MnCl<sub>2</sub> 3 mM, GTP 0.6 mM, creatine phosphate 5 mM, creatine phosphokinase 150 U/L, nitroprusside (NPS) 0.3 mM. The NO-donor NPS was omitted for assays in absence of NO. The reaction was stopped by precipitation with Zn acetate and Na<sub>2</sub>CO<sub>3</sub> that we put directly in the assay tube, which was centrifuged. 10  $\mu$ L of supernatant containing cGMP were then pipetted for assay. After this step, the immunoenzymatic assay was performed according to the ELISA Enzo kit instructions with acetylation protocol. A standard curve of known cGMP concentrations was measured together with each experiment.

### **2.3 – Enzyme-linked immunosorbent assay**

ELISA is a competitive immunoassay for the quantitative determination of cyclic GMP in samples. The protocol uses a polyclonal antibody to cGMP to bind in a competitive manner the cGMP in the standard or sample or an alkaline phosphatase molecule which has cGMP covalently attached to it. After a simultaneous incubation, the excess reagents are washed away and the substrate is added. After incubation, the enzymatic reaction is stopped and the yellow color generated is read on a microplate reader at 405 nm. The intensity of the bound yellow color is inversely proportional to the concentration of cGMP from either standard or samples, within a two decades range. For higher sensitivity, experiments were performed according to acetylation protocol of ELISA ENZO kit.

### **2.4 – Culture of HUVEC cells**

Human umbilical vein endothelial cells (HUVEC) are derived from the endothelium of veins from the umbilical cord. These cells contribute to the maintenance of vascular homeostasis. The cells produce and secrete activators and inhibitors of the coagulation and fibrinolysis system. In addition, they mediate the adhesion and aggregation of blood platelets and release molecules that regulate cell proliferation and control vessel wall tone. HUVEC cells isolated from normal vein was purchased from Gibco. For multiplying HUVEC cells we used complete medium (medium 200), low serum growth supplement (LSGS) X50 factor, antibiotic X100 factor, serum bovine albumin (10% from the total volume). Cells were multiplied in 75 ml flasks from Thermo Fisher Scientific Company in a CO<sub>2</sub> incubator at 37 °C in the dark. For the experiment, cells were replaced from flasks to 12-well plates

(individual surface 3.8 cm<sup>2</sup>). The density of cells before adding the inhibitors / activators was 4 – 6 × 10<sup>4</sup> cells/ml.

### 2.5 – Activity and inhibition of sGC in HUVEC cells

When the cells were at ~90% confluence, the medium was replaced (500 µL final volume) and activators or inhibitors at varying concentrations (or pure DMSO for control) were added to the wells (10 µL; 2% DMSO final concentration), then incubated for 2 hours in a CO<sub>2</sub> incubator at 37 °C in the dark. Selected compounds from Greenpharma necessitated longer incubation with HUVEC up to 48 h due to their low hydrophobicity and ability to pass through cell membrane. The cells incubated with compounds were then lysed for 20 minutes with 50 µL of the following lysis buffer: TEA 500 mM, IBMX 10 mM, Triton X100 10%, pH = 7.4. The lysed cell suspension was incubated directly in the wells of the culture plate with same assay buffer (50 µL; 10X) as used for purified sGC (in the presence or absence of NPS) for 20 minutes with mild shaking at room temperature. Then 500 µL from each well was transferred into polypropylene tubes for acetylation of synthesized cGMP. After this step, immunoenzymatic assay of cGMP was performed by Enzyme-linked immunosorbent assay (ELISA) using kits from Enzo according to manufacturer's instructions.

### 2.6 – Surface plasmon resonance imaging

The principle of SPRi is described in CHAPTER VII. Proteins were immobilized on the gold layer of a CS-LD or CS-HD SPRi Biochip<sup>TM</sup> (Horiba) with high or low-density direct amine coupling (NHS) with help of automatic SPRi-Arrayer system with a 500-µm internal diameter needle. Cytochrome c (50 µM) and hemoglobin (Hb 1 µM) were used as control proteins for binding of compounds detection to human sGC (7 µM and 3.5 µM), and H-NOX proteins from *Nostoc punctiforme* (NP 13 µM) and from *Clostridium botulinum* (CB 10 µM). For experimental statistics, 16 drops of each protein were spotted on the biochips (Figure 1). Each experiment was repeated 4 times.

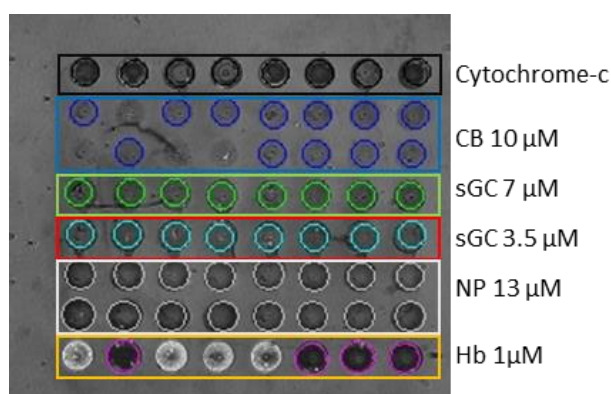


**Figure 1.** Image of the SPRi-Biochip<sup>TM</sup> surface after spotting of proteins. Cytochrome c (50 µM), hemoglobin (Hb 1 µM), human sGC (7 µM and 3.5 µM), H-NOX proteins from *Nostoc punctiforme* (NP 13 µM) and from *Clostridium botulinum* (CB 10 µM).

Glycerol and dithiotheritol were removed, so that proteins were diluted in TEA 10 mM and NaCl 5 mM buffer, pH 7.4 and re-concentrated by ultrafiltration in tubes having a 100 KDa molecular weight cut off (Amicon, Millipore). After spotting and 16 hours of fixation, the biochip was incubated in a blocking solution of  $\beta$ -ethanolamine-HCl (pH 9) to make unreactive the non-spotted gold surface, then rinsed with water. The biochip was equilibrated in place with running buffer (TEA 10 mM, NaCl 5 mM, DMSO 2.5%, pH = 7.4) having exactly the same composition as the buffer containing the analytes to be injected.

### 2.6.1 – Injected compounds

The activators and inhibitors of sGC were diluted at various concentrations in running buffer with 2.5% final DMSO concentration. Through the 200- $\mu$ L injection loop, the compounds were injected on the surface of the bioship with a flow rate of 25  $\mu$ L/min, so that the binding step duration was 8 minutes allowing to measure  $k_{on}$ . After each injection, the prism surface was washed with running buffer for 15 minutes allowing to measure  $k_{off}$ . A CCD video camera provided real-time difference images of the array of active spots (Figure 1) while monitoring the binding process. For each protein, the sensorgrams of selected spots were averaged.

### 2.7 – Cross-linking of an activator analog (IWP-854)

To test whether hypericin binds to the same site as the sGC stimulator BAY 41-2272, a competition experiment was carried out in the presence of increasing concentrations of hypericin. It was performed by our colleagues J. Wales and W. Montfort from University of Arizona Cancer Center, Tucson (USA) who have designed the compound IWP-845, a cross-linking compound [2]. The photoactive IWP-854 comprises the stimulator BAY 41-2272 fused with a diazirine functional group capable of cross-linking to all 20 amino acids, biotin and long peptide backbone (Figure 2B). Diazirines are a class of organic molecules consisting of a carbon bound to two nitrogen atoms, which are double-bonded to each other, forming a cyclopropene-like ring. Upon irradiation with ultraviolet light, diazirines form reactive carbenes, which can insert into C-H, N-H, and O-H bonds [3] close to the BAY 41-2272 binding site. The cross-linking was performed on a truncated sGC variant from *Manduca sexta*, referred to as *Ms* sGC-NT23 (Figure 2A).

*Ms* sGC-NT23 lacks the  $\alpha$ 1 H-NOX domain and both cyclase domains, but possesses the heme domain and responds to gaseous ligands and stimulators in a similar manner as full-length sGC. IWP-854 (1  $\mu$ M) and hypericin (5-20  $\mu$ M) were added to *Ms* sGC-NT23. Samples were incubated for 15 minutes at room temperature in the dark and irradiated with 350-365 nm UV light for 30 minutes on ice. IWP-854 cross-linking was detected by probing the biotin affinity-tag via western-blot imaging.

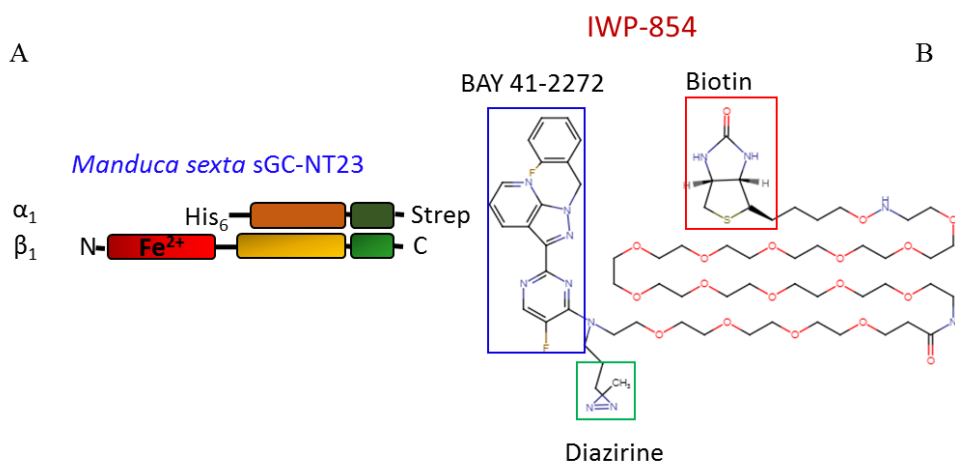


**Figure 2.** Ms sGC-NT23, truncated sGC variant from *Manduca sexta* (left). IWP-854, a photoactive stimulator fused BAY 41-2272, a diazirine functional group, biotin and the peptide backbone.

To further verify that hypericin does not interfere with the heme, the  $K_D$  of CO binding to sGC was measured as a function of hypericin by absorption spectroscopy. The protein *Ms* sGC-NT23 (1  $\mu$ M) was suspended in 20 mM Tris (pH 7.5), 100 mM NaCl,  $\pm$  2  $\mu$ M hypericin. Increasing concentrations of CO (0.5  $\mu$ M to 115  $\mu$ M) dissolved in 20 mM Tris (pH 7.5), 100 mM NaCl was added to the sample. Hypericin at 1 mM in pure ethanol was diluted to 0.2 mM hypericin in 20 mM Tris (pH 7.5), 100 mM NaCl, 20% ethanol. This solution was further diluted to a final concentration of 2  $\mu$ M hypericin in 20 mM Tris (pH 7.5), 100 mM NaCl, 0.2% ethanol. The optical path length of the cuvettes was 1 cm.

## 2.8 – Inhibition of angiogenesis by identified compounds

Since sGC is involved in angiogenesis (see CHAPTER II) we aimed at investigating whether the discovered sGC inhibitors could slow down angiogenesis in a model of cells which can develop vessels. We have used two different cell lines [4, 5]: human skin mature endothelial cells (HSKMEC) and human endothelial progenitor cells (HEPC.CB1) which have the ability of developing pseudo neo-vessels when grown in a special medium (Matrigel) [4].

The cells prepared at twice the working density in the medium were mixed with the 2-times concentrated inhibitor dissolved in 2.5% DMSO in the culture medium. The final DMSO concentration in the culture medium was always 1.25% in a total volume of 500  $\mu$ L. An aliquot of 100  $\mu$ L was immediately pipetted into the wells of the plate coated with Matrigel [4]. The cell density in each well was 15,000 cells/100  $\mu$ L. The medium was OptiMEM with gentamicine and fungizonemais. Sterilized H<sub>2</sub>O was used. All inhibitors at each concentration were tested in quadruplicates with same DMSO concentration. Control was performed with cells in absence of inhibitors with DMSO alone. All measurements were performed in normoxy. The plate is incubated at 37 °C with 5% CO<sub>2</sub> and angiogenesis is followed during 24 hours by means of a computer-controlled video camera.

### 3 – Results of the screening of natural compounds

#### 3.1 – Screening of the GreenPharma library

The screening of 300 natural compounds from Greenpharma library allowed us to select four compounds which fully inhibit purified sGC activity at 20  $\mu\text{M}$  concentration (Figure 3) and were never reported to have an action on sGC. These compounds, from plants, yeast and fungi and whose structures are shown in Figure 4, are the following: stictic acid (**3**), violastyrene (**4**), 2-hydroxy-3,5,8-triaceto-1,4-naphthoquinone (HTANQ, **5**) and 3,6-dibromo-purpurogallin (DBPG, **6**).

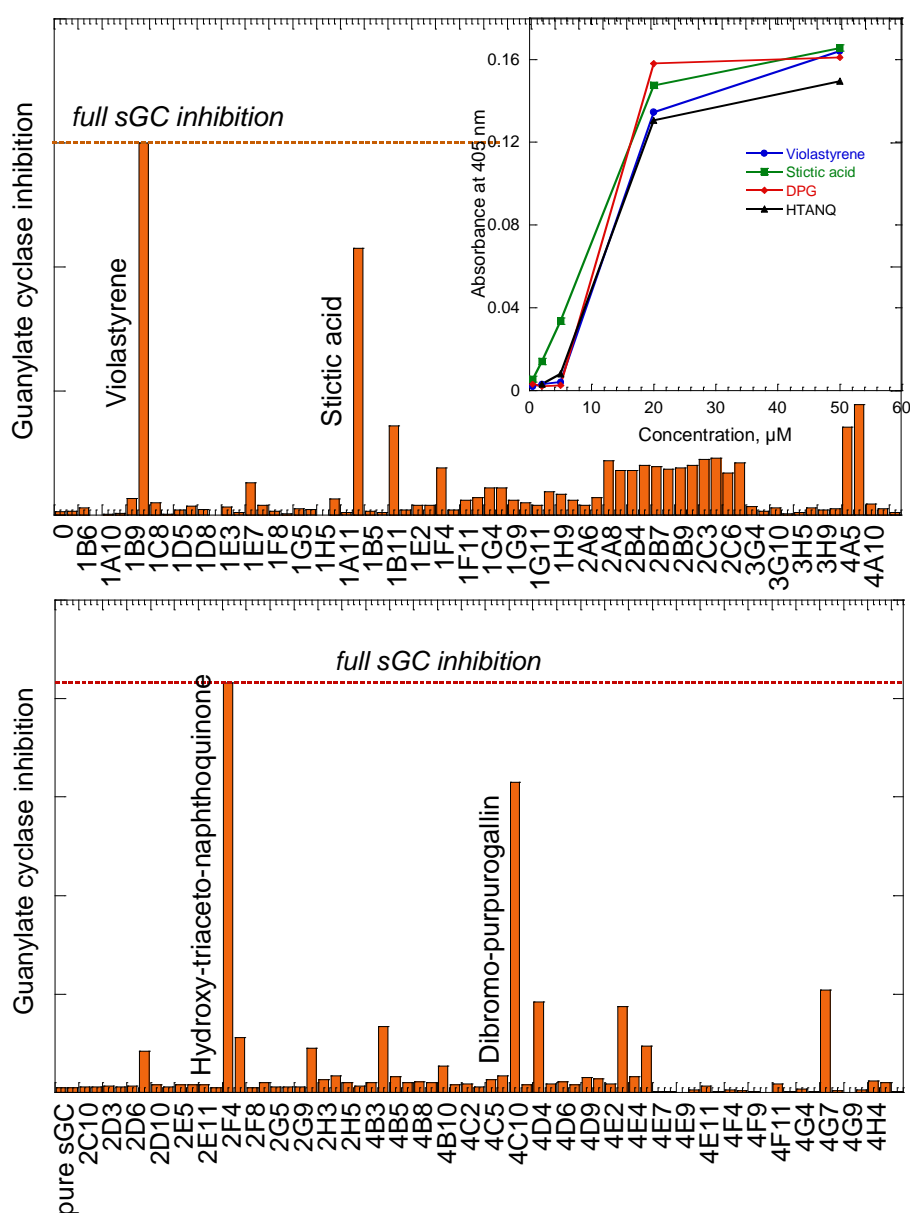


**Figure 3.** Example of screening of 200 natural compounds. Inhibition of purified sGC under influence of 20  $\mu\text{M}$  compounds from Greenpharma library. High columns show the inhibition of the sGC. Inset: sGC activity (absorbance) versus inhibitors concentration.

We were also interested in inhibition mechanism of sGC by compounds not present in the Greenpharma library, hypericin (**1**) and the cognate compound hypocrellin A (**2**), since hypericin was demonstrated to have an action on cardiomyocytes and on their cGMP content [6]. All compounds contain aromatic cycles (Figure 4).

#### *Some known properties of the identified compounds*

**Hypericin (1)** is extracted from the plant *Hypericum perforatum* (St John's Wort). MW = 504.45 g/mol. It is an anti-retroviral agent [7], antidepressant and a protein kinase-C inhibitor [8], a cytochrome P450 inhibitor [9] and may have other targets [10] in signal transduction. Hypericin is also extensively studied for its possible action in photodynamic therapy. It has been shown that in frog atrial cardiomyocytes, hypericin increased the conductance of cardiac L-type Ca<sup>2+</sup> channels by decreasing the cellular cGMP level by 69% in atrial myocytes via a possible inhibition of soluble guanylate cyclase [6]. Blocking of sGC activity by ODQ (1H-[1,2,4]-oxadiazolo[4,3-a]quinoxalin-1-one) mimicked the effects of hypericin. The assays of this previous study were performed on the entire cytosol of cardiomyocytes so that other proteins than sGC could interact with ODQ which is not specific.

**Hypocrellin A (2)** is a pigment, isolated from the parasitic fungi *Hypocrella bambuase sacc* and *Shiraia bambusicola P.* MW = 546.52 g/mol. This agent belongs to the general class of *perylene quinonoid* pigments. Hypocrellin A is being investigated as photosensitizing agent for photodynamic therapy and antiviral agent. Hypocrellin A may be a potentially novel treatment for endothelial dysfunction in diabetes acting through inhibition of protein kinase C (PKC) [11]. It is known that increased endothelin-1 (ET-1), vascular endothelial growth factor (VEGF) and activation of protein kinase C (PKC) are co-contributors to endothelial hyperpermeability in diabetes.

Because hypericin [12] and hypocrellin [13] have a wide range of targets in cells, they cannot be used in therapy as sGC inhibitors, but studying their mode of action may reveal an allosteric site for inhibitors, and lead compounds can be derived from their structure.

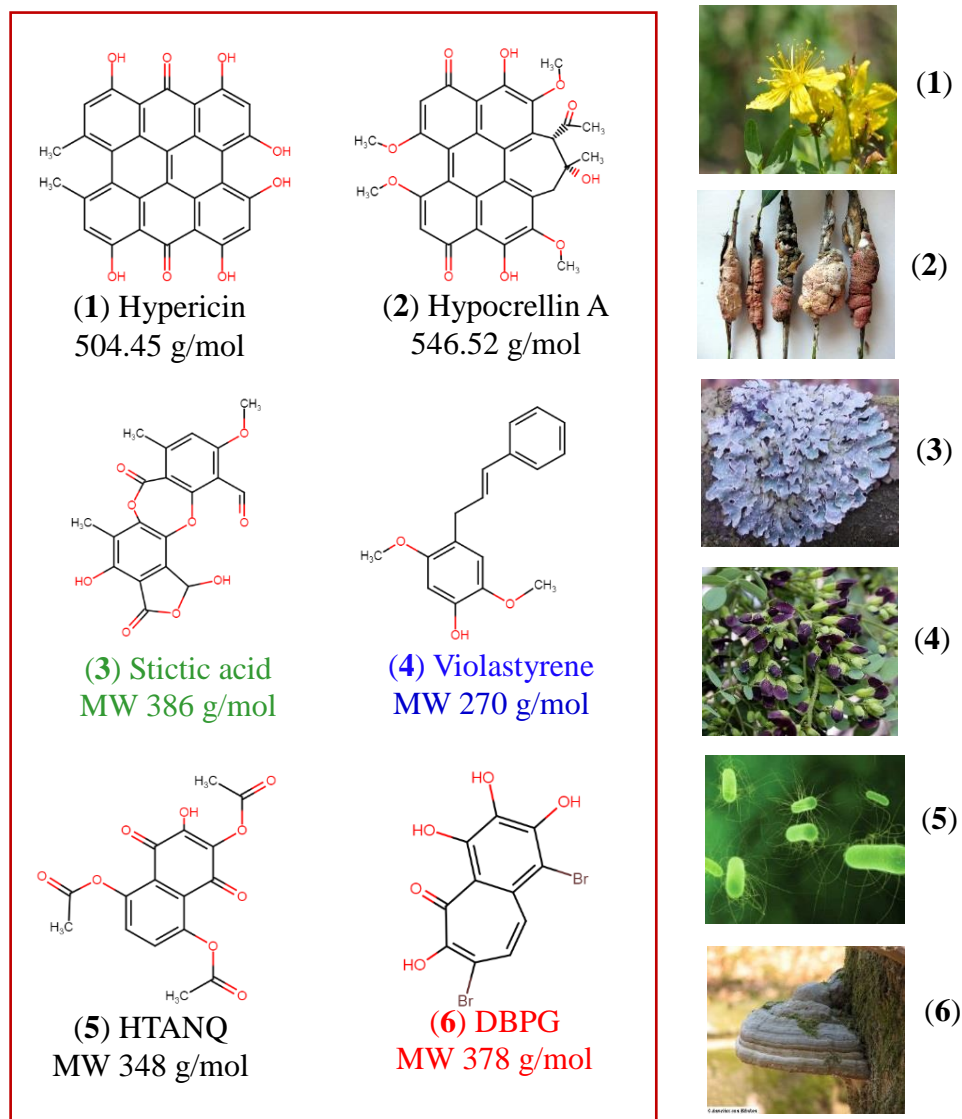
**Stictic acid (3)** is an aromatic organic compound, produced by secondary metabolism of lichens *Parmeliaceae Parmelia* [14]. MW = 386.312 g/mol. Stictic acid extracted from antarctic lichens has an apoptotic effect [15]. Subsequent cancer research has found that stictic acid has tumor-suppressing effects via action on mutant p53 proteins in cancer cells [16].

**Violastylene (4)** from the heartwood of *Fabaceae Dalbergia miscolobium* is active compound in yeast anticancer drug for the *cln2 rad14* strain and inhibitor of the human vitamin D3 receptor isoform a (VDRa) (50 μM) [17]. MW = 270.328 g/mol.

**Other identified compounds:** no physiological action are known for these compounds:

2-hydroxy-3,5,8-triaceto-1,4-naphthoquinone (**HTANQ**, **5**) is a compound synthesized from *Pseudomonas putida*. MW = 348 g/mol.

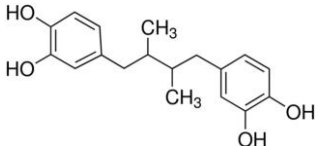
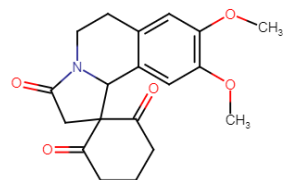
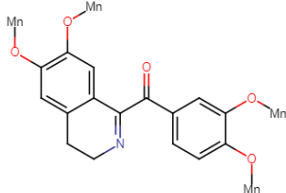
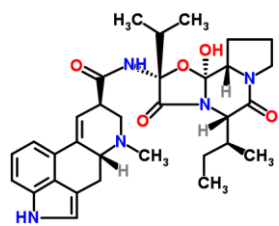
3,6-dibromo-purpurogallin (**DBPG**, **6**) is from skin of *Polyporaceae Fomes fomentarius* (MW = 377 g/mol).



**Figure 4.** Structure of the sGC inhibitors: (1) hypericin, (2) hypocrellin A, (3) stictic acid, (4) violastylene [2,5-dimethoxy-4-(3-phenylallyl)phenol], (5) 2-hydroxy-3,5,8-triaceto-1,4-naphthoquinone (HTANQ), (6) 3,6-dibromo-purpurogallin (DBPG). The organisms from which the compounds were obtained are depicted on the right.

Several compounds had partial inhibition activity on sGC (Figure 3), their structures and known properties are summarized in Table 1. For further experiments, we studied compounds with high sGC inhibition activity.

**Table 1.** Structure of the compounds that have partial inhibition activity on sGC.

Compound	Properties
<p>(1B11) Nordihydroguaiaretic acid (NDGA)</p> 	<p>From <i>Larrea tridentate</i> MW = 302.37 g/mol It has both anti-oxidant and anti-inflammatory properties [18]. Nordihydroguaiaretic acid was reported to lengthen the lifespan of male mice, but not of female mice [19].</p>
<p>(4A5) spirocyclohexane-1,5-dione-3-dehydroxy-peyoglutam</p> 	<p>From <i>Cactaceae Lophophora williamsii</i> MW = 343,38292 g/mol</p>
<p>(4D4) 3,4-dihydro-papaveraldin</p> 	<p>From <i>Berberidaceae Berberis actinacantha</i> MW = 355,39407 g/mol Air oxidation of 3,4-dihydropapaverine yields 3,4-dihydro-papavelardine [20]</p>
<p>(4G7) <math>\beta</math>-ergocryptine</p> 	<p>From <i>Clavicipitaceae Claviceps purpurea</i> MW = 575,71407 g/mol It is a natural ergoline alkaloid, one of the two isomers of ergocryptine.</p>

### 3.2 – Inhibition by the identified compounds of sGC purified and in HUVEC

We measured the half maximal inhibitory concentration ( $IC_{50}$ ) of compounds **1 – 6**. The  $IC_{50}$  is the concentration of an inhibitor where the protein response (or binding) is reduced by half, provided that the protein concentration is much lower than  $IC_{50}$ . The catalytic activity of sGC was measured in the presence of NO, the natural sGC activator, both *in vitro*

with purified sGC and in HUVEC (*in vivo*). For all six compounds, the purified sGC could be fully inhibited (Figure 5). In the case of HUVEC the assay curves did not reach full inhibition (zero baseline), demonstrating that the cell cytosol contains cGMP prior to activation of sGC by NO from the assay buffer. Despite the fact that hypericin and hypocrellin possess several targets in cells [12, 13], the half maximal inhibitory concentration of **1** ( $IC_{50} = 0.7 \mu\text{M}$ ) and **2** ( $IC_{50} = 1.5 \mu\text{M}$ ) on purified sGC have the values of the same order *in vitro* and with HUVEC (Figure 5A and Table 2).

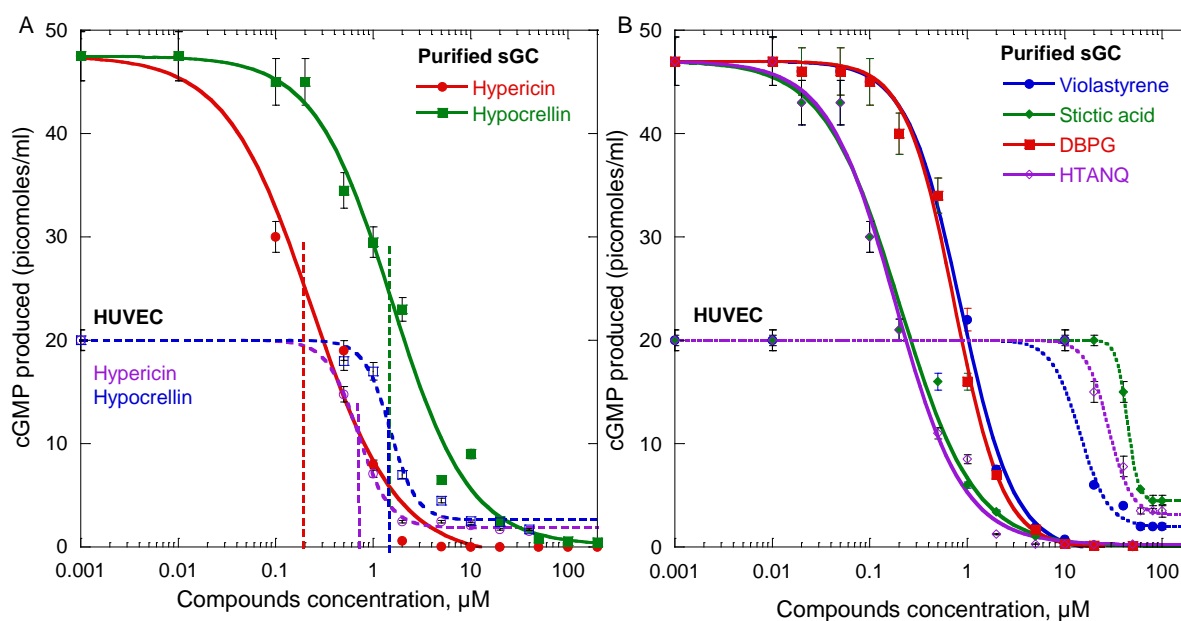


**Figure 5.** Inhibition of purified sGC and sGC in HUVEC cells by the natural compounds **1** and **2** (A) and **3** – **6** (B). Curves were normalized to sGC activity in the absence of inhibitor, which was measured independently for each curve. For HUVEC measurements, the curves were also normalized to the density of cells ( $5.6 \times 10^5$  cells/mL). The activity was measured as synthesized cGMP in the presence of the NO-donor nitroprusside ( $300 \mu\text{M}$ ). Maximal activity is not the same for purified sGC and in HUVEC due to different sGC concentrations in cells. For HUVEC, incubation time with the inhibitors **1** – **2** was 2 h and **3** – **6** was 48 h.

This fact is readily explained by the ability of inhibitors **1** and **2** to easily insert into the cell membrane due to the simultaneous presence of hydrophobic and hydrophilic hydroxylated groups. Although the intracellular location of the inhibitors is unknown, they may accumulate in cytoplasmic membranes such as the endoplasmic reticulum, the Golgi apparatus [21] and in mitochondria [22]. Before reaching organelles, hypericin and hypocrellin may bind first to sGC, which is located in the cytosol of cells.

Compounds **3** and **5** inhibited purified sGC with the same constant ( $IC_{50} = 0.2 \mu\text{M}$ ) whereas **4** and **6** disclosed a slightly larger constant ( $IC_{50} = 0.7 \mu\text{M}$ ). Contrary to **1** and **2**, compounds **3** – **5** required a larger concentration for inhibition of sGC in cells (Table 2).

**Table 2.** IC<sub>50</sub> of natural compounds for NO-activated sGC

Compounds		IC <sub>50</sub> (μM)	
		Purified sGC	HUVEC
1	Hypericin	0.2 ± 0.03	0.7 ± 0.02
2	Hypocrellin A	1.5 ± 0.20	1.5 ± 0.1
3	Stictic acid	0.2 ± 0.02	47 ± 5
4	Violastylene	0.8 ± 0.05	16 ± 3
5	HTANQ	0.2 ± 0.02	28 ± 2
6	DBPG	0.7 ± 0.04	> 200

Surprisingly, compound **6** did not have an effect on sGC in HUVEC up to 100 μM. The reason could be a sequestration or adsorption of **6** on the cell membrane, precluding its diffusion into the cytosol. No physiological action was reported for compounds **5** and **6** up to date.

### 3.3 – Inhibition of sGC in HUVEC cells

Since the time required for small molecules to penetrate through the cell membrane into the cytosol may greatly vary, we evaluated the dynamics of the inhibitory effect on HUVEC (Figure 6).

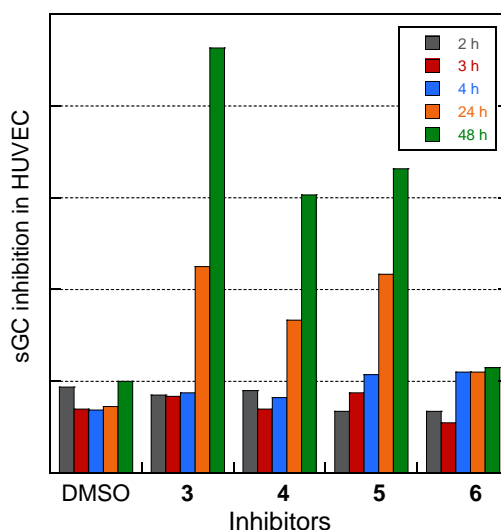


**Figure 6.** Inhibition of sGC in HUVEC as a function of the incubation time after introducing the inhibitors **3** – **6** in the growth medium (final concentration: 60 μM). cGMP production by sGC is activated by NO.

Contrary to the purified protein, no inhibition was detected up to 4 h after introducing the inhibitors in the growth medium. Compound **3** has the faster effect, whereas compound **6** (at 60 μM) does not have a significant effect on sGC activity in HUVEC after 48 h, contrastingly with its action on the purified protein which was inhibited by **6** as efficiently as compound **5** (Figure 5). Compound **6** departs from others by the presence of 2 Br atoms

whose electronegativity can preclude or considerably slow down its insertion into the cell membrane. Should these natural compounds be used as templates for designing drug candidates, this property will have consequences on pharmacokinetics.

HUVEC cells were incubated with the inhibitors (60  $\mu$ M) during 48 h without adding growth factor and serum bovine albumin in the medium. Therefore, cells did not have the resource for the cell division during experimental time. Initial density of cells before adding the inhibitors was  $6 \times 10^4$  cells/ml with well-attached cells to the surface of the plate. The density of cells in control plates and in the presence of 2% DMSO was not significantly decreased or increased after 24 h ( $6 \times 10^4$  cells/ml) and after 48 h ( $5 \times 10^4$  cells/ml). DMSO up to 2% is not toxic for HUVEC cells. After 24 h of the inhibitors incubation at 60  $\mu$ M with HUVEC, 20% of cells were detached from the surface of the plate in the presence of compound **3**, **4** and after 48 h of incubation, 100% of cells were detached but without lysis (Table 3).

**Table 3.** Density of HUVEC cells incubated with 60  $\mu$ M of the inhibitors during 48 hours

Compound		Density of HUVEC cells		
		0 h	24 h	48 h
	Control	$6 \times 10^4$ cells / ml normal	$6 \times 10^4$ cells / ml normal	$5 \times 10^4$ cells / ml normal
	2% DMSO	$6 \times 10^4$ cells / ml normal	$6 \times 10^4$ cells / ml normal	$5 \times 10^4$ cells / ml normal
<b>3</b>	Stictic acid (60 $\mu$ M)	$6 \times 10^4$ cells / ml normal	$5 \times 10^4$ cells / ml 20% detached	$5 \times 10^4$ cells / ml 100 % detached
<b>4</b>	Violastyrene (60 $\mu$ M)	$6 \times 10^4$ cells / ml normal	$6 \times 10^4$ cells / ml 20% detached	$5 \times 10^4$ cells / ml 100% detached
<b>5</b>	HTANQ (60 $\mu$ M)	$6 \times 10^4$ cells / ml normal	$4 \times 10^4$ cells / ml 20% normal 80% detached, lysis	$4 \times 10^4$ cells / ml 20% normal 80% detached, lysis
<b>6</b>	DBPG (60 $\mu$ M)	$6 \times 10^4$ cells / ml normal	$6 \times 10^4$ cells / ml normal	$5 \times 10^4$ cells / ml 80% normal 20% detached

Normal: cells are well attached to the surface of the plate, detached: cells are detached from the surface of the plate but not lysed, lysis: lysed cells.

Only compound **5** (at 60  $\mu$ M) led to lysis of cells and 80% detached cells from the plate surface after 24 h and 48 h of incubation with HUVEC with decreased density of cells from  $6 \times 10^4$  cells/ml before adding the inhibitor to  $4 \times 10^4$  cells/ml after. Compound **6** did not affect the cells after 24 h and led to 20% detached cells after 48h of incubation.

The inhibitors up to 40  $\mu$ M did not detach the cells from the surface of the plate and did not lyse the cells after 48 h of incubation. The concentration of inhibitors up to 40  $\mu$ M is not toxic for HUVEC cells. In our case, compounds **4** and **5** have  $IC_{50} \leq 40 \mu$ M and  $IC_{50} \geq 40$  for compounds **3** and **6**.

For evaluating the  $IC_{50}$  and the cross effects with activators (NO and BAY 41-2272) we therefore used in all experiments an incubation time of 48 h.

### 3.4 – Cross-effect of NO with the identified inhibitors on sGC activity in HUVEC

We verified the effect of the inhibitors in the presence and absence of NO on sGC activity in HUVEC cells and whether the identified compounds are NO-dependent or independent (Figure 7). Such experiment was not performed with purified sGC because the enzyme *in vitro* cannot be activated without NO or artificial activators (BAY 41-2272, YC-1). The control for all experiment with cells was 1% DMSO only in the growth medium, which did not inhibit the formation of cGMP.

Inhibition of sGC in HUVEC by **1** and **2** was influenced by NO which induced a small two-fold increase of  $IC_{50}$  to 0.7  $\mu$ M and 1.5  $\mu$ M respectively (Figure 7A), whereas **3** – **5** were not influenced by the presence of NO (Figure 7B). We notice that for the five compounds the basal level of cGMP production (in the range 1 – 5 picomoles/mL) increased with increasing  $IC_{50}$ . This level represents cGMP produced during cell growth, including the period of incubation with inhibitors, but not cGMP produced during the assay from provided external GTP.

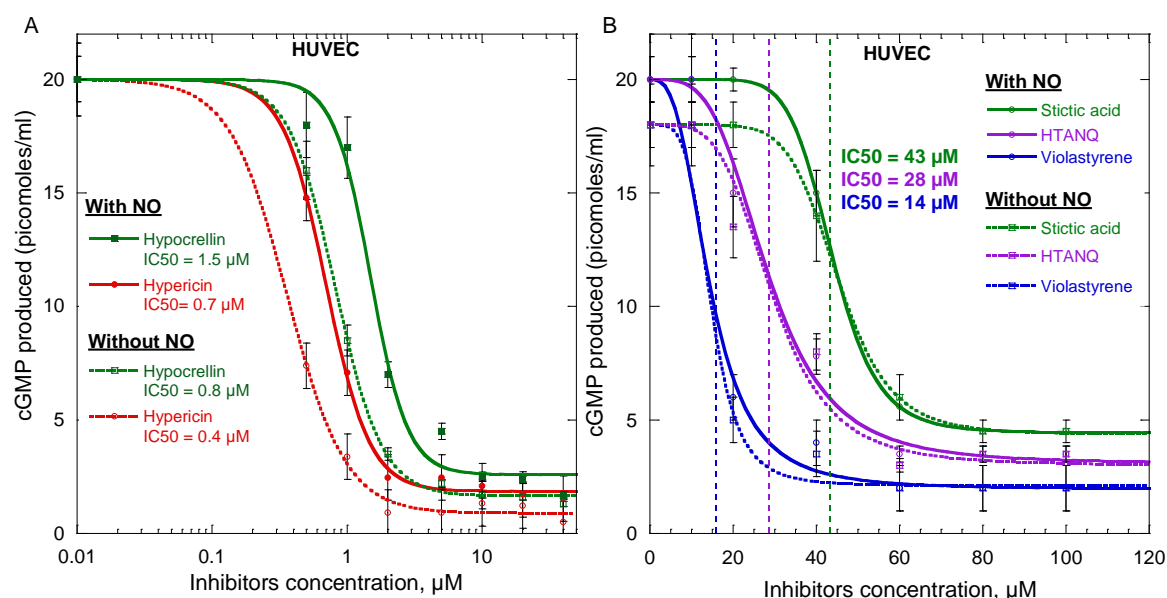


**Figure 7.** Inhibition of sGC activity in HUVEC cells by compounds **1** – **5** in the presence and absence of the NO-donor nitroprusside (300  $\mu$ M) in the assay buffer. Density of cells is  $5.6 \times 10^5$  cells/mL. Volume of DMSO added 10  $\mu$ L. The respective  $IC_{50}$  were calculated from the fit of each data set to a sigmoid curve. Incubation time of cells with **1** and **2** was 2 hours and with **3** – **5** was 48 h. Incubation was performed at 37  $^{\circ}$ C with  $CO_2$  in the dark. The measurement was repeated 3 times.

We conclude that inhibitors **1** and **2** do not preclude NO binding to the heme site and therefore do not oxidize the heme. The unchanged inhibition effect by compounds **3** – **5** in the presence of NO may be explained by several ways: this behavior is compatible with the blockage of the heme access for NO, the locking of sGC in its resting inactivated state, or the

oxidation of the heme. This last point will be verified by absorption spectroscopy (see section 6 of this chapter).

### 3.5 – Cross-effect of inhibitors with NO and BAY 41-2272 on sGC activity

To investigate a possible interaction between inhibitors and allosteric activators, we measured sGC inhibition by the identified compounds in the presence of the activator BAY 41-2272 that stimulates sGC through a NO-independent regulatory site (Figures 8 and 9). Purified sGC and cells were incubated with increasing concentration of hypericin / hypocrellin and with BAY 41-2272 (100  $\mu\text{M}$ ) in the presence and absence of NO (300  $\mu\text{M}$ ). After two hours of simultaneous incubation of cells with BAY 41-2272 and compounds at 20  $\mu\text{M}$ , partial cell death was observed. Such effect may be caused by a toxicity of high concentration of activator. It has been previously shown that 10  $\mu\text{M}$  of BAY 41-2272 induce 80% death of cells of pancreatic islets from rat (BRIN-BD11) after 48 hours of incubation [23]. Incubation of rat A7R5 VSM cells with BAY 41-2272 (10 – 100  $\mu\text{M}$ ) significantly reduces cell growth (80%) in a dose-dependent fashion after 72 hours as measured with fluorescent nucleic acid staining [24]. However, we tested the effect of 100  $\mu\text{M}$  BAY 41-2272 incubated only 2 hours for measuring the sGC activity in HUVEC cells.

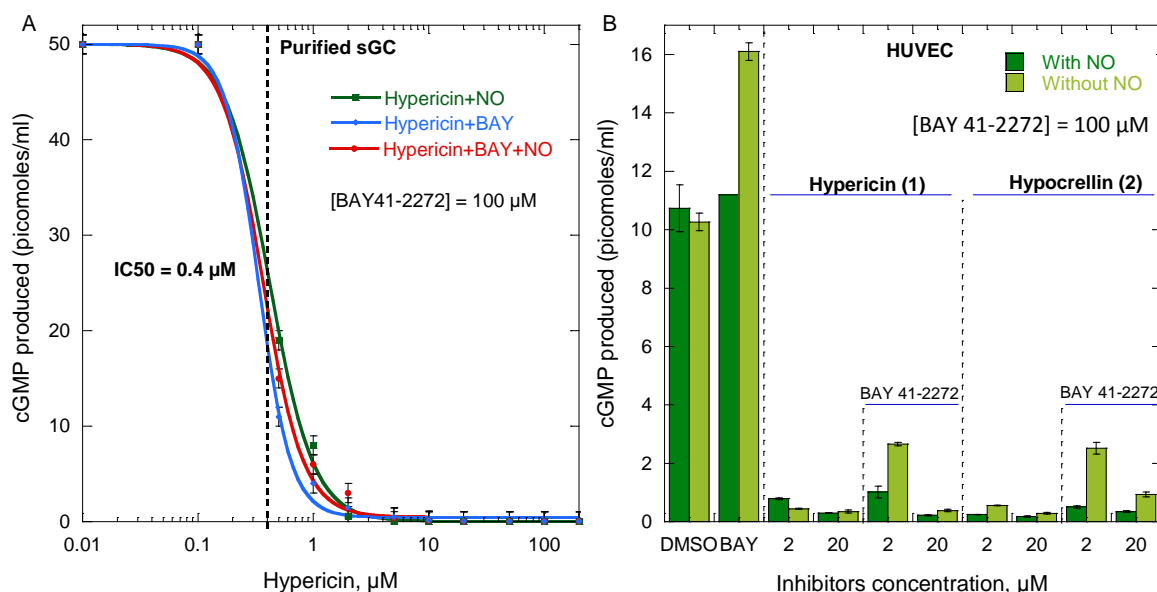


**Figure 8.** Effect of BAY 41-2272 on inhibition of sGC activity by **1** and **2** *in vitro* (A) and *in vivo* (B). The concentration of BAY 41-2272 is 100  $\mu\text{M}$  for both *in vitro* and *in vivo* experiments. Inhibitors and BAY 41-2272 were dissolved in DMSO. Standard errors were calculated from triplicate measurements. Density of cells was  $5.6 \times 10^5$  cells/mL. Concentration of nitroprusside is 300  $\mu\text{M}$ . Controls for HUVEC (left columns) were performed with 2% DMSO only and with BAY 422272 in 2% DMSO without inhibitor.

*In vitro*, the activator BAY 41-2272 does not change IC<sub>50</sub> (0.4  $\mu\text{M}$ ) of sGC inhibition by hypericin (Figure 8A) whether NO is present or not. Thus, hypericin does not compete with the activator site, and the presence of activator cannot rescue the inhibition. In cells,

BAY-412272 more efficiently activates sGC alone than in presence of additional NO. At low concentration of hypericin and hypocrellin (2  $\mu\text{M}$ ), BAY-412272 (100  $\mu\text{M}$ ) increases 2-fold the activation of sGC, compared to its absence, but this effect is abolished at higher (20  $\mu\text{M}$ ) concentration of inhibitors showing that BAY 41-2272 actually rescued sGC from inhibition, contrary to the observation *in vitro* (Figure 8A). This can be explained by a differential access to sGC for hypericin (hypocrellin) and BAY 41-2272 in the cytosol, so that sGC is only partially bound with inhibitors at 2  $\mu\text{M}$ .

Figure 9 shows inhibition of sGC by the identified GreenPharma compounds in the presence of BAY 41-2272 from two separate experiments. The sGC activity and the sensitivity of assay kit may vary between experiments, therefore, we have different cGMP maximum activities in both cases and we compared only the half maximal inhibitory concentration (Table 4).

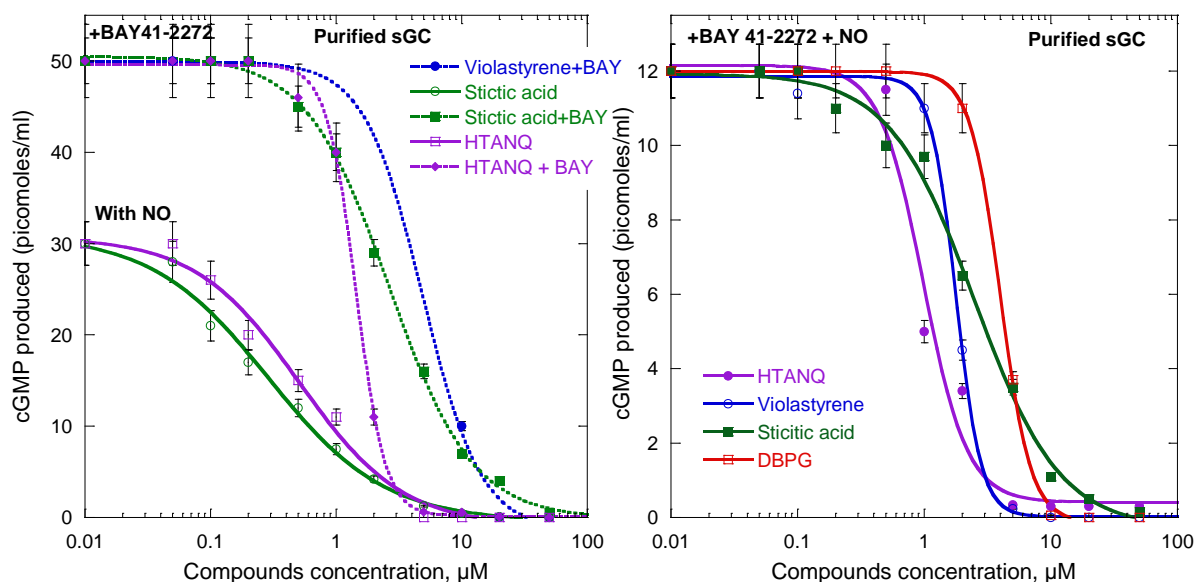


**Figure 9.** Effect of the sGC activator BAY-412272 (100  $\mu\text{M}$ ) in absence (A) and presence (B) of NO on the inhibition of purified sGC by compounds 3 – 6. Measurements in A and B were performed separately.

In general, the activator BAY 41-2272 increased  $\text{IC}_{50}$  toward purified sGC for four GreenPharma inhibitors, which was not the case for hypericin. For example,  $\text{IC}_{50}$  for the stictic acid increased  $\sim 8$  times, from  $0.3 \pm 0.04 \mu\text{M}$  in absence of BAY 41-2272 to  $2.5 \pm 0.2 \mu\text{M}$  in its presence, whatever the presence of NO. Albeit with smaller amplitude, a same trend is observed for other compounds. Thus, the activator at 100  $\mu\text{M}$  could partially rescue inhibition. The  $K_D$  of BAY 41-2272 changes from 17  $\mu\text{M}$  when the heme is free to 0.08  $\mu\text{M}$  when the heme site is occupied by CO [25], however we did not observe changes of  $\text{IC}_{50}$  in absence or presence of NO. For this reason we discarded the possibility of competitive binding between the inhibitors and BAY 41-2272 and NO for the binding site.

**Table 4.** Half maximal inhibitory concentration of natural compounds for sGC in the presence of BAY 41-2272.

Compound		IC <sub>50</sub> (μM) with purified sGC		
		+ NO	+ BAY 41-2272 + NO	+ BAY 41-2272 alone
1	Hypericin	0.4 ± 0.02	0.35 ± 0.02	0.32 ± 0.02
2	Hypocrellin A	1.5 ± 0.20	Not measured	
3	Stictic acid	0.3 ± 0.04	2.5 ± 0.2	2.6 ± 0.1
4	Violastylene	0.8 ± 0.05	1.8 ± 0.05	4.9 ± 2
5	HTANQ	0.5 ± 0.07	1 ± 0.1	1.4 ± 0.04
6	DBPG	0.7 ± 0.04	4 ± 0.1	-

Experiments of sGC inhibition in the presence of BAY 41-2272 in HUVEC cells by GreenPharma compounds was not performed due to lack of the inhibitors and their unavailability as individual commercialized products. In the next section, we will present some strategies to identify or exclude binding sites in sGC for inhibitors.

#### 4 – Interaction of inhibitors with sGC

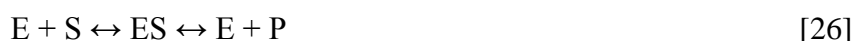
We aimed here at excluding some sites for hypericin binding by competitive measurements. We measured the binding parameters of inhibitors by surface plasmon resonance. Michaelis-Menten experiments for hypericin was performed, but not for the GreenPharma compounds. We could measure the binding rates by SPR experiments despite the low molecular weight of the inhibitors at the low limit of the method.

##### 4.1 – Inhibition of purified sGC by hypericin

##### 4.1.1 – Competition of hypericin with the substrate GTP

Mechanism and type of inhibition of sGC by hypericin (compound **1**) were determined by measuring the Michaelis-Menten constant  $K_M$  (Figure 10). Purified sGC was incubated overnight with different concentrations of substrate GTP in the presence and absence of hypericin (0.6 μM).

The Michaelis-Menten equation arises from the general equation for an enzymatic reaction:



Where E is the enzyme, S is the substrate, ES is the enzyme-substrate complex, and P is the product.

According to Michaelis-Menten's kinetics equations, at high substrate concentrations,  $[S] \geq K_M$ , and thus the term  $[S]/([S] + K_M)$  becomes essentially one and the initial velocity approached  $V_{max}$ , which resembles zero order reaction.

The Michaelis-Menten equation is:

$$V_0 = V_{max} \left( \frac{[Substrate]}{[Substrate] + K_M} \right) \quad [26]$$

where  $V_0$  is the initial velocity of the reaction;  $V_{max}$  is the maximal rate of the reaction;  $[Substrate]$  is the concentration of the substrate;  $K_M$  is the Michaelis-Menten constant which shows the concentration of the substrate when the reaction velocity is equal to one half of the maximal velocity for the reaction.

From our experiment, the reaction does not reach the normal  $V_{max}$  in the presence of hypericin, regardless of how much substrate was added (Figure 10). A subset of the enzyme molecules will always be poisoned by the inhibitor, so the effective concentration of available enzyme ( $V_{max} = 180 \text{ min}^{-1} \text{ cm}^{-1}$ ) is reduced in the presence of **1** ( $V_{max} = 5 \text{ min}^{-1}$ ). However, the reaction reaches half of its new  $V_{max}$  at the same substrate concentration, within the error of the measurements, so the Michaelis-Menten constant in the presence of the inhibitor ( $K_M = 193 \text{ }\mu\text{M}$ ) was not significantly changed ( $K_M = 130 \text{ }\mu\text{M}$ ).

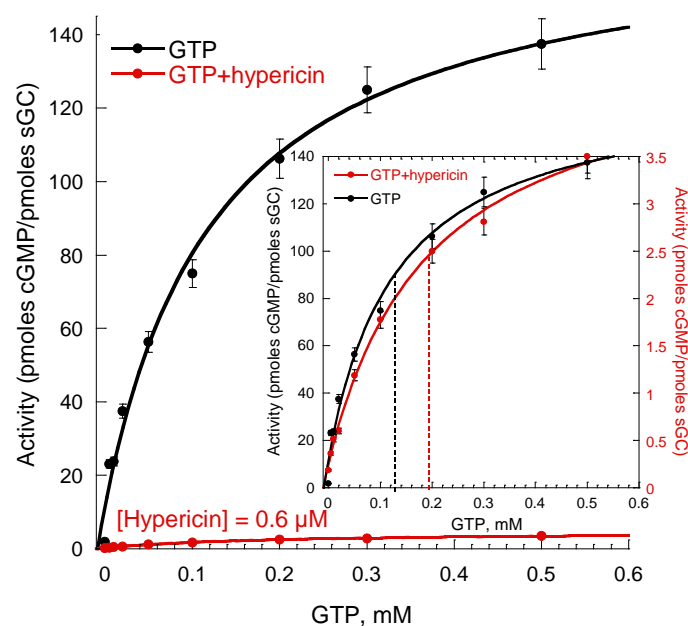


**Figure 10.** Catalytic activity of purified sGC in the presence and absence of hypericin as a function of GTP concentration in the range 0.005 – 0.5 mM. Data were fitted with the Michaelis–Menten equation. Enzymatic reactions were conducted for 10 min at 37 °C in the presence of NO donor NPS (300  $\mu\text{M}$ ). Note the dual Y-axis in the insert, for the purpose of comparing  $K_M$ . Concentration of hypericin is 0.6  $\mu\text{M}$ . Experiments were repeated 4 times.

The unchanged  $K_M$  indicates that the inhibitor does not prevent the binding of the substrate GTP to sGC, just lowers the concentration of active sGC. Inhibition by hypericin is

therefore noncompetitive. To determine the reversibility of hypericin binding to sGC, we measured the association and dissociation constants using surface plasmon resonance (see section 4.2).

#### 4.1.2 – The binding site of hypericin

To test whether hypericin binds to the binding site of the sGC stimulator BAY 41-2272 located in  $\beta 1$  H-NOX domain, a competition experiment was performed with a photoactivatable analogue of the stimulator. The cross-linking of the compound IWP-854 [27] was measured in the presence of increasing concentrations of hypericin. IWP-854 cross-linking to *Ms* sGC-NT23 was visualized by probing the biotin affinity-tag via western blot analysis. A Streptavidin affinity-tag on the C-terminus of the  $\alpha 1$  subunit was probed as a control. As shown in Figure 11A,  $\alpha 1$  and  $\beta 1$  subunits of *Ms* sGC-NT23 are clearly distinguished by differences in molecular weight,  $\alpha 1$  is ~22 kDa,  $\beta 1$  is ~45 kDa. The intensity of the photoaffinity-labelled bands of  $\beta 1$  subunit in the presence of increasing concentration of hypericin (5  $\mu$ M, 10  $\mu$ M, 20  $\mu$ M) normalized to the intensity of the loading control (without hypericin) did not differ significantly (Figure 11B). Hypericin failed to inhibit labelling of *Ms* sGC-NT23 by the photoactive stimulator IWP-854, indicating that the two compounds do not share a common binding site. In contrast, competition with BAY 41-2272 greatly diminishes crosslinking [2]. This result fully agrees with our previous observation that  $IC_{50}$  of hypericin did not change in the presence of the activator BAY 41-2272. The effect of hypericin toward sGC is inferred to be allosteric.

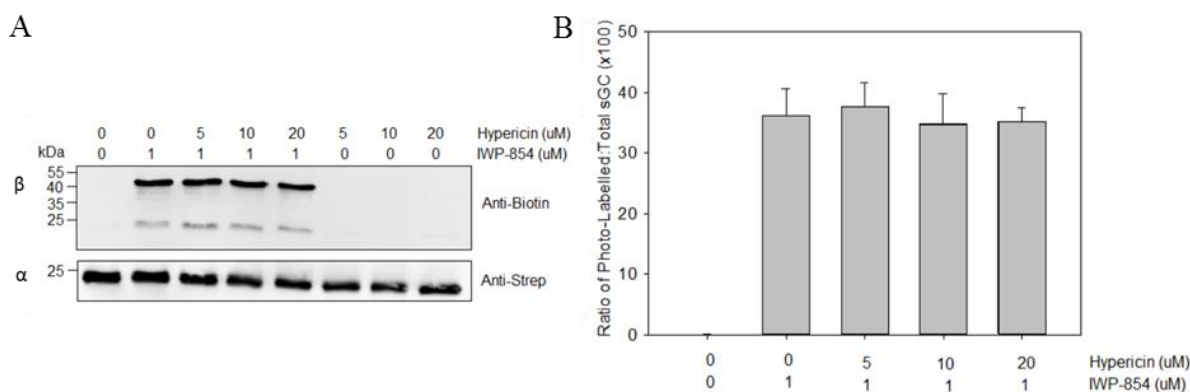


**Figure 11.** Western blot of IWP-854 cross-linking to *Ms* sGC-NT23 in the presence of hypericin (A) The intensity of the photoaffinity-labelled bands normalized to the intensity of the loading control (B). Experiment was performed in duplicate.

#### 4.1.3 – Determining the $K_D$ of CO with *Ms* sGC-NT23 in the presence of hypericin

The truncated sGC from *Manduca sexta*, *Ms* sGC-NT23, has a high affinity for CO and we aimed at determining whether hypericin affect the CO affinity and compete for the heme binding site. The  $K_D$  of CO with *Ms* sGC-NT23 was measured in the presence and

absence of 2  $\mu\text{M}$  hypericin (method in section 2.7). The difference absorbance spectra of sGC *minus* sGC+CO as a function of CO concentration and in the presence of 2  $\mu\text{M}$  hypericin are shown in Figure 12A. The change of absorption from 437 nm to 424 nm upon CO increase and binding demonstrates that sGC is not oxidized in the presence of hypericin, in agreement with our previous observation that the presence of NO modify hypericin inhibition (Figure 7).

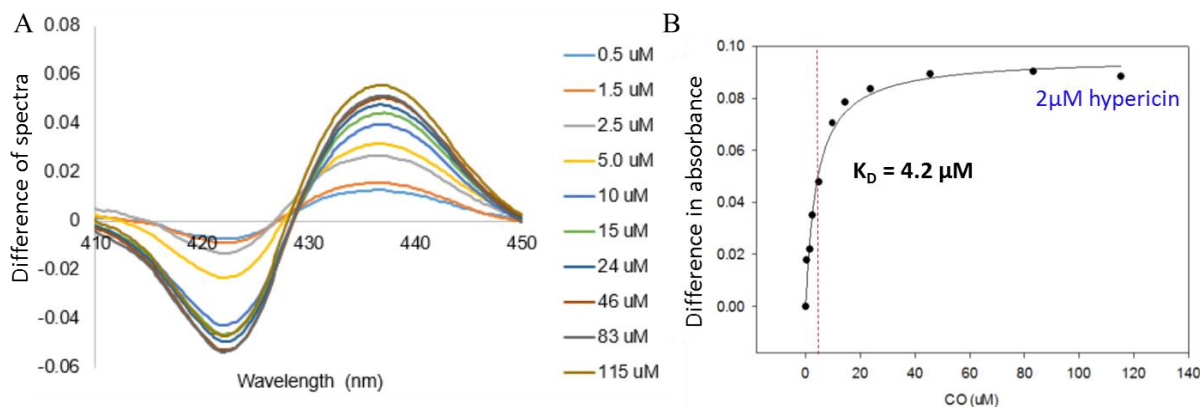


**Figure 12.** Measurement of CO binding to *Ms* sGC-NT23 in the presence of 2  $\mu\text{M}$  hypericin. (A) Difference spectra: spectrum of sGC – spectrum sGC+CO. Concentration of CO was varied from 0.5 to 115  $\mu\text{M}$ . (B) Titration of CO binding to *Ms* sGC-NT23 in the presence of 2  $\mu\text{M}$  hypericin.

The  $K_D$  of CO binding to *Ms* sGC-NT23 in the absence or presence of 2  $\mu\text{M}$  hypericin was measured in duplicate and determined from the titration curve to be  $4.2 \pm 0.1 \mu\text{M}$  and  $3.5 \pm 0.1 \mu\text{M}$ , respectively (Figure 12B). We concluded that hypericin does not affect the affinity of CO to truncated sGC, *Ms* sGC-NT23 and does not bind to the heme and, therefore, does not oxidize the heme.

## 4.2 – Kinetics of inhibitors binding

### 4.2.1 – Hypericin binding to purified sGC

The kinetics of hypericin binding to sGC were measured by surface plasmon resonance (detailed description of SPRi setup is in CHAPTER VII), injecting an increasing concentration of hypericin on the spotted sGC at the surface of the bioship.

Figure 13A shows that the maximum reflectivity index of sGC spots still increases after each injection of hypericin, despite washing steps, and reaches 5% at 200  $\mu\text{M}$  of inhibitor. In the case of cytochrome c (cyt c) and hemoglobin (Hb), the reflectivity does not increase significantly up to 1% and come back to the initial state close to zero baseline, contrary to sGC. Consequently, the reflectivity change can be explained by non-specific and reversible binding of hypericin to cyt c and Hb. Contrarily, we assign the behavior of the sGC curve to partly reversible binding of hypericin to sGC and progressive saturation. At concentration lower than 10  $\mu\text{M}$  no signal could be detected.

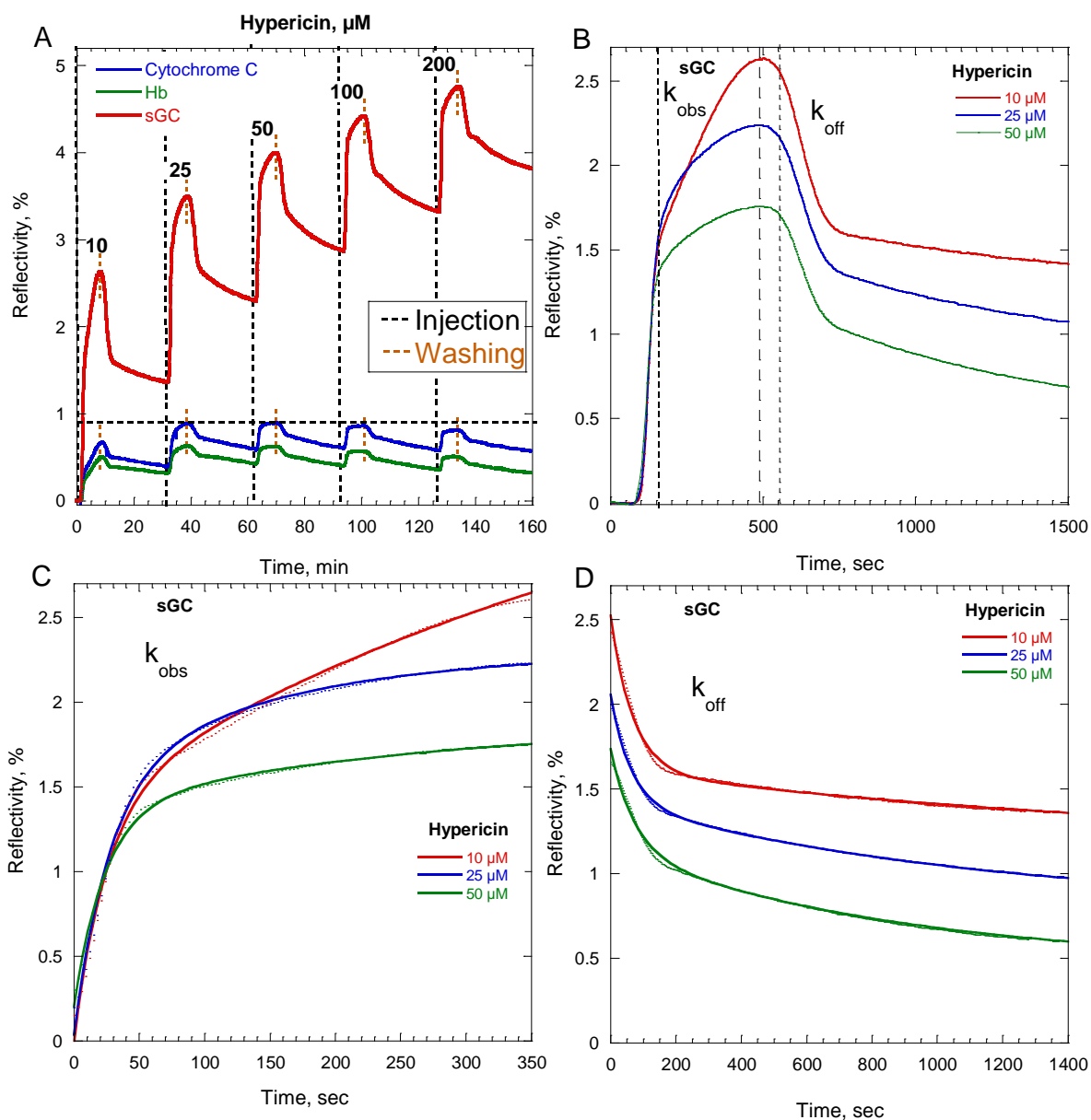


**Figure 13.** Kinetics of hypericin binding to sGC examined by surface plasmon resonance (A). Black dotted vertical lines represent beginning of compound injection, orange dotted lines is beginning of washing step after each injection. Concentration of hypericin is 10  $\mu\text{M}$ , 25  $\mu\text{M}$ , 50  $\mu\text{M}$ , 100  $\mu\text{M}$  and 200  $\mu\text{M}$ . Injection flow rate is 25  $\mu\text{L}/\text{min}$ . Sensorgram for the interaction between sGC and hypericin (B). Association (C) and dissociation (D) curves for 10  $\mu\text{M}$ , 25  $\mu\text{M}$  and 50  $\mu\text{M}$  hypericin. Curves were fitted to a multiexponential function. The experiment was repeated 3 times on different bioships having each 10 spots of sGC. Concentration of proteins 3.5  $\mu\text{M}$ . Hemoglobin (Hb) and cytochrome c were used as controls for nonspecific binding of hypericin.

The superposition of the kinetics curves at increasing concentration of hypericin (10  $\mu\text{M}$  to 50  $\mu\text{M}$ ) binding to sGC (Figure 13B) highlights the change of reflectivity index. This effect can be due to the availability of two binding sites of sGC for hypericin, where only one reversibly binds the inhibitor. To quantify the association kinetics of hypericin to sGC, the washing part of the curve was fitted with the sum of two different exponential functions,

which correspond to two observed (apparent) rate constants ( $k_{\text{obs}}$ ) that depend on the concentration of binding compound. The first  $k_{\text{obs}}$  were similar for all proteins and concentrations, and was therefore assigned to a change of refractive index of the injected solution sensed by the surface of the prism before the binding of molecules of interest to the proteins.

This effect can be detected because all compounds that we studied have a low molecular weight for SPR (MW = 504 g/mol) which implies a reflectivity response of same order of amplitude. Second  $k_{\text{obs}}$  is the apparent rate constant of binding which depends on the concentration of binding compounds, which we used to calculate association rate ( $k_{\text{on}}$ ). Therefore, we excluded the first part of the signal and fitted only second part of the curve (dotted vertical lines in Figure 13B). The dissociation curves also consist of two parts: dissociation of compounds from proteins that we assigned to simultaneous specific and non-specific binding (Figure 13D). The kinetic parameters are presented in Table 5. At 10 and 25  $\mu\text{M}$  hypericin,  $k_{\text{obs}}$  follows the concentration but not at 50  $\mu\text{M}$ , a behavior in agreement with partly reversibility and saturation of sGC. Therefore, kinetic parameters were calculated only for 10  $\mu\text{M}$  and 25  $\mu\text{M}$ , yielding  $k_{\text{on}} = (2 - 3) \times 10^2 \text{ s}^{-1}\text{M}^{-1}$ , a slow rate in agreement with the size of the molecule (Figure 4) and  $K_{\text{D}} = 2.5 - 3.2 \mu\text{M}$ .

We assigned the second dissociation constant (50 – 75  $\mu\text{M}$ ) to non-specific binding. Formally, the  $K_{\text{D}}$  should be lower or equal to  $\text{IC}_{50} = 0.2 \mu\text{M}$ . However we must note that in SPR experiments the protein is attached in high density on the prism, a condition is not favorable for measuring true  $K_{\text{D}}$ .

**Table 5.** Kinetic parameters of hypericin binding to sGC.

Parameters	Hyp 10 $\mu\text{M}$	Hyp 25 $\mu\text{M}$	Hyp 50 $\mu\text{M}$
$K_{\text{obs}} (\text{s}^{-1})$	$0.002 \pm 0.0005$	$0.007 \pm 0.001$	$0.004 \pm 0.001$
$k_{\text{on}} (\text{s}^{-1}\text{M}^{-1})$	$0.0002 \times 10^6$	$0.00028 \times 10^6$	$0.0001 \times 10^6$
$k_{\text{off}} (\text{s}^{-1})$	$0.015 \pm 0.0003$ <b><math>0.0005 \pm 0.0001</math></b>	$0.016 \pm 0.0003$ <b><math>0.0009 \pm 4 \times 10^{-5}</math></b>	$0.014 \pm 0.0003$ $0.001 \pm 6 \times 10^{-5}$
$K_{\text{A}} (\text{M}^{-1})$	$0.013 \times 10^6$ <b><math>0.4 \times 10^6</math></b>	$0.017 \times 10^6$ <b><math>0.3 \times 10^6</math></b>	-
$K_{\text{D}} (\text{M})$	$75 \times 10^{-6}$ <b><math>2.5 \times 10^{-6}</math></b>	$57 \times 10^{-6}$ <b><math>3.2 \times 10^{-6}</math></b>	-

The errors indicated are from the fitting procedure, not from multiple measurements.

Because the SPR experiment showed partly reversible binding of hypericin to sGC, we designed a protocol to verify this point on the catalytic activity. We measured sGC activity in the presence and absence of hypericin before and after ultrafiltration of protein at high speed in order to remove hypericin.

After one night of incubation of sGC with 10  $\mu\text{M}$  and 20  $\mu\text{M}$  hypericin, the enzyme was centrifuged in ultrafiltration tubes with 100-kDa cut-off membrane in 2.4 mL of TEA buffer at 4000 G for 4 minutes. The activity of sGC was measured by ELISA. Activity of

centrifuged sGC was compared to that of not centrifuged sGC/hypericin samples and sGC without inhibitor (Figure 14). The activity of sGC was not restored after centrifugation of sGC/hypericin compared to not centrifuged sGC/hypericin (Figure 14, insert). The activity of the enzyme without hypericin was 60 – 70 picomoles/ml, that is ~200 times higher than with the inhibitor (0.25 – 0.3 picomoles/ml), whatever it was centrifuged or not. This activity measurement confirms the irreversible binding of hypericin previously observed by SPR.

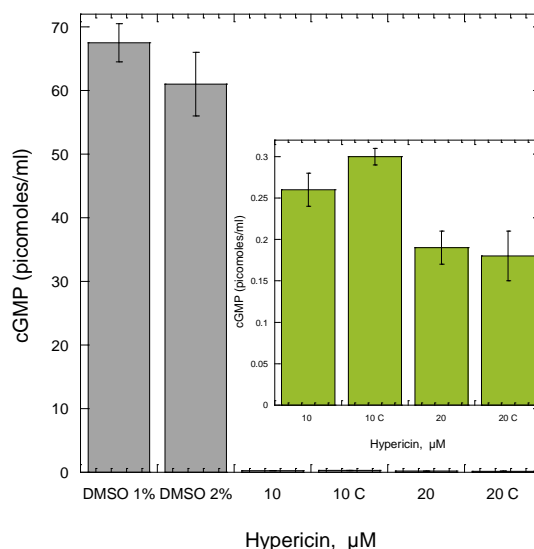


**Figure 14.** Irreversible binding of hypericin on cGMP production by purified sGC. «10C» and «20C» represent centrifuged sGC after one night of incubation with hypericin. Concentration of hypericin is 10 μM and 20 μM, [sGC] = 25 nM.

#### 4.2.2 – Hypocrellin binding to purified sGC

Hypocrellin A is an analog of hypericin with a similar frame but different side groups (Figure 4) and molecular weight of 546 g/mol. We could not obtain reliable kinetic parameters for hypocrellin (Table 6). Increasing concentration of hypocrellin gave a much high reflective response ( $R_{\max} = 35\%$ , Figure 15A) compared to hypericin ( $R_{\max} = 5\%$ , Figure 13A), but after second injection (25 μM), hypocrellin precipitated on the surface of prism and the sGC response was saturated. Hypocrellin binds partly reversibly even with hemoglobin and cytochrome c, but with a lower response (Figure 15A).

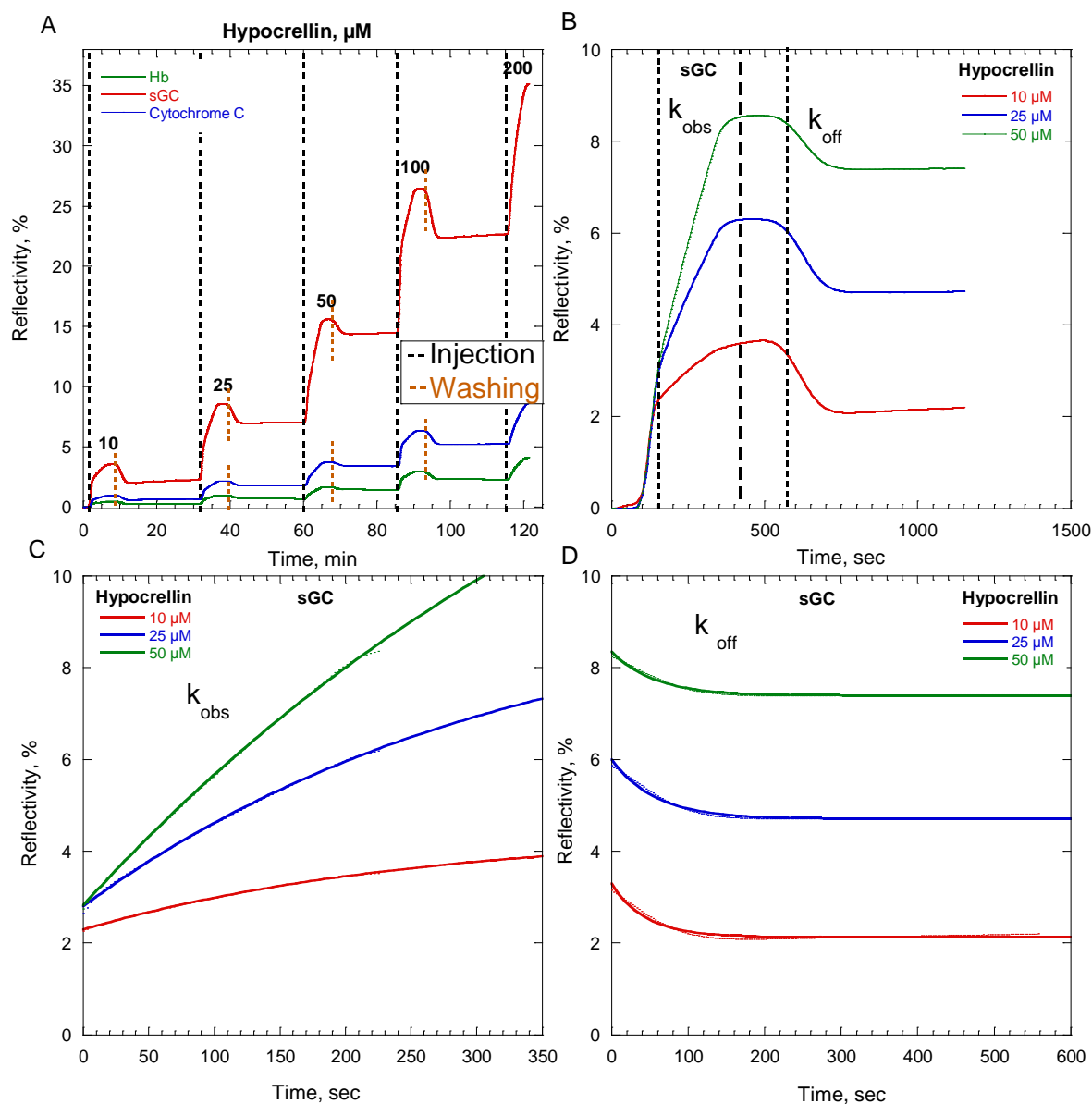


**Figure 15.** Kinetics of hypocrellin binding to sGC examined by surface plasmon resonance (A). Black dotted vertical lines represent beginning of compound injection, orange dotted lines is beginning of washing step after each injection. Sensorgram for the interaction between sGC and hypocrellin (B). Association (C) and dissociation (D) curves for 10 μM, 25 μM and 50 μM hypocrellin. Curves were fitted to a multiexponential function. Concentration of hypocrellin is 10 μM, 25 μM, 50 μM, 100 μM and 200 μM. Injection flow rate is 25 μL/min. The experiment was repeated 3 times on different bioships having each 10 spots of sGC. Concentration of proteins 3.5 μM. Hemoglobin (Hb) and cytochrome c were used as a control.

Due to systematic precipitation, the kinetic curves show inconsistent association and dissociation rates (Table 6). Despite the similarities in the catalytic inhibition of two compounds, hypocrellin behaves very differently with SPR and we could not reliably study its binding because of its propensity to precipitate.

**Table 6.** Kinetics parameters of hypocrellin binding to sGC.

Parameters	HcrI 10 $\mu\text{M}$	HcrI 25 $\mu\text{M}$	HcrI 50 $\mu\text{M}$
$K_{\text{obs}} (\text{s}^{-1})$	$0.004 \pm 9 \times 10^{-5}$	$0.003 \pm 1 \times 10^{-4}$	$0.002 \pm 8 \times 10^{-5}$
$k_{\text{on}} (\text{s}^{-1}\text{M}^{-1})$	$0.0004 \times 10^6$	$0.00012 \times 10^6$	$0.00004 \times 10^6$
$k_{\text{off}} (\text{s}^{-1})$	$0.02 \pm 0.001$	$0.02 \pm 0.001$	$0.02 \pm 0.001$
$K_{\text{D}} (\text{M})$	$50 \times 10^{-6}$	-	-

#### 4.2.3 – GreenPharma compounds binding to sGC and bacterial H-NOXs

The binding kinetics of two active sGC inhibitors from GreenPharma, stictic acid and DBPG were measured for purified sGC and two bacterial H-NOX proteins from *Clostridium botulinum* (Cb-H-NOX) and *Nostoc punctiforme* (Np-H-NOX).

##### *Kinetics of stictic acid binding*

Maximal reflectivity ( $R_{\text{max}} = 0.7$ , Figure 16) from superposed kinetics curves is very low compare to hypericin (Figure 13B), which can be explained by the lower molecular weight of compound (MW = 386 g/mol). The binding of stictic acid to the three proteins appeared reversible. Despite a low signal, we could measure kinetic parameters of stictic acid binding, which are presented in Table 7.

**Table 7.** Kinetic parameters of stictic acid binding to sGC, Np-H-NOX and Cb-H-NOX.

Parameters	Stictic acid at 5 $\mu\text{M}$	Stictic acid at 10 $\mu\text{M}$	Stictic acid at 25 $\mu\text{M}$	Stictic acid at 50 $\mu\text{M}$
<b>Full length sGC</b>				
$k_{\text{obs}} (\text{s}^{-1})$	0.004	0.0097	0.02	0.009
$k_{\text{on}} (\text{s}^{-1}\text{M}^{-1})$	<b><math>0.0008 \times 10^6</math></b>	<b><math>0.0009 \times 10^6</math></b>	<b><math>0.0008 \times 10^6</math></b>	$0.00018 \times 10^6$
$k_{\text{off}} (\text{s}^{-1})$	0.02	0.02	0.02	0.02
$K_{\text{A}} (\text{M}^{-1})$	$0.04 \times 10^6$	$0.045 \times 10^6$	$0.04 \times 10^6$	$0.009 \times 10^6$
$K_{\text{D}} (\text{M})$	<b><math>25 \times 10^{-6}</math></b>	<b><math>22 \times 10^{-6}</math></b>	<b><math>25 \times 10^{-6}</math></b>	$111 \times 10^{-6}$
<b>Np-H-NOX</b>				
$k_{\text{obs}} (\text{s}^{-1})$	0.004	0.013	0.03	0.01
$k_{\text{on}} (\text{s}^{-1}\text{M}^{-1})$	<b><math>0.0008 \times 10^6</math></b>	<b><math>0.0013 \times 10^6</math></b>	<b><math>0.0012 \times 10^6</math></b>	$0.0002 \times 10^6$
$k_{\text{off}} (\text{s}^{-1})$	0.02	0.02	0.02	0.02
$K_{\text{A}} (\text{M}^{-1})$	$0.04 \times 10^6$	$0.06 \times 10^6$	$0.06 \times 10^6$	$0.01 \times 10^6$
$K_{\text{D}} (\text{M})$	<b><math>25 \times 10^{-6}</math></b>	<b><math>16 \times 10^{-6}</math></b>	<b><math>17 \times 10^{-6}</math></b>	$100 \times 10^{-6}$
<b>Cb-H-NOX</b>				
$k_{\text{obs}} (\text{s}^{-1})$	0.004	0.006	0.007	0.008
$k_{\text{on}} (\text{s}^{-1}\text{M}^{-1})$	<b><math>0.0008 \times 10^6</math></b>	<b><math>0.0006 \times 10^6</math></b>	$0.0003 \times 10^6$	$0.00016 \times 10^6$
$k_{\text{off}} (\text{s}^{-1})$	0.02	0.02	0.02	0.02
$K_{\text{A}} (\text{M}^{-1})$	$0.04 \times 10^6$	$0.03 \times 10^6$	$0.15 \times 10^6$	$0.008 \times 10^6$
$K_{\text{D}} (\text{M})$	<b><math>25 \times 10^{-6}</math></b>	<b><math>33 \times 10^{-6}</math></b>	$66 \times 10^{-6}$	$125 \times 10^{-6}$

At 5, 10 and 25  $\mu\text{M}$ ,  $k_{\text{obs}}$  appeared proportional to the inhibitor concentration for sGC and *Np*-H-NOX, but not at 50  $\mu\text{M}$ , again pointing out saturation of the proteins spotted on the bioship. For *Cb*-H-NOX  $k_{\text{obs}}$  was proportional only at 5 and 10  $\mu\text{M}$ .

The obtained dissociation constants for *Np*-H-NOX ( $K_D = 16 - 25 \times 10^{-6} \text{ M}$ ), *Cb*-H-NOX ( $K_D = 25 - 33 \times 10^{-6} \text{ M}$ ) and full-length sGC ( $K_D = 22 - 25 \times 10^{-6} \text{ M}$ ) are in the same range and stictic acid binds to sGC and H-NOX proteins with the same affinity. Similar dissociation constant indicates one binding site for the inhibitor in H-NOX domain of sGC. Similarly to hypericin,  $K_D$  is larger than  $\text{IC}_{50}$  (Table 2), which formally should be the same, implying that SPR protocol may not be well-suited.

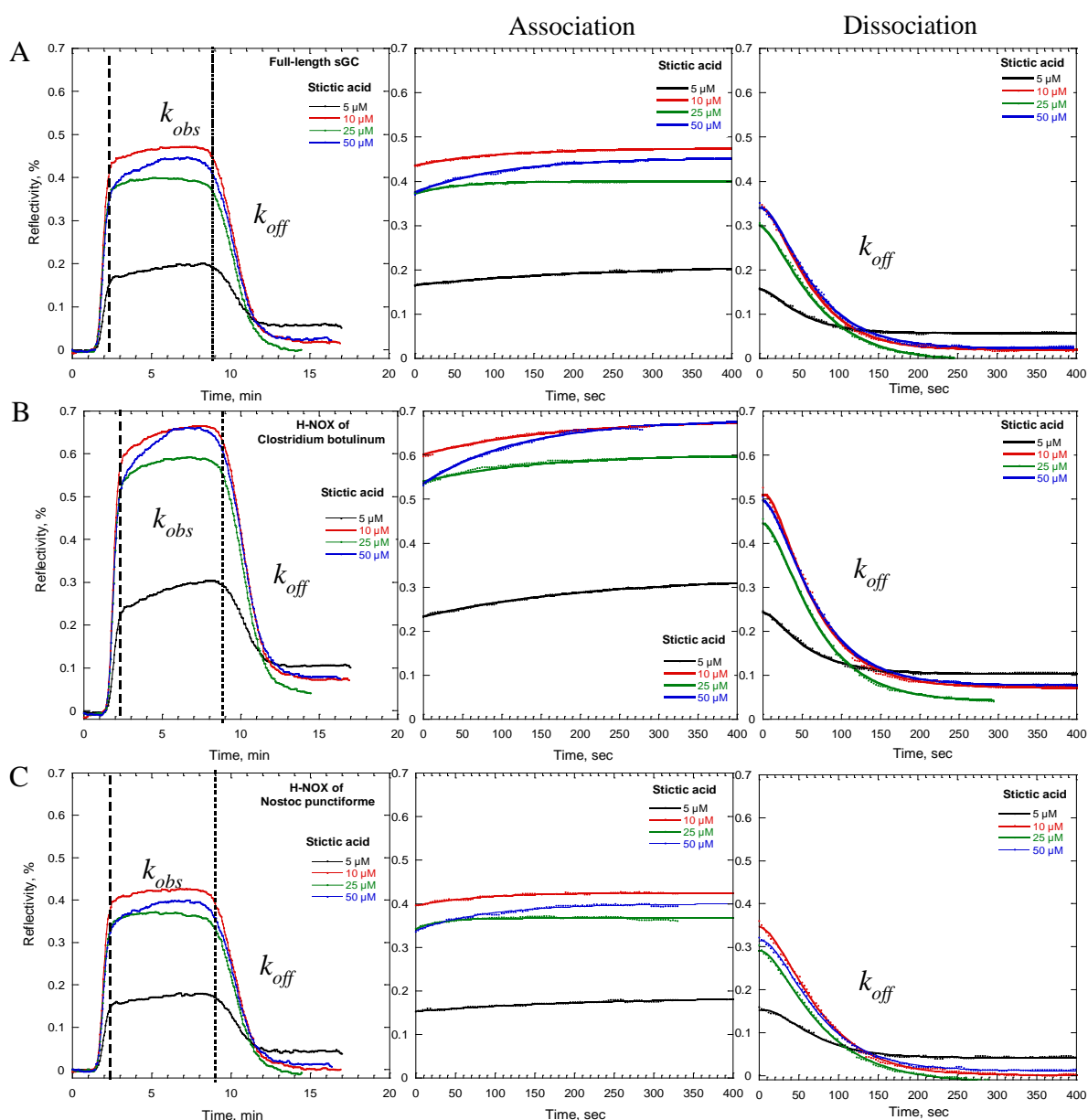


**Figure 16.** Sensogram for the binding of stictic acid to bacterial H-NOX protein of *Nostoc punctiforme* (NP-H-NOX), *Clostridium botulinum* (*Cb*-H-NOX) and full-length human sGC. Injection flow rate is 25 $\mu\text{L}/\text{min}$ . Concentration of [sGC] = 3.5  $\mu\text{M}$ , [*Np*-H-NOX] = 13  $\mu\text{M}$ , [*Cb*-H-NOX] = 10  $\mu\text{M}$ .

### Kinetics of DBPG binding

DBPG (3,6-dibromo-purpurogallin) has an oily consistency when dissolved in DMSO. Therefore, we could test only one concentration (10  $\mu\text{M}$ ) of the inhibitor on affinity constant by SPRi method. Although the maximal reflectivity for DBPG binding to sGC and H-NOXs proteins is higher than for cyt c and Hb, the inhibitor binds irreversibly to all proteins (Figure 17) with same kinetic parameters for all proteins (Table 8). Albeit we could measure its inhibition constant, the oily nature of DBPG makes it binding nonspecific with the entire surface of the bioship and it was not possible to separate the signal to recover the binding rates.

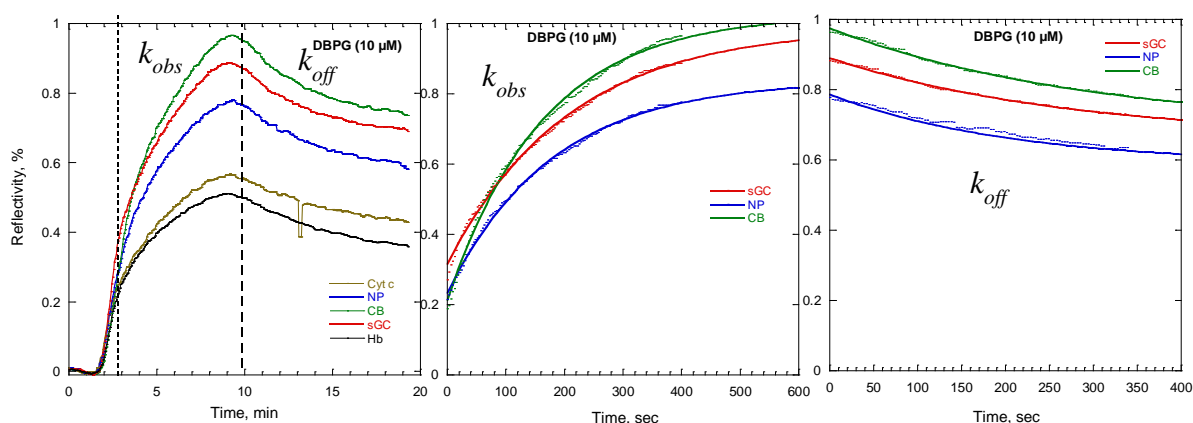


**Figure 17.** Sensorgram for the binding of DBPG to bacterial H-NOX protein of *Nostoc punctiforme* (*Np*-H-NOX), of *Clostridium botulinum* (*Cb*-H-NOX) and full-length human sGC. Hemoglobin (Hb) and cytochrome c (cyt c) were used like control proteins. Injection flow rate is 25  $\mu\text{L}/\text{min}$ . Concentration of [sGC] = 3.5  $\mu\text{M}$ , [*Np*-H-NOX] = 13  $\mu\text{M}$ , [*Cb*-H-NOX] = 10  $\mu\text{M}$ .

**Table 8.** Kinetic parameters of DBPG binding to sGC, *Np*-H-NOX and *Cb*-H-NOX

DBPG (10 $\mu\text{M}$ )	<i>Cb</i> -H-NOX	<i>Np</i> -H-NOX	sGC
$k_{\text{obs}}$ ( $\text{s}^{-1}$ )	0.004	0.004	0.004
$k_{\text{on}}$ ( $\text{s}^{-1}\text{M}^{-1}$ )	$0.0004 \times 10^6$	$0.0004 \times 10^6$	$0.0004 \times 10^6$
$k_{\text{off}}$ ( $\text{s}^{-1}$ )	0.004	0.004	0.004
$K_{\text{D}}$ (M)	$10 \times 10^{-6}$	$10 \times 10^{-6}$	$10 \times 10^{-6}$

In conclusion, SPR is a powerful technique to measure binding rates, but should the properties of the ligand under study make it hardly soluble or interactive with the entire surface, the measurement is compromised. We still have to adjust the protocol for hypericin and stictic acid binding parameters determination.

## 5 – Analogues of the identified compounds

Analogues of violastylene (**9** – **14**) and 2-hydroxy-3,5,8-triaceto-1,4-naphthoquinone (HTANQ, **7**, **8**) were tested for inhibition of the purified sGC. Two concentrations of

compound (2 and 10  $\mu\text{M}$ ) were first incubated with sGC for 2 hours and activity was measured by ELISA. Figure 18 shows the inhibition of sGC in the presence of violastylene analogues (9-14) and HTANQ analogues (7, 8). The horizontal line is the basal activity of sGC. Compounds 7, 8 exert higher inhibition for sGC at 10  $\mu\text{M}$ , consequently their activity was further tested in a wider concentration range on purified sGC and in HUVEC.

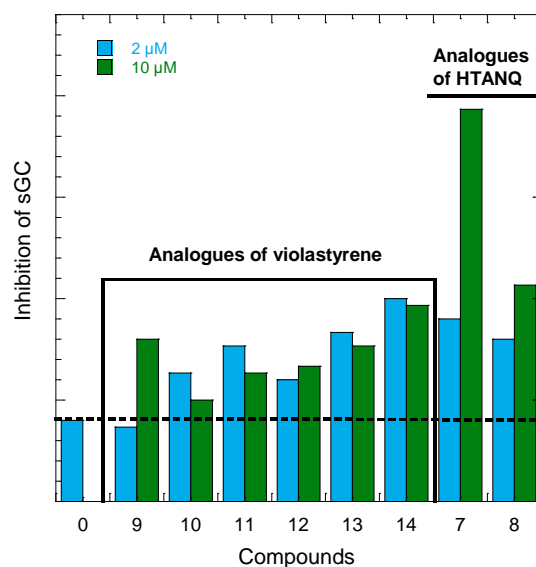


**Figure 18.** Inhibition of sGC activity by violastylene analogues (compounds 9 – 14) and 2-hydroxy-3,5,8-triaceto-1,4-naphthoquinone (HTANQ) analogues (compounds 7, 8). 0 is sGC basal activity.

### 5.1 – Analogues of HTANQ

Physiological action HTANQ and its analogues **Ambinter537501** (7, MW = 348 g/mol) and **Ambinter537686** (8, MW = 348 g/mol) is not known. HTANQ and its analogues consist of two adjacent phenol rings, several hydroxyl (OH) and methyl (CH<sub>3</sub>) groups (Figure 19).

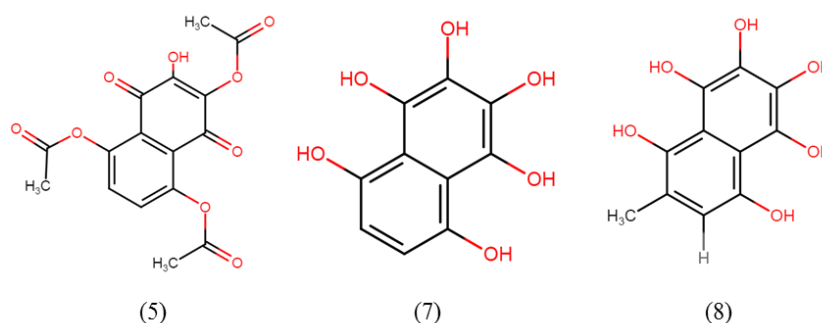


**Figure 19.** Chemical structures of 2-hydroxy-3,5,8-triaceto-1,4-naphthoquinone (HTANQ, 5) and its analogues (7, 8).

All compounds are inhibitors of sGC. Half maximal inhibitory concentration of HTANQ analogues (IC<sub>50</sub> (7) = 5  $\mu\text{M}$ , IC<sub>50</sub> (8) = 3  $\mu\text{M}$ ) are higher than for HTANQ (IC<sub>50</sub> (5) =

0.2  $\mu\text{M}$ ) on purified sGC. We measured by SPR the kinetics of compound **7** (MW = 348 g/mol) binding to H-NOX protein from *Nostoc punctiforme* (*Np*-H-NOX), shown in Figure 20. The dissociation constant obtained for the first two concentrations of injected compound is  $K_D = 11 \mu\text{M}$ . At higher concentration (100  $\mu\text{M}$ ) saturation of the protein occurred (Table 9). The affinity of compound **7** appears higher than that of (**3**) for *Np*-H-NOX, *Cb*-H-NOX and full-length sGC ( $K_D = 25 \times 10^{-6} \text{ M}$ ).

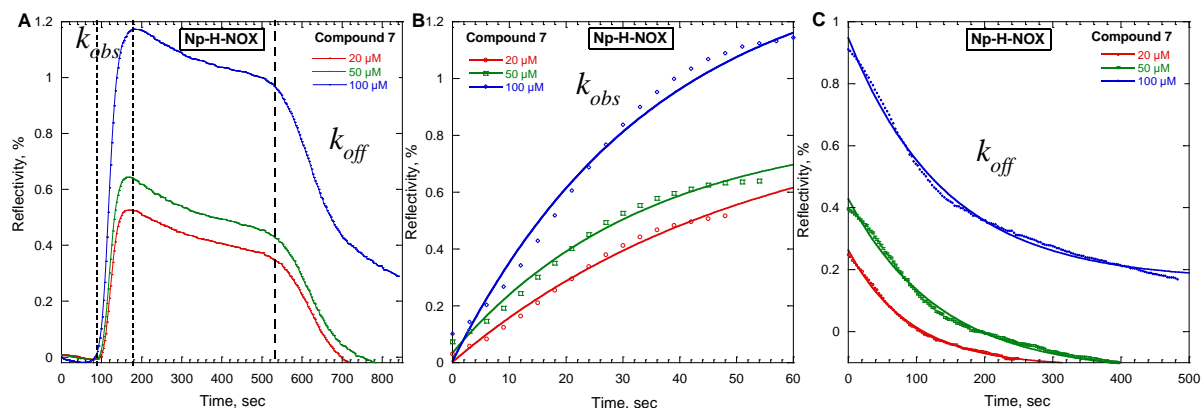


**Figure 20.** Sensogram for compound (**7**) binding to bacterial H-NOX protein of *Nostoc punctiforme* (*Np*-H-NOX) (A). Association (B) and dissociation (C) curves. Injection flow rate is 25 $\mu\text{L}/\text{min}$ . Concentration of protein is 13  $\mu\text{M}$ , concentration of compound is 20  $\mu\text{M}$ , 50  $\mu\text{M}$ , 100  $\mu\text{M}$ . The shape of binding curves in A is explained by a leak of the protein spotted on the bioship.

**Table 9.** Kinetics parameters of compound **7** (HTANQ 537501) binding to bacterial H-NOX from *Nostoc punctiforme*

Parameters	HTANQ 537501 concentration		
	20 $\mu\text{M}$	50 $\mu\text{M}$	100 $\mu\text{M}$
$k_{\text{obs}} (\text{s}^{-1})$	0.018	0.03	0.03
$k_{\text{on}} (\text{s}^{-1}\text{M}^{-1})$	$0.0009 \times 10^6$	$0.0006 \times 10^6$	$0.0003 \times 10^6$
$k_{\text{off}} (\text{s}^{-1})$	0.01	0.007	0.007
$K_A (\text{M}^{-1})$	$0.09 \times 10^6$	$0.08 \times 10^6$	$0.04 \times 10^6$
$K_D (\text{M})$	$11 \times 10^{-6}$	$11 \times 10^{-6}$	$23 \times 10^{-6}$

The half maximal inhibitory concentration toward purified sGC are respectively 3  $\mu\text{M}$  and 5  $\mu\text{M}$  for the compounds **7** and **8**. In HUVEC cells, half maximal inhibitory concentration ( $\text{IC}_{50}$  (**5**) = 28  $\mu\text{M}$ ,  $\text{IC}_{50}$  (**7**) = 10  $\mu\text{M}$ ,  $\text{IC}_{50}$  (**8**) = 13  $\mu\text{M}$ ) were increased for both compounds (Figure 21A, Table 10) compared to  $\text{IC}_{50}$  *in vitro*. Half maximal inhibitory concentration for **7** ( $\text{IC}_{50}$  (**7**) = 15  $\mu\text{M}$ ) and **8** ( $\text{IC}_{50}$  (**8**) = 13  $\mu\text{M}$ ) were not changed in the absence of additional NO in HUVEC cells (Figure 21B).

Interestingly,  $\text{IC}_{50}$  of **7** and **8** decreased in HUVEC compared to HTANQ (**5**), probably because of its better ability to pass through the cell membrane. Obviously, the distribution of OH groups plays a role. The dipolar nature of the O–H bond is such that

hydroxyl is slightly acidic and the unpaired electrons of oxygen make the molecule highly susceptible to bond formation. The reactivity of these groups can facilitate the binding of **5**, **7** and **8** to other compounds and proteins inside the cells, but may also slow down its diffusion through membrane and in cytosol.

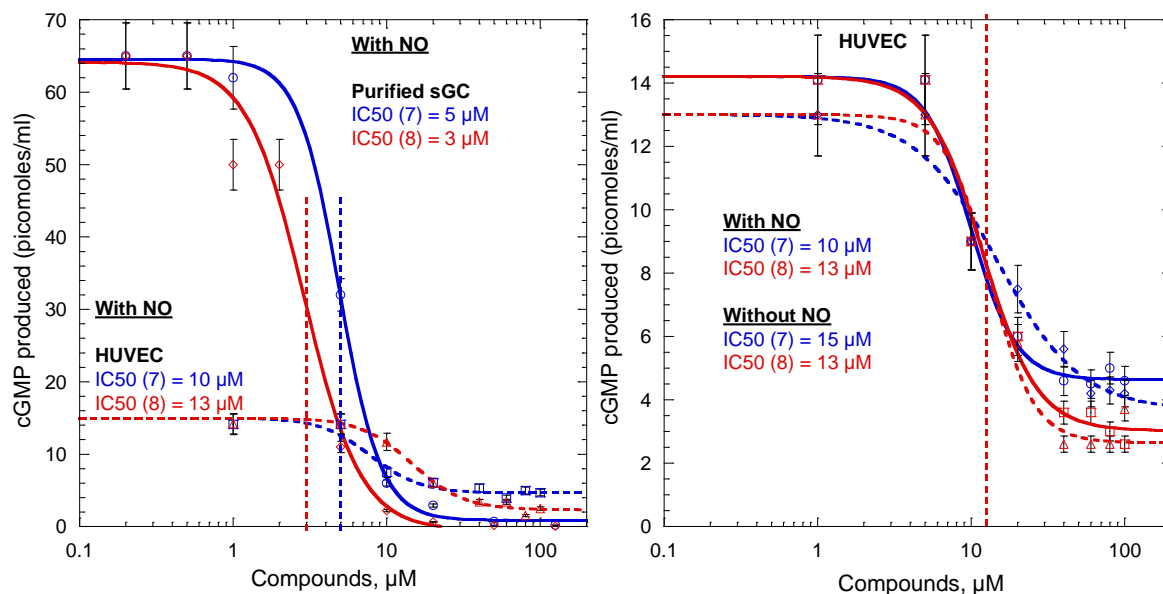


**Figure 21.** Inhibition activity of purified sGC and sGC from HUVEC cells by compounds **7** (HTANQ 537501) and **8**, (HTANQ 537686) (A) in the presence and absence of the NO-donor nitroprusside (300 µM) in the assay buffer (B). Density of cells is  $4 \times 10^4$  cells/mL. Volume of DMSO added 10 µL. The respective  $IC_{50}$  were calculated from the fit of each curve to a sigmoid. Incubation time of cells with (**7**) and (**8**) was 48 h. Incubation performed at 37 °C with CO<sub>2</sub> in the dark. The measurement in duplicates was repeated 2 times.

**Table 10.** Half maximal inhibitory concentration of HTANQ analogues.

Compounds		$IC_{50}$ (µM)	
		Purified sGC	HUVEC
<b>5</b>	HTANQ	$0.2 \pm 0.02$	$28 \pm 2$
<b>7</b>	Amb537501	$5 \pm 0.5$	$10 \pm 2$
<b>8</b>	Amb537686	$3 \pm 0.5$	$13 \pm 2$

The viability of HUVEC cells were measured in the presence of HTANQ 537501 (**7**) and HTANQ 537686 (**8**) during 48 h (Table 11).

After adding **7** and **8** at 60 µM, some cells were detached from the surface of the plate. Density of cells before adding the compounds **7** and **8** was  $5 \times 10^4$  cells/mL, in 24 h and 48 h,  $4 - 3 \times 10^4$  cells/mL. Incubation of cells with **8** during 24 h and 48 h leads to 50% of cell lysis. Up to 60 µM, the inhibitors did not affect the cells. Taken into account that  $IC_{50} \leq 30$  µM for compound **7** and **8**, these concentration do not reach the toxic concentration of the inhibitors.

In conclusion, HTANQ analogues bind to the heme-containing protein from *Nostoc punctiforme* homologous to sGC indicating that they bind to the H-NOX domain of full-length of sGC. Moreover, there is no competition of HTANQ analogues for NO binding site. Both analogues **7** and **8** possess a better ability to inhibit sGC in HUVEC than **5**.

**Table 11.** Density of HUVEC cells incubated with 60  $\mu\text{M}$  of compounds **7** and **8** during 48 h

Compound		Density of HUVEC cells		
		0 h	24 h	48 h
	Control	$5 \times 10^4$ cells / ml normal	$4 \times 10^4$ cells / ml normal	$4 \times 10^4$ cells / ml normal
	2% DMSO	$5 \times 10^4$ cells / ml normal	$4 \times 10^4$ cells / ml normal	$4 \times 10^4$ cells / ml normal
<b>7</b>	Amb537501 (60 $\mu\text{M}$ )	$5 \times 10^4$ cells / ml 95 % normal 5 % detached	$4 \times 10^4$ cells / ml 90 % normal 10 % detached	$4 \times 10^4$ cells / ml 50 % normal 50 % detached
<b>8</b>	Amb537686 (60 $\mu\text{M}$ )	$5 \times 10^4$ cells / ml 90 % normal 10 % detached	$3 \times 10^4$ cells / ml 50 % normal 50 % detached, lysis	$3 \times 10^4$ cells / ml 50 % normal 50 % detached, lysis

Normal: cells are well attached to the surface of plate, detached: cells are detached from the surface of plate, lysis: lysed cells.

## 6 – Properties of the inhibitors

### 6.1 – Heme-oxidized properties of the inhibitors

Because of the compounds **3** – **8** bind to bacterial H-NOX proteins from *Nostoc punctiforme* and *Clostridium botulinum*, we verified their heme-oxidizing properties. The full-length sGC (2  $\mu\text{M}$ ) was incubated with inhibitors **3** – **8** (20  $\mu\text{M}$ ) for two hours and the equilibrium spectra were measured in absence and presence of the inhibitors.

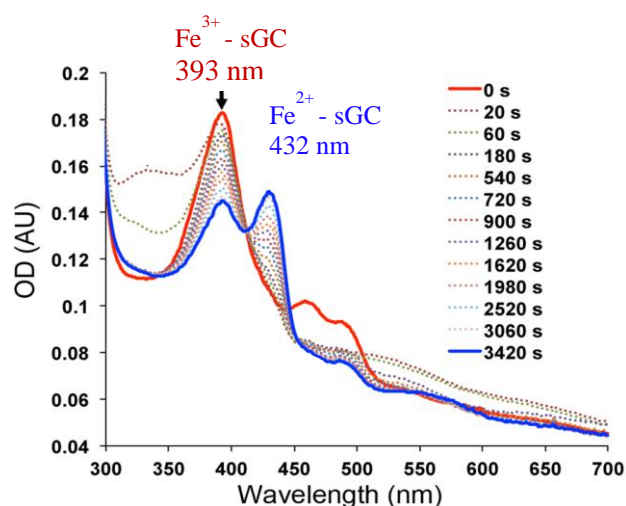


**Figure 22.** Equilibrium spectra of full-length sGC (1  $\mu\text{mol/L}$ ). The band at 393 nm corresponds to oxidized state  $\text{Fe}^{3+}$  of the heme of sGC and the band at 432 nm is due to  $\text{Fe}^{2+}$  heme state of sGC. The graph is taken from reference [28].

The maximum absorbance of the Soret band of full-length sGC at 432 nm is a signature of the ferrous state of the heme ( $\text{Fe}^{2+}$ ) and at 393 nm of the ferric ( $\text{Fe}^{3+}$ ) heme state (Figure 22).

In the absence of inhibitors, sGC has a Soret peak at 432 nm and Q band at 573 nm indicating a  $\text{Fe}^{2+}$  heme state (Figure 23A). Addition of violastystyrene (**4**) to sGC led to the appearance of second Soret peak at 393 nm and shift of Q band to 550 nm indicating the heme-oxidized state ( $\text{Fe}^{3+}$ ) of sGC. In the presence of HTANQ (**5**), a broad increasing shoulder appeared with two bands with maximum at 393 nm and 350 nm, where 393 nm is due to the heme-oxidized state of sGC (Figure 23A) and 350 nm is the contribution of HTANQ spectrum without sGC (Figure 24). Such contribution does not allow to calculate the difference of spectrum of sGC alone with its spectra in the presence of the inhibitor. The Q band was also shifted from ferrous to ferric heme state of sGC in the presence of HTANQ indicating the heme-oxidizing properties of HTANQ.

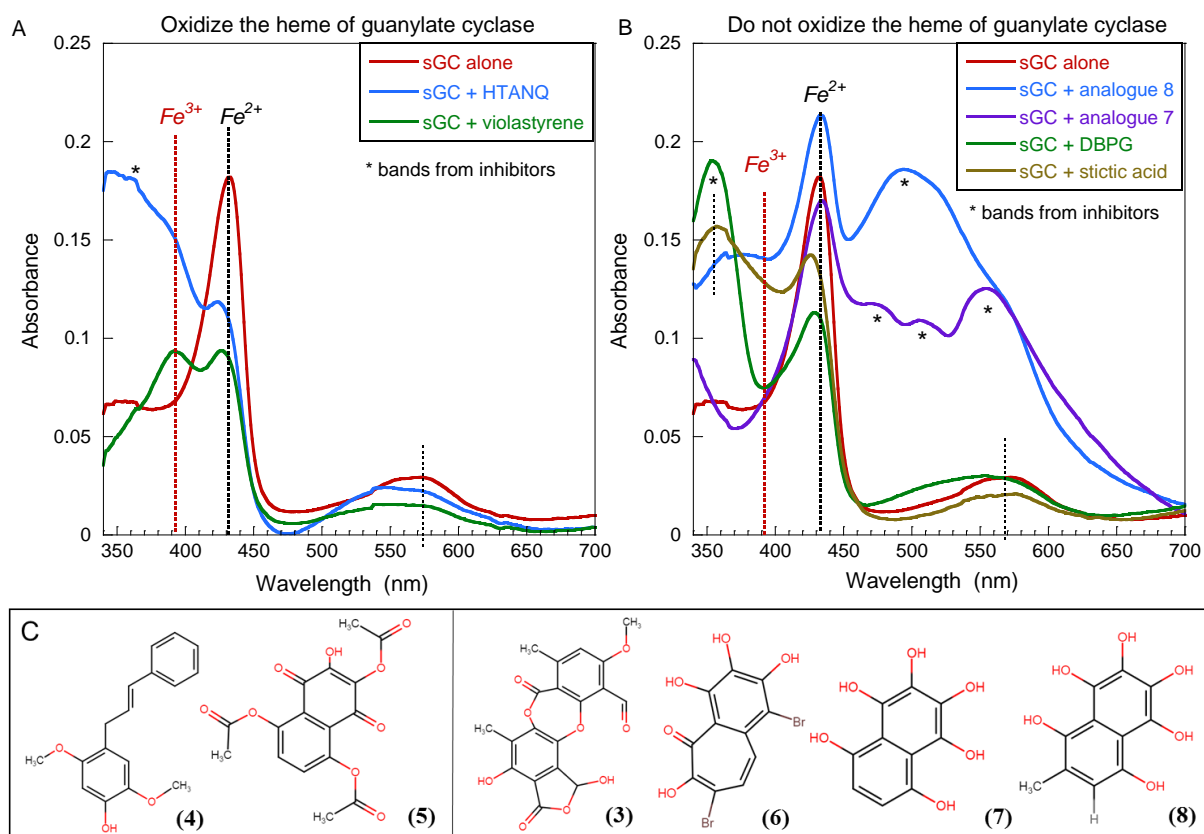


**Figure 23.** Equilibrium spectra of full-length sGC in the absence and presence of the inhibitors. [sGC] = 2  $\mu\text{M}$ , [inhibitors] = 20  $\mu\text{M}$ . Incubation time of inhibitors with sGC before measuring the equilibrium spectra was 2 h. The band at 393 nm corresponds to oxidized state  $\text{Fe}^{3+}$  of the heme of sGC and band at 432 nm to  $\text{Fe}^{2+}$  heme state of sGC. Indication (\*) is a spectral contribution of the inhibitors without sGC (Figure 21). Two inhibitors (violastystyrene (**4**) and HTANQ (**5**)) oxidize the heme of sGC (A) and four other inhibitors (stictic acid (**3**), DBPG (**6**) and analogues of HTANQ, compounds (**7**) and (**8**)) do not oxidize the heme (B). Formulas of the inhibitors (C).

Remarkably, sGC spectra in the presence of HTANQ analogues (**7**) and (**8**) did not show a Soret band at 393 nm ( $\text{Fe}^{3+}$  heme state) compared to HTANQ (**5**) (Figure 23B). Appearance of bands of sGC in the presence of **7** and **8** in Q range are due to spectral contribution of inhibitors (Figure 24). The spectrum of some compounds, for example analogue 7, changed upon binding to sGC (Figure 23B). This is why it is not possible to fully subtract their spectrum in the mixture sGC-inhibitor.

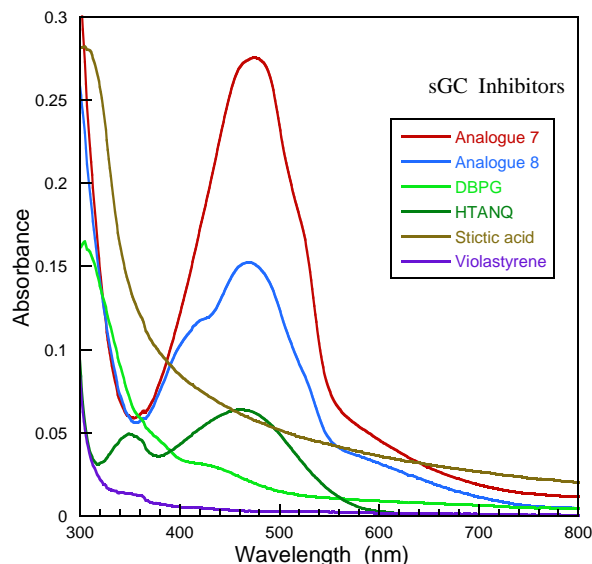


**Figure 24.** Absorption spectra of pure sGC inhibitors in TEA buffer/DMSO 2.5 %. Concentration of all compounds = 20  $\mu\text{M}$ . Optical pathlength = 1 cm.

Analogues of HTANQ (**7** and **8**) do not oxidize the heme of sGC despite their similarity in chemical structure with HTANQ (**5**) (Figure 23C). Spectra of sGC in the presence of stictic acid (**3**) and DBPG (**6**) also do not have Soret band at 393 nm indicating the heme-oxidized state and appearance of bands at 360 nm are again due to spectra of inhibitors without sGC. In section 4.1.3 we demonstrated that hypericin also does not oxidize the heme of sGC.

Thus, we found that violastyrene (**4**) and HTANQ (**5**) oxidize the heme of sGC and the inhibition mechanisms of others compounds (**1 – 3**, **6 – 8**) are still not known.

One of well-studied nonspecific sGC inhibitor acting through heme oxidation is ODQ. There are two mechanisms that could explain the oxidation of sGC heme by ODQ. First, ODQ could bind to sGC and cause a conformational change that increases the affinity of sGC for oxygen. The resulting ferrous oxygen complex might undergo autoxidation to generate ferric heme and superoxide [29]. However, it has been shown that such mechanism is unlikely because anaerobic addition of ODQ to  $\alpha 1(1-385)$  mutant also led to oxidation of the heme [29].

The second mechanism involves transfer of an electron from sGC to ODQ to generate an ODQ radical. In experiment where  $\alpha 1(1-385)$  was mixed with ODQ in an electron

paramagnetic resonance tube and immediately frozen in liquid nitrogen, a signal from a radical was observed [29]. This organic radical is likely an ODQ radical or protein-based radical. Therefore, inhibition of NO-stimulated sGC activity by ODQ is almost certainly due to oxidation of the sGC heme [30].

Chemical structures of ODQ, violastylene (4) and HTANQ (5) do not look similar (Figure 25). Possibly, the oxidation mechanism of the heme of sGC by these inhibitors are different and some experiments are required to answer this question.

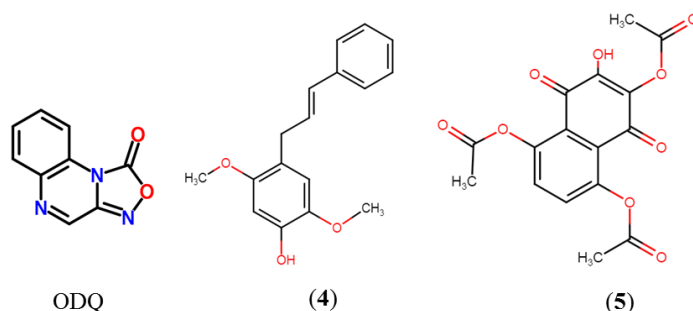


**Figure 25.** Chemical structure of ODQ, violastylene (4) and HTANQ (5)

The overall affinity of NO for ferric hemoproteins is much lower than for ferrous hemoproteins. For example, the  $K_D$  for NO binding to ferrous myoglobin at 20 °C is  $7.0 \times 10^{-12}$  M, while for ferric myoglobin the  $K_D$  is  $2.6 \times 10^{-4}$  M [29, 31]. Thus, oxidation of sGC heme will lead to a lower NO affinity. Ferrous heme in sGC is very stable and resistant to heme loss both in the absence and presence of NO, but the ferric heme in sGC more readily loses its heme.

## 6.2 – Comparison of the identified inhibitors

We have identified a new type of small molecule inhibitors of sGC, which act through allosteric regulation of the enzyme.

The first type of compounds is hypericin and its cognate molecule hypocrellin A (Figure 26).

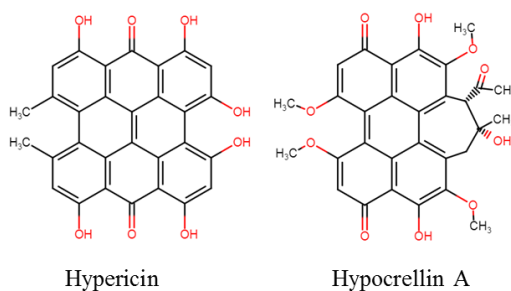


**Figure 26.** Chemical structure of hypericin (1) and hypocrellin A (2).



Violastylene (**4**) and its analogs (**9** – **14**) contain two phenol rings, hydroxyl (OH), oxygen (O) and methyl (CH<sub>3</sub>) groups mostly on one phenol ring (Figure 29).

Surprisingly, analogs of violastylene did not inhibit GC. Subtle differences in the structure of violastylene analogs lead to inactivity of the compound. Violastylene (**4**) has hydroxyl and O–CH<sub>3</sub> groups in positions 3 and 6, but neither on the backbone linking the rings, nor on the upper phenol ring and, possibly, the free positions 2 and 5 have a significant effect for binding and/or inhibiting sGC. In section 6.1 we showed that violastylene oxidizes the heme of guanylate cyclase.

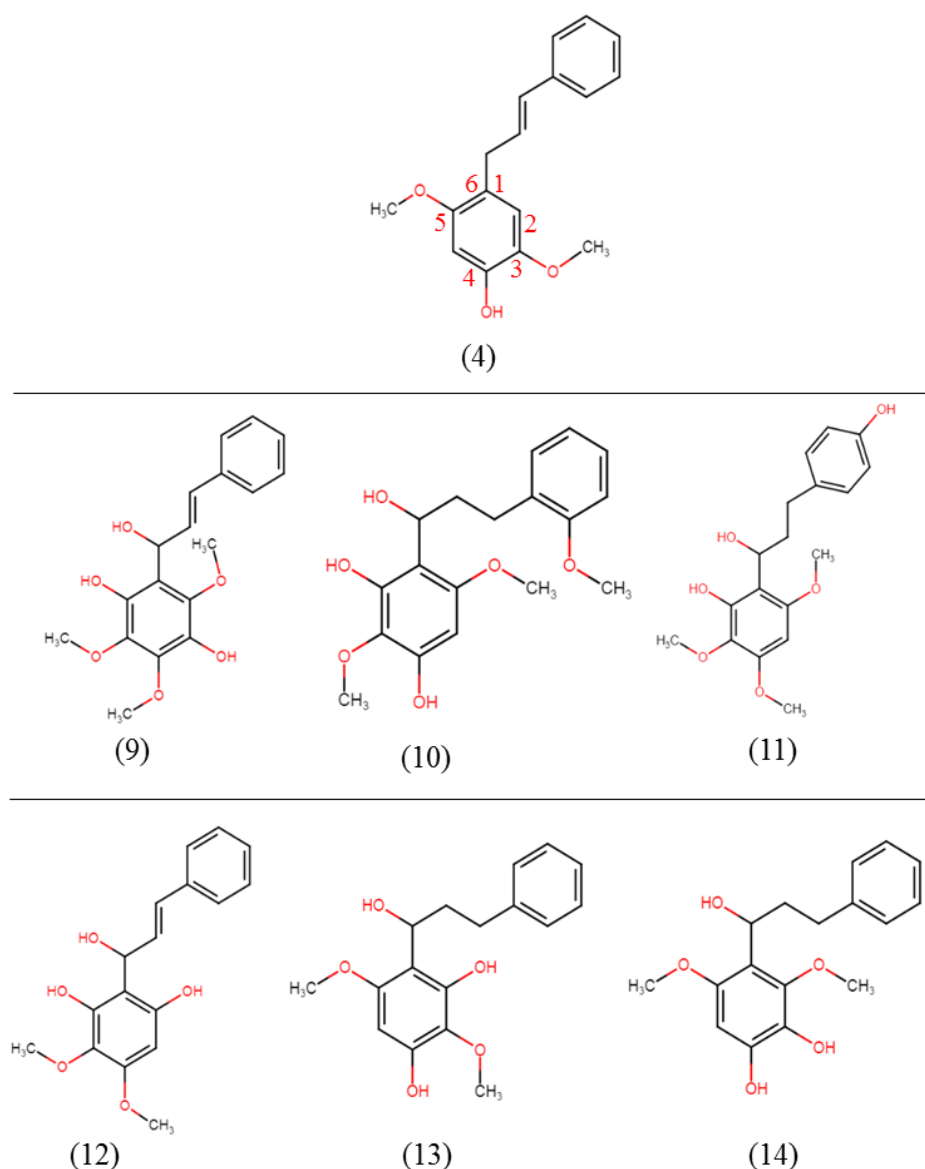


**Figure 29.** Chemical structures of violastylene (**4**) and its analogues (**9** – **14**).

## 7 – Inhibition of angiogenesis

Since sGC is involved in angiogenesis (see CHAPTER II) we aimed at investigating whether the discovered sGC inhibitors could slow down angiogenesis in a model of cells which can develop vessels. The possible inhibition effect of compounds **3**, **5**, **7**, **8** was evaluated on human skin microvascular endothelial cells (HSkMEC) [4, 5] in collaboration with Catherine Grillon and Fabienne Fasani (Center for Molecular Biophysics, Orléans). The experiment was performed under conditions of normoxia in matrigel diluted in medium OptiMEM. This medium has been developed for optimum formation of neo-vessels by HSkMEC whose evolution was recorded during 24 hours with a camera. Images of HSkMEC cells were taken after 5 h and 22 h of incubation with and without the inhibitors (Figure 30).

After 22 h vessels were formed by untreated cells (image c1). First we note that in the presence of 1.25% DMSO only short and scarce vessels between cells were formed (image c2) after 22 h, showing that DMSO precluded full microvascular formation. Because of all studied compounds were solubilized in DMSO at final concentration 1.25%, the real effect of the inhibitors could be difficult to distinguish from the DMSO effect. After 5 h of HSkMEC incubation with inhibitors we see few connections between cells (Figure 30, column b). However some effects observed at 22 h are worthwhile to be reported (Figure 30, column c).

The images at 22 h in the presence of inhibitors must be compared to that with DMSO alone (image c2). For example, hypericin at 10  $\mu\text{M}$  completely inhibited the formation of neo-vessels (image c4 compared to c2). We have measured  $\text{IC}_{50} = 0.4 \mu\text{M}$  for hypericin in HUVEC. We also note that the two analogues of HTANQ (Ambinter 537501 and 537686) inhibited neo-vessels formation at 50 and 35  $\mu\text{M}$  respectively (images c5 and c6 compared to c2). Their  $\text{IC}_{50} = 3 - 5 \mu\text{M}$  in vitro and  $\text{IC}_{50} = 10 - 13 \mu\text{M}$  in HUVEC. No effect was observed for stictic acid at 30  $\mu\text{M}$  (image c3).

In a control experiment we evaluated the effect of DMSO from several suppliers. It demonstrated that the ability of DMSO alone (at concentration up to 1%) to affect microvascular connections from HSkMEC crucially depends on the source of DMSO. Without exploring their precise composition, we attributed this variation to the presence of different impurities between suppliers. There was no effect of DMSO measured on HUVEC cells after 26 h of incubation, showing that the toxicity of DMSO at concentration up to 1.25 % also depends on the cell type. We have selected a DMSO source which do not affect HSkMEC, so that the experiment presented in Figure 26, performed in quadruplicate will be reproduced in optimized conditions.

Since inhibitors targeting the NO/cGMP pathway have effects on angiogenesis [34] this approach is worthwhile to be further explored. However, some side-effects, especially hypertension, may occur but strategies for rescuing the control of vascular tone are being developed [34].

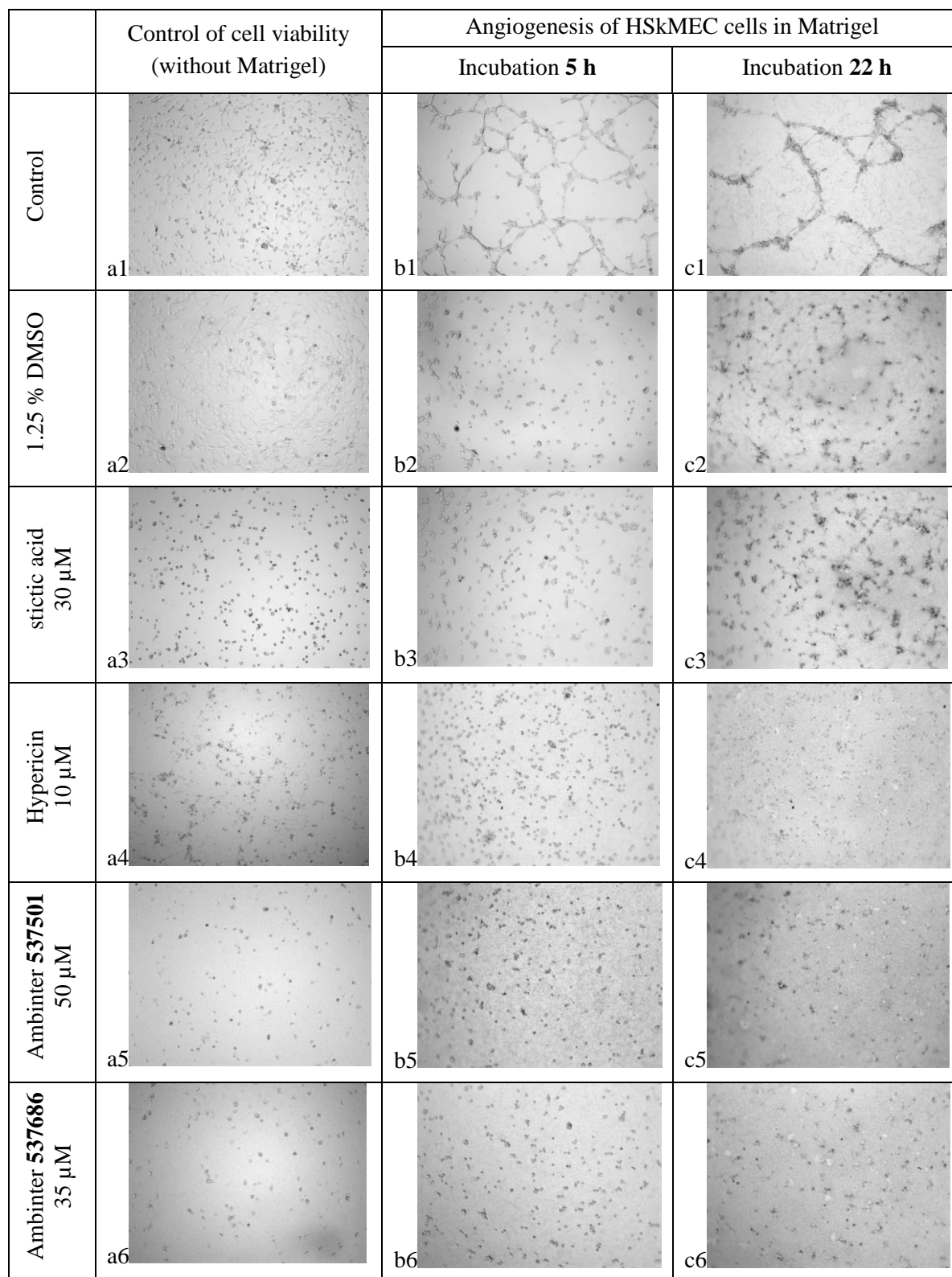


**Figure 30.** Effect of DMSO 1.5%, compounds **1**, **3**, **7** and **8** in DMSO 1.25% on the ability of HSkMEC cells to form microvessels connections.

## 8 – Conclusions

1. Screening of natural compounds from GreenPharma library led to the discovery of four new inhibitors of sGC and their analogues.
2. Hypericin and hypocrellin (two photoactive agents in cancer therapy) were found to be inhibitors of sGC.
3. Hypericin does not have the same binding site as NO, GTP and the stimulator BAY 41-2272 and does not oxidizes the heme of sGC.
4. Two compounds from GreenPharma inhibitors: HTANQ and violastylene act through the heme oxidation of sGC. Four other compounds do not compete with BAY41-2272 and NO for the binding site.
5. Found inhibitors act in low micromolar range on the purified sGC.
6. Analogues of HTANQ had inhibition activity in a similar concentration range as HTANQ, while analogues of violastylene did not inhibit sGC.
7. All these characterized inhibitors of sGC can be used to study NO/cGMP pathway *in vivo* and lead compounds can be derived from their structure.

## 9 – Bibliography

1. Negrerie, M.; Bouzahir, L.; Martin, J. L.; Liebl, U. Control of nitric oxide dynamics by guanylate cyclase in its activated state. *J Biol Chem* **2001**, 276, 46815-21.
2. Wales, J. A.; Chen, C.-Y.; Brecci, L.; Weichsel, A.; Bernier, S. G.; Sheppeck, J. E.; Solinga, R.; Nakai, T.; Renhowe, P. A.; Jung, J.; Montfort, W. R. Discovery of stimulator binding to a conserved pocket in the heme domain of soluble guanylyl cyclase. *Journal of Biological Chemistry* **2017**.
3. Dubinsky, L.; Krom, B. P.; Meijler, M. M. Diazirine based photoaffinity labeling. *Bioorganic and Medicinal Chemistry*. **2012**, 20, 554-570.
4. Carreau, A.; Kieda, C.; Grillon, C. Nitric oxide modulates the expression of endothelial cell adhesion molecules involved in angiogenesis and leukocyte recruitment. *Exp Cell Res* **2011**, 317, 29-41.
5. Collet, G.; Szade, K.; Nowak, W.; Klimkiewicz, K.; El Hafny-Rahbi, B.; Szczepanek, K.; Sugiyama, D.; Weglarczyk, K.; Foucault-Collet, A.; Guichard, A.; Mazan, A.; Nadim, M.; Fasani, F.; Lamerant-Fayel, N.; Grillon, C.; Petoud, S.; Beloeil, J. C.; Jozkowicz, A.; Dulak, J.; Kieda, C. Endothelial precursor cell-based therapy to target the pathologic angiogenesis and compensate tumor hypoxia. *Cancer Lett* **2016**, 370, 345-57.
6. Sauviat, M. P.; Colas, A.; Chauveau, M. J.; Drapier, J. C.; Negrerie, M. Hypericin activates L-type Ca<sup>2+</sup> channels in cardiac myocytes. *J. Nat. Prod.* **2007**, 70, 510-514.
7. Miskovsky, P. Hypericin - A New Antiviral and Antitumor Photosensitizer: Mechanism of Action and Interaction with Biological Macromolecules. *Current Drug Targets*. **2002**, 3, 55-84.
8. Galeotti, N.; Vivoli, E.; Bilia, A. R.; Vincieri, F. F.; Ghelardini, C. Reduces neuropathic pain through a hypericin-mediated inhibition of the protein kinase C gamma and epsilon activity. *Biochem. Pharmacol.* **2010**, 79, 1327-1336.

9. Foster, B. C.; Sockovie, E. R.; Vandenhoeck, S.; Bellefeuille, N.; Drouin, C. E.; Krantis, A.; Budzinski, J. W.; Livesey, J.; Arnason, J. T. In Vitro Activity of St. John's Wort Against Cytochrome P450 Isozymes and P-Glycoprotein. *Pharmaceutical Biology*. **2004**, 42, 159-169.
10. Pajonk, F.; Scholber, J.; Fiebich, B. Hypericin—an inhibitor of proteasome function. *Cancer Chemotherapy and Pharmacology* **2005**, 55, 439-446.
11. Dang, L.; Seale, J. P.; Qu, X. Effects of hypocrellin A on expression of vascular endothelial growth factor and endothelin-1 in human umbilical endothelial cells. *Am J Chin Med* **2007**, 35, 713-23.
12. BioActivity Data for Compound hypericin *PubChem BioAssay*, <http://pubchem.ncbi.nlm.nih.gov/assay/assay.cgi?cid=5281051>.
13. BioActivity Data for Compound hypocrellin A *PubChem BioAssay*, <https://pubchem.ncbi.nlm.nih.gov/compound/14502645>.
14. Lohézic-Le Dévéhat, F.; Tomasi, S.; Elix, J. A.; Bernard, A.; Rouaud, I.; Uriac, P.; Boustie, J. Stictic Acid Derivatives from the Lichen *Usnea articulata* and Their Antioxidant Activities. *Journal of Natural Products* **2007**, 70, 1218-1220.
15. Correche, E. R.; Enriz, R. D.; Piovano, M.; Garbarino, J.; Gomez-Lechon, M. J. Cytotoxic and apoptotic effects on hepatocytes of secondary metabolites obtained from lichens. *Altern Lab Anim* **2004**, 32, 605-15.
16. Wassman, C. D.; Baronio, R.; Demir, Ö.; Wallentine, B. D.; Chen, C.-K.; Hall, L. V.; Salehi, F.; Lin, D.-W.; Chung, B. P.; Wesley Hatfield, G.; Richard Chamberlin, A.; Luecke, H.; Lathrop, R. H.; Kaiser, P.; Amaro, R. E. Computational identification of a transiently open L1/S3 pocket for reactivation of mutant p53. *Nat Commun* **2013**, 4, 1407.
17. Bioactivity Data for Compound VIOLASTYRENE [CID: 5458526]. *PubChem BioAssay*, <https://pubchem.ncbi.nlm.nih.gov/assay/bioactivity.html?cid=5458526>.
18. Youngren, J. F.; Gable, K.; Penaranda, C.; Maddux, B. A.; Zavodovskaya, M.; Lobo, M.; Campbell, M.; Kerner, J.; Goldfine, I. D. Nordihydroguaiaretic acid (NDGA) inhibits the IGF-1 and c-erbB2/HER2/neu receptors and suppresses growth in breast cancer cells. *Breast Cancer Res Treat* **2005**, 94, 37-46.
19. Strong, R.; Miller, R. A.; Astle, C. M.; Floyd, R. A.; Flurkey, K.; Hensley, K. L.; Javors, M. A.; Leeuwenburgh, C.; Nelson, J. F.; Ongini, E.; Nadon, N. L.; Warner, H. R.; Harrison, D. E. Nordihydroguaiaretic acid and aspirin increase lifespan of genetically heterogeneous male mice. *Aging Cell* **2008**, 7, 641-50.
20. Burger, A. Chapter 28 The Benzylisoquinoline Alkaloids. In *The Alkaloids: Chemistry and Physiology*, Manske, R. H. F.; Holmes, H. L., Eds. Academic Press: 1954; Vol. 4, pp 29-75.
21. Delaey, E. M.; Obermuëller, R.; Zupkó, I.; De Vos, D.; Falk, H.; De Witte, P. A. M. In Vitro Study of the Photocytotoxicity of Some Hypericin Analogs on Different Cell Lines. *Photochemistry and Photobiology* **2001**, 74, 164-171.
22. Theodossiou, T. A.; Noronha-Dutra, A.; Hothersall, J. S. Mitochondria are a primary target of hypericin phototoxicity: Synergy of intracellular calcium mobilisation in cell killing. *The International Journal of Biochemistry & Cell Biology* **2006**, 38, 1946-1956.
23. Russell, M. A.; M., N. Expression and functional roles of guanylate cyclase isoforms in BRIN-BD11  $\beta$ -cells. *Islets*. **2010**, 374-382.
24. Mendeleev, N. N.; Verietta, S. W.; Tulis, D. A. Anti-growth properties of BAY 41-2272 in vascular smooth muscle cells. *J Cardiovasc Pharmacol*. **2009**, 121-131.
25. Purohit, R.; Fritz, B. G.; The, J.; Issaian, A.; Weichsel, A.; David, C. L.; Campbell, E.; Hausrath, A. C.; Rassouli-Taylor, L.; Garcin, E. D.; Gage, M. J.; Montfort, W. R. YC-1 Binding to the  $\beta$  Subunit

of Soluble Guanylyl Cyclase Overcomes Allosteric Inhibition by the  $\alpha$  Subunit. *Biochemistry*. **2014**, 53, 101-114.

26. Hames, D.; Hooper, N. Enzyme kinetics. *Biochemistry* **2005**, 100.

27. Wales, J. A.; Cheng-Yu Chen; Brecci, L.; Weichsel, A.; Bernier, S. G.; Sheppeck, J. E.; Jung, J.; Renhowe, P. A.; Montfort, W. R. Localizing Stimulator Binding to the  $\hat{\text{P}}^21$  H-NOX Domain of Soluble Guanylate Cyclase. *Protein Science* **2016**.

28. Rahaman, M. M.; Nguyen, A. T.; Miller, M. P.; Hahn, S. A.; Sparacino-Watkins, C.; Jobbagy, S.; Carew, N. T.; Cantu-Medellin, N.; Wood, K. C.; Baty, C. J.; Schopfer, F. J.; Kelley, E. E.; Gladwin, M. T.; Martin, E.; Straub, A. C. Cytochrome b5 Reductase 3 Modulates Soluble Guanylate Cyclase Redox State and cGMP Signaling. *Circ Res* **2017**, 121, 137-148.

29. Zhao, Y. D.; Brandish, P. E.; Di Valentin, M.; Schelvis, J. P. M.; Babcock, G. T.; Marletta, M. A. Inhibition of soluble guanylate cyclase by ODQ. *Biochemistry* **2000**, 39, 10848-10854.

30. Campbell, M. G.; Underbakke, E. S.; Potter, C. S.; Carragher, B.; Marletta, M. A. Single-particle EM reveals the higher-order domain architecture of soluble guanylate cyclase. *Proceedings of the National Academy of Sciences* **2014**, 111, 2960-2965.

31. Cooper, C. E. Nitric oxide and iron proteins. *Biochim Biophys Acta* **1999**, 1411, 290-309.

32. Jung, J.; Wales, J. A.; Chen, C. Y.; Brecci, L.; Weichsel, A.; Bernier, S. G.; Solinga, R.; Sheppeck, J. E.; Renhowe, P. A.; Montfort, W. R. Discovery of a conserved stimulator binding pocket in soluble guanylate cyclase. *cGMP: generators, effectors and therapeutic implications*. **2017**, 95-96.

33. Mota, F.; Gane, P.; Hampden-Smith, K.; Allerston, C. K.; Garthwaite, J.; Selwood, D. L. A new small molecule inhibitor of soluble guanylate cyclase. *Bioorg Med Chem* **2015**, 23, 5303-10.

34. Isenberg, J. S.; Martin-Manso, G.; Maxhimer, J. B.; Roberts, D. D. Regulation of nitric oxide signaling by thrombospondin-1: implications for anti-angiogenic therapies. *Nature reviews. Cancer* **2009**, 9, 182-194.

---



---

**CHAPTER IV**  
**THE MECHANISM OF ACTION OF sGC ACTIVATORS**

**SYNOPSIS**

---

<b>1 – Methodology .....</b>	<b>102</b>
<b>2 – Materials and methods.....</b>	<b>103</b>
2.1 – Activation constant of activators in purified sGC ( <i>in vitro</i> ).....	103
2.2 –Activity of sGC under influence of ILQG in HUVEC cells .....	105
2.3 – Time-resolved measurement of CO dynamics .....	105
A. Preparation of the samples .....	105
B. Spectral analysis .....	107
<b>3 – Quantifying the activation .....</b>	<b>107</b>
3.1 – Activation of sGC by BAY-412272 in the presence of different CO donors .....	107
3.2 – Riociguat (BAY 63-2521) interaction with purified sGC .....	109
3.3 – Effect of isoliquiritigenin on sGC .....	110
<b>4 – Mechanism of action of sGC activators.....</b>	<b>113</b>
4.1 – Time-resolved spectroscopy for probing allostery in sGC.....	113
4.1.1 – The Spectral Components .....	114
4.1.2 – The Kinetics of CO .....	116
4.1.3 – Interpretation of the transient spectral components with their time constant ...	117
4.2 – Mechanistic model and activation efficiency of the allosteric effectors .....	119
4.3 – Modeling the binding of activators .....	122
<b>5 – Conclusions .....</b>	<b>123</b>
<b>6 – Bibliography .....</b>	<b>123</b>

---

## 1 – Methodology

Due to the high potential of sGC as a pharmacological target, specific activators were keenly searched and discovered: one of them was recently medically approved (Adempas, Bayer). These compounds have revealed the existence of an allosteric site on sGC. In particular, the NO-independent activators YC-1, BAY 41-2272 and the cognate compound riociguat (BAY 63-2521) induce the activation of sGC *in vitro* and *in vivo*, however, there is no consensus on their mode of action on sGC at the molecular level. Using activators in synergy with CO stimulates sGC at similar levels to that obtained by NO alone.

This chapter is devoted to the study of the mechanism of sGC activation by riociguat in the presence of and absence of CO, which was measured for the first time. The activity of riociguat was reported only *in vivo* in several cell lines by Bayer's researchers, in the presence and absence of NO. We studied the structural transition induced in sGC by riociguat in synergy with CO using transient absorption spectroscopy in order to demonstrate conformational changes at the heme level. We analyzed the transient spectra to demonstrate quantitatively whether or not the drug activator riociguat induces the breaking of the Fe-His bond as does NO, the natural effector of sGC. There is already a qualitative indication from steady-state Raman [1] that the cognate compound YC1 may facilitate the breaking of the Fe-His. Does the drug riociguat act as YC1? It is mandatory to precisely quantify the proportion of bond breaking during the activation by activators in synergy with CO, especially by riociguat which is commercialized. We must note that the steady-state absorption spectra do not allow to answer this question, so that we choose to measure by time-resolved absorption spectroscopy the exact amount of sGC 5-coordinate CO-bound heme (5c-CO). Because riociguat and CO act in synergy, this chemical form of the heme is hypothesized to correspond to activated sGC. The two forms 6c-CO and 5c-CO were never distinguished so far and our leading idea is to distinguish their photo-products after CO photodissociation. The photodissociation of CO should result in two entangled processes that we will separate:



This strategy necessitates to record transient spectra at various time delays in the picosecond range. We will then quantify the amount of 4c-heme produced from photodissociated 5c-CO. This quantification of 5-coordinate with CO and 6-coordinate with CO heme species will be performed by spectral component analysis of the data matrix *time* × *wavelength* containing transient spectra of CO-bound sGC in the presence of riociguat, in both 5- and 6-coordination states. The analysis of data matrix will allow to disentangle the spectral components and the associated kinetic components. The novelty of the method is that data are analyzed using singular value decomposition (SVD, see details in Chapter VII) to obtain and quantify a spectral signature. The purpose of SVD analysis is to obtain the exact

amplitude of the transient spectra, and thus the exact contribution of the  $5c\text{-CO} \rightarrow 4c$  photodissociation process, which will give the proportion of Fe-His bond breaking. These amplitudes will be correlated to sGC enzymatic activity. The results will confirm (or reject) the working hypothesis as whether the activator favor or not the cleavage of the Fe-His bond. Based on the data obtained, we propose a mechanistic model of sGC activation by the stimulators.

In addition, we aimed at verifying whether the mechanism of isoliquiritigenin (ILQG), which is sold by several chemical companies as a sGC activator and was used as such in several studies [2-4], was similar to that of the activators of the YC1 family. In particular, it was shown that ILQG induces vascular smooth muscle relaxations in rat aorta via activation of the sGC / cGMP pathway [2, 3]. However, ILQG was never reported to have an action on purified sGC.

## 2 – Materials and methods

Similarly with the study of inhibitors, the "*in vitro*" measurements were performed with the purified protein, whereas the "*in vivo*" experiments refer to those performed in the present work with HUVEC living cells. This may differ from some published articles, especially those of the Bayer company reporting pharmacokinetic data, where "*in vivo*" refer to experiments with animals.

### 2.1 – Activation constant of activators in purified sGC (*in vitro*)

For activity measurements we used recombinant purified full-length human sGC from ENZO company and for spectroscopy overexpressed human sGC from Pr. Emil Martin (Internal Medicine, University of Texas, Houston, USA). The sGC from Pr. Emil Martin was purified from *Sf9* cells as described [5] and kept at  $-80\text{ }^{\circ}\text{C}$  in 20 % glycerol with DTT. The activators BAY 41-2272 (from ENZO) and riociguat (from MedChemExpress) and isoliquiritigenin (from Sigma-Aldrich) were diluted in DMSO at the desired concentration. sGC was resuspended in TEA buffer (triethanolamine 25 mM, NaCl 10 mM, DTT 1 mM, pH 7.4). The activators at increasing concentration were mixed with sGC and incubated in the dark 30 minutes at  $20\text{ }^{\circ}\text{C}$ . In the case of ILQG, increasing concentration of the compound was incubated with or without BAY 41-2272 (0.5 mM) for 30 min. The final concentration of DMSO is 2.5%.

For the immuno-enzymatic assay, sGC (2.5 nM, 5 nM, 10 nM final) was incubated in assay buffer (100  $\mu\text{L}$  final volume) for 10 minutes at  $37\text{ }^{\circ}\text{C}$ . The assay buffer composition was: TEA 100 mM, pH 7.4, DTT 1 mM,  $\text{MnCl}_2$  3 mM, GTP 0.6 mM, creatine phosphate 5 mM, creatine phosphokinase 150 U/L. Depending on the experiment, CO- or NO-donors were added to assay buffer. The CO-donors CORM-3 and CORM-401 were used at 0.1 mM final

concentration and CO gas at a pressure of 1.2 bar yielding a CO concentration of ~1 mM in the aqueous phase at 20 °C. When used, the NO-donor was nitroprusside (NPS) at 0.3 mM. The reaction was stopped by precipitation with Zn acetate and Na<sub>2</sub>CO<sub>3</sub> and 10 μL of supernatant were pipetted for assaying synthesized cGMP from GTP. After this step, the immuno-enzymatic assay was performed according to the ELISA kits (either from Enzo or Biotrak-GEH) instructions with acetylation protocol. A standard curve of known cGMP concentrations was measured simultaneously with each experiment. We must note that the measurement of sGC activity induced by activators is different than in the case of inhibitors, since we expect an increase of cGMP content. Because the colorimetric response of the reagents used is not linear with cGMP concentration we had to determine first the best conditions of assay and we have tested different concentrations of sGC, incubation times, volume of supernatant in the second step and volume of acetylated samples to be pipetted. This is why the method is slightly changed compared to the inhibitors study.

We always performed the assays using several dilutions of sGC samples in order to obtain values within the linear range as a function of log[cGMP] standards, depending on the ELISA kit (Figure 1). The linear range of the measurement corresponds to an absolute amount of 2 to 512 femtomoles of cGMP for one well. Outside of this range there was either saturation of the response or no response. Some assay was not absolute, omitting the cGMP standard and the activity was expressed as a value proportional to the amount of cGMP produced, which is linear to log[cGMP] only within a range of about two orders of magnitude. The points were fitted to the sigmoid curve  $A = A_0 + A_{max} / (([cGMP] / C_{1/2}) + 1)$ .  $A_0$  is the absorbance in absence of cGMP (blank),  $A_{max}$  is the maximum of absorbance, and  $C_{1/2}$  is the cGMP concentration for which  $A = A_{max} / 2$ , defining the middle of the linear range.

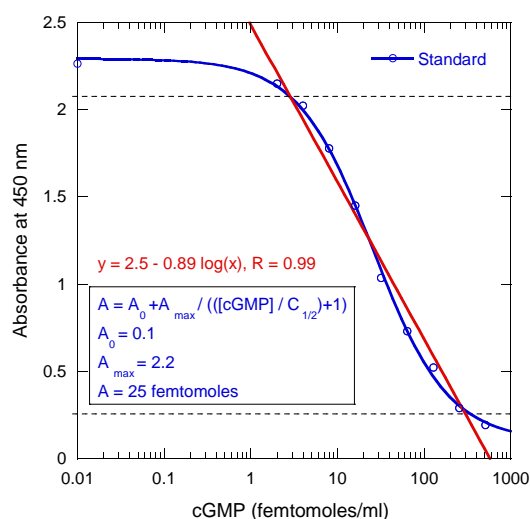


**Figure 1.** cGMP standard curve for acetylated Biotrak assay. Absorption (A) of wells containing the increasing amount of cGMP. This assay must be performed for each different plate coated with antibody anti-cGMP in order to determine the linear zone.

## 2.2 –Activity of sGC under influence of ILQG in HUVEC cells

The full procedure of cell culture and cell harvesting is described in CHAPTER III, section 1.4. Cells were incubated with increasing concentration of ILQG for 2 h in a CO<sub>2</sub> incubator at 36 °C in the dark. Immunoenzymatic assay of cGMP was performed with the Biotrak kit (GE-Healthcare) according to manufacturer's instructions.

## 2.3 – Time-resolved measurement of CO dynamics

### A. Preparation of the samples

The sGC sample was provided by Pr Emil Martin (Internal Medicine, University of Texas, Houston, USA). The full-length sGC was purified from *Sf9* cells as described by Martin *et al.* [5] and kept at –80°C in 20 % glycerol with DTT. For spectroscopy, the buffer was exchanged with TEA 25 mM, pH 7.4, NaCl 25 mM, DTT 1 mM, MnCl<sub>2</sub> 2 mM, glycerol 5 % (centrifugal filter unit Amicon Ultrafree-4, MW cut-off 100 kDa. 4,000 rpm, 10 min). The protein was concentrated to 35 μM and 100 μL were placed in a 1-mm quartz cell (Hellma). As indicated by its spectrum, purified sGC has a ferrous heme with a Soret band maximum at 432 nm (Figure 3) without the need of using a reducing agent. The cell was vacuumed and pure CO was directly introduced in the gas phase (pressure 1.2 bar yielding a CO concentration of ~1 mM in the aqueous phase) and the cell was capped with a second silicon stopper. The Soret band maximum immediately shifted to 424 nm (Figure 3) indicating a 6c-His-CO heme state. The kinetics of CO rebinding after photodissociation was recorded (see below). After addition of riociguat, the same sample was used to investigate its effect. Since the allosteric equilibrium depends upon the occupancy of the catalytic site of sGC [6], we introduced into the cell an aliquot (5 μL) of a non-hydrolyzable analog of GTP, β,γ-Methyleneguanosine 5'-triphosphate (GMPPCP, Sigma M3509) to obtain a final concentration of 1 mM (Figure 2).

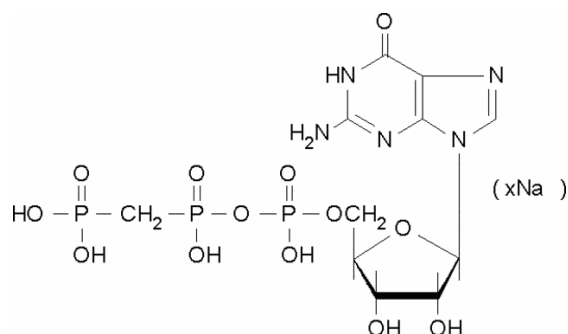


**Figure 2.** The non-hydrolyzable analog of GTP, β,γ-Methyleneguanosine 5'-triphosphate.

Riociguat (obtained from MedChemExpress) was dissolved in DMSO then introduced into the cell (2.5  $\mu\text{L}$ ) to get a final concentration of 300  $\mu\text{M}$  with DMSO at 2.5 %. The sample was incubated 1 hour in the dark. The Soret band maximum shifted to 418 nm, as observed earlier with the activator BAY-412272 [6]. The sample was continuously moved in the laser beam during the measurement performed at 20  $^{\circ}\text{C}$ . The photodissociating pulse wavelength was 564 nm and the probing pulse possesses a broad band spectrum (375 – 550 nm). Both pulses have a time duration of  $\sim 70$  fs. The kinetics of CO rebinding after photodissociation was recorded in the 1 – 600 ps time range by increasing the time delay between the excitation and probe pulses. At each time delay a transient spectrum was recorded in the range 375 – 500 nm. Up to 32 scans were averaged. See the CHAPTER VII, Annex C for a complete description of the set-up used for time-resolved absorption.

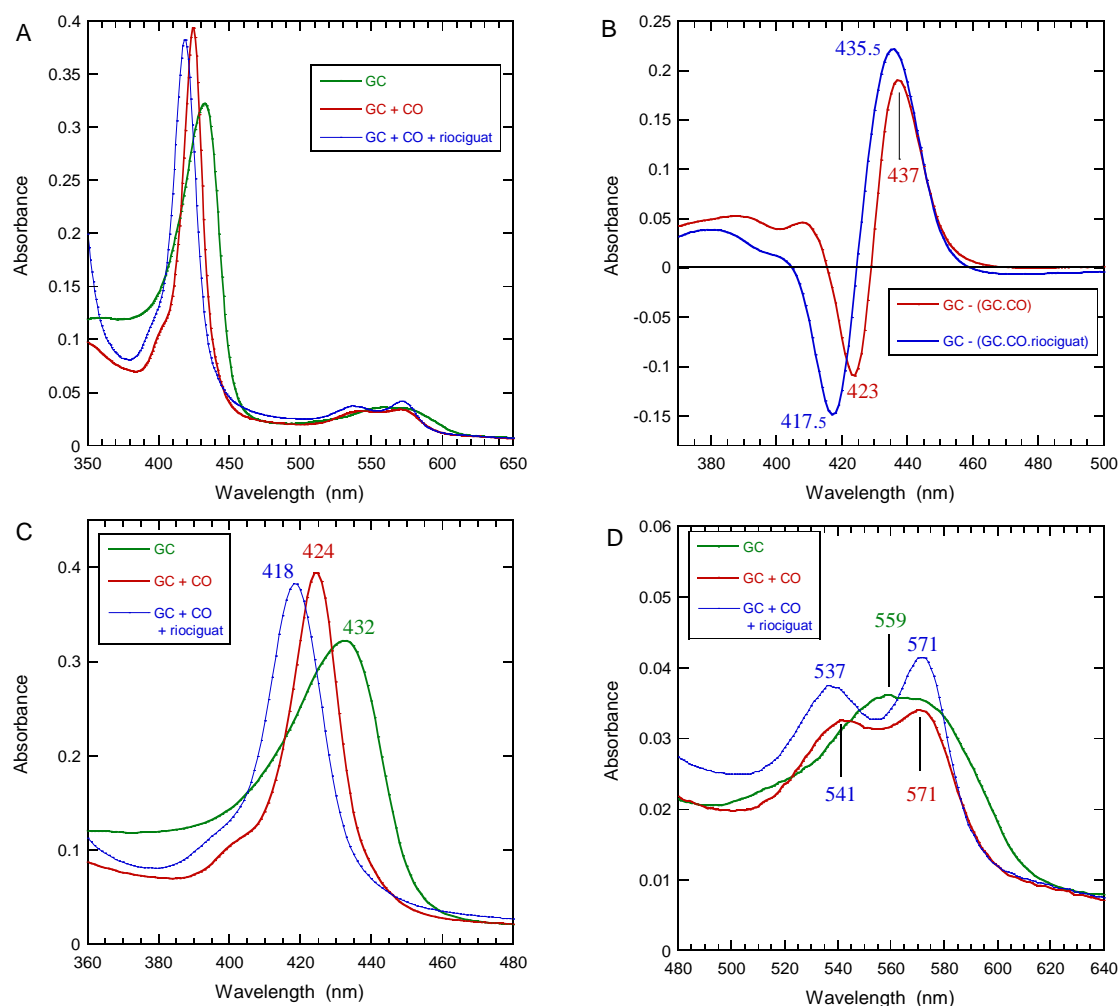


**Figure 3.** (A) Steady-state spectra of sGC as purified (35  $\mu\text{M}$ ), bound with CO (1 mM) and bound with CO in the presence of Riociguat (300  $\mu\text{M}$ ) and the substrate analogue GMPPCP (1 mM). (B) Difference spectra between the unliganded sGC minus the two CO-bound forms. Close-up on the Soret absorption band (C) and on the Q-bands (D). Concentration of sGC is 35  $\mu\text{M}$ . Optical path length is 1 mm. This sample was used for time-resolved measurements.

## B. Spectral analysis

The spectral data were obtained as a *time* × *wavelength* matrix which contains both the spectral and kinetic information. It was analyzed using Singular Value Decomposition (SVD). This mathematical tool allows to separate the spectral components and their evolutions within the data matrix (see CHAPTER VII). Two SVD spectral components with the largest singular value were taken into account because they are associated with meaningful spectra and kinetics. The remaining components however represent noise from several origins, which rough the shape of the plotted data matrix. Two SVD kinetic components were fitted to a multiexponential function:

$$A(t) = A_1 \times \exp(-t/\tau_1) + A_2 \times \exp(-t/\tau_2) + A_3 \times \exp(-t/\tau_3) + A_0$$

## 3 – Quantifying the activation

### 3.1 – Activation of sGC by BAY-412272 in the presence of different CO donors

To measure the activity of sGC as a function of BAY 41-2272 / riociguat concentration in the presence of a saturating concentration of CO, different CO-donors were first tested: CORM-3 (tricarbonylchloro(glycinato)ruthenium(II)) and CORM-401 ( $\text{Mn}(\text{CO})_4$  ( $\text{S}_2\text{CNMe}$  ( $\text{CH}_2\text{CO}_2\text{H}$ ))) and CO gas. The CO-releasing molecules CORM-3 and CORM-401 are fully water-soluble and have been shown to simulate the bioactivities of gaseous CO including vasodilation [7, 8], protection against organ ischemia-reperfusion injury [7-9] and inhibition of platelet aggregation [10]. The chemical structure of two CORMs are given below. They contain metal (ruthenium and manganese) surrounded by carbonyl (CO) groups as coordinated ligands.

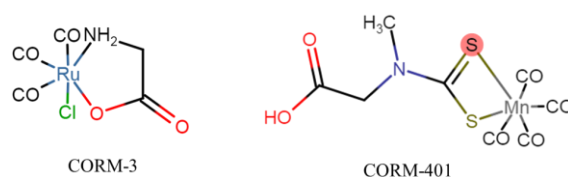


**Figure 4.** Structure of carbon monoxide-releasing molecules: CORM-3 and CORM-401

As was shown from the Mb assay, CORM-3 liberate only one equivalent of CO per mole of compound while CORM-401 liberates three equivalents of CO per mole with different half-live. Whereas CORM-3 has a half-life of 1 min [7], CORM-401 liberates CO at a much slower rate (half-life 21 min) under physiological conditions [11]. With the aim of

avoiding the use of CO gas in each assay tubes, we tried both CORMs compounds, alone and simultaneously.

Figure 5 shows cGMP production by sGC stimulated by increasing concentration of BAY 41-2272 in the presence of CO-donors. CORM-401 has a higher activation efficiency toward sGC, despite a slower half-life for CO release. Its use provided the lowest measured  $EC_{50} = 0.07 \pm 0.05 \mu\text{M}$  for BAY 41-2272 (Figure 5A), compared to CORM-3 which yielded an  $EC_{50} = 3.6 \pm 0.1 \mu\text{M}$ . As a control we performed a cooperative incubation of both CO donors to stimulate sGC (CORM-3, CORM-401 and CO gas together) which resulted in  $EC_{50} = 0.7 \pm 0.1 \mu\text{M}$ .

We then used CO gas alone (absence of CO-donors) which activates synergistically sGC with BAY 41-2272 to yield  $EC_{50} = 0.2 \pm 0.05 \mu\text{M}$  for the activator (Figure 5B), close to the value obtained with CORM-401. We concluded that the CO-donor CORM-3 precluded the full activation of sGC, even in the presence of CO gas. As a hypothesis, CORM-3 binds to the heme, resulting in partial activation even if CO is released. This population of sGC cannot be activated by BAY 41-2272 in synergy with CO, shifting to  $EC_{50}$  larger values. Indeed, if there were a mere CO release, CO donors should not change  $EC_{50}$  for BAY 41-2272 with respect to CO gas, like reported in [12, 13] ( $EC_{50} = 0.3 \mu\text{M}$ ). Variation of  $EC_{50}$  for BAY 41-2272 in presence of CORMs, especially the apparent decrease of BAY 412272 efficacy in presence of CORM-3, can be explained by the interaction of CORM molecule with the heme before CO release, which partially inhibits sGC.

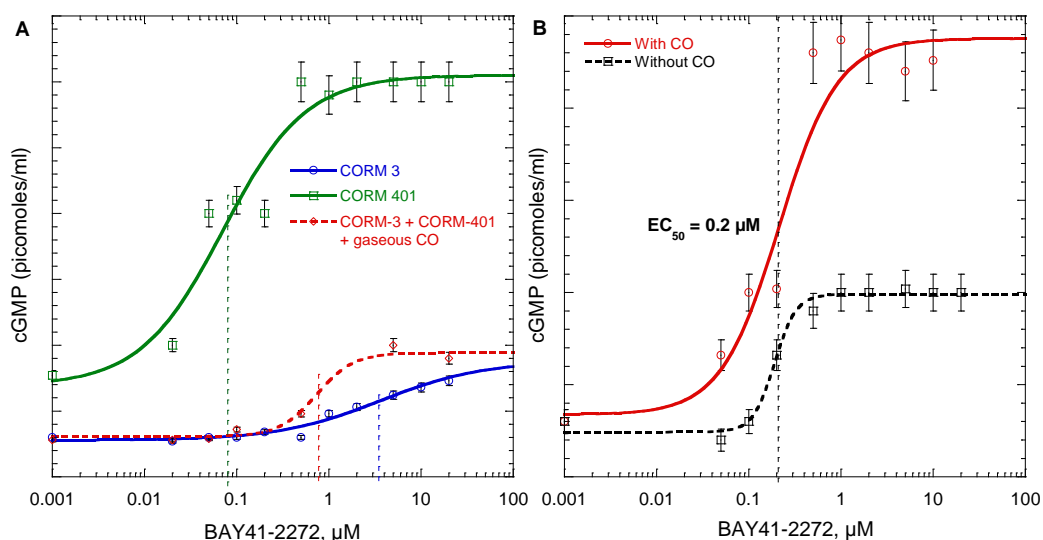


**Figure 5.** (A) cGMP production by sGC in the presence of BAY 41-2272 and different carbon monoxide donors CORM-401, CORM-3 and CORM-3 + CORM-401 + CO gas. (B) Synthesis of cGMP by sGC in the presence or absence of CO gas (100% in gas phase). X-axis is log scale. Final concentration of CO donors is 0.1 mM, [sGC] = 10 nM. Experiments were performed using ENZO kits.

Since we observed many variations with CO-releasing molecules CORMs which do not fully activate sGC compared to CO gas, subsequent experiments were performed using only CO gas to activate sGC in synergy with the allosteric activators.

### 3.2 – Riociguat (BAY 63-2521) interaction with purified sGC

Carbon monoxide (CO) shares with NO a high affinity towards the heme group and binds to sGC, but does not induce the cleavage of the Fe-His bond which is the primary molecular event of sGC activation. Nitric oxide stimulates purified sGC activity up to 200-fold compared with only 4-fold by CO alone [14]. However, CO in synergy with the sGC activator YC-1 stimulates 106-fold [15] and BAY 41-2272 up to 200-fold [16] resulting in enzyme activation similar to that obtained by NO. Riociguat alone stimulates purified sGC activity up to 73-fold [17]. The purified sGC activity as a function of riociguat concentration either in the presence or absence of CO has not been reported yet, a measurement necessary to investigate the activation mechanism of riociguat, so that we measured it.

The experimental protocol for measuring sGC activity in presence of riociguat and CO was adapted with respect to the protocol used for inhibitors. We tested different concentrations of sGC (from 2.5 nM to 25 nM) at different incubation time (from 8 to 10 min) and have found that [sGC] = 5 nM with 8 min of incubation constituted optimal conditions for using the full dynamic range of the immunoenzymatic assay. Such conditions differ from the conditions for the experiments with the inhibitors (see CHAPTER III) because probing increase and decrease of activity with respect to the basal level do not require the same dynamic range. Other methods exist for measuring sGC activity such as use of cGMP labelled with a radioactive isotope. Despite the fact that  $^{32}\text{P}$  labeling method has larger dynamic range to measure cGMP concentration, for practical and safety reasons we preferred to adapt a protocol for immuno-enzymatic assay.

Our results showed that sGC is more activated by riociguat when acting in synergy with CO, therefore sGC maximum activity (picomoles/ml) after 10 minutes in the absence of CO is lower (Figure 6). Half-maximal effective concentration ( $EC_{50}$ ) of riociguat with CO for sGC ( $EC_{50}^{\text{rioc}+\text{CO}} = 0.15 \pm 0.09 \mu\text{M}$ ) was 63 times lower than without CO ( $EC_{50}^{\text{rioc}-\text{CO}} = 9.5 \pm 0.9 \mu\text{M}$ ) (Table 1). This result agrees with those previously reported *in vivo* [18], showing that riociguat in the presence of NO stimulates recombinant sGC in Chinese Hamster Ovary cells with  $EC_{50} = 0.1 - 0.2 \mu\text{M}$ . The same value was obtained *in vitro* on rat sGC, but in absence of CO and NO [17].

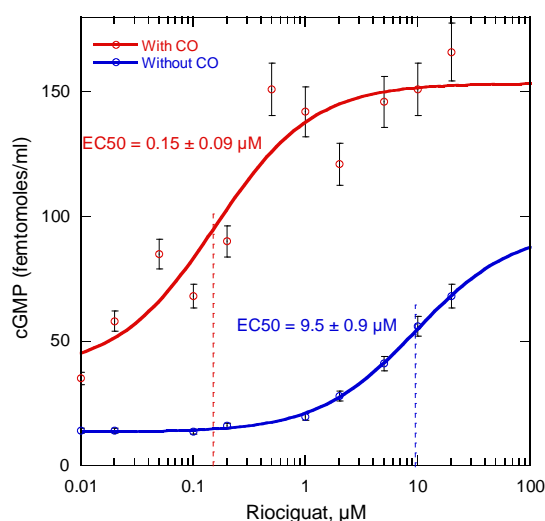


**Figure 6.** cGMP produced by sGC in the presence of riociguat in synergy with CO. [sGC] = 5 nM. Incubation time of sGC with riociguat 30 minutes. EC<sub>50</sub> are reported in Table 1. Activity of sGC was measured with Biotrak GEH kit. Experiment was repeated 4 times. X-axis is log scale.

**Table 1.** EC<sub>50</sub> of two allosteric activators for purified sGC

Activators	EC <sub>50</sub> <sup>+CO</sup> (μM)	EC <sub>50</sub> <sup>-CO</sup> (μM)	Ref.	EC <sub>50</sub> <sup>+NO</sup> (μM)	EC <sub>50</sub> <sup>-NO</sup> (μM)	Ref.
BAY41-2272	<b>0.2 ± 0.01</b>	<b>0.2 ± 0.01</b>	<b>Our work</b>	0.3	0.3	[12, 13]
Riociguat	<b>0.15 ± 0.09</b>	<b>9.5 ± 0.9</b>	<b>Our work</b>	0.1 – 0.2	0.2	[18]

The dependence of riociguat concentration on sGC activity in synergy with CO gave us an important guideline for designing spectroscopic experiment and to elaborate the model of the stimulator binding to sGC. In the case of *in vitro* experiments, EC<sub>50</sub> of riociguat depends on the dissociation constant  $K_D$  but is not necessarily equal to  $K_D$ . In Section 4 of this chapter, we will present the dynamics of CO binding to sGC in the presence of riociguat measured by time-resolved spectroscopy and we will propose a mechanistic and allosteric model of sGC activation in presence of this and cognate activator.

### 3.3 – Effect of isoliquiritigenin on sGC

Isoliquiritigenin [(E)-1-(2,4-dihydroxyphenyl)-3-(4-hydroxyphenyl)prop-2-en-1-one] (Figure 7) is an aromatic compound present in liquorice from the plant *Glycyrrhiza glabra* (febacea). Some physiological actions of isoliquiritigenin (ILQG) have already been described: it may have effect in preventing diabetic complications through inhibition of lens aldose reductase in rat (IC<sub>50</sub> = 320 nM) and sorbitol accumulation in human red blood cells (IC<sub>50</sub> = 2.0 μM) [19]. It also inhibits tyrosinase activities (IC<sub>50</sub> = 8.1 μM) [20] and induces

cell growth inhibition in prostate cancer cell lines (DU145 and LNCaP) [21]. ILQG induces apoptosis of human gastric cancer MGC-803 cells through increasing the intracellular free calcium concentration and decreasing the mitochondrial transmembrane potential [22].

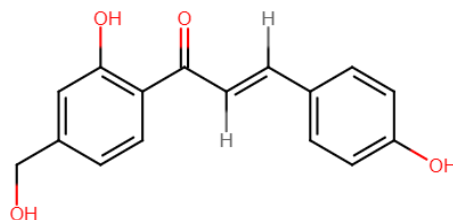


**Figure 7.** Structure of isoliquiritigenin (ILQG)

ILQG is currently sold by several chemical companies as a sGC activator and was used as such in several studies [2-4]. For example, it was shown that ILQG induced a concentration-dependent relaxation of rat aortic rings with  $IC_{50} = 9.4 \mu\text{M}$  and the heme-oxidizing sGC inhibitor ODQ ( $30 \mu\text{M}$ ) did not suppress the effect of ILQG [3]. These results suggest that the effects of isoliquiritigenin are due to sGC activation. However, ILQG was never reported to have an action on purified sGC, but its effect was always reported in cells and tissues, where many partner proteins are also present, especially PDE5. In order to investigate the possibility of allosteric activation and to compare with the activator BAY-412272, we tested its action *in vitro* with purified sGC.

Surprisingly, we have found that ILQG is an inhibitor of purified sGC with  $IC_{50} = 9.5 \pm 0.5 \mu\text{M}$  when activated by NO (Figure 8A and Table 2) in the concentration range 2 – 100  $\mu\text{M}$ . Incubation with 0.5 mM activator BAY 41-2272 in presence or absence of NO-donor did not change the inhibition constant of ILQG ( $IC_{50} = 12.5 \pm 1 \mu\text{M}$  and  $IC_{50} = 9.4 \pm 0.5 \mu\text{M}$  respectively). The sGC activity inhibited by ILQ was increased in the presence of NO with respect to its activity in absence of NO. Such results shows that ILQG does not compete for NO or BAY 41-2272 binding site.

**Table 2.** Inhibition of purified sGC by isoliquiritigenin

Compounds	$IC_{50}$ , $\mu\text{M}$ (purified sGC)
ILQG alone	$9.5 \pm 0.5$
ILQG + BAY 41-2272	$9.4 \pm 0.5$
ILQG + BAY 41-2272 + NO	$12.5 \pm 1$

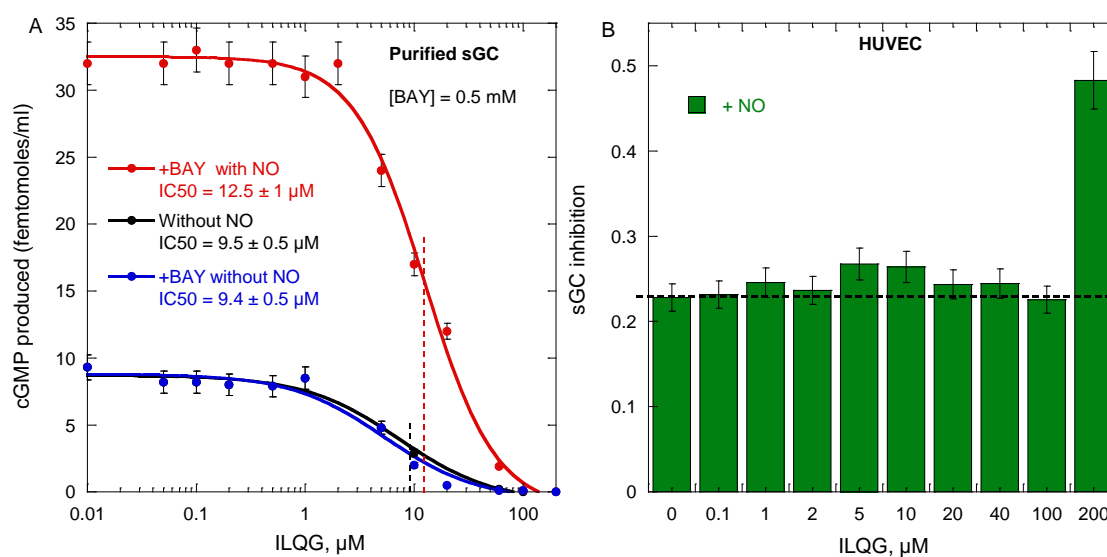


**Figure 8.** (A) Effect of the presence or absence of the sGC activator BAY-412272 on the inhibition of purified sGC by isoliquiritigenin (ILQG). X-axis is log scale. [sGC] = 5 nM, [nitroprusside] = 0.3 mM, [BAY 41-2272] = 0.5 mM. (B) ILQG Inhibition of sGC from HUVEC. Incubation time of cells with ILQG was 2 hours at 37 °C with CO<sub>2</sub> in the dark, [nitroprusside] = 0.3 mM. Dotted horizontal line is basal activity of sGC. Activity was measured with Biotrak kit.

When incubated in HUVEC cells, ILQG did not inhibit activity of sGC up to 100  $\mu\text{M}$  but only at 200  $\mu\text{M}$  (Figure 8B). The dotted horizontal line indicates level of basal sGC activity. The absence of inhibitory effect of ILQG on sGC *in vivo* at concentration lower than 200  $\mu\text{M}$  could be explained by the difficulty of the compound to diffuse through the cell membrane. However we discarded this hypothesis because an effect of ILQG was demonstrated in various kinds of cells in the concentration range 2 – 10  $\mu\text{M}$  [3, 20-22] and ILQG (30  $\mu\text{M}$ ) induced half-maximal relaxation of rat aortic ring after 48 min [3]. We thus made the working hypothesis that ILQG has other targets in cells, therefore the inhibition effect of sGC can start only from 200  $\mu\text{M}$  if cGMP is not (or very slowly) hydrolyzed by phosphodiesterase 5 (PDE5), as proposed in some studies [2]. To test the hypothesis it is necessary to measure the effect of ILQG on purified PDE5 which has never been reported so far. Such activity assays with purified PDE5 are currently under way at LOB.

In some studies ILQG was used as a sGC activator [23, 24] and our finding may impact their conclusions. ILQG has various targets [25, 26] and was demonstrated to exert anti-angiogenic effects [27] but sGC was not considered in this last study. It would be of interest to investigate the effect of sGC inhibitors (CHAPTER III) on the cells used in Ref. [27].

## 4 – Mechanism of action of sGC activators

### 4.1 – Time-resolved spectroscopy for probing allostery in sGC

For the first time, time-resolved measurements of full-length sGC interacting with riociguat in the presence of CO and the GTP analog GMPPCP (Figure 2) were performed. The dynamics of CO and heme coordination changes in the time range 0 – 600 ps after CO photodissociation from sGC are compared in the absence and presence of the activator riociguat (Figure 9). After photodissociation of CO, a negative absorption (bleaching) band, corresponding to the disappearance of CO-bound sGC, appears immediately in the difference transient spectrum (423 nm), together with an induced absorption counterpart at 437 nm due to the appearance of CO-free sGC (Figure 9A). The decrease of intensity of these two bands is due to CO rebinding. In the absence of riociguat, no shift of the isosbestic point (430 nm), of the bleaching minimum (423 nm) and induced absorption band maximum (437 nm) could be observed (Figure 9A). The presence of riociguat induces important changes in the evolution of the transient spectra.

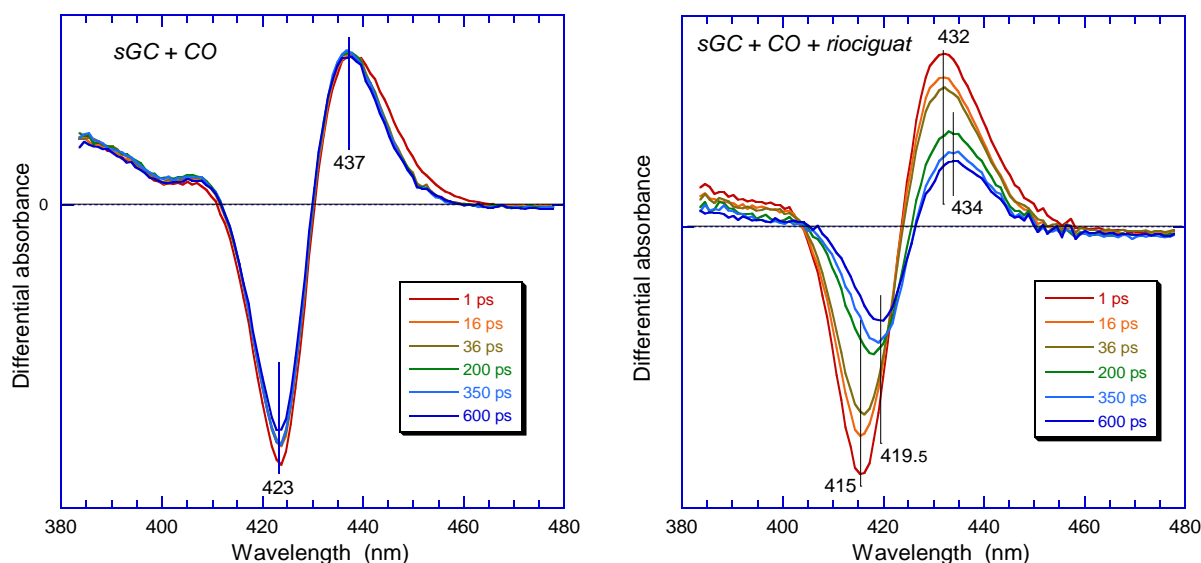


**Figure 9.** Changes in CO dynamics (0-600 ps) within the heme pocket of full-length sGC induced by the activator riociguat. Raw transient absorption spectra of the heme Soret band at selected time delays probing the CO rebinding to the heme after photodissociation in the absence (A) and in the presence of riociguat (B).

In the presence of riociguat, the minimum of the bleaching band shifts from 415 nm to 419.5 nm while the maximum of induced absorption centered at 433 nm decreases with a simultaneous shift from 432 nm to 434 nm at a delay of 566 ps (Figure 9B). Importantly, this spectral change in the presence of riociguat is paralleled by the shift of isosbestic point from

423 nm to 427 nm (Figure 9B), contrastingly with the absence of the activator (Figure 9A). These shifts indicate that two processes are involved in the kinetics and two different heme species are formed after the photodissociation of CO induced by the interaction of the drug riociguat with sGC. A similar observation was obtained in the case of the cognate activator BAY 41-2272 [28], but the effect appears larger with riociguat. This point will be discussed later.

To evaluate each contribution precisely, we performed a singular value decomposition (SVD) of the time-wavelength matrix whose calculation principle is described in CHAPTER VII. We found that the two components with largest singular value correspond to distinct spectral species which convey biological information (Figure 10). SVD does not always strictly separate the simultaneous processes because SVD is a mathematical procedure which only separates orthogonal components. We did not retain other SVD components because they corresponded to correlated noise due to laser instability (producing variations in the excitation pulse intensity) and a slow drift (hours) of the laser pointing (producing variations in the probe pulse intensity). In the presence of riociguat, the first main component SVD1 corresponds to geminate rebinding of CO to the 5c-His heme of sGC, as shown by the minimum of bleaching at 416.5 nm together with the maximum of the induced absorption at 433 nm (Figure 10B) which matches the equilibrium difference (Figure 3B). The spectral component SVD1 was therefore assigned to the formation of 5c-His heme species from 6c-His-CO. In the SVD2 spectrum, the bleaching and induced absorption peaks at different wavelengths represent a contribution of CO rebinding to a different species. We hypothesize that SVD2 can be due to the formation of 4c-heme (at 412 nm) from 5c-heme-CO species (at 423 nm) because its relative amplitude increased largely upon the binding of riociguat to sGC. A difficulty of the assignment is that the spectrum of 6-coordinate heme-CO is not necessarily the same in the presence and absence of riociguat, even if the iron coordination is the same.

#### 4.1.1 – The Spectral Components

##### *1- SVD in absence of riociguat*

In absence of riociguat the major component SVD1 (Figure 10A, red spectrum) matches the shape of the equilibrium difference spectrum  $GC - GC-CO$  (Figure 3B) and is readily assigned to CO photodissociation and rebinding. CO geminate rebinding is observed up to 600 ps, and the constant term  $A_C$  reflects mainly CO exiting from the protein and its subsequent bimolecular rebinding on longer time scale ( $\mu s$  and  $ms$ ).  $A_C$  may also contain slow geminate rebinding components in the upper nanosecond range.

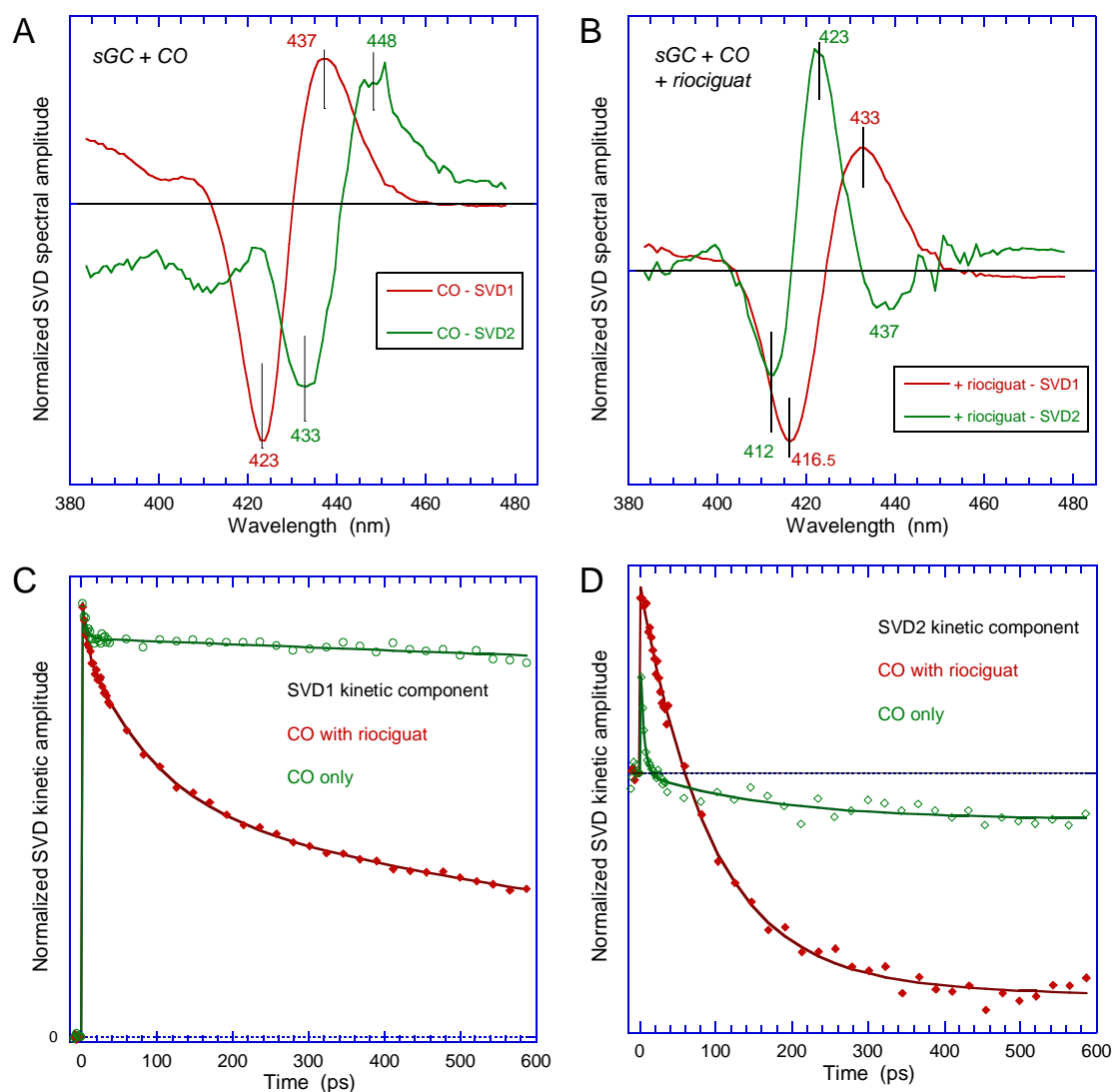


**Figure 10.** Decomposition of the raw data matrix  $time \times wavelength$  of CO dynamics (0 – 600 ps) by SVD method. Two spectral components were obtained in both cases after SVD analysis in the absence of riociguat (**A**) and in the presence of riociguat (**B**) together with their associated kinetic components (**C** and **D**). In **C** and **D** the curves are fits to a using a multiexponential function:  $A_{obs} = \sum_i A_i \times \exp^{-t/\tau_i} + A_c$  ( $i = 1, 2, 3$ ) whose parameters are given in Table 3.

The second minor component SVD2 (Figure 10A, green spectrum) discloses a negative absorption band at 433 nm due to the disappearance of the photo-excited 5-coordinate heme accompanied with an induced absorption band centered at 448 nm. Such shift of the Soret band is assigned to vibrational excitation of the heme [29] and this difference spectrum reflects only heme relaxation which cools down in 5 ps, not CO dynamics. Thus, in absence of riociguat there exists only one process readily assigned to CO dissociation and rebinding:



## 2- SVD in presence of riociguat

In the presence of riociguat the major component SVD1 (Figure 10B) again matches the shape of the equilibrium difference spectrum GC-(riociguat) *minus* GC-(riociguat)-CO (Figure 3B) and is also assigned to CO photodissociation and rebinding. However, since we have hypothesized the presence of a 5-coordinate heme with CO, that-is-to-say with a cleaved His105, this component requires further analysis, as detailed below.

The SDV2 spectral component (Figure 10B) has a complex shape, which does not correspond to any equilibrium difference spectrum. Its interpretation will require also to calculate the transient spectrum of the 4-coordinate heme.

### 4.1.2 – The Kinetics of CO

The kinetics associated with the two main SVD components, which corresponds to CO geminate recombination, are shown in Figure 10C and D. The CO dynamics appear multiphasic throughout the time range and the parameters of the fitting function are presented in Table 3. First observation is that the time constants and corresponding amplitudes are changed after riociguat binding to sGC. We infer that riociguat induces a conformational change of the heme site and heme domain which increases the energy barrier for CO to leave the heme pocket and consequently increases the amplitude of geminate rebinding. Especially, the amount of CO which exits the protein and does not rebind geminately is quantified by the constant term  $A_c$ , which reaches 92 % in absence of riociguat whereas it decreases down to 16 % in the presence of the activator. We observe a fast component (6 ps) in the presence of riociguat which is characteristic of the direct rebinding to a 4-coordinate heme from the distal heme pocket. The amplitude of the intermediate component (90 ps) corresponding to CO rebinding from a docking site is largely increased, again reflecting the change of heme pocket conformation induced by the effector.

**Table 3.** Fit parameters for the SVD kinetics of CO rebinding in Figure 10C and D.

Sample	Component	Singular value	Time constant and <i>amplitude</i>			
			$\tau_1$ $A_1$	$\tau_2$ $A_2$	$\tau_3$ $A_3$	Constant term $A_c$
sGC-CO	SVD1	0.9030	$4.7 \pm 0.2$ ps 0.08	–	–	0.92
	SVD2	0.0240	$5.0 \pm 0.2$ ps 0.60	$180 \pm 20$ ps 0.20	–	0.20
sGC-CO + riociguat	SVD1	0.2937	$6.0 \pm 0.5$ ps 0.06	$90 \pm 5$ ps 0.29	$1550 \pm 40$ ps 0.55	0.10
	SVD2	0.0476	–	$95 \pm 5$ ps 0.65	–	0.35

The mechanistic significance of all rebinding phases are given in Figure 11. The CO dynamics appear multiphasic throughout the entire time range, revealing multiple energy barriers for CO rebinding. The observed phases are assigned to the dynamics of CO in the

heme pocket ( $\tau_1$  and  $\tau_2$ ), CO in docking sites ( $\tau_2$  and  $\tau_3$ ), and bimolecular rebinding  $A_C$  (diffusion from solvent) [6].

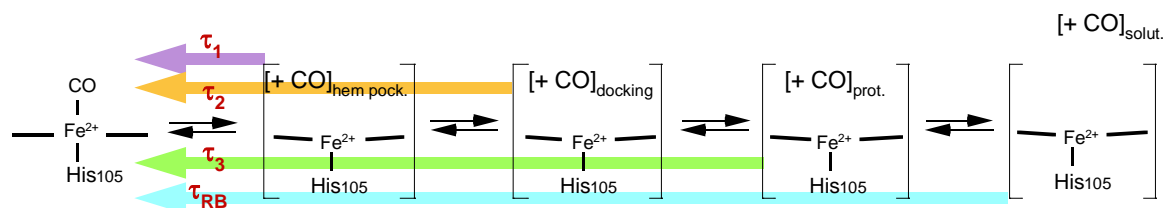


**Figure 11.** Correspondence between the measured time constants and the rebinding of CO to the heme from different states of the protein-ligand system. The subscripts indicate the different positions of CO with respect to the protein: in heme pocket, docking site, protein core, or in solvent, respectively.  $\tau_1$  corresponds to geminate rebinding of CO located in close vicinity of the iron;  $\tau_2$  corresponds to geminate rebinding of CO in a docking site within the heme pocket, whereas  $\tau_3$  corresponds to CO in the entry channel of the protein. These three phases involve the very same CO molecule that was photodissociated. Contrarily, the bimolecular rebinding  $\tau_{RB}$  involves CO in solvent, which corresponds to the constant  $A_C$  in Table 3.

#### 4.1.3 – Interpretation of the transient spectral components with their time constant

One must remind that the SVD spectral components do not necessarily represent an elementary process, but may comprise the transient spectra of processes which are not strictly orthogonal (for example having very close spectra or close time constants). In order to rigorously assign the SVD spectral component after the photodissociation of CO from a 5C-heme in the presence of riociguat, we attempted to calculate the difference spectrum corresponding to the processes. We first obtained the spectrum of the transient 4c-heme from its picosecond measurement after NO photodissociation in sGC (Figure 12) since we know that NO induces the cleavage of Fe-His105 bond:

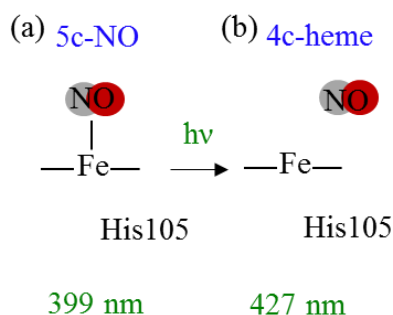


**Figure 12.** Scheme of iron coordination in the heme of sGC: (a) after NO binding to iron and broken of His bond (Fe-5c-NO at 399 nm) and (b) after photodissociation of NO bond from iron (Fe-4c-heme at 427 nm).

Then, the equilibrium spectrum of sGC-CO in the presence of riociguat was subtracted from the 4c-heme spectrum yielding the theoretical difference spectrum of the process.

Remarkably this difference spectrum appears similar with the SVD1 component (Figure 10B) which is consequently assigned to the rebinding of CO to the 4c-heme with time constants  $\tau_2 = 90 \pm 5$  ps and  $\tau_3 = 1550 \pm 40$  ps (Figure 14 a).

The second spectral component SVD2 in presence of riociguat was more difficult to assign. Following the hypothesis of the existence of a 5-coordinate heme-CO (Figure 14a), the cleaved proximal His105 should rebind to the 4c-heme, exactly as demonstrated in the case of NO for sGC [30] and cytochrome c' AXCP [31]. Importantly, the proximal His105 rebinds with a time constants of 70 ps and 100 ps for sGC and AXCP, respectively, after NO dissociation from the 5c-NO heme, and should have similar time constant after CO dissociation.

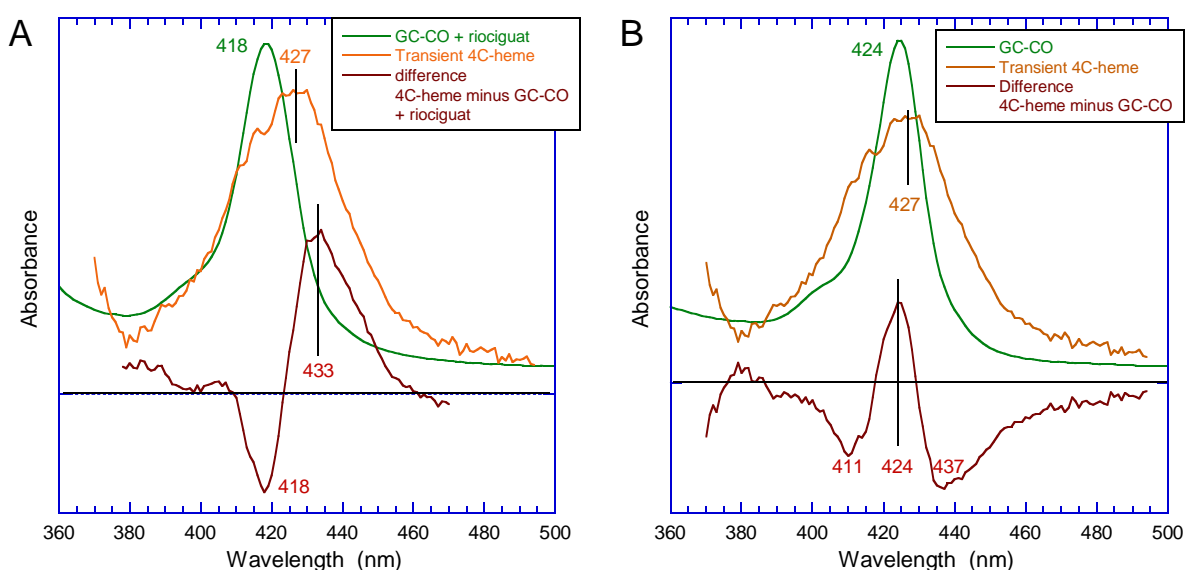


**Figure 13.** Calculation of the absolute spectrum of 4-coordinate heme and of the difference transient spectra of CO-dissociated heme in the presence of riociguat. (A) The equilibrium absorption spectra of CO-bound sGC in the presence of riociguat (green) has been subtracted from the spectrum of the 4c-heme (orange) to yield a difference spectrum (dark red) similar to the SVD1 component in Figure 10B. (B) The equilibrium absorption spectra of CO-bound sGC in the absence of riociguat (green) has been subtracted from the spectrum of the 4c-heme (orange) to yield a difference spectrum (dark red) similar to the SVD2 component in Figure 10B.

We found that the SVD2 spectrum corresponds exactly to the spectral difference 6c-CO in absence of riociguat (424 nm) minus the spectrum of 4c-heme (Figure 13B). Such a process was initially discarded since riociguat was assumed to produce a 5-coordinate heme with CO, not a 6c-heme. However, no other calculated difference between species could reproduce the SVD2 spectrum. Thus, we must conclude that SVD2 spectrum represents the simultaneous rebinding of CO and His105 to the 4C-heme and the subsequent formation of 6c-CO heme (Figure 14b, c). This is possible because CO rebinds more slowly (90 – 180 ps) than NO (7 ps), with same time constant as does His105 [30, 31] and the two processes are

consequently contained in one SVD component due to their very close kinetics, both starting with a 4c-heme:

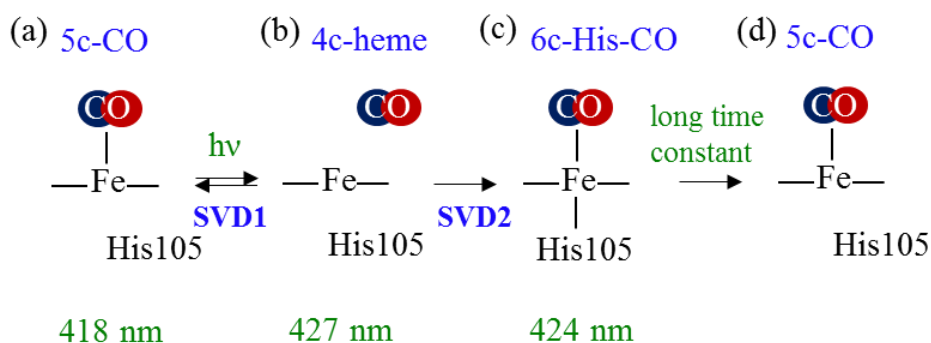


**Figure 14.** Sequence of the heme iron coordination in sGC in the presence of riociguat. (a) 5c-CO at 418 nm; (b) after photodissociation of CO bond from iron (4c-heme at 427 nm); (c) CO and His simultaneously bind to Fe forming 6c-CO. At longer time constant, dissociation of His bound occurs forming 5c-CO species (d).

We must thus conclude that: 1- All processes in the presence of riociguat involve the 5c-CO heme as starting species; 2- The 6-coordinate sGC-CO with bound riociguat cannot be distinguished by its spectrum (424 nm) from 6-coordinate sGC-CO in absence of riociguat. The equilibrium between species is illustrated in the model below (Figure 15).

#### 4.2 – Mechanistic model and activation efficiency of the allosteric effectors

All observed coordination transitions are summarized in a model of heme dynamics in Figure 15. After binding of CO from solution to form the 6c-CO species, the extent of cleavage of the Fe-His bond depends on the presence of the activators, but it depends also on the efficiency of the activators to shift the equilibrium once bound, that we attempted to quantify. Two different activation states of sGC by CO 6c-heme and 5c-heme can exist simultaneously in the presence of the activators (but may be very minor). Thus, the activators increase the proportion of 5c-heme CO, which is negligible in presence of CO alone. Our hypothesis of the allosteric mechanism of sGC activators is as follows: YC-1, BAY 41-2272, and riociguat induce the breaking of the Fe-His bond as does NO, the sGC natural effector, but activators do not act with same efficacy. We quantified the efficacy of the transition toward activated state by using the proportion of 5c-CO / 6-CO heme, which is, in first approximation, equal to the ratio of singular values which is assumed to represent the 5c-CO / 6-CO heme ratio, and that we called "activation factor" ( $\gamma_{act}$ ). This factor  $\gamma_{act}$  is an allosteric parameter, is pharmacologically relevant and represents the ability of an activator to shift the protein to its allosteric activated state. The sGC activators, independently of their  $K_D$ , have different activation factors, in the order:

$$[\gamma_{act}^{YC1} = 0.05] < [\gamma_{act}^{BAY412272} = 0.1] < [\gamma_{act}^{riociguat} = 0.16] \quad (\text{Table 4}).$$

The half maximal effective concentration ( $EC_{50}$ ) of BAY 41-2272 and riociguat in the presence of CO have almost the same value *in vitro* ( $EC_{50}^{BAY41-2272} = 0.2 \mu\text{M}$  and  $EC_{50}^{rioc} = 0.15 \mu\text{M}$ ). Unfortunately,  $K_D$  of riociguat was never reported and we cannot compare with BAY-412272. However, since the activation factor of riociguat is larger than that of BAY-412272, riociguat should appear as a more efficient drug, which is indeed the case when comparing the *in vitro*  $EC_{50}$  either in presence or absence of NO.

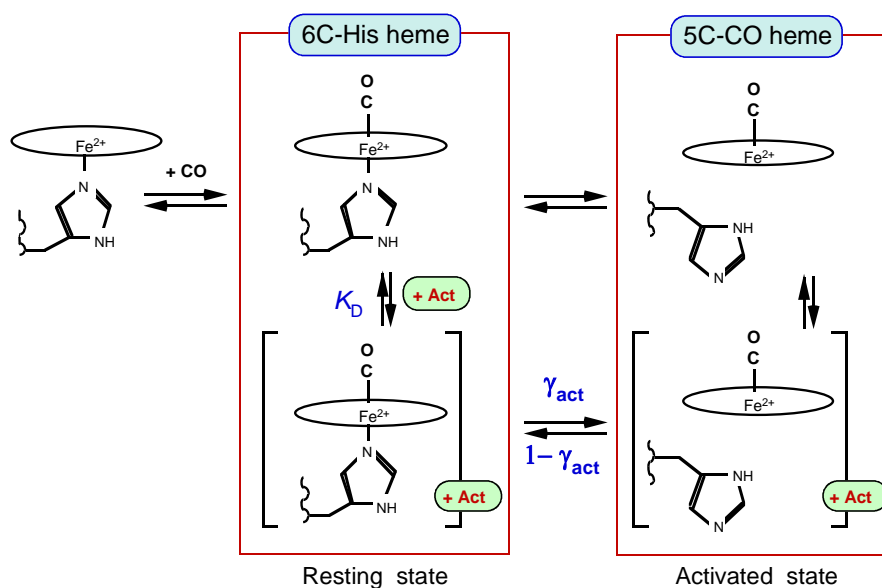


**Figure 15.** Mechanistic and allosteric model of sGC activation in presence of an activator (Act) of the BAY-412272 family. The binding of activators to sGC shifts the equilibrium 6-coordinate to 5-coordinate heme independently from the activator affinity ( $K_D$ ). The activation factor can be measured in the presence of CO.

*In vivo*,  $EC_{50}$  of activators was measured also in the presence of NO. However, the effect of NO is largely predominant and the synergy between NO and activators can be hardly established. In the absence of NO, *in vivo*  $EC_{50}$  ( $EC_{50}^{BAY412272} = 0.09 \mu\text{M}$ ,  $EC_{50}^{riociguat} = 0.1 \mu\text{M}$ ) are similar with *in vitro*  $EC_{50}$  measured in presence of CO (Table 4).

The efficiency of drugs *in vivo*, and finally the half maximal effective concentration ( $EC_{50}$ ), is determined with complexity by multiple factors: ability to reach the target, affinity with the target ( $K_D$ ) and allosteric efficacy ( $\gamma_{act}$ ), all three factors being determined by the chemical properties of a drug. The ability to reach the target in cells and tissues is connected to pharmacokinetics. It may occur that a change in a drug formula favor a factor, detrimental to another one. For example, *in vitro*  $EC_{50}$  of BAY-412272 in the presence of CO is only twice that of riociguat, but *in vivo*  $EC_{50}$  in the presence of NO (Table 4) of the latter is much lower than that of BAY-412272. We must note that  $EC_{50}$  are not necessarily measured with the same cell line.

**Table 4.** Activation properties of sGC stimulators (see formula in Figure 16).

sGC Activator	<i>in vitro</i> (purified protein)				<i>in vivo</i> (cell lines below)		
	K <sub>D</sub> (μM)	EC <sub>50</sub> (μM)	γ <sub>act</sub> SVD2/SVD1	Ref.	EC <sub>50</sub> (μM)		Ref.
					+ NO	- NO	
None	-	-	0.026	This work	-	-	
YC1	1.1 (a)	20 (b)	0.05	[15, 28, 33]	-	-	
BAY-412272	0.08 (a)	<b>0.2</b> (b)	0.1	[28, 33] This work	0.09 (c)	0.6 – 1 (d)	[34-36]
Riociguat	-	<b>0.1</b> (b)	<b>0.16</b>	This work	~10 <sup>-4</sup> (c)	0.1 – 1 (c)	[18]
Vericiguat	-	-	-	-	-	1 ± 0.1 (e)	[37]
Nelociguat	-	-	-	-	-	0.3 ± 0.09 (f)	[38]

Cell lines: (a) Truncated sGC without the catalytic domain from *Manduca sexta*. (b) Full length human sGC. (c) Chinese Hamster Ovary (CHO) cells. (d) Endothelial cells. (e) Recombinant CHO cell line overexpressing rat sGC. (f) Rat aortic smooth muscle cells.

The stimulators of sGC YC-1, BAY 41-2272, BAY 63-2521 (riociguat), and its newly discovered derivatives BAY 60-4552 (nelociguat), and BAY 1021189 (vericiguat) increase sGC activity in heme-dependent manner in synergy with diatomic ligands NO or CO. Based on similarities of their chemical structure presented in Figure 16, their mechanism of action towards sGC should also occur according to the proposed generalized model of Figure 15.

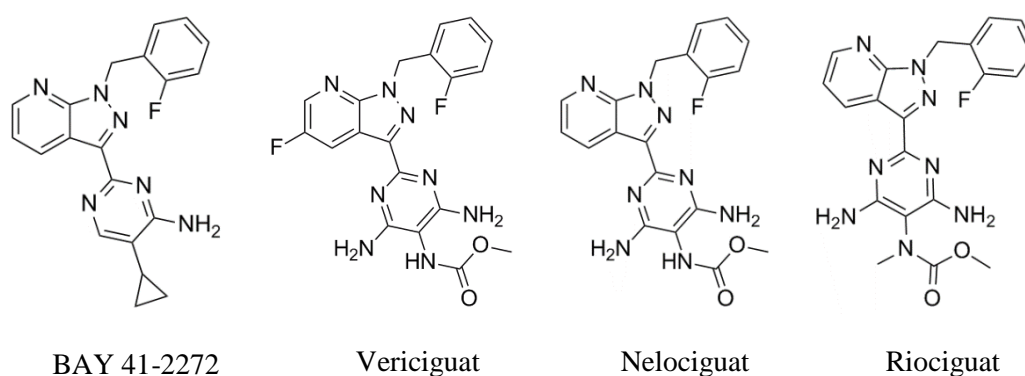


**Figure 16.** Chemical structure of cognate sGC stimulators.

These stimulators provoke a conformational change of sGC which facilitates the breaking of the iron-histidine bond, increases the proportion of a 5c-heme liganded with CO

and therefore increases the proportion of activated sGC, just like NO activation. Biochemical parameters of these new compounds ( $K_D$ ,  $EC_{50}$ ) are not yet totally known. As a perspective, we will attempt to measure their allosteric efficacy  $\gamma_{act}$  to further develop the model of sGC activation.

### 4.3 – Modeling the binding of activators

We have modeled with the help from J.-C. Lambry at LOB the H-NOX domain of  $\beta$  subunit in human sGC in different coordination states of the heme from the structure file provided by Laleh Alisaraie (School of Pharmacy, Memorial University of Newfoundland, Canada) who described a potential BAY 41-2272 binding site.

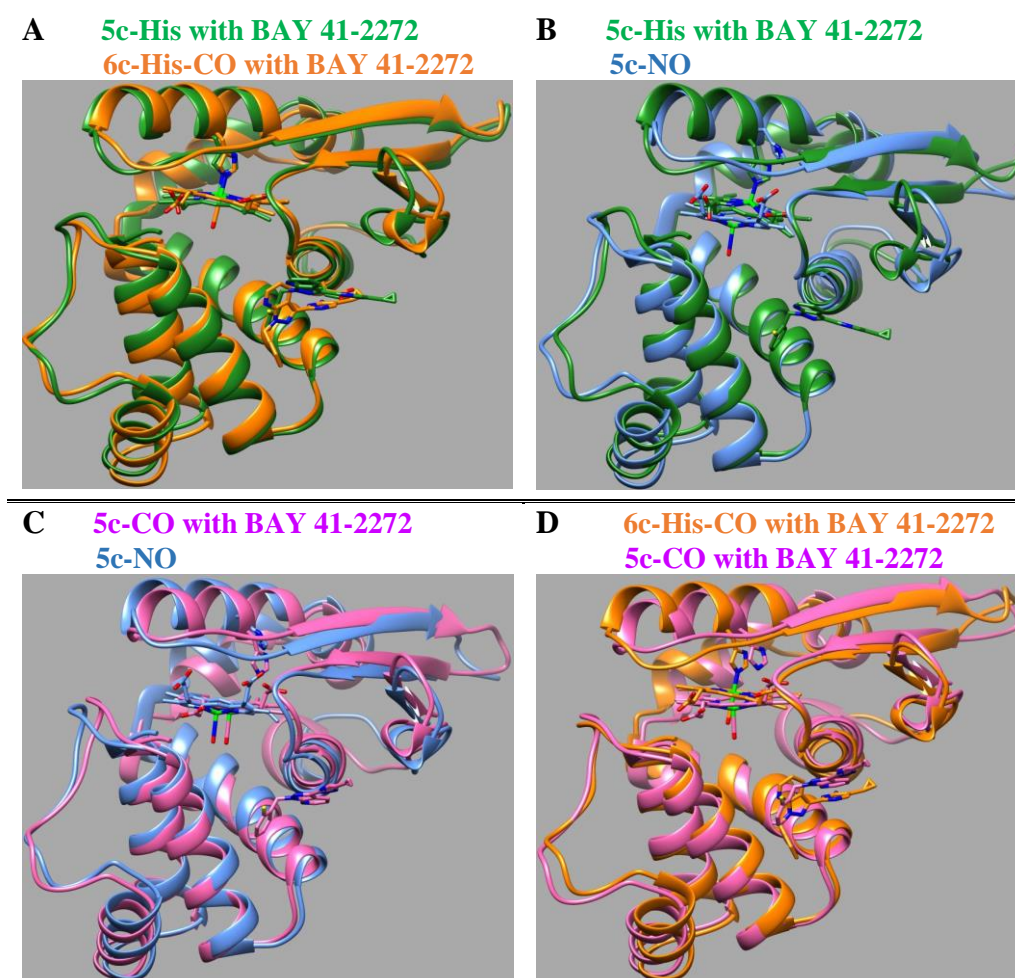


**Figure 17.** Superposition of modeled structures of the H-NOX domain of human sGC. (A) 5-c His (green) and 6-c CO (orange). (B) 5-c His (green) and 5-c NO without BAY (blue). (C) 5-c NO without BAY412272 (blue) and 5-c CO (pink). (D) 6-c CO (orange) and 5-c CO (pink). In each case in the presence of CO BAY412272 is bound to the protein.

This three-dimensional model structure is based on the template of H-NOX domain from *Nostoc sp.* The purpose is to identify structural differences between the coordination

states of the heme by molecular dynamic simulations. Here the activator BAY 41-2272 is present with CO, but not with NO. The structures presented in Figure 17 are energy minimized and demonstrate that the heme has a different distortion and geometry depending on its coordination state. Now, to identify differences in the protein backbone itself, it is necessary to run a time long dynamics with each. This very time-consuming calculation is currently under way.

## 5 – Conclusions

We demonstrated that Isoliquiritigenin (ILQG), considered so far as a sGC activator, actually inhibits sGC *in vitro* with  $IC_{50} = 9.5 \pm 0.5 \mu\text{M}$ . Even in the presence of BAY 41-2272 and NO its inhibition is efficient ( $IC_{50} = 12.5 \pm 1 \mu\text{M}$ ) so that it does not compete with activators. However, in HUVEC cells, the inhibitory effect of ILQG requires a larger concentration up to 100  $\mu\text{M}$ . The most probable target of ILQG is PDE5 which degrades cGMP.

We have measured the  $EC_{50}$  of riociguat towards purified sGC, a value never reported despite its status of commercial drug:

$$EC_{50}^{\text{rioc}} = 9.5 \pm 0.9 \mu\text{M} \text{ and } EC_{50}^{\text{rioc}+\text{CO}} = 0.15 \pm 0.1 \mu\text{M}.$$

We have demonstrated that activators of the BAY-412272 family (one is commercially available and one is in clinical trial) induce the breaking of the Fe-His bond, and thus activate sGC as does its natural effector NO, verifying our working hypothesis. These activators act in synergy with CO, however with different efficacy.

We have introduced the notion of activation factor which translates the ability of an allosteric modulator to shift sGC towards its activated state. Independently of their  $K_D$ , the activators have different activation factors, in the order:

$$[\gamma_{\text{act}}^{\text{YC1}} = 0.05] < [\gamma_{\text{act}}^{\text{BAY412272}} = 0.1] < [\gamma_{\text{act}}^{\text{riociguat}} = 0.16].$$

Besides the affinity, the specificity and the pharmacokinetics, this factor must be taken into account when designing a drug from a lead compound.

## 6 – Bibliography

1. Makino, R.; Obayashi, E.; Homma, N.; Shiro, Y.; Hori, H. YC-1 facilitates release of the proximal His residue in the NO and CO complexes of soluble guanylate cyclase. *J. Biol. Chem.* **2003**, 278, 11130-11137.
2. Yu, S. M.; Kuo, S. C. Vasorelaxant effect of isoliquiritigenin, a novel soluble guanylate cyclase activator, in rat aorta. *Br. J. Pharmacol.* **1995**, 114, 1587-1594.
3. Wegener, J. W.; Nawrath, H. Differential effects of isoliquiritigenin and YC-1 in rat aortic smooth muscle. *European Journal of Pharmacology.* **1997**, 323, 89-91.
4. Wegener, J. W.; Nawrath, H. Cardiac effects of isoliquiritigenin. *Eur. J. Pharmacol.* **1997**, 326, 37-44.

5. Martin, E.; Lee, Y. C.; Murad, F. YC-1 activation of human soluble guanylyl cyclase has both heme-dependent and heme-independent components. *Proc Natl Acad Sci USA*. **2001**, 98, 12938-12942.
6. Yoo, B. K.; Lamarre, I.; Rappaport, F.; Nioche, P.; Raman, C. S.; Martin, J. L.; Negrerie, M. Picosecond to second dynamics reveals a structural transition in *Clostridium botulinum* NO-sensor triggered by the activator BAY-41-2272. *ACS Chem Biol*. **2012**, 7, 2046-2054.
7. Clark, J. E.; Naughton, P.; Shurey, S.; Green, C. J.; Johnson, T. R.; Mann, B. E.; Foresti, R.; Motterlini, R. Cardioprotective actions by a water-soluble carbon monoxide-releasing molecule. *Circ. Res.* **2003**, 93, e2-e8.
8. Foresti, R.; Hammad, J.; Clark, J. E.; Johnson, T. R.; Mann, B. E.; Friebe, A.; Green, C. J.; Motterlini, R. Vasoactive properties of CORM-3, a novel water-soluble carbon monoxide-releasing molecule. *Br J. Pharmacol.* **2004**, 142, 453-460.
9. Guo, Y.; Stein, A. B.; Wu, W. J.; Tan, W.; Zhu, X.; Li, Q. H.; Dawn, B.; Motterlini, R.; Bolli, R. Administration of a CO-releasing molecule at the time of reperfusion reduces infarct size in vivo. *Am. J. Physiol. Heart Circ. Physiol.* **2004**, 286, H1649-653.
10. Chlopicki, S.; Lomnicka, M.; Fedorowicz, A.; Grochal, E.; Kramkowski, K.; Mogielnicki, A.; Buczko, W.; Motterlini, R. Inhibition of platelet aggregation by carbon monoxide-releasing molecules (CO-RMs): comparison with NO donors. *Naunyn Schmiedebergs Arch Pharmacol.* **2012**, 385, 641-650.
11. Fayad-Kobeissi, S.; Ratovonantenaina, J.; Dabire, H.; Wilson, J. L.; Rodriguez, A. M.; Berdeaux, A.; Dubois-Rande, J. L.; Mann, B. E.; Motterlini, R.; Foresti, R. Vascular and angiogenic activities of CORM-401, an oxidant-sensitive CO-releasing molecule. *Biochem. Pharmacol.* **2016**, 102, 64-77.
12. Stasch, J.-P.; Becker, E. M.; Alonso-Alija, C.; Apeler, H.; Dembowski, K.; Feurer, A.; Gerzer, R.; Minuth, T.; Perzborn, E.; Pleisz, U.; Schroder, H.; Schroeder, W.; Stahl, E.; Steinke, W.; Straub, A.; Schramm, M. NO-independent regulatory site on soluble guanylate cyclase. *Nature*. **2001**, 410, 212-215.
13. Mullershausen, F.; Russwurm, M.; Friebe, A.; Koesling, D. Inhibition of Phosphodiesterase Type 5 by the Activator of Nitric Oxide-Sensitive Guanylyl Cyclase BAY 41-2272. *Circulation* **2004**, 109, 1711-1713.
14. Ma, X.; Sayed, N.; Beuve, A.; van den Akker, F. NO and CO differentially activate soluble guanylyl cyclase via a heme pivot-bend mechanism. *The EMBO Journal* **2007**, 26, 578-588.
15. Friebe, A.; Schultz, G.; Koesling, D. Sensitizing soluble guanylyl cyclase to become a highly CO-sensitive enzyme. *The EMBO Journal*. **1996**, 15, 6863-6868.
16. Evgenov, O. V.; Pacher, P.; Schmidt, P. M.; Haskó, G.; Schmidt, H. H. H. W.; Stasch, J.-P. NO-independent stimulators and activators of soluble guanylate cyclase: discovery and therapeutic potential. *Nature reviews. Drug discovery*. **2006**, 5, 755-768.
17. Schermuly, R. T.; Stasch, J.-P.; Pullamsetti, S. S.; Middendorff, R.; Müller, D.; Schlüter, K.-D.; Dingendorf, A.; Hackemack, S.; Kolosionek, E.; Kaulen, C. Expression and function of soluble guanylate cyclase in pulmonary arterial hypertension. *European Respiratory Journal*. **2008**, 32, 881-891.
18. Ltd, B. A. Australian Public Assessment Report for Riociguat. *Health Safety Regulation*. **2014**.
19. Aida, K.; Tawata, M.; Shindo, H.; Onaya, T.; Sasaki, H.; Yamaguchi, T.; Chin, M.; Mitsuhashi, H. Isoliquiritigenin: a new aldose reductase inhibitor from glycyrrhizae radix. *Planta Med.* **1990**, 56, 254-258.
20. Nerya, O.; Vaya, J.; Musa, R.; Izrael, S.; Ben-Arie, R.; Tamir, S. Glabrene and isoliquiritigenin as tyrosinase inhibitors from licorice roots. *J. Agric. Food Chem.* **2003**, 51, 1201-1207.

21. Kanazawa, M.; Satomi, Y.; Mizutani, Y.; Ukimura, O.; Kawauchi, A.; Sakai, T.; Baba, M.; Okuyama, T.; Nishino, H.; Miki, T. Isoliquiritigenin Inhibits the Growth of Prostate Cancer. *European Urology*. **2003**, 43, 580-586.
22. Ma, J.; Fu, N. Y.; Pang, D. B.; Wu, W. Y.; Xu, A. L. Apoptosis induced by isoliquiritigenin in human gastric cancer MGC-803 cells. *Planta Med*. **2001**, 67, 754-757.
23. Smith, A. D.; Dar, M. S. Involvement of the alpha4beta2 nicotinic receptor subtype in nicotine-induced attenuation of delta9-THC cerebellar ataxia: role of cerebellar nitric oxide. *Pharmacol Biochem Behav* **2007**, 86, 103-112.
24. Al-Rejaie, S.; Dar, M. S. Antagonism of ethanol ataxia by intracerebellar nicotine: possible modulation by mouse cerebellar nitric oxide and cGMP. *Brain Res Bull* **2006**, 69, 187-196.
25. Dandawate, P. R.; Subramaniam, D.; Jensen, R. A.; Anant, S. Targeting cancer stem cells and signaling pathways by phytochemicals: Novel approach for breast cancer therapy. *Semin Cancer Biol* **2016**, 40-41, 192-208.
26. Peng, F.; Du, Q.; Peng, C.; Wang, N.; Tang, H.; Xie, X.; Shen, J.; Chen, J. A Review: The Pharmacology of Isoliquiritigenin. *Phytother Res* **2015**, 29, 969-977.
27. Sulaiman, R. S.; Basavarajappa, H. D.; Corson, T. W. Natural product inhibitors of ocular angiogenesis. *Exp Eye Res* **2014**, 129, 161-171.
28. Yoo, B.-K. Investigation of the mechanisms of regulations, activation, and deactivation of Guanylate Cyclase, the endogenous NO-receptor, and NO-sensors. Ecole Polytechnique, **2010**.
29. Negrerie, M.; Cianetti, S.; Vos, M. H.; Martin, J. L.; Kruglik, S. G. Ultrafast heme dynamics in ferrous versus ferric cytochrome c studied by time-resolved resonance Raman and transient absorption spectroscopy. *J Phys Chem B* **2006**, 110, 12766-12781.
30. Yoo, B.-K.; Lamarre, I.; Martin, J.-L.; Rappaport, F.; Negrerie, M. Motion of proximal histidine and structural allosteric transition in soluble guanylate cyclase. *Proceedings of the National Academy of Sciences*. **2015**, 112, E1697-E1704.
31. Yoo, B.-K.; Lamarre, I.; Martin, J.-L.; Andrew, C. R.; Negrerie, M. Picosecond Binding of the His Ligand to Four-Coordinate Heme in Cytochrome c': A One-Way Gate for Releasing Proximal NO. *Journal of the American Chemical Society*. **2013**, 135, 3248-3254.
32. Pal, B.; Tanaka, K.; Takenaka, S.; Kitagawa, T. Resonance Raman spectroscopic investigation of structural changes of CO-heme in soluble guanylate cyclase generated by effectors and substrate. *Journal of Raman Spectroscopy* **2010**, 41, 1178-1184.
33. Purohit, R.; Fritz, B. G.; The, J.; Issaian, A.; Weichsel, A.; David, C. L.; Campbell, E.; Hausrath, A. C.; Rassouli-Taylor, L.; Garcin, E. D. YC-1 binding to the  $\beta$  subunit of soluble guanylyl cyclase overcomes allosteric inhibition by the  $\alpha$  subunit. *Biochemistry*. **2013**, 53, 101-114.
34. Stasch, J.-P.; Becker, E. M.; Alonso-Alija, C.; Apeler, H.; Dembowski, K.; Feurer, A.; Gerzer, R.; Minuth, T.; Perzborn, E.; Zlig, U. P.; Schröder, H.; Schroeder, W.; Stahl, E.; Steinke, W.; Straub, A.; Schramm, M. NO-independent regulatory site on soluble guanylate cyclase. The first biochemical and pharmacological characterization of BAY 41-2272 as a novel NO-independent but haem-dependent stimulator of sGC. *Nature* **2001**, 212-215.
35. Bischoff, E.; Stasch, J.-P. Effects of the sGC Stimulator BAY 41-2272 Are Not Mediated by Phosphodiesterase 5 Inhibition. *Circulation* **2004**, 110, e320-e321.
36. Hoffmann, L. S.; Schmidt, P. M.; Keim, Y.; Schaefer, S.; Schmidt, H. H.; Stasch, J. P. Distinct molecular requirements for activation or stabilization of soluble guanylyl cyclase upon haem oxidation-induced degradation. *Br J Pharmacol* **2009**, 157, 781-795.
37. Follmann, M.; Ackerstaff, J.; Redlich, G.; Wunder, F.; Lang, D.; Kern, A.; Fey, P.; Griebenow, N.; Kroh, W.; Becker-Pelster, E. M.; Kretschmer, A.; Geiss, V.; Li, V.; Straub, A.; Mittendorf, J.;

Jautelat, R.; Schirok, H.; Schlemmer, K. H.; Lustig, K.; Gerisch, M.; Knorr, A.; Tinel, H.; Mondritzki, T.; Trubel, H.; Sandner, P.; Stasch, J. P. Discovery of the Soluble Guanylate Cyclase Stimulator Vericiguat (BAY 1021189) for the Treatment of Chronic Heart Failure. *J Med. Chem.* **2017**, 60, 5146-5161.

38. Costell, M. H.; Ancellin, N.; Bernard, R. E.; Zhao, S.; Upson, J. J.; Morgan, L. A.; Maniscalco, K.; Olzinski, A. R.; Ballard, V. L.; Herry, K.; Grondin, P.; Dodic, N.; Mirguet, O.; Bouillot, A.; Gellibert, F.; Coatney, R. W.; Lepore, J. J.; Jucker, B. M.; Jolivet, L. J.; Willette, R. N.; Schnackenberg, C. G.; Behm, D. J. Comparison of soluble guanylate cyclase stimulators and activators in models of cardiovascular disease associated with oxidative stress. *Front Pharmacol.* **2012**, 3, 128.

---

## CHAPTER V

### CONTROL OF DIATOMICS BINDING BY BACTERIAL NO-SENSORS

#### SYNOPSIS

---

<b>1 – Ligand dynamics .....</b>	<b>128</b>
<b>2 – Materials and methods.....</b>	<b>130</b>
2.1 – Preparation of the samples .....	130
2.2 – Time-resolved measurement of ligand dynamics.....	131
2.3 – Molecular dynamics simulation protocol.....	131
2.3 – Reactivity with ligands with the <i>Tt</i> -sensor and temperature dependence .....	132
<b>3 – L16A mutant of the NO-sensor from <i>Alcaligenes xylosoxydans</i> .....</b>	<b>133</b>
3.1 – Dynamics of nitric oxide .....	134
3.2 – Dynamics of dioxygen .....	136
3.3 – Dynamics of carbon monoxide .....	137
3.4 – Internal dynamics and affinity.....	140
3.5 – Conclusion for AXCP affinity.....	142
<b>4 – Dioxygen binding to the NO-sensor from <i>Thermoanaerobacter tengcongensis</i> .....</b>	<b>142</b>
4.1 – Temperature dependence on heme coordination of <i>Tt</i> -H-NOX.....	142
4.2 – Dynamics of dioxygen binding to <i>Tt</i> -H-NOX.....	144
4.2.1 – Interpretation of the spectral components .....	146
4.2.2 – The kinetics of O <sub>2</sub> binding to <i>Tt</i> -H-NOX.....	147
4.3 – Hypothesis of the physiological role of <i>Tt</i> -H-NOX .....	150
<b>5 – Conclusions .....</b>	<b>152</b>
<b>6 – Bibliography .....</b>	<b>152</b>

---

## 1 – Ligand dynamics

Molecular oxygen (O<sub>2</sub>) and nitric oxide (NO) sensor proteins are essential to monitor changes in the environment of bacteria. One particular protein sensor found in different species of bacteria, heme nitric oxide/oxygen binding (H-NOX) proteins, was originally identified based on their significant sequence homology with the heme domain [ $\beta I(1-194)$ ] of the mammalian heme NO receptor soluble guanylyl cyclase (sGC) [1, 2]. Bacterial H-NOX proteins can be divided into two subfamilies based on ligand-binding specificity. The first subfamily is found in facultative anaerobes, most commonly gamma-proteobacteria (*Shewanella oneidensis* and *Vibrio cholerae*). These H-NOX proteins are specific NO sensors that do not form a stable complex with O<sub>2</sub> similarly with sGC  $\beta$ -subunit [3]. The function of such bacterial H-NOX proteins is to regulate biofilm formation or quorum sensing circuits in an NO-dependent manner [4-6]. The second subfamily of bacterial H-NOX is obligate anaerobes, most commonly from the genus *Clostridia*. The first discovered bacterial sensor H-NOX was from *Thermoanaerobacter tengcongensis* (*Tt*-H-NOX), which has a living temperature of 75 – 85 °C. Unlike the NO-sensing H-NOX domains, *Tt*-H-NOX bind O<sub>2</sub> with very high affinity and forms stable a 6-coordinate Fe(II)-O<sub>2</sub> complex [7]. The binding of O<sub>2</sub> to H-NOXs in obligate anaerobes may provide these organisms a mechanism to sense O<sub>2</sub> for adaptation or avoidance reactions. Similarly with sGC, histidine is attached to heme iron at the proximal side and the vacant distal side is available for binding a ligand. The crystal structure of *Tt*-H-NOX is displayed on Figure 1. *Tt*-H-NOX shares a 18 % sequence identity with the  $\beta$  H-NOX domain of sGC. The exact role of O<sub>2</sub> binding for *Tt*-H-NOX proteins is not well known.

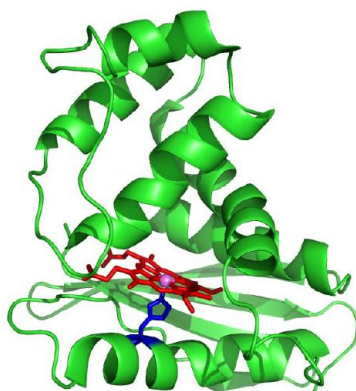


**Figure 1.** 3D structure of the first 181 amino acid of the HNOX domain from the protein Tt-SONO. The heme prosthetic group and the proximal histidine (His102) coordinating its iron are shown respectively in red and blue. The figure was generated using Chimera. PDB ID: 1XBN [8].

Another protein of our interest is cytochrome *c'* (Cyt *c'*) found in various bacterial organisms, which are photosynthetic, denitrifying, and nitrogen-fixing [9, 10]. Cyt *c'* consists of a four  $\alpha$ -helical bundle structure which are isolated as homodimers, each carrying a heme

attached to the protein by covalent links with sulfur atoms from cysteines (c-type heme) [10]. Generally, the c-type heme proteins have particular redox properties conferred to the heme thanks to the covalent linkage of the heme to the protein backbone, imposing restraints to its planarity. Cyt *c'* possess a heme with a vacant distal coordination in the unliganded state [11]. In the case of the denitrifier bacteria *Alcaligenes xylosoxidans* (AXCP) a unique heme coordination chemistry was revealed by X-ray studies from [12] with two possible positions for NO at both proximal or distal side (Figure 2).

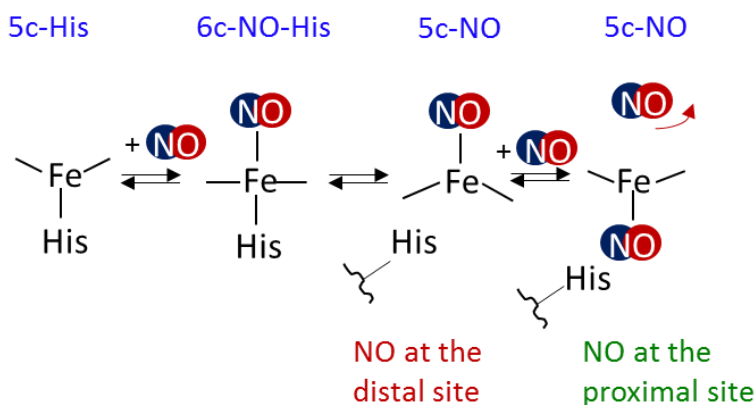


**Figure 2.** Coordination of the heme iron of cytochrome *c'* from *Alcaligenes xylosoxidans*. NO can bind at the distal site of the heme and can displace the proximal histidine residue site.

Figure 3 shows the X-ray structure of unliganded (5c-His) ferrous AXCP at equilibrium. The structure of AXCP totally differs from that of *Tt-H-NOX*. Whereas CO forms a 6-coordinate heme complex at the vacant distal side, NO displaces the proximal histidine residue site by occupying the proximal position [13], contrarily to CO. The exact biochemical function of Cyt *c'* is not clear, but the hypothesis of a role as NO transporter [14, 15] is supported by the formation of the 5c-NO species and the “one way-gate” mechanism of NO release [4, 12].

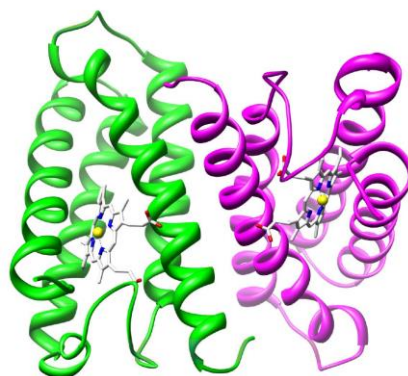


**Figure 3.** Structure of the unliganded (5c-His) ferrous AXCP. The active form of the protein is a homodimer, each monomer being a bundle of four  $\alpha$ - helices harboring a heme. The figure was created using Chimera. PDB ID: 1E84 [8].

The present chapter is devoted to the study of diatomic gases binding to two bacterial proteins, the NO transporter AXCP and the sensor *Tt*-H-NOX. First, we studied the dynamics and affinity of ligands CO, NO, and O<sub>2</sub> with the wild type of Cyt *c'* from *Alcaligenes xylosoxidans* (WT-AXCP) and its mutant L16A-AXCP. The diatomic binding properties were previously measured [16] in AXCP variants in which the occluding distal residue Leu16 was replaced with smaller (Ala, Val), of comparable size (Ile) or larger residues (Phe). These studies revealed a dramatically increased affinity for NO, CO, O<sub>2</sub> in the L16A variant of AXCP [16-18] and we aimed at comparing the dynamics of diatomic ligands in the WT and mutant in order to understand the origin of the extremely large increase of affinity. We measured the diatomic dynamics over 12 orders of magnitude in time after their photodissociation from the ferrous heme of the mutant and wild type protein. We showed that the mere replacement Leu16Ala, which leads to a 10<sup>8</sup>-fold increase of CO affinity, ~10<sup>6</sup>-fold NO affinity and makes this protein reactive to O<sub>2</sub>, induces a new way to control the dynamics.

Secondly, we measured the temperature dependence on the heme coordination and redox states of *Tt*-H-NOX, probing the stability of different species of the heme at different temperature. The dynamics of O<sub>2</sub> binding to *Tt*-H-NOX protein was recorded using transient absorption spectroscopy in 1 ps to 5 ns time range, then up to 0.1 s. This experiment helped us to interpret the physiological role of *Tt*-H-NOX.

## 2 – Materials and methods

### 2.1 – Preparation of the samples

Cytochrome *c'* from *Alcaligenes xylosoxidans* and its L16A mutant were expressed, purified and provided by Pr. Colin Andrew's laboratory (Eastern Oregon University, USA). The solution of ferric WT or L16A-AXCP (100 μL, 50 μM in 10 mM TEA buffer, pH 7.4) was put in a 1-mm optical path length quartz cell sealed with a rubber stopper and degassed by means of four successive cycles of vacuum (0.3 mbar) and purging with pure argon (1.3 bar) for 15 min between each cycles. The ferrous heme was obtained by the addition of 10 μL of degassed sodium ascorbate solution (2 mM final concentration) which also eliminates remaining O<sub>2</sub>. For preparing ferrous NO-liganded AXCP, gas phase 100 % NO or 10 % in N<sub>2</sub> was directly introduced into the spectroscopic cell (total pressure of 1.3 bar, yielding 2 mM and 200 μM of NO in the aqueous phase respectively). A second silicone stopper was put on the cell. Equilibrium spectra were recorded at each step for monitoring the coordination state with the evolution of Soret band. The absorbance of the sample was in the range 0.5 – 0.8 at the Soret maximum for 1-mm path length.

## 2.2 – Time-resolved measurement of ligand dynamics

The photo-dissociation of NO, CO and O<sub>2</sub> was achieved with an excitation pulse at 564 nm, in the Q-band absorption of the heme, whose duration was ~50 fs with a repetition rate of 30 Hz. The probe pulse was generated from a continuum with a broad spectrum pulse (375 – 500 nm). The transient Soret absorption was recorded as a function of time delay between pump and probe pulses. The optical path length of the cell was 1 mm. The sample was continuously moved perpendicularly to the laser beam and the temperature was 20 °C. Transient spectra were recorded with a CCD detector simultaneously to the kinetics as a time-wavelength matrix data. Analysis of the data was performed by singular value decomposition (SVD) of this time-wavelength matrix (see CHAPTER VII, Annex C) such that all transient spectral components were identified in the time window 0.5 ps – 5 ns. Up to 40 scans were recorded and averaged with a dwell time of 1 s at each individual transient spectrum. The SVD kinetic components were fitted to the sum of a minimum number of exponential components. Alternatively, kinetics were also performed at particular wavelengths of the raw data matrix.

For time-resolved absorption in the extended time-range nanosecond to millisecond, we have used the home-built spectrophotometer at Laboratoire de Physiologie Membranaire et Moléculaire du Chloroplaste (Institut de Biologie Physico-Chimique, Paris). This system comprises two lasers which are electronically synchronized [19]. The dissociating pulse is provided by the second harmonic (532 nm) of a Nd/YAG laser and has a duration of 6 ns. The probing pulses (duration 5 ns) were provided by a tunable optical parametric oscillator pumped by the third harmonic of a Nd/YAG laser. The sample cell compartment and light collection design [19] allowed us to record signal variations  $\Delta OD/OD$  as low as  $10^{-5}$ . The kinetics of differential absorption changes were probed at particular wavelengths by tuning the OPO. Up to twelve scans were averaged for each kinetics. The time delay after the dissociating pulse was changed linearly from 1 to 30 ns, then was changed with a logarithmic progression from 30 ns to 1 s. The kinetics at a particular wavelength were globally fitted to the sum of a minimum number of exponential components.

## 2.3 – Molecular dynamics simulation protocol

We constructed with the help from Jean-Christophe Lambry at LOB the WT and L16A dimer models of *Achromobacter xylosoxidans* cytochrome *c'*, using the PDB crystal structures files code 2YLD and 2YLG, respectively [18]. All molecular dynamic simulations were performed with the program CHARMM. Electrostatic interactions were computed together with boundary conditions and all bonds with hydrogen atoms were constrained. The AXCP model was solvated using a water box shape with a 76 Å edge length and neutralized with potassium and chloride ions at 0.15 M concentration. After energy minimization, the AXCP structures were heated to 310 K and equilibrated with periodic assignment of velocities

every 1 ps. The equilibration phase duration varies from 1.25 ns to 3 ns in order to generate eight independent trajectories. Free dynamic over 250 ps and 500 ps were performed before 500 ps CO ligand dissociation simulations.

To simulate the dissociation, the bond between heme iron and ligand was deleted and liganded parameters switched to unliganded parameters at the two heme sites simultaneously. This method produces an energy excess of the same order of magnitude that the photon energy used to photodissociate the CO ligand in the experiment. The unliganded CO was simulated using a three charge model. The ligand recombination process was not treated in these simulations since we aimed at determining the motion of CO within the heme pocket. An integration time step of 1 fs was used and the structure was saved every 1 ps for analysis. The root mean square deviation of backbone atoms of the WT and L16A trajectories remains below 3 Å.

### 2.3 – Reactivity with ligands with the *Tt*-sensor and temperature dependence

The sample of bacterial H-NOX domain from *Thermoanaerobacter tencongensis* comprising the first 191 amino-acids (*Tt*-H-NOX) which is homologous to the heme domain of sGC (see CHAPTER II) was overexpressed [15] and provided by Dr. Pierre Nioche (Université Paris Descartes, Laboratoire de Toxicologie et Signalisation Cellulaire).

#### *Temperature dependence of Tt-H-NOX liganded states*

For all spectroscopic steady-state and time-resolved measurements a quartz cell was used (Hellma, 110-QX), having an optical path of 1 mm. The steady-state absorption spectrophotometer is a Shimadzu UV-1700. The purified protein was kept at – 80 °C in buffer TEA supplemented with 5 % glycerol and was thawed immediately before use. *Tt*-H-NOX in the O<sub>2</sub>-liganded ferrous state was systematically verified by its absorption spectrum with a Soret band maximum located at 416 nm (Figure 4A) [20].

#### *Heme oxidation state upon temperature*

An aliquot of *Tt*-H-NOX (120 µL at 50 µM) in buffer E (50 mM Tris-HCl pH 7.5) was placed in a cell. It was not degassed but kept in equilibrium with air, corresponding to 280 µM of O<sub>2</sub> in the aqueous phase at 20 °C. The absorption spectrum was recorded at increasing temperatures from 20 °C to 76 °C with a home-built thermostated cell holder adapter to the Shimadzu UV-1700 spectrophotometer.

#### *Heme coordination state in the presence of NO upon temperature*

A sample of *Tt*-H-NOX (120 µL at 50 µM) in buffer E (50 mM Tris-HCl pH 7.5) was thoroughly degassed directly in the spectroscopic cell previously sealed with a rubber stopper. Then, degassed sodium dithionite (7 µL) was added (500 µM final concentration) and the cell was heated 10 min at 50 °C to speed up O<sub>2</sub> dissociation. The fully reduced unliganded *Tt*-H-NOX was obtained, with a Soret band maximum at 432 nm (Figure 4A). The nitrosylated species was obtained by introducing 10 % NO gas diluted in nitrogen in the vacuumed cell, at

a final pressure of ~1.2 bar, yielding 200  $\mu\text{M}$  NO in the aqueous phase at 20 °C. Airtightness of the cell was ensured by putting vacuum grease at the top of the first stopper and then a second stopper in silicone. The spectrum was recorded at 20 °C.

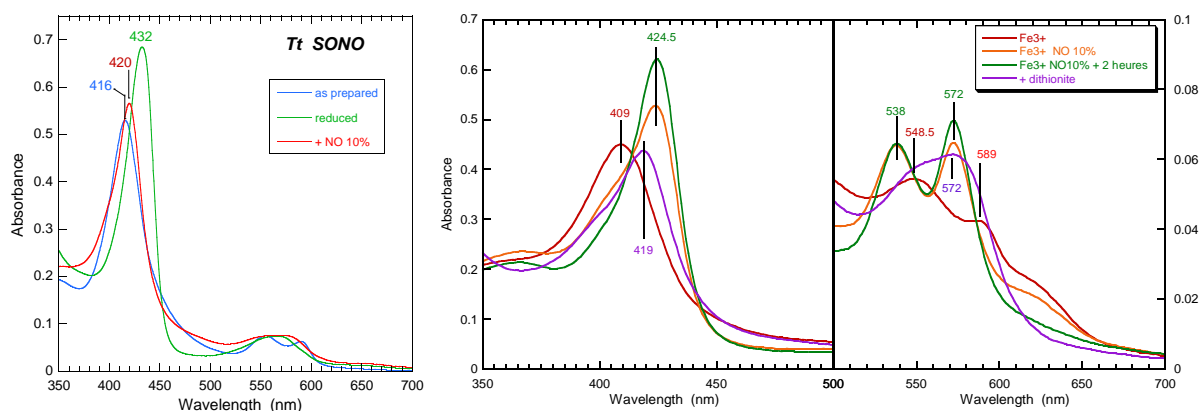


**Figure 4.** Equilibrium spectra of *Tt*-H-NOX protein before time-resolved measurements monitored by UV-visible spectra at RT. (A) Spectra of thawed *Tt*-H-NOX ( $\text{Fe}^{2+} - \text{O}_2$ ) before degassing, reduced ( $\text{Fe}^{2+}$ ) and NO-bounded ( $\text{Fe}^{2+} - \text{NO}$ ) forms. (B) Oxidized form of *Tt*-H-NOX ( $\text{Fe}^{3+}$ ) and NO-bounded ( $\text{Fe}^{3+} - \text{NO}$ ) in the Soret band region and (C) in the Q-bands region.

#### *NO reactivity with O<sub>2</sub>-liganded ferrous Tt-H-NOX*

An aliquot of  $\text{O}_2$  bound *Tt*-H-NOX in TEA buffer (100  $\mu\text{L}$  at 20  $\mu\text{M}$ ) was placed in a cell (total volume 400  $\mu\text{L}$ ). The solution was degassed with four cycles of vacuuming and purging with argon (Air Liquide, 99.999 %) so that  $\text{O}_2$  was removed completely from both aqueous and gas phases. The absorption spectrum of degassed *Tt*-H-NOX was recorded, confirming that it was still in the  $\text{O}_2$ -liganded state in spite of degassing. In the gas phase of the cell, argon was replaced with NO diluted to 1 % in  $\text{N}_2$  (Air Liquide) and directly introduced in the vacuumed cell at a pressure of 1.2 bar, yielding 20  $\mu\text{M}$  NO in the aqueous phase. The absorption spectrum was recorded at different times at 20 °C and 65 °C on two different samples.

#### *Preparation of ferric Tt-H-NOX*

The sample of *Tt*-H-NOX (~40  $\mu\text{M}$ , 120  $\mu\text{L}$ ) is placed in a spectroscopic cell (1 mm) and is thoroughly degassed and argon is introduced in the gas phase, but no reductant was used. Then the sample is oxidized by mild heating (65 °C for 20 min). The Soret appeared at 409 nm. The cell is again degassed and NO (10% in  $\text{N}_2$  yielding 200  $\mu\text{M}$  of NO in solution) is introduced in the cell. The Soret consequently slowly shifts to 424.5 nm (Figure 4B).

### **3 – L16A mutant of the NO-sensor from *Alcaligenes xylosoxydans***

We demonstrated that binding and affinity of the three diatomic ligands CO, NO and  $\text{O}_2$  can be governed by factors which can supplant the steric barriers and induce a very high affinity. For that, the dynamics of CO, NO and  $\text{O}_2$  were measured over twelve orders of

magnitude in time after their photodissociation from the ferrous heme of the wild type of cytochrome *c'* from *Alcaligenes xylosoxydans* (WT-AXCP) and mutant of AXCP, L16A.

### 3.1 – Dynamics of nitric oxide

The equilibrium spectra of ferrous L16A-AXCP unliganded and NO-liganded are shown in Figure 5. The Soret band of the reduced L16A-AXCP mutant discloses a doublet like the WT protein [25], but with a shoulder at 432 nm and a maximum at 418.5 nm witnessing that it is partly in a 6-coordinate ferrous form (Figure 5A). This differs slightly from ferrous WT AXCP, which has a maximum at 424 nm and a shoulder at 434 nm [21]. The external ligand could be either O<sub>2</sub> or CO which remains partly bound as deduced from the crystal structures. To avoid effect of remaining O<sub>2</sub>, we used 2 mM ascorbate as reductant and a thorough degassing before putting NO in the cell [22]. The equilibrium spectra of NO-ligand L16A-AXCP shows the shift of the Soret maximum to 416 nm as a sharp band.

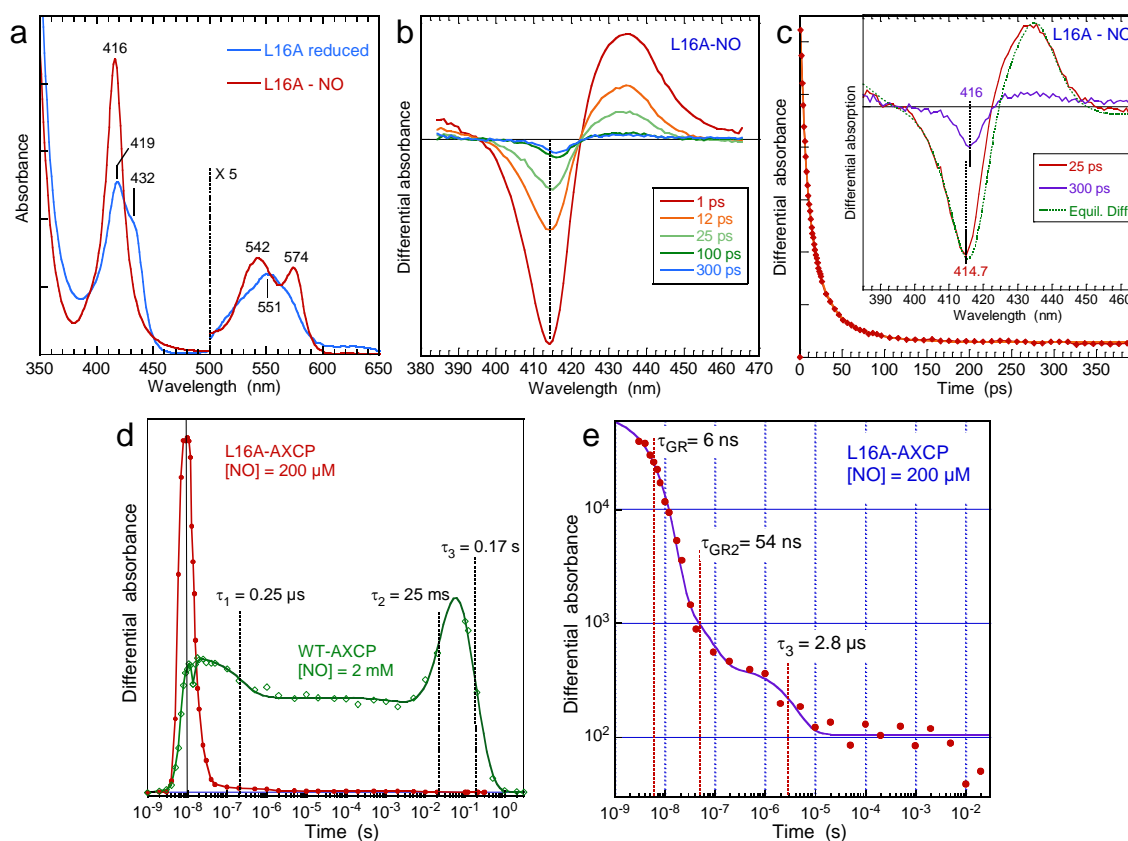


**Figure 5.** Kinetics of NO rebinding to L16A-AXCP from 1 ps to 1 s. **(a)** Equilibrium spectra of ferrous L16A-AXCP unliganded and NO-liganded. **(b)** Transient absorption spectra at selected time delays after NO photodissociation recorded with a 50-fs probe pulse. **(c)** Kinetics of NO rebinding to the heme in the ps time range. Insert: comparison of the difference transient spectra at 25 and 300 ps with the steady-state difference spectrum (green dotted line). **(d)** Kinetics of NO rebinding to the heme probed at 432 nm in the ns to second time range. **(e)** Double-log view of the kinetics fitted in the entire time range together with the time constants. The time origin in **d** is that of the electronic delay whereas the time origin for fitting the data points in **e** was set to the maximum of the initial absorption rise. For all data the concentration was [NO] = 200  $\mu$ M. (T = 20°C).

After NO photodissociation, the bleaching band appears at 415 nm due to NO release with the induced absorption counterpart at 434 nm (Figure 5b, c). Their amplitude decreased up to 300 ps, but with a slight shift of the bleaching from 414.5 to 416 nm (insert in Figure 5c). The kinetics were fitted to the sum of two exponential functions, yielding the time constants  $\tau_{G1} = 13.9$  ps ( $A_{G1} = 67.3$  %) and  $\tau_{G2} = 41$  ps ( $A_{G2} = 26.7$  %) and a constant term ( $A_3 = 6\%$ ) which represents all other slower components (Table 1). The presence of two geminate rebinding components is a common property of 6-coordinate NO heme proteins [23, 24]. Especially, the first fast component, which corresponds to NO still located in the heme pocket, has the same time constant as in myoglobin (14 ps). The second geminate component corresponds to NO escaped from the heme pocket but still present in the protein core, whereas the constant  $A_3$  corresponds to NO diffusing farther than the heme pocket and to the solvent.

**Table 1.** Kinetics of NO geminate rebinding to the mutant L16A-AXCP, compared with other 6c-NO heme proteins and 5c-NO WT-AXCP.

Protein (b)	NO geminate rebinding			Bimolecular rebinding	References
	$\tau_1$ ( $A_1$ ) (a)	$\tau_2$ ( $A_2$ )	$\tau_3$ ( $A_3$ ); $\tau_4$ ( $A_4$ )	$A_4$ (%)	
L16A-AXCP	13.9 ps (67.3)	41 ps (26.7)	6 ns (6) 54 ns (< 0.2)	0	Our work
WT AXCP 6c-NO (distal)	–	52 ps (43)	–	ND	[25]
WT AXCP 5c-NO (proximal)	7 ps (98)	–	–	2	[25, 26]
sGC	7.5 ps (97)	–	–	3	[27]
WT Mb	13 ps (40)	148 ps (50)	–	10	[23]
<i>Lp</i> -HbI	8.0 ps (36)	90 ps (62)	–	2	[24]
Ferric eNOS	15 ps (7)	200 ps (30)	2 ns (53)	10	[28]

(a)  $A_i$  (%) are the relative amplitudes of each exponential component.  
(b) Abbreviations: Mb: myoglobin; eNOS: endothelial NO-synthase; *Lp*-Hb, hemoglobin from *Lucina Pectinata*. ND: not determined.

This constant component was further investigated by recording the dynamics of NO rebinding up to 0.3 s (Figure 5d) by means of a detection system [19] whose sensitivity allows the measurements of variation as low as  $\Delta OD/OD = 10^{-5}$ . The disappearance of the unliganded heme was studied at 423 nm. Fitting the kinetics over the entire time range results in three time constants:  $\tau_3 = 6$  ns,  $\tau_4 = 54$  ns and  $\tau_5 = 2.8$   $\mu$ s but no other components at larger time delays (Figure 5e). The duration of the photo-dissociating pulse of 5 ns is much longer than the geminate rebinding whose yield is high ( $\phi_G = 94$  %). This implies that during 5 ns the same molecule L16A-AXCP-NO has the ability to dissociate and reform several times, inducing an apparent larger photo-dissociation yield, but the ps geminate rebinding remains the major process. The total amplitude of all components in the ns-ms time range account for only 6% of the entire NO dynamics after photodissociation, which decompose as a 6-ns

component and two other processes 54 ns and 2.8  $\mu$ s. Considering the association constant of NO to L16A-AXCP ( $k_{\text{on}} = 2.9 \times 10^6 \text{ M}^{-1}\text{s}^{-1}$ ) [22] and the concentration used  $[\text{NO}] = 200 \mu\text{M}$ , the bimolecular rebinding constant should appear at  $\sim 1.6 \text{ ms}$  ( $k_{\text{obs}} = \sim 0.6 \times 10^3 \text{ s}^{-1}$ ) so that the third transition measured at  $\tau_5 = 2.8 \mu\text{s}$  is not due to bimolecular association, but can be assigned either to NO geminate rebinding or to a heme conformational relaxation.

### 3.2 – Dynamics of dioxygen

The photodissociation of  $\text{O}_2$  from L16A-AXCP, similarly with NO, gives rise to a bleaching centered at 416 nm and an induced absorption at 433 nm due to the appearance of the ferrous 5c-His heme (Figure 6a). In the ps to ns time range, the amplitude of the transient spectrum decreases with a multi-exponential behavior (Figure 6b) and gives three geminate phases of  $\text{O}_2$  rebinding. The first, initial phase ( $\tau_{\text{G1}} = 7.5 \text{ ps}$ ;  $A_1 = 27.5 \%$ ) is as fast as the rebinding of NO to the 4c heme of AXCP [25] and is due to  $\text{O}_2$  which remains in close proximity to the iron. Two subsequent phases spaced by one order of magnitude in time ( $\tau_{\text{G2}} = 120 \text{ ps}$ ;  $A_2 = 22 \%$ .  $\tau_{\text{G3}} = 2 \text{ ns}$ ;  $A_3 = 45 \%$ ). A constant phase whose relative amplitude is 5.2 % is revealed, which is assigned to  $\text{O}_2$  having left the heme pocket to diffuse into the solvent. Compared with other diatomics,  $\text{O}_2$  has a  $k_{\text{off}}$  more than  $10^4$  larger than NO and CO, which allows one to observe its escape into the solvent.

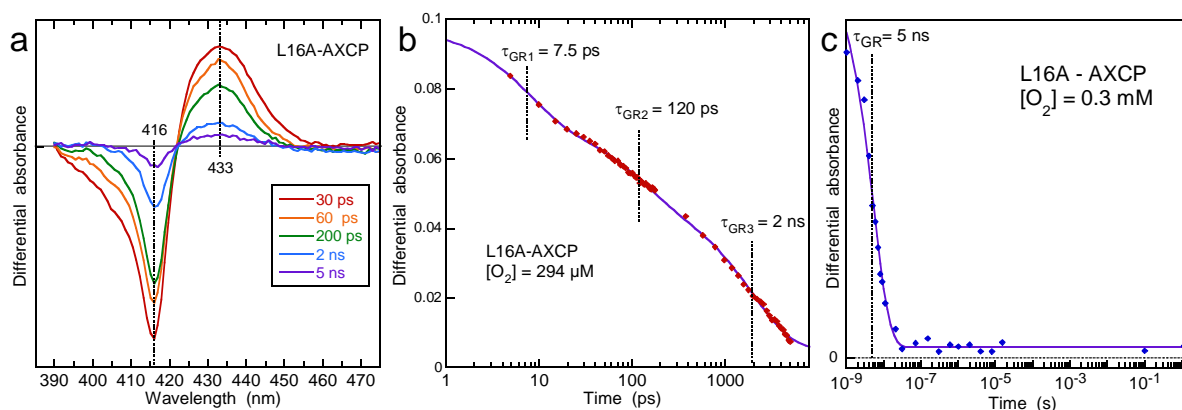


**Figure 6.** Kinetics of  $\text{O}_2$  rebinding to L16A-AXCP from 1 ps to 1 s. **(a)** Transient absorption spectra at selected time delays after  $\text{O}_2$  photodissociation recorded with a 50-fs probe pulse. **(b)** Kinetics of  $\text{O}_2$  rebinding to the heme in the ps time range up to 5 ns. The curve is a fit to a function with three exponential decays whose time constants are indicated. The relative amplitudes are given in Table 3. **(c)** Kinetics of  $\text{O}_2$  rebinding to the heme probed at 434 nm in the ns to second time range. The curve is a mono-exponential fit. The time origin was set to the maximum of the initial absorption rise. The protein was exposed to air:  $[\text{O}_2] = 0.3 \text{ mM}$ .  $T = 20^\circ\text{C}$ .

To resolve other possible transitions, the  $\text{O}_2$  dynamics was recorded up to 1 s with the highly sensitive detection. The first two geminate rebinding phases  $\tau_{\text{G1}}$  and  $\tau_{\text{G2}}$  are contained within the pulse width. The subsequent decay, slower than the rise, was fitted to a single exponential with  $\sim 5 \text{ ns}$  time constant (Figure 6c) and corresponds to the geminate  $\text{O}_2$

rebinding observed previously  $\tau_{G3} = 2$  ns, but with a smaller time resolution in the broad time range (Table 2).

**Table 2.** Kinetics of O<sub>2</sub> rebinding to the mutant L16A-AXCP, myoglobin and hemoglobin

Protein	O <sub>2</sub> geminate rebinding			Bimolecular rebinding	References
	$\tau_{G1}$ (A <sub>1</sub> ) <sup>a</sup>	$\tau_{G2}$ (A <sub>2</sub> )	$\tau_{G3}$ (A <sub>3</sub> )	A <sub>4</sub> (%)	
L16A - AXCP	7.5 ps (27.5)	120 ps (22)	2000 ps (45.3)	5.2	
WT Mb	6.3 ps (28)	291 ps (6)	–	65	[24]
<i>Lp</i> -HbI	6.0 ps (20.5)	396 ps (18)	–	61.5	[24]

(a) A<sub>i</sub> (%) are the relative amplitudes of each exponential component.  
Abbreviations: Mb: myoglobin; *Lp*-Hb, hemoglobin from *Lucina Pectinata*.

The dynamics of O<sub>2</sub> binding to L16A-AXCP cannot be compared with WT-AXCP which does not bind O<sub>2</sub>. There are other O<sub>2</sub>-binding proteins such as hemoglobin and myoglobin (Table 2). The difference between three proteins is the presence of a third component in L16A-AXCP having a large amplitude ( $\tau_3 = 2$  ns; A<sub>3</sub> = 45.3 %), which decreases the amplitude of O<sub>2</sub> escape (A<sub>4</sub> = 5.2 %). This determines the O<sub>2</sub> affinity and leads to a ~20 times smaller K<sub>D</sub>.

### 3.3 – Dynamics of carbon monoxide

The equilibrium spectra of ferrous CO-liganded L16A-AXCP discloses a very sharp Soret absorption band after CO binding with a maximum at 418 nm (Figure 7a). The transient spectra after CO photodissociation from L16A-AXCP discloses a pronounced bleach at 416 nm (Figure 7b), similarly to WT-AXCP (Figure 7c) and an induced absorption centered at 434 nm characteristic of the 5c-His ferrous heme. The amplitude of the transient absorption and bleaching rapidly decreases within a few nanoseconds due to CO rebinding.

The kinetics of CO rebinding were fitted to a bi-exponential function (Figure 7d) and parameters are presented in Table 3. The time constants are about two times faster for the WT-AXCP ( $\tau_{G1} = 218$  ps and  $\tau_{G2} = 1.9$  ns) than for the mutant L16A-AXCP ( $\tau_{G1} = 543$  ps and  $\tau_{G2} = 3.6$  ns). The complete CO rebinding occurs in the case of the mutant L16A-AXCP and, in spite of fast time constants, CO cannot completely rebind to WT-AXCP, as reflected by the constant term (Figure 7e) which represents the proportion of CO which has left the interior of the protein and experiences bimolecular rebinding from the solvent.

To compare the bimolecular rebinding for both proteins, the dynamics of heme-CO interaction were recorded in a very broad time scale, from 1 ns to 30 s (Figure 7e). Since a fast geminate recombination occurs during the first 4 ns, several cycles of photodissociation and rebinding take place for the very same heme within the pulse duration (5 ns) in this kind

of experiment. This explains the apparently larger dissociation yield in the broad time range kinetics (Figure 7e) than in the ps-ns range kinetics (Figure 7d). This effect is smaller than for NO and O<sub>2</sub>.

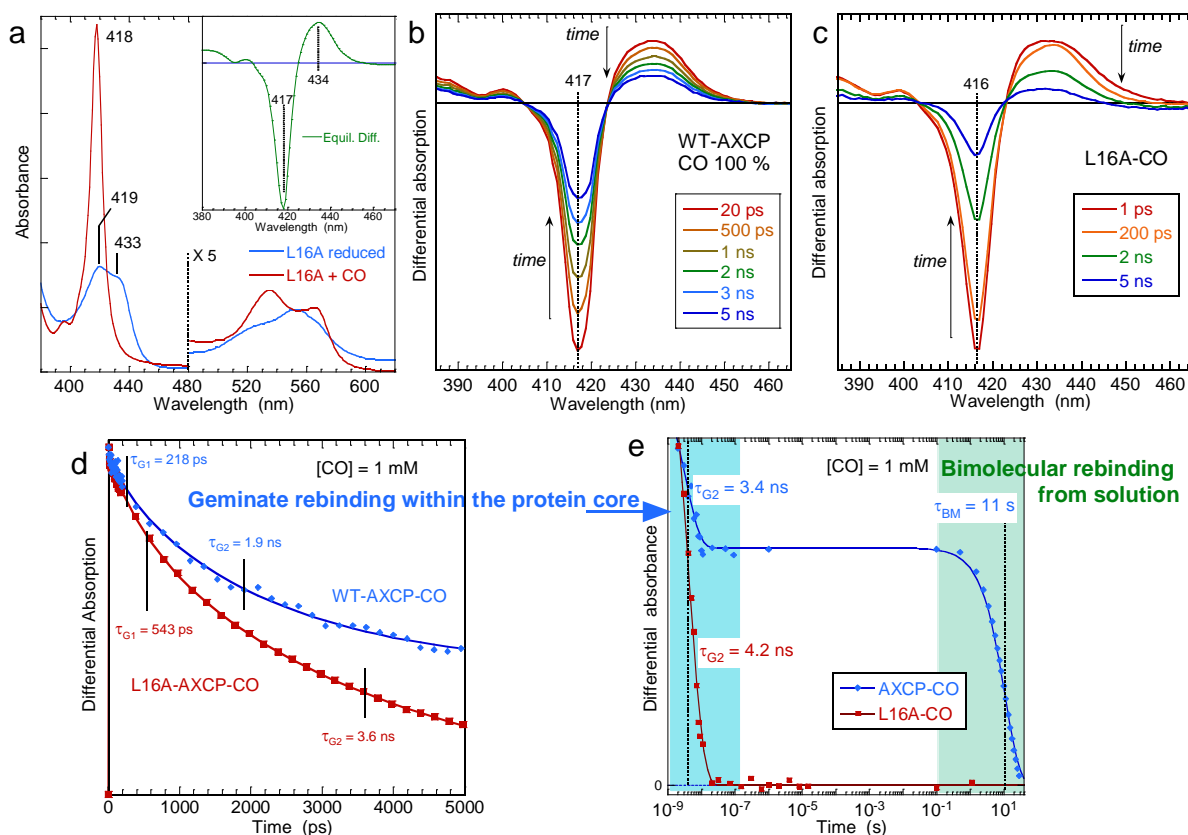


**Figure 7.** Broad time scale dynamics of CO to WT-AXCP and L16A-AXCP mutant. **(a)** Equilibrium spectra of ferrous L16A-AXCP unliganded (blue) and CO-liganded (red). Insert: the steady-state difference spectrum. **(b)** Transient absorption spectra at selected time delays after CO photodissociation from WT-AXCP recorded with a 50-fs probe pulse. **(c)** Transient absorption spectra for L16A-AXCP-CO. **(d)** Kinetics of CO rebinding to in the ps to 5-ns time range. After the initial rise a small decay with  $\tau_{ex} = 4.5$  ps is observed, due to the heme excited states relaxation. The curves through data points are fits to a bi-exponential function. **(e)** Kinetics of CO rebinding to WT-AXCP and L16A-AXCP probed at 434 nm in the ns to second time range. The curve is a mono-exponential fit for L16A-AXCP-CO and a bi-exponential fit for WT-AXCP-CO. The time origin was set to the maximum of the initial absorption rise. For all data the concentration was  $[CO] = 1$  mM.  $T = 20$  °C.

The induced absorbance conspicuously reaches zero for L16A-AXCP at  $\sim 20$  ns with a fitted time constant  $\tau_{G2} = 4.2$  ns (Figure 7e), corresponding to that measured ( $\tau_{G2} = 3.6$  ns) in the ps-ns time scale with the 50-fs pulse. In the case of WT-AXCP, after a 3.4-ns decay, a plateau is reached, which extends for about 8 orders of magnitude in time with no change of the signal amplitude, until the slow bimolecular rebinding of CO to WT-AXCP with a constant  $\tau_{BR} = 11$  s. Taking into account the ligand concentration  $[CO] = 1$  mM, this time exactly corresponds to the association rate  $k_{on} = 100 \text{ M}^{-1}\text{s}^{-1}$  [18].

**Table 3.** Parameters of CO rebinding to WT-AXCP and L16A-AXCP compared with other proteins.

Protein	CO geminate rebinding			Bimolecular rebinding	References
	$\tau_{4C}$ ( $A_1$ ) ( $a$ )	$\tau_{G1}$ ( $A_2$ )	$\tau_{G2}$ ( $A_3$ )	$A_4$ (%)	
L16A-AXCP	–	543 ps (18)	3.6 ns (82)	0	our work
WT AXCP	–	218 ps (4)	1.9 ns (58)	38	our work
sGC	6 ps (7)	120 ps (1)	5.7 ns (5)	87	[29]
sGC + BAY	6 ps (9)	90 ps (20)	1.2 ns (13)	58	[29]
Cb-SONO	7 ps (5)	100 ps (3)	8.0 ns (8)	84	[29]
WT Mb	–	–	180 ns (4)	96	[23]

$A_i$  (%) are the relative amplitudes of each exponential component. The excited state decay ( $\tau_{ex} = 4.5$  ps) was not taken into account for calculating the amplitude of CO rebinding phases.  $\tau_{4C}$  corresponds to the CO rebinding to the 4-coordinate heme.

Based on these results, the dynamics of CO within the heme pocket following its dissociation have been calculated up to 500 ps, using 32 trajectories for each protein. In these calculated dynamics, CO dissociated from the WT-AXCP moved away up to 15-20 Å from the heme Fe during 500 ps. In the case of the calculated trajectories in L16A-AXCP, the dissociated CO always stays at constant distance of 4 Å from the Fe atom during 500 ps (Figure 8b). The Fe has itself experienced a fast displacement of  $\sim 0.3$  Å after dissociation (in less than 100 fs) toward the proximal heme side. The fact that CO does not move away from Fe explains the absence of any measurable bimolecular rebinding from the solution in the case of L16A-AXCP. Accordingly, CO rebinds only geminately from within the heme pocket.

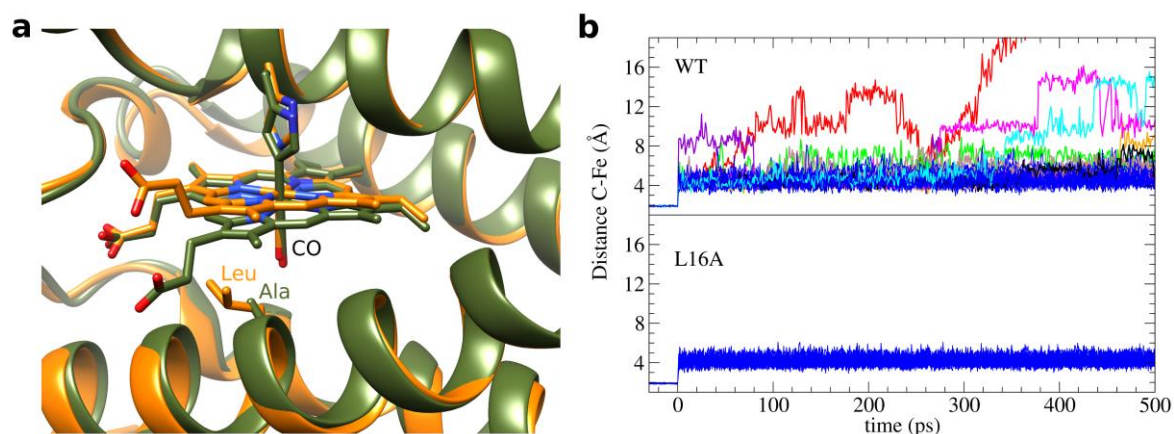


**Figure 8.** Molecular dynamics calculations. (a) Superposition of the heme pocket structures of WT-AXCP (orange) and L16A-AXCP mutant (green) with bound CO, after energy minimization. This figure was generated with Chimera (version 1.10.2). (b) Calculated trajectories after CO dissociation for both proteins with the CO position expressed as the atomic distance Fe-C. For both proteins, 32 dynamic trajectories (16 for each monomers) were calculated and are represented here.

There is no steric energy barrier for CO motion before binding back to Fe<sup>2+</sup> and the time constants ( $\tau_{G1} = 543$  ps and  $\tau_{G2} = 3.6$  ns) originate only from the need for waiting the Fe atom moved stochastically in the heme plane (due to thermal fluctuations) to allow CO binding [30]. Since CO stays at constant distance from the heme for both monomers of L16A-AXCP, the presence of two time constants probably originates from conformational fluctuations and not from differences between monomers because their relative amplitudes are not 50%.

The superposed structures of WT-AXCP and L16A-AXCP (Figure 8a) show that the distortion of the heme appears different in the two variants, with a propionate side-chain tilted toward the proximal side for the mutant. The smaller Ala side-chain allows the heme propionate to rotate, relaxing the heme, and no other supplementary steric constraints or other structural changes occurred, so that the potential well in which CO is held is induced by this distortion. This heme conformational relaxation explains that in 6c-NO form of L16A-AXCP the electronic trans effect due to NO is not sufficient to cleave the Fe-His bond.

### 3.4 – Internal dynamics and affinity

The single mutation of leucine to alanine in AXCP protein (L16A-AXCP) is responsible for a 10<sup>4</sup>-fold  $k_{on}$  increase and a 10<sup>4</sup>-fold  $k_{off}$  decrease for CO (10<sup>8</sup>-fold decrease of  $K_D$ ) which cannot be due to a change of steric barrier for CO diffusion which would slow down simultaneously the *on* and *off* CO dynamics.

**Table 4.** Kinetic parameters for 6c-NO and 6c-CO complexes of L16-AXCP variants.

Protein	$k_{on}$ NO (M <sup>-1</sup> s <sup>-1</sup> )	$k_{off}$ NO (s <sup>-1</sup> )	$K_D$ NO (M)	$k_{on}$ CO (M <sup>-1</sup> s <sup>-1</sup> )	$k_{off}$ CO (s <sup>-1</sup> )	$K_D$ CO (M)	Ref
WT AXCP	$4.4 \times 10^4$ (a)	$6 \times 10^{-3}$ (a)	$1.4 \times 10^{-7}$ (a)	101	$2.8 \times 10^{-2}$	$2.8 \times 10^{-4}$	[22, 31]
L16A	$2.9 \times 10^6$	$2 \times 10^{-7}$	$6.9 \times 10^{-14}$	$1.1 \times 10^6$	$3.7 \times 10^{-6}$	$3.4 \times 10^{-12}$	[22, 31]
L16G	–	–	$1.5 \times 10^{-11}$	$5 \times 10^5$	$7.4 \times 10^{-6}$	$1.5 \times 10^{-11}$	[18, 22]
sGC 6c-XO	$4.5 \times 10^8$	27	$1.7 \times 10^{-7}$	$4 \times 10^4$	10.7	$2.6 \times 10^{-4}$	[32, 33]
sGC 5c-NO (c)	$1.4 \times 10^8$	$6 \times 10^{-4}$	$4.3 \times 10^{-12}$	–	–	–	[27, 33]
heme model	$1.8 \times 10^8$	$2.9 \times 10^{-4}$	$1.6 \times 10^{-12}$	$1.1 \times 10^7$	$2.5 \times 10^{-2}$	$2.3 \times 10^{-9}$	[34, 35]
Mb	$2.2 \times 10^7$	$1 \times 10^{-4}$	$4.5 \times 10^{-12}$	$5.1 \times 10^5$	$1.9 \times 10^{-2}$	$3.7 \times 10^{-8}$	[36]

The discrimination between CO and NO in 5c-His heme proteins can be explained by diatomics electronic configurations. NO possesses an unpaired electron whereas CO has a pair of electrons, resulting in a high energy barrier for CO binding but a negligible one for NO [30,

37]. Consequently, NO can bind to  $\text{Fe}^{2+}$  positioned out of the heme plane (domed heme) [30] but CO has to wait for favorable fluctuations of the heme to become close to an in-plane conformation. The CO overall dissociation constant is the same for sGC and WT-AXCP ( $K_D = 2.6 \times 10^{-4}$  M) but for WT-AXCP both  $k_{\text{on}}$  and  $k_{\text{off}}$  rate constants are lower by a factor of 400, demonstrating the existence of a steric barrier for CO in WT-AXCP with respect to sGC [13] (Table 4).

The release of this barrier in L16A-AXCP is not sufficient for explaining the  $10^8$ -fold increase of CO affinity. Whereas the  $k_{\text{off}}$  of both CO and NO decreased by the same order of magnitude ( $\sim 10^4$ ), their  $k_{\text{on}}$  increased differently by factors of  $10^4$  and  $10^2$ , respectively, to reach similar values. Such behavior cannot be induced by the simple release of a steric hindrance, but agrees with a difference of the heme reactivity with CO and NO induced by a heme conformational change.

The geminate rebinding phases in the upper nanosecond time range are due to diatomic ligands which are located in the protein core but not within the heme pocket [38]. We did not observe component in the time range extending from  $5 \times 10^{-8}$  to  $10^{-1}$  s in the case of L16A-AXCP, whatever the diatomic (only a 54-ns component for NO with amplitude  $< 0.5\%$ ) until bimolecular rebinding. This again implies that diatomics are trapped in the heme pocket and forced to stay close to the heme, as demonstrated by molecular dynamics calculations (Figure 8b).

In the picosecond time range, the NO geminate rebinding to L16A-AXCP mutant is bi-exponential, like all 6-coordinate NO-heme (6c-NO) proteins, but is the more efficient (94%) ever measured in 6c-NO hemes. The faster time constant is similar to those of myoglobin and NO-synthase, but its relative amplitude (13.9 ps; 67%) is predominant, with no measurable exit of NO from the protein. A very low  $k_{\text{off}}$  ( $2 \times 10^{-7} \text{ s}^{-1}$ ) characterized by the confinement of NO in the distal heme pocket of L16A-AXCP. The very fast geminate NO rebinding to the 4c-heme in sGC [33] and in isolated heme is correlated with a NO  $k_{\text{off}}$  rate ( $6 \times 10^{-4}$  and  $2.9 \times 10^{-4} \text{ s}^{-1}$  respectively) which is one order of magnitude smaller than the  $k_{\text{off}}$  rate from the distal side in 6c-NO WT-AXCP ( $6 \times 10^{-3} \text{ s}^{-1}$ ) [31]. In 5c-NO proteins  $k_{\text{off}}$  is mainly determined by the reactivity of the 4c-heme whereas in 6c-NO proteins  $k_{\text{off}}$  is mainly determined by the partitioning between the heme pocket and the channel to solvent, controlled by steric barriers. The trapping of diatomics very closely to the heme iron appears here as another mechanism, at the origin of the very high affinity.

The overall  $\text{O}_2$  rebinding to L16A-AXCP appears much more efficient ( $\sim 95\%$ ) than to Mb ( $\sim 35\%$ ) as a consequence of the considerably decreased proportion of  $\text{O}_2$  exiting the distal heme pocket (5.2% versus 65%) revealing again a trapping of  $\text{O}_2$ . But the first component of  $\text{O}_2$  geminate rebinding to Mb- $\text{O}_2$  ( $\tau_1 = 6.3$  ps;  $A_1 = 28\%$ ) is similar to that of L16A-AXCP ( $\tau_1 = 7.5$  ps;  $A_1 = 27.5\%$ ). Only factors at the heme level intervene in the decrease of the  $k_{\text{off}}$  rate due to absence of H-bond in the distal heme pocket [18] which would stabilize bound  $\text{O}_2$ . The

mutation L16A confers to the heme pocket of AXCP the ability to retain diatomics within very close distance from the  $\text{Fe}^{2+}$ , so that the probability of rebinding after photoactivated or thermal dissociation is maximized and the probability of escape from the protein is minimized.

### 3.5 – Conclusion for AXCP affinity

The affinity between the three diatomic ligands CO, NO, and  $\text{O}_2$  is governed by steric hindrances in the access channel, by reactivity of the ligand XO with the ferrous heme and by ligand stabilization by hydrogen bonds pattern. Here, we have shown that a constraint at the heme level provided by a tilted propionate may force the three diatomics without discrimination to stay close to the iron, and constitutes a novel mechanism for modulating the heme-gas affinity in proteins.

## 4 – Dioxygen binding to the NO-sensor from *Thermoanaerobacter tengcongensis*

### 4.1 – Temperature dependence on heme coordination of *Tt*-H-NOX

The bacteria *Caldanaerobacter subterraneus subsp. Tengcongensis* is a strict anaerobe living at optimal temperature of 75 °C – 86 °C [39] and has a very high affinity for  $\text{O}_2$  (nM range) at room temperature [3]. *Tt*-H-NOX forms a stable 6c-NO complex at 20 °C [40] while the homologous sensing H-NOX domain of sGC forms a 5c-NO heme complex. Surprisingly, it was previously suggested that the  $\text{O}_2$ -bound *Tt*-H-NOX complex was stable up to 80°C [3]. We therefore investigated the influence of temperature on the ligation and redox states of the heme during the interaction of *Tt*-H-NOX with NO and  $\text{O}_2$  as a function of temperature. We then studied the dynamics of  $\text{O}_2$  binding to *Tt*-H-NOX in the pico- to millisecond time range.

First, the 6c-NO *Tt*-H-NOX complex was anaerobically prepared at 20 °C, resulting in a Soret band maximum at 420 nm (Figure 9A), then the temperature was increased step by step until 86 °C, recording a UV/visible spectrum at each stabilized temperature. After 70 °C the sample started to precipitate, inducing the shift of the isosbestic point at 403 nm and appearance of a slight scattering background. The 420 nm Soret band gradually decreases while simultaneously increasing at 398 nm, characteristic of a 5c-NO species (Figure 9A-B). These data prove that at high temperature, conditions where the bacteria lives, the isolated *Tt*-H-NOX domain forms mainly a stable 5c-NO species in which the  $\text{Fe}^{2+}$ -His coordination bond is broken, similarly to sGC at 20 °C. Increasing and decreasing the temperature from 20 °C to 60 °C three times with the same sample demonstrated the reversibility of the formation of 5c-NO species (Figure 9C and scheme in Figure 10).

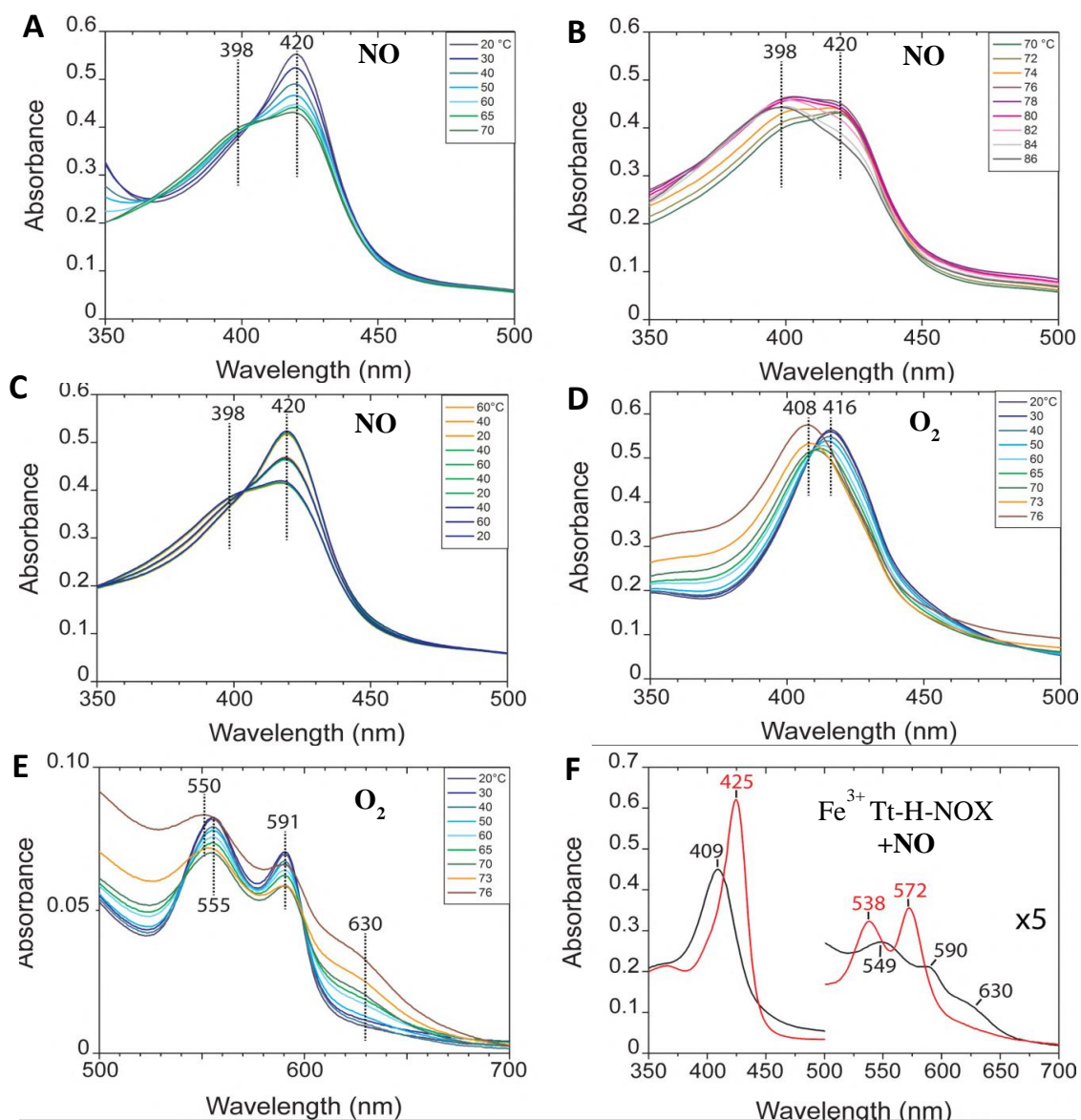


**Figure 9.** Temperature dependence on NO and O<sub>2</sub> binding monitored by UV-visible spectra. (A) NO-bound *Tt-H-NOX*<sup>191</sup> as a function of temperature from 20 to 70 °C. (B) From 70 to 86 °C. (C) Repeated temperature variation on the Fe(II)(NO) complex. (D) O<sub>2</sub>-bound *Tt-H-NOX*<sup>191</sup> as a function of temperature from 20 to 76 °C in the Soret band region and (E) In the Q-bands region. (F) Ferric *Tt-H-NOX*<sup>191</sup> (black line) and after addition of an equimolar amount of NO (red line).

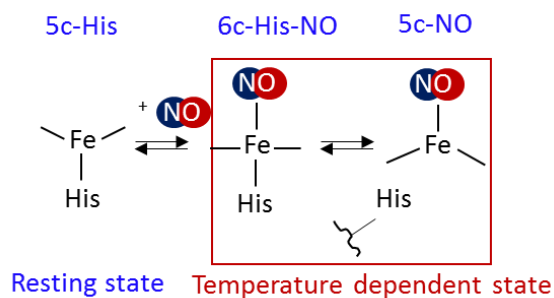


**Figure 10.** Change of iron coordination of the heme of *Tt-H-NOX*<sup>191</sup> under binding of NO.

Secondly, a 6c-O<sub>2</sub> *Tt*-H-NOX complex was aerobically prepared at 20 °C with a Soret band maximum at 416 nm and Q-bands at 555 and 591 nm, characteristic of a Fe(II)-(O<sub>2</sub>) species (Figure 9D-E). As the temperature was raised, the 416 nm Soret band decreased with a concomitant increase at 408 nm (Figure 9D), which reaches its maximum at 76 °C, after the protein started precipitating past 70 °C. The Soret band 408 nm is characteristic of the Fe(III)-(H<sub>2</sub>O) species of *Tt*-H-NOX, that is confirmed by the increase of the 630 nm charge transfer band as the temperature rises (Figure 9E).

Therefore, as a partial conclusion, the NO-bound *Tt*-H-NOX complex is more stable at high temperature with respect to oxidation than its molecular oxygen bound form.

Next, a degassed O<sub>2</sub>-bound *Tt*-H-NOX sample with low concentration of NO was prepared to probe whether NO could react on the Fe(II)(O<sub>2</sub>) species. In this case O<sub>2</sub> is still bound to the high affinity *Tt*-H-NOX but is absent from the gase phase. A red shift of the Soret band, from 409 to 425 nm, and a blue shift of the Q bands to 538 and 572 nm (Figure 9F). These values are the signature of a Fe(III)(NO) species, which is confirmed by comparison with the nitrophorin Fe(III)(NO) complexes for which the corresponding bands are at 422, 533 and 569 nm [41, 42] with very similar prominent Q bands. To confirm this result, an equimolar amount of NO was added to a prepared ferric *Tt*-H-NOX, resulting in a spectra which exactly matched that obtained from Fe(II)(O<sub>2</sub>) species with added NO (Figure 9F, black lines). Upon reduction with dithionite, this sample generated a characteristic 6c-Fe(II)NO spectra. We therefore concluded that in the presence of NO, the O<sub>2</sub>-bound *Tt*-H-NOX sample reacts quickly with a molecule of NO, then forms nitrate by oxidizing the heme iron like in myoglobin or hemoglobin [43].

#### 4.2 – Dynamics of dioxygen binding to *Tt*-H-NOX

It has been previously shown that for *Tt*-H-NOX bacterial protein, the proportion of 5c-NO and 6c-NO liganded forms depends upon the temperature and H-NOX proteins form a mixture of 5c-NO and 6c-NO liganded species, which is not found for sGC [8]. Furthermore, O<sub>2</sub> does bind to sGC, contrary to *Tt*-H-NOX. We thus analyzed the species generated after the photo-dissociation of O<sub>2</sub> from 6c-O<sub>2</sub> *Tt*-H-NOX.

In the equilibrium spectra of *Tt*-H-NOX measured before time-resolved experiment at room temperature, the Soret band at 416 nm corresponds to O<sub>2</sub>-bound heme of *Tt*-H-NOX (Figure 11A), similarly with the HbI-O<sub>2</sub> and Mb-O<sub>2</sub> complex [24]. The unliganded heme generated with the reductant dithionite has a Soret at 432 nm.

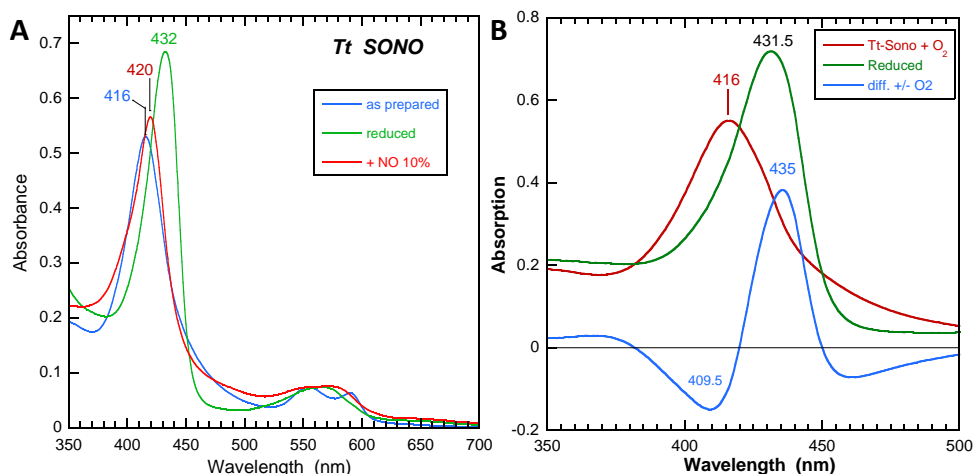


**Figure 11.** Equilibrium spectra of *Tt*-H-NOX protein before time-resolved measurements monitored by UV-visible spectra at RT. (A) Spectra before removing O<sub>2</sub> from *Tt*-H-NOX (Fe<sup>2+</sup>-O<sub>2</sub>), reduced form (Fe<sup>2+</sup>) and NO-bounded (Fe<sup>2+</sup>-NO). (B) Spectra of O<sub>2</sub>-bound *Tt*-H-NOX, its reduced form (Fe<sup>2+</sup>) and equilibrium difference between the two spectra.

We then performed time-resolved measurements at room temperature on this prepared 6c-O<sub>2</sub> form of *Tt*-H-NOX in two time ranges, in 0 – 200 ps with better time resolution for fast components, then in 0 – 5 ns to better define the longer kinetic components. The raw transient spectra are presented in Figure 12 AB. In both time ranges, two minima of bleaching (negative band) appeared after O<sub>2</sub> photodissociation, centered at 409 nm and 430 nm, and have opposite evolution at early time (< 200 ps): the amplitude of the first one decreases (arrows at 405 nm in Figure 12 AB) while the amplitude of the second increases up to ~30 ps and then remarkably decreases (curved arrow at 430 nm in Figure 12 B). The induced absorption presents a very broad and unstructured band around 450–470 nm which does not change with time (Figure 12 AB). The isosbestic points are shifted from 438 nm to 445 nm and at 395–400 nm in both time ranges, indicating that two different kinetic processes are involved after O<sub>2</sub> photodissociation. The broad band at 380–400 nm can be assigned to the ferric heme [24] and its appearance supports the identification of the second process as photo-oxidation. Its evolution parallels that of the bleaching band at 430 nm (Figure 12A). As we can see from the equilibrium difference spectra of O<sub>2</sub>-bound *Tt*-H-NOX (Figure 11B), a simple dissociation should have produced a reduced heme, thus an induced positive band at 435 nm. However O<sub>2</sub> photodissociation produced the ferric band at 409 nm band and the subsequent disappearance of the reduced heme (bleaching at 430 nm). We conclude that photo-oxidation occurs after O<sub>2</sub> dissociation together with a small amount of O<sub>2</sub> geminate rebinding.

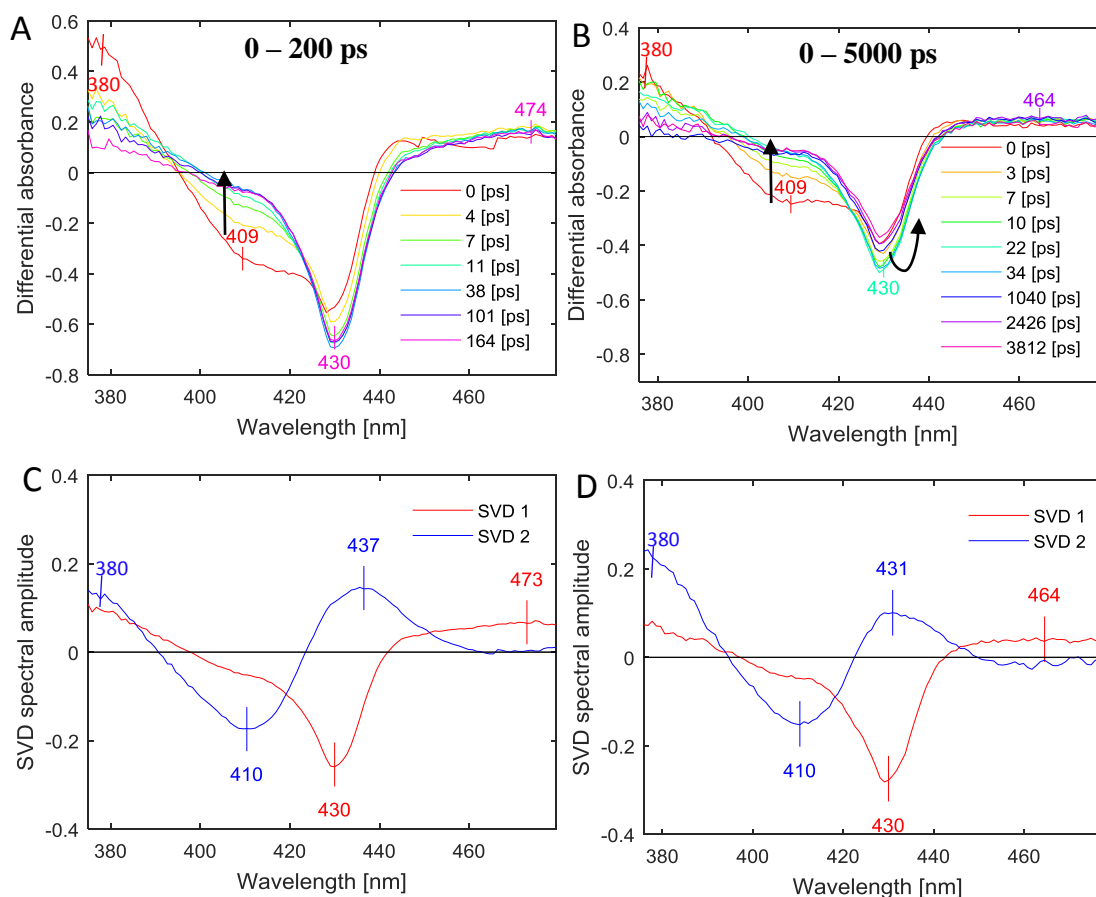


**Figure 12.** O<sub>2</sub> dynamics with *Tt*-SONO at 20 °C. (A, B) Raw transient absorption spectra at selected time delays showing that O<sub>2</sub> binding to the heme is being probed. (C, D) Two spectral component obtained after SVD analysis for the raw transient spectra data matrix. Panels A and C: dynamics up to 200 ps; B and D: up to 5 ns.

#### 4.2.1 – Interpretation of the spectral components

To rigorously identify the two simultaneous processes, a SVD analysis of the time-wavelength matrix was performed as we did for investigating the sGC activator (the principle of SVD calculation is described in CHAPTER VII). We obtained two distinct significant SVD components (Figure 12C, D). In SVD2 (lower singular value) the induced absorption at 437 nm is due to the formation of Fe(II) 5c-His state following O<sub>2</sub> photodissociation (Table 5). The bleaching at 409-410 nm in SVD2 component corresponds to disappearance of the Fe(II) 6c-O<sub>2</sub> species, so that the SVD2 spectrum is assigned to the geminate recombination of dioxygen.

In SVD1 (larger singular value), the negative absorbance at 430 nm indicates the disappearance of ferrous Fe(II) 5c-His. Because there is no band indicating the geminate rebinding of O<sub>2</sub> in SVD1, but a broad band centered at 380-390 nm (Figure 12C, D) assigned to a ferric heme, we concluded that SVD1 corresponds to photo-oxidation of the heme iron.

There exist two forms of ferric heme, the first one is 5-coordinate, having at a broad Soret band centered at 380-395 nm, whereas the 6-coordinate form has an H<sub>2</sub>O (or OH<sup>-</sup>) molecule bound on the distal side with a Soret usually positioned at 403-410 nm. In our case, because photo-oxidation occurred immediately after O<sub>2</sub> photodissociation, a H<sub>2</sub>O molecule cannot have time to diffuse and bind to the heme, a process which would take place in the lower  $\mu$ s time range. Consequently the bleaching centered at 410 nm is not due to the formation of a 6-coordinate Fe(III)-H<sub>2</sub>O heme, but to the disappearance of the Fe(II)-O<sub>2</sub> heme. After having separated the spectral contributions of the two processes, we will analyze their kinetics in the next section.

**Table 5.** The peak positions in absorption spectra of *Tt*-H-NOX.

Proteins	Coordination	Soret band (nm)	Q-band (nm)
<b>Unliganded</b>			
<b>sGC</b>	Fe(II) 5c-His	431.5	555
<b><i>Tt</i>-H-NOX</b>	Fe(II) 5c-His	431.5 – 432	566
<b><i>Tt</i>-H-NOX</b>	Fe(III) 5c-His	380 – 390	
<b>Heme-NO complex</b>			
<b>sGC</b>	Fe(II) 5c-NO	398	
<b><i>Tt</i>-H-NOX</b>	Fe(II) 6c-NO	420	548/575
	Fe(III) 6c-NO	425	538/572
<b>Heme-O<sub>2</sub> complex</b>			
<b><i>Tt</i>-H-NOX</b>	Fe(II) 6c-O <sub>2</sub>	416	555/591
	Fe(II) 6c-O <sub>2</sub>	409 – 410	
	Fe(II) 5c-His	437	

#### 4.2.2 – The kinetics of O<sub>2</sub> binding to *Tt*-H-NOX

The kinetics of each SVD component after O<sub>2</sub> photodissociation represent the evolution of the associated SVD spectral component. In both time ranges (1 – 200 ps and 1 ps – 5 ns) these kinetics were fitted using a bi-exponential function (Figure 13); adding a third exponential term did not improve the fit. The O<sub>2</sub> dynamics appear multiphasic throughout the time range and the parameters of fit are presented in Table 6. The kinetics of O<sub>2</sub> rebinding is better resolved in a short time scale whereas slower processes are better distinguished in the long-time range.

For SVD1 component, the kinetics consist of two phases of opposite sign, the first one is oxidation of the heme which occurs with time constant  $\tau_1 = 12 \pm 4$  ps better resolved in short time-range and the second kinetic component with opposite sign is heme reduction with time-constant  $\tau_2 = 1611 \pm 142$  ps better resolved in long time-range. This sequence of

processes was identified from spectra (Figure 12B), where differential absorbance at 430 nm first decreases, then increases.

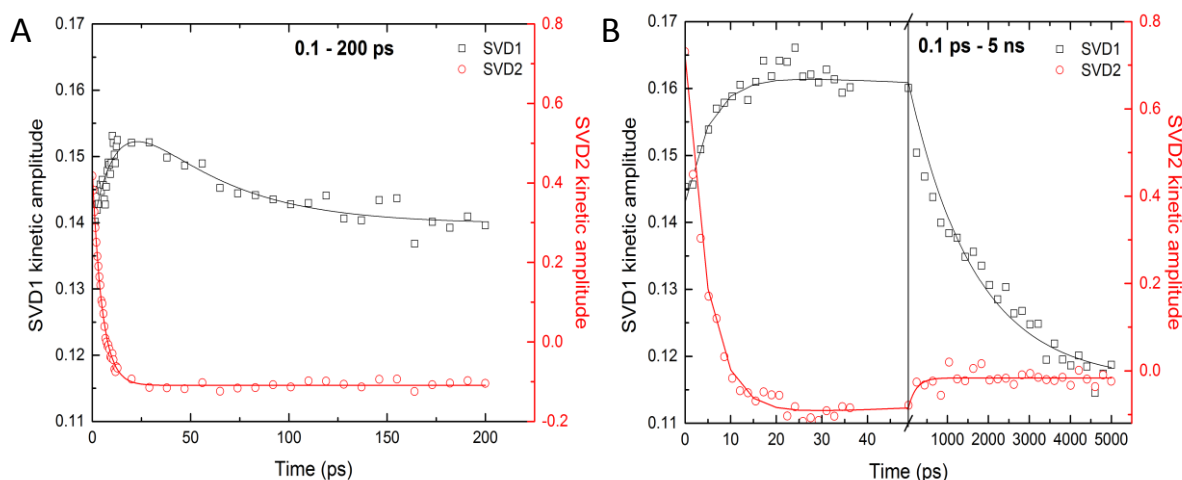


**Figure 13.** Kinetics of the two significant SVD components having larger singular value in short 0.1 – 200 ps (A) and in long 0.1 ps – 5 ns time ranges (B). The curves are fits to a multiexponential function:  $A(t) = \sum_i A_i \times \exp(-t/\tau_i) + A_c$  ( $i = 1, 2$ ) whose parameters are given in Table 6.

**Table 6.** Fit parameters for kinetics of O<sub>2</sub> photodissociation from *Tt* N-NOX

<i>Tt</i> -H-NOX - O <sub>2</sub>	Component	Time constant and Amplitude			Assignment
		$\tau_1$ $A_1$	$\tau_2$ $A_2$	Constant term $A_c$	
up to 200 ps	<i>SVD1</i>	$12 \pm 4.6$ ps 15 %	$45 \pm 19$ ps 15 %	70 %	Heme oxidation
	<i>SVD2</i>	$4.9 \pm 0.1$ ps 84 %	-	15.6 %	O <sub>2</sub> rebinding
up to 5 ns	<i>SVD1</i>	$5.5 \pm 1$ ps 10 %	$1611 \pm 142$ ps 27 %	63 %	Heme oxidation
	<i>SVD2</i>	$4.8 \pm 0.2$ ps 88 %	$189 \pm 90$ ps 9.8 %	2.2 %	O <sub>2</sub> rebinding

For SVD2, the O<sub>2</sub> rebinding to *Tt*-H-NOX in both time scales (Table 7) occurred with a fast time constant ( $\tau_1 = 4.8 \pm 0.2$  ps,  $A_1 = 88\%$ ) with a large amplitude similar to O<sub>2</sub> binding to myoglobin ( $\tau_1 = 6 - 6.3$  ps) but with different amplitudes [24]. The fast phase corresponds to O<sub>2</sub> rebinding from close vicinity to the heme iron ( $< 5$  Å) as we saw in Section 3 for AXCP. Again similarly with myoglobin a slower phase took place ( $\tau_2 = 189 \pm 90$  ps,  $A_2 = 9.8\%$ ) which corresponds to O<sub>2</sub> rebinding from farther location than for the fast phase. Therefore, the species 6c-Fe(II)-His-O<sub>2</sub> decreases and 5c-Fe(II)-His increases. In interpretation of SVD2 component, the amount of O<sub>2</sub> which exits in the protein and does not rebind geminately is quantified by the constant term  $A_c$ , which reaches 15.6% at a short-time

range kinetics and decreases down to 2.2% a long-time range kinetics. For SVD1,  $A_c$  represents the percentage of heme will not be reduced after 5 ns.

On the 5-ns time scale, the kinetic component with large time constant, indicates that the back reduction process is not completed but occurs on a much larger time after oxidation. The question arises as whether the back reduction of the heme occurs at the same time as  $O_2$  bimolecular rebinding.

To answer this question, we recorded the dynamics of  $O_2$  rebinding to ferrous 5c-His *Tt*-HNOX in the presence of 20 %  $O_2$  and 100 %  $O_2$  in the gas phase on the  $\mu$ s-ms time scale (Figure 14). We used the set-up at Laboratoire Physiologie Membranaire et Moléculaire du Chloroplaste (Institut de Biologie Physico-Chimique, Paris). This set-up consists of two electronically synchronized lasers (with 6-ns excitation and probe pulses) allowing to acquire kinetics from 1 ns to tens of seconds at individual wavelengths [19]. We recorded the kinetics at the Soret absorption wavelength of the ferrous 5c-His *Tt*-HNOX (434 nm) but we could not probe the decrease of the ferric 5c-His heme because its absorption wavelength (380 – 390 nm) is not accessible to this system.

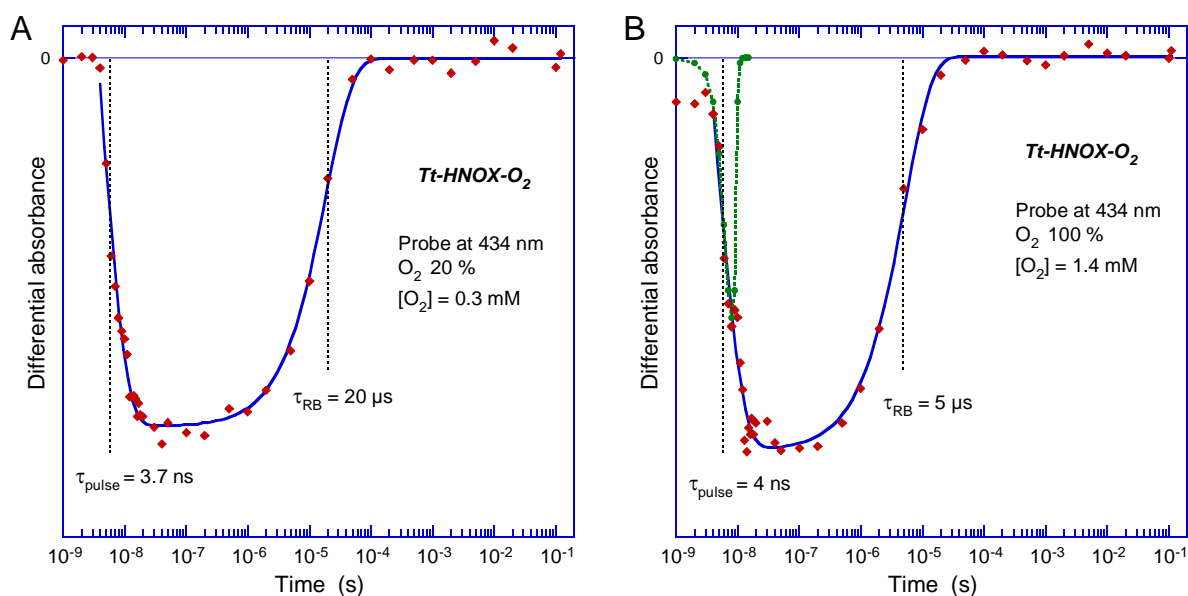


**Figure 14.** Dynamics of  $O_2$  rebinding to ferrous 5c-His *Tt*-HNOX on the  $\mu$ s-time scale recorded at 434 nm in the presence of 20 %  $O_2$  (A) and 100 %  $O_2$  (B) in the gas phase. In A, the sample cell was open to the air; in B pure  $O_2$  at 1 bar was used (Air Product). The kinetics could be fitted to only two exponential components. The first fast component ( $\tau_1 = 3.7 - 4$  ns) corresponds to the leading edge of the 6-ns pulse and thus to the rise of the signal (the gaussian pulse is indicated in green in panel B). The second one is assigned to  $O_2$  bimolecular rebinding from the solution since it varies accordingly to the  $O_2$  concentration ( $\tau_2 = 20$  and  $5$   $\mu$ s).

The first obvious observation is the negative absorption change at the 5c-Fe(II)-His heme wavelength, exactly as probed in ps-ns time range, which confirms its disappearance and oxidation to 5c-Fe(III)-His. Due to the time resolution (6 ns) the fast ps geminate rebinding cannot be observed here. After a rise of the signal ( $\tau_1 = 3.7 - 4$  ns) which is due to

the pulse shape and duration (green gaussian curve in Figure 14B), only one exponential component could be identified. Importantly, its time constant varies as a function of O<sub>2</sub> concentration:  $\tau_2 = 20 \mu\text{s}$  at 0.3 mM and  $\tau_2 = 5 \mu\text{s}$  at 1.4 mM in solution. This fact allows to readily assign the transition to O<sub>2</sub> bimolecular rebinding from the solution, whose association rate can be calculated:  $k_{\text{on}} = (1.5 \pm 0.2) \times 10^8 \text{ M}^{-1}\text{s}^{-1}$  (at 20 °C), a value 3.5 times larger than reported data measured by stopped-flow [44] with a steady-state 5c-His ferrous heme. This very high rate indicates the absence of steric barrier and a diffusion controlled O<sub>2</sub> binding. Importantly, we note that our measurement was performed after photo-oxidation of the *Tt*-H-NOX heme and that here O<sub>2</sub> rebinds to a non-equilibrium system, which may react faster than the steady-state 5c-His ferrous heme. We must note that X-ray crystal structures indicate that O<sub>2</sub> binding to the heme of *Tt*-H-NOX does not induce the same heme distortion as CO and NO do [*personal communication from Dr. Pierre Nioche, unpublished data*], a property which may change the heme redox potential.

The partial conclusion from this measurement is consequently that the back reduction of the heme occurs simultaneously with O<sub>2</sub> bimolecular rebinding. Further experiments are necessary to identify the electron acceptor within this H-NOX domain. This aim will be reached by comparing the behavior of single mutants in the distal heme pocket.

### 4.3 – Hypothesis of the physiological role of *Tt*-H-NOX

Bacterial H-NOX proteins from obligate anaerobes are encoded as domains of transmembrane methyl-accepting chemotaxis proteins (MCP). Unlike other NO-sensing H-NOX domains, *Thermoanaerobacter tengcongensis* (*Tt*-H-NOX) protein from this subfamily forms a high-affinity, stable 6-coordinate Fe(II)-O<sub>2</sub> complex. Some studies showed that a conserved H-bonding network composed of tyrosine Y140, tryptophan W9 and asparagine N74 residues is directly involved in O<sub>2</sub> binding [4, 45]. Substitution of Y140 with a hydrophobic residue (Y140L or Y140F) decreases affinity for O<sub>2</sub>, and a double mutant (Y140L/W9F) has no measurable affinity for O<sub>2</sub> [3, 45]. In addition, three of these residues are not present in H-NOX proteins that do not bind O<sub>2</sub> [45]. One of these side-chains could be the electron acceptor from the heme when in its excited electronic state in presence of O<sub>2</sub>. In general, the function of bacterial H-NOX proteins is still poorly understood. Several hypothesis about the role of *Tt*-H-NOX protein from obligate anaerobes exist, suggesting a mechanism for self-defense and a sensor for chemotaxis signaling.

The fusion of proteins H-NOX-MCP encoded by *Thermoanaerobacter tengcongensis* may signal for a repellent chemotactic response to acute concentrations of NO or O<sub>2</sub>, which would be toxic [46, 47], especially at high temperature. Alternatively, the H-NOX-MCP may act as a form of nutrient sensing for CO since *Tt*-H-NOX also forms a stable Fe(II)-CO complex and *Tt* can be oxidized by CO [48]. Some studies proposed that *Tt*-H-NOX may

function as NO sensors [20], forming 6-coordinate Fe(II)-NO complex at room temperature and a 5-coordinate Fe(II)-NO at growing temperature (75 – 85 °C).

We have observed two features of *Tt*-H-NOX domain. First, it appears less stable as the temperature is increased in presence of O<sub>2</sub>, keeping in mind that *Tt* lives at high temperature. Secondly, when photodissociation of O<sub>2</sub> occurs at room temperature, the ferric heme state is generated with the slow recovery of ferrous state as O<sub>2</sub> rebinds. It was not possible here to identify the electron acceptor. We must also note that known homologs H-NOX domains from other bacteria do not behave like *Tt*-H-NOX, which is the unique in this case. *Tt*-H-NOX binds NO with smaller dissociation constant ( $K_D^{NO} = 2.3 \times 10^{-11}$  M) than O<sub>2</sub> ( $K_D^{O_2} = 4.4 \times 10^{-8}$  M) and CO ( $K_D^{CO} = 1.6 \times 10^{-7}$  M) (Table 6).

We defined an oxidation factor ( $\gamma_{oxid}$ ) which represents the proportion of ferric heme generated by photodissociation of O<sub>2</sub> which is in first approximation the ratio SVD1/SVD2 (Table 7). This factor for *Tt*-H-NOX is smaller in presence of NO ( $\gamma_{oxid} = 1.92$ ) than in the presence of O<sub>2</sub> ( $\gamma_{oxid} = 5.9$  up to 200 ps and  $\gamma_{oxid} = 10$  up to 5 ns). This property confirms that the NO-bound *Tt*-H-NOX complex is more stable with respect to oxidation than the molecular oxygen complex. Although the affinity of O<sub>2</sub> for *Tt*-H-NOX is highest compared to other H-NOX proteins (Table 7). As the temperature increases, the solubility of O<sub>2</sub> in H<sub>2</sub>O decreases (by a factor of ~2 at 76 °C) and it is crucial for the bacteria *Tt* to control its position with respect to O<sub>2</sub> gradient.

**Table 7.** Ratio of SVD components for NO and O<sub>2</sub> binding to *Tt*-H-NOX at RT and  $K_D$ .

Species	$\gamma_{oxid} = \text{SVD1/SVD2}$	Reference	$K_D$ (M)	Reference
<i>Tt</i> -H-NOX/NO	1.92	[8]	$2.3 \times 10^{-11}$	[44, 49]
<i>Tt</i> -H-NOX/O <sub>2</sub>	5.9 (up to 200 ps) 10 (up to 5 ns)	This work	$4.4 \times 10^{-8}$	
<i>Tt</i> -H-NOX/CO	-	-	$1.6 \times 10^{-7}$	[49]
<i>Cb</i> H-NOX/ O <sub>2</sub>			$5.3 \times 10^{-5}$	
<i>Ns</i> H-NOX/ O <sub>2</sub>			$1.3 \times 10^{-2}$	
<i>So</i> H-NOX/ O <sub>2</sub>			$4.5 \times 10^{-3}$	
<i>Vc</i> H-NOX/ O <sub>2</sub>			$1.3 \times 10^{-3}$	
HbI/O <sub>2</sub>			$0.3\text{-}0.6 \times 10^{-6}$	[24]

Abbreviations: *Tt*: *Thermoanaerobacter tengcongensis*, *Cb*: *Clostridium botulinum*, *Ns*: *Nostoc* sp, *So*: *Shewanella oneidensis*, *Vc*: *Vibrio cholera*, Mb: myoglobin.

Possibly, *Tt*-H-NOX is involved in such control and the protein response may take place through a change of its redox state. Therefore, the properties of H-NOX domain from *Tt*-H-NOX is not compatible with the role a mere NO-carrier.

## 5 – Conclusions

We showed that bacterial heme nitric oxide binding protein from *Thermoanaerobacter tengcongensis* (*Tt*-H-NOX) and NO sensor cytochrome *c'* from *Alcaligenes xylosoxidans* (AXCP) behave differently with diatomic gases. They have different tertiary folds and probably different functions.

The single change of only one amino acid residue leucine to alanine in AXCP, increases the affinity for gas ligands by a remarkable  $10^6 - 10^8$ -fold. This mutation dramatically changed the kinetics for the three diatomic gaseous ligands NO, O<sub>2</sub> and CO, with a complete CO and NO rebinding for the mutant L16A-AXCP, contrary to WT-AXCP.

A new way of controlling the ligand affinity is discovered: dissociated diatomics is forced to stay within 4 Å from Fe<sup>2+</sup>, contrarily to wild-type AXCP, maximizing the probability of recombination and directly explaining the highest affinities measured for CO, NO and O<sub>2</sub>.

In the case of the heme sensor *Tt*-H-NOX, the protein forms a mixture of 5c-NO and 6c-NO liganded species depending upon the temperature, which is not found for sGC. We could observed the following properties of this sensor:

- 1 - Although the affinity of O<sub>2</sub> for *Tt*-H-NOX is the highest compared to other H-NOX proteins, when photodissociation of O<sub>2</sub> from *Tt*-H-NOX occurs, the ferric heme state is generated with the slow recovery of ferrous state. This unusual properties is not found in any other heme sensor.
- 2 - We defined an oxidation factor ( $\gamma_{\text{oxid}}$ ) for *Tt*-H-NOX which is higher in presence of O<sub>2</sub> ( $\gamma_{\text{oxid}} = 5.9$ ) than in the presence of NO ( $\gamma_{\text{oxid}} = 1.92$ ).
- 3 - The back reduction of the heme occurs simultaneously with O<sub>2</sub> bimolecular rebinding.

The properties of *Tt*-H-NOX domain is not compatible with the role a simple NO-carrier. Our spectroscopic experiments showed that *Tt*-H-NOX may not be a NO-sensor *stricto sensu* but a redox sensor, changing its redox state in the presence of NO or O<sub>2</sub> in a certain temperature range, when the bacteria encounters particular conditions in its environment. To ascertain this hypothesis, more studies are required.

## 6 – Bibliography

1. Boon, E. M.; Marletta, M. A. Ligand specificity of H-NOX domains: from sGC to bacterial NO sensors. *J Inorg Biochem.* **2005**, 99, 892-902.
2. Shimizu, T.; Huang, D.; Yan, F.; Stranova, M.; Bartosova, M.; Fojtikova, V.; Martinkova, M. Gaseous O<sub>2</sub>, NO, and CO in signal transduction: structure and function relationships of heme-based gas sensors and heme-redox sensors. *Chem Rev.* **2015**, 115, 6491-533.
3. Boon, E. M.; Huang, S. H.; Marletta, M. A. A molecular basis for NO selectivity in soluble guanylate cyclase. *Nat Chem Biol* **2005**, 1, 53-59.

4. Pellicena, P.; Karow, D. S.; Boon, E. M.; Marletta, M. A.; Kuriyan, J. Crystal structure of an oxygen-binding heme domain related to soluble guanylate cyclases. *Proceedings of the National Academy of Sciences of the United States of America*. **2004**, 101, 12854-12859.
5. Ma, X.; Sayed, N.; Beuve, A.; van den Akker, F. NO and CO differentially activate soluble guanylyl cyclase via a heme pivot-bend mechanism. *The EMBO Journal*. **2007**, 26, 578-588.
6. Erbil, W. K.; Price, M. S.; Wemmer, D. E.; Marletta, M. A. A structural basis for H-NOX signaling in *Shewanella oneidensis* by trapping a histidine kinase inhibitory conformation. *Proc Natl Acad Sci U S A* **2009**, 106, 19753-60.
7. Gong, W.; Hao, B.; Chan, M. K. New mechanistic insights from structural studies of the oxygen-sensing domain of *Bradyrhizobium japonicum* FixL. *Biochemistry* **2000**, 39, 3955-62.
8. Yoo, B.-K. Investigation of the mechanisms of regulations, activation, and deactivation of Guanylate Cyclase, the endogenous NO-receptor, and NO-sensors. Ecole Polytechnique X, 2010.
9. Yoshimura, T.; Fujii, S.; Kamada, H.; Yamaguchi, K.; Suzuki, S.; Shidara, S.; Takakuwa, S. Spectroscopic characterization of nitrosylheme in nitric oxide complexes of ferric and ferrous cytochrome *c'* from photosynthetic bacteria. *Biochim Biophys Acta*. **1996**, 1292, 39-46.
10. Messerschmidt, A.; Huber, R.; Wieghardt, K.; Cygler, M.; Poulos, T.; Bode, W. *Handbook of Metalloproteins*. **2001**, 1-2, 1472.
11. Meyer, T. E.; Cheddar, G.; Bartsch, R. G.; Getzoff, E. D.; Cusanovich, M. A.; Tollin, G. Kinetics of electron transfer between cytochromes *c'* and the semiquinones of free flavin and clostridial flavodoxin. *Biochemistry*. **1986**, 25, 1383-90.
12. Lawson, D. M.; Stevenson, C. E.; Andrew, C. R.; Eady, R. R. Unprecedented proximal binding of nitric oxide to heme: implications for guanylate cyclase. *Embo. J*. **2000**, 19, 5661-71.
13. Andrew, C. R.; Petrova, O. N.; Lamarre, I.; Lambry, J.-C.; Rappaport, F.; Negrierie, M. The Dynamics Behind the Affinity: Controlling Heme-Gas Affinity via Geminant Recombination and Heme Propionate Conformation in the NO Carrier Cytochrome *c'*. *ACS Chemical Biology*. **2016**, 11, 3191-3201.
14. Andrew, C. R.; George, S. J.; Lawson, D. M.; Eady, R. R. Six- to five-coordinate heme-nitrosyl conversion in cytochrome *c'* and its relevance to guanylate cyclase. *Biochemistry*. **2002**, 41, 2353-60.
15. Nioche, P.; Berka, V.; Vipond, J.; Minton, N.; Tsai, A. L.; Raman, C. S. Femtomolar sensitivity of a NO sensor from *Clostridium botulinum*. *Science*. **2004**, 306, 1550-3.
16. Kekilli, D.; Petersen, C. A.; Pixton, D. A.; Ghafoor, D. D.; Abdullah, G. H.; Dworkowski, F. S. N.; Wilson, M. T.; Heyes, D. J.; Hardman, S. J. O.; Murphy, L. M.; Strange, R. W.; Scrutton, N. S.; Andrew, C. R.; Hough, M. A. Engineering proximal vs. distal heme-NO coordination via dinitrosyl dynamics: implications for NO sensor design. *Chemical Science* **2017**, 8, 1986-1994.
17. Garton, E. M.; Pixton, D. A.; Petersen, C. A.; Eady, R. R.; Hasnain, S. S.; Andrew, C. R. A distal pocket Leu residue inhibits the binding of O<sub>2</sub> and NO at the distal heme site of cytochrome *c'*. *J Am Chem Soc* **2012**, 134, 1461-3.
18. Antonyuk, S. V.; Rustage, N.; Petersen, C. A.; Arnst, J. L.; Heyes, D. J.; Sharma, R.; Berry, N. G.; Scrutton, N. S.; Eady, R. R.; Andrew, C. R.; Hasnain, S. S. Carbon monoxide poisoning is prevented by the energy costs of conformational changes in gas-binding haemproteins. *Proc Natl Acad Sci USA*. **2011**, 108, 15780-5.
19. Béal, D.; Rappaport, F.; Joliot, P. A new high-sensitivity 10-ns time-resolution spectrophotometric technique adapted to in vivo analysis of the photosynthetic apparatus. *Review of scientific instruments*. **1999**, 70, 202-207.
20. Karow, D. S.; Pan, D.; Tran, R.; Pellicena, P.; Presley, A.; Mathies, R. A.; Marletta, M. A. Spectroscopic Characterization of the Soluble Guanylate Cyclase-like Heme Domains from *Vibrio cholerae* and *Thermoanaerobacter tengcongensis*. *Biochemistry*. **2004**, 43, 10203-10211.

21. Hough, M. A.; Andrew, C. R. Cytochromes c': Structure, Reactivity and Relevance to Haem-Based Gas Sensing. *Advances in Microbial Physiology*. **2015**, 67, 1-84.
22. Garton, E. M.; Pixton, D. A.; Petersen, C. A.; Eady, R. R.; Hasnain, S. S.; Andrew, C. R. A distal pocket Leu residue inhibits the binding of O<sub>2</sub> and NO at the distal heme site of cytochrome c'. *Journal of the American Chemical Society*. **2012**, 134, 1461-1463.
23. Kruglik, S. G.; Yoo, B. K.; Franzen, S.; Vos, M. H.; Martin, J. L.; Negrerie, M. Picosecond primary structural transition of the heme is retarded after nitric oxide binding to heme proteins. *Proc Natl Acad Sci USA*. **2010**, 107, 13678-83.
24. Ramos-Alvarez, C.; Yoo, B. K.; Pietri, R.; Lamarre, I.; Martin, J. L.; Lopez-Garriga, J.; Negrerie, M. Reactivity and dynamics of H<sub>2</sub>S, NO, and O<sub>2</sub> interacting with hemoglobins from *Lucina pectinata*. *Biochemistry*. **2013**, 52, 7007-21.
25. Yoo, B.-K.; Lamarre, I.; Martin, J.-L.; Andrew, C. R.; Negrerie, M. Picosecond Binding of the His Ligand to Four-Coordinate Heme in Cytochrome c': A One-Way Gate for Releasing Proximal NO. *Journal of the American Chemical Society*. **2013**, 135, 3248-3254.
26. Kruglik, S. G.; Lambry, J.-C.; Cianetti, S.; Martin, J.-L.; Eady, R. R.; Andrew, C. R.; Negrerie, M. Molecular basis for nitric oxide dynamics and affinity with *Alcaligenes xylosoxidans* cytochrome c. *Journal of Biological Chemistry*. **2007**, 282, 5053-5062.
27. Yoo, B.-K.; Lamarre, I.; Martin, J.-L.; Rappaport, F.; Negrerie, M. Motion of proximal histidine and structural allosteric transition in soluble guanylate cyclase. *Proceedings of the National Academy of Sciences*. **2015**, 112, E1697-E1704.
28. Negrerie, M.; Berka, V.; Vos, M. H.; Liebl, U.; Lambry, J.-C.; Tsai, A.-L.; Martin, J.-L. Geminate recombination of nitric oxide to endothelial nitric-oxide synthase and mechanistic implications. *Journal of Biological Chemistry*. **1999**, 274, 24694-24702.
29. Yoo, B. K.; Lamarre, I.; Rappaport, F.; Nioche, P.; Raman, C. S.; Martin, J. L.; Negrerie, M. Picosecond to second dynamics reveals a structural transition in *Clostridium botulinum* NO-sensor triggered by the activator BAY-41-2272. *ACS Chem Biol*. **2012**, 7, 2046-54.
30. Ionascu, D.; Gruia, F.; Ye, X.; Yu, A.; Rosca, F.; Beck, C.; Demidov, A.; Olson, J. S.; Champion, P. M. Temperature-dependent studies of NO recombination to heme and heme proteins. *Journal of the American Chemical Society*. **2005**, 127, 16921-16934.
31. Pixton, D. A.; Petersen, C. A.; Franke, A.; van Eldik, R.; Garton, E. M.; Andrew, C. R. Activation parameters for heme-NO binding in *alcaligenes xylosoxidans* cytochrome c': the putative dinitrosyl intermediate forms via a dissociative mechanism. *J Am Chem Soc*. **2009**, 131, 4846-53.
32. Tsai, A.-L.; Berka, V.; Martin, E.; Olson, J. S. A "sliding scale rule" for selectivity among NO, CO, and O<sub>2</sub> by heme protein sensors. *Biochemistry*. **2011**, 51, 172-186.
33. Yoo, B. K.; Lamarre, I.; Martin, J. L.; Negrerie, M. Quaternary structure controls ligand dynamics in soluble guanylate cyclase. *J Biol Chem*. **2012**, 287, 6851-9.
34. Tani, F.; Matsu-ura, M.; Ariyama, K.; Setoyama, T.; Shimada, T.; Kobayashi, S.; Hayashi, T.; Matsuo, T.; Hisaeda, Y.; Naruta, Y. Iron twin-coronet porphyrins as models of myoglobin and hemoglobin: amphibious electrostatic effects of overhanging hydroxyl groups for successful CO/O<sub>2</sub> discrimination. *Chemistry*. **2003**, 9, 862-70.
35. Laverman, L. E.; Ford, P. C. Mechanistic studies of nitric oxide reactions with water soluble iron(II), cobalt(II), and iron(III) porphyrin complexes in aqueous solutions: implications for biological activity. *J Am Chem Soc*. **2001**, 123, 11614-22.
36. Springer, B. A.; Sligar, S. G.; Olson, J. S.; Phillips, G. N., Jr. Mechanisms of Ligand Recognition in Myoglobin. *Chemical Reviews*. **1994**, 94, 699-714.
37. Franzen, S. Spin-dependent mechanism for diatomic ligand binding to heme. *Proceedings of the National Academy of Sciences*. **2002**, 99, 16754-16759.

38. Sugimoto, T.; Unno, M.; Shiro, Y.; Dou, Y.; Ikeda-Saito, M. Myoglobin mutants giving the largest geminate yield in CO rebinding in the nanosecond time domain. *Biophys J.* **1998**, *75*, 2188-94.
  39. Xue, Y.; Xu, Y.; Liu, Y.; Ma, Y.; Zhou, P. Thermoanaerobacter tengcongensis sp. nov., a novel anaerobic, saccharolytic, thermophilic bacterium isolated from a hot spring in Tengcong, China. *Int J Syst Evol Microbiol* **2001**, *51*, 1335-41.
  40. Nioche, P.; Berka, V.; Vipond, J.; Minton, N.; Tsai, A.-L.; Raman, C. S. Femtomolar Sensitivity of a NO Sensor from Clostridium botulinum. *Science* **2004**, *306*, 1550-1553.
  41. Champagne, D. E.; Nussenzveig, R. H.; Ribeiro, J. M. Purification, partial characterization, and cloning of nitric oxide-carrying heme proteins (nitrophorins) from salivary glands of the blood-sucking insect Rhodnius prolixus. *J Biol Chem* **1995**, *270*, 8691-5.
  42. Andersen, J. F.; Champagne, D. E.; Weichsel, A.; Ribeiro, J. M.; Balfour, C. A.; Dress, V.; Montfort, W. R. Nitric oxide binding and crystallization of recombinant nitrophorin I, a nitric oxide transport protein from the blood-sucking bug Rhodnius prolixus. *Biochemistry* **1997**, *36*, 4423-8.
  43. Gardner, P. R. Nitric oxide dioxygenase function and mechanism of flavohemoglobin, hemoglobin, myoglobin and their associated reductases. *J Inorg Biochem* **2005**, *99*, 247-66.
  44. Wu, G.; Liu, W.; Berka, V.; Tsai, A. L. H-NOX from Clostridium botulinum, like H-NOX from Thermoanaerobacter tengcongensis, Binds Oxygen but with a Less Stable Oxyferrous Heme Intermediate. *Biochemistry* **2015**, *54*, 7098-109.
  45. Hespen, C. W.; Bruegger, J. J.; Phillips-Piro, C. M.; Marletta, M. A. Structural and Functional Evidence Indicates Selective Oxygen Signaling in Caldanaerobacter subterraneus H-NOX. *ACS Chem Biol* **2016**, *11*, 2337-46.
  46. Reddy, D.; Lancaster, J. R., Jr.; Cornforth, D. P. Nitrite inhibition of Clostridium botulinum: electron spin resonance detection of iron-nitric oxide complexes. *Science* **1983**, *221*, 769-70.
  47. Imlay, J. A. Pathways of oxidative damage. *Annu Rev Microbiol* **2003**, *57*, 395-418.
  48. Fardeau, M. L.; Bonilla Salinas, M.; L'Haridon, S.; Jeanthon, C.; Verhe, F.; Cayol, J. L.; Patel, B. K.; Garcia, J. L.; Ollivier, B. Isolation from oil reservoirs of novel thermophilic anaerobes phylogenetically related to Thermoanaerobacter subterraneus: reassignment of T. subterraneus, Thermoanaerobacter yonseiensis, Thermoanaerobacter tengcongensis and Carboxydibrachium pacificum to Caldanaerobacter subterraneus gen. nov., sp. nov., comb. nov. as four novel subspecies. *Int J Syst Evol Microbiol* **2004**, *54*, 467-74.
  49. Wu, G.; Liu, W.; Berka, V.; Tsai, A. L. Gaseous ligand selectivity of the H-NOX sensor protein from Shewanella oneidensis and comparison to those of other bacterial H-NOXs and soluble guanylyl cyclase. *Biochimie* **2017**, *140*, 82-92.
-



## CHAPTER VI

### OVERVIEW AND PERSPECTIVES

In this thesis we focused on the activation and deactivation of soluble guanylate cyclase by natural and artificial compounds which are linked to pathological processes. The involvement of NO-cGMP-sGC system in proliferation, angiogenesis and tumor formation motivates the search for inhibitors of sGC, which might serve as a basis for the creation of new drugs able to slow down tumor progression. Such inhibitors are currently absent.

In CHAPTER III we focused on the discovery of new active compounds for sGC. The screening of natural compounds from a chemical library, tested on purified sGC activity, revealed six active inhibitors ( $IC_{50} = 0.2 - 1 \mu M$ ). We demonstrated that two inhibitors oxidize the heme of sGC whereas others act allosterically and bind neither to the heme nor to the catalytic and activator sites, revealing a new class of pharmacological compounds targeting the NO/cGMP signaling pathway. These inhibitors can be used as tools to study the NO-cGMP-sGC in cells and tissues and also serve as structural lead compounds to derive drugs. The binding site of four inhibitors remains unknown and we plan future spectroscopic experiments (Raman) to find this site (noting that such experiments will require a large amount of protein).

The NO-cGMP-sGC signaling pathway is also involved in resistance to apoptosis in many kinds of human cancers [1-5]. A valuable perspective would be to study the effect of inhibitors on these cancer cells. The insight that tumor growth requires angiogenesis led to the development of angiogenesis inhibitors as cancer therapeutics. Such drugs for the treatment of several cancers are already approved [6]. Our preliminary study of inhibitors effects on angiogenesis with human skin mature endothelial cells (HskMEC) must be continued.

Hypertension has been extensively studied and specific sGC activators were discovered (Bayer). One was recently medically approved to treat pulmonary hypertension (riociguat, commercial name Adempas). These compounds have revealed the existence of an allosteric site on sGC, but there is no consensus on their mode of action on sGC at the molecular level.

CHAPTER IV was devoted to the study of the mechanism of sGC activation by the drug commercial riociguat. We measured  $EC_{50}$  of riociguat towards purified sGC ( $EC_{50} = 9.5 \mu M$ ) that was never reported despite its status of commercial drug. Taking advantage of the synergistic activation between CO and riociguat and using time-resolved absorption spectroscopy, we showed that the extent of cleavage of the Fe-His bond depends on the presence and on the nature of the activators. Two different states of sGC, 6c-CO and 5c-CO

heme, can exist simultaneously in the presence of the activators and we proposed a model for the mechanism of sGC allosteric activators. They induce the breaking of the Fe-His bond, as does the sGC natural effector NO.

The efficacy of an activator translates its ability to shift sGC towards its activated state and is an important allosteric parameter. Allosteric effectors of an enzyme crucially depend on their affinity ( $K_D$ ) for acting. However, even having the same binding site and  $K_D$ , a series of activators have different efficacies for activating the enzyme, a fact that we have evidenced in CHAPTER IV. To quantify this property, we have introduced the activation factor which characterizes individual activator independently of its  $K_D$ . Besides the affinity and the pharmacokinetics, this factor must be taken into account when designing a drug from a lead compound. We would like to develop this approach with newly discovered derivatives of riociguat in the context of the theory of allostery.

Our efforts to understand sGC activation lead us to re-examine the exact role of the natural compound isoliquiritigenin (ILQG). Commercialized as a sGC activator and used as such in several studies [7-11] it has various targets [12-13] and was demonstrated to exert anti-angiogenic effects [14]. Surprisingly, we discovered that ILQG is actually an efficient sGC inhibitor ( $IC_{50} = 9.5 \mu\text{M}$ ). An extensive literature search indicates that it was never tested with purified sGC but only in cells. We concluded that PDE5 inhibition by ILQG predominates that of sGC in cells, and that one must not derive firm conclusions on signaling pathways in cells without definitively knowing the action of the chemical tools on purified target proteins.

CHAPTER V focuses on the mechanism of diatomic gases binding to bacterial sensors. Using transient absorption spectroscopy in the broadest time range picosecond to millisecond time range, we probed the dynamics of the three diatomic ligands CO, NO and O<sub>2</sub> in a NO transporter (AXCP). In the case of CO and NO, whose affinities for L16A-AXCP are the largest ever measured, the bimolecular rebinding is absolutely not detectable. Such results indicate a novel mechanism for modulating heme-gas affinities in proteins. Indeed, molecular dynamic simulation demonstrated that dissociated CO is forced to remain within 4 Å from Fe<sup>2+</sup>, in contrast to wild-type AXCP.

AXCP forms a very short lifetime dinitrosyl species which leads to the formation of a 5c-NO complex, with NO replacing the proximal His. Because of similarities in absorption spectra and behavior observed in stopped-flow, sGC was hypothesized to also form a 5c-NO proximal complex. However, this species was never evidenced in sGC. As a perspective, it would be of high interest to compare the heme and NO kinetics of binding to AXCP and full-length sGC in picosecond to second time range over the entire spectrum to resolve this issue.

The exact role of *Tt*-H-NOX sensor is totally unknown [17]. In the absence of microbiologic data and biochemical tools addressing this protein, we used a spectroscopic approach, which of course does not allow to find its role, but allowed to describe some binding and redox properties of this sensor. We concluded that *Tt*-H-NOX is involved in signaling through a change of its redox state. Therefore, the properties of H-NOX domain from *Tt*-H-NOX are not compatible with the role of a simple NO-carrier. This result can orient future experiments, whatever the approach. In particular, monitoring the growth of bacteria and detection of products of *Tt* metabolism in different conditions modulating O<sub>2</sub> / NO, would help to understand the role of diatomic ligands in bacteria life.

In conclusion, we would like to emphasize that the unifying theme of this thesis was to link the biochemical properties of allosteric effectors together with their dynamical behavior. Especially, using together biochemical techniques and time-resolved spectroscopy, we linked the very first structural events which trigger allosteric transitions in sGC at molecular level with sGC activation in cells.

## Bibliography

1. Grimm, E. A.; Ellerhorst, J.; Tang, C.-H.; Ekmekcioglu, S. Constitutive intracellular production of iNOS and NO in human melanoma: possible role in regulation of growth and resistance to apoptosis. *Nitric Oxide* **2008**, *19*, 133-137.
2. Leung, E. L.; Wong, J. C.; Johlfs, M. G.; Tsang, B. K.; Fiscus, R. R. Protein Kinase G Type I $\alpha$  Activity in Human Ovarian Cancer Cells Significantly Contributes to Enhanced Src Activation and DNA Synthesis/Cell Proliferation. *Molecular Cancer Research* **2010**, *8*, 578-591.
3. Cai, C.; Chen, S. Y.; Zheng, Z.; Omwancha, J.; Lin, M. F.; Balk, S. P.; Shemshedini, L. Androgen regulation of soluble guanylyl cyclase[ $\alpha$ ]1 mediates prostate cancer cell proliferation. *Oncogene* **2006**, *26*, 1606-1615.
4. Menéndez, L.; Juárez, L.; García, V.; Hidalgo, A.; Baamonde, A. Involvement of nitric oxide in the inhibition of bone cancer-induced hyperalgesia through the activation of peripheral opioid receptors in mice. *Neuropharmacology* **2007**, *53*, 71-80.
5. Park, S.-W.; Lee, S.-G.; Song, S.-H.; Heo, D.-S.; Park, B.-J.; Lee, D.-W.; Kim, K.-H.; Sung, M.-W. The effect of nitric oxide on cyclooxygenase-2 (COX-2) overexpression in head and neck cancer cell lines. *International Journal of Cancer* **2003**, *107*, 729-738.
6. Isenberg, J. S.; Martin-Manso, G.; Maxhimer, J. B.; Roberts, D. D. Regulation of nitric oxide signaling by thrombospondin-1: implications for anti-angiogenic therapies. *Nature reviews. Cancer* **2009**, *9*, 182-194.
7. Yu, S. M.; Kuo, S. C. Vasorelaxant effect of isoliquiritigenin, a novel soluble guanylate cyclase activator, in rat aorta. *Br J Pharmacol.* **1995**, *114*, 1587-94.
8. Wegener, J. W.; Nawrath, H. Differential effects of isoliquiritigenin and YC-1 in rat aortic smooth muscle. *European Journal of Pharmacology.* **1997**, *323*, 89-91.
9. Wegener J. W.; Nawrath H. Cardiac effects of isoliquiritigenin. *Eur J Pharmacol* **1997**, *326*, 37-44.

10. Smith, A. D.; Dar, M. S. Involvement of the alpha4beta2 nicotinic receptor subtype in nicotine-induced attenuation of delta9-THC cerebellar ataxia: role of cerebellar nitric oxide. *Pharmacol Biochem Behav* **2007**, 86, 103-12.
  11. Al-Rejaie, S.; Dar, M. S. Antagonism of ethanol ataxia by intracerebellar nicotine: possible modulation by mouse cerebellar nitric oxide and cGMP. *Brain Res Bull* **2006**, 69, 187-96.
  12. Dandawate, P. R.; Subramaniam, D.; Jensen, R. A.; Anant, S. Targeting cancer stem cells and signaling pathways by phytochemicals: Novel approach for breast cancer therapy. *Semin Cancer Biol* **2016**, 40-41, 192-208.
  13. Peng, F.; Du, Q.; Peng, C.; Wang, N.; Tang, H.; Xie, X.; Shen, J.; Chen, J. A Review: The Pharmacology of Isoliquiritigenin. *Phytother Res* **2015**, 29, 969-77.
  14. Sulaiman, R. S.; Basavarajappa, H. D.; Corson, T. W. Natural product inhibitors of ocular angiogenesis. *Exp Eye Res* **2014**, 129, 161-71.
  15. Andrew, C. R.; George, S. J.; Lawson, D. M.; Eady, R. R. Six- to five-coordinate heme-nitrosyl conversion in cytochrome c' and relevance to guanylate cyclase. *Biochemistry*. **2002**, 41, 2353-60.
  16. Nioche, P.; Berka, V.; Vipond, J.; Minton, N.; Tsai, A. L.; Raman, C. S. Femtomolar sensitivity of a NO sensor from *Clostridium botulinum*. *Science*. **2004**, 306, 1550-1553.
  17. Karow, D. S.; Pan, D.; Tran, R.; Pellicena, P.; Presley, A.; Mathies, R. A.; Marletta, M. A. Spectroscopic Characterization of the Soluble Guanylate Cyclase-like Heme Domains from *Vibrio cholerae* and *Thermoanaerobacter tengcongensis*. *Biochemistry*. **2004**, 43, 10203-10211.
-

---

## VII – ANNEXES

### SYNOPSIS

---

A – List of abbreviations .....	161
B – Principles of Surface plasmon resonance imaging .....	163
C – Principles and methods of time-resolved absorption spectroscopy .....	166
1 – Correction of distortion in early time transient spectra .....	167
2 – Analysis of data matrix by singular value decomposition .....	170
D – Molecular dynamics simulation – CHARMM .....	170
E – Bibliography .....	172

---

### A – List of abbreviations

<b>ATP</b>	Adenosine triphosphate
<b>AXCP</b>	<i>Alcaligenes xylooxidans</i> cytochrome c prime
<b>BAY 41-2272</b>	Pyrazolopyridine
<b>BAY 63-2521</b>	Riociguat, commercialized as Adempas®
<b>DBPG</b>	3,6-dibromo-purpurogallin
<b>CAM</b>	Chorioallantoic membrane
<b>CHARMM</b>	Chemistry at HARvard Molecular Mechanics
<b>cAMP</b>	3',5'-cyclic adenosine monophosphate
<b>cGMP</b>	3',5'-cyclic guanosine monophosphate
<b>cGK</b>	cGMP-dependent protein kinases
<b>CNG</b>	Nucleotide-gated channels
<b>CORM</b>	CO-releasing molecules
<b>Cyt c</b>	Cytochrome c
<b>DMSO</b>	Dimethyl sulfoxide
<b>EC</b>	Endothelial cells
<b>EC<sub>50</sub></b>	Half-maximal effective concentration
<b>EDRF</b>	Endothelium-derived relaxing factor
<b>eNOS</b>	Endothelial nitric oxide synthase
<b>GMP</b>	non cyclic guanosine monophosphate
<b>GMPPCP</b>	β,γ-Methylene guanosine 5'-triphosphate
<b>GTP</b>	Guanosine triphosphate

---

<b>GVD</b>	Group Velocity Dispersion
<b>Hb</b>	Hemoglobin
<b>HCN</b>	Hyperpolarization-activated cyclic nucleotide-gated channels
<b>H-NOX</b>	Heme-containing NO/oxygen-binding domain
<b>H-NOX <i>Cb</i></b>	H-NOX protein from <i>Clostridium botulinum</i>
<b>H-NOX <i>Np</i></b>	H-NOX protein from <i>Nostoc punctiforme</i>
<b>H-NOX <i>Tt</i></b>	H-NOX from <i>Thermoanaerobacter tengcongensis</i>
<b>HOMO</b>	Highest occupied molecular orbital
<b>HTANQ</b>	2-hydroxy-3,5,8-triaceto-1,4-naphthoquinone
<b>HUVEC</b>	Human umbilical vein endothelial cells
<b>HSkMEC</b>	Human skin microvascular endothelial cells
<b>IHP</b>	Inositol hexakisphosphate
<b>iNOS</b>	Inducible nitric oxide synthase
<b>ILQG</b>	Isoliquiritigenin
<b>InsP<sub>3</sub></b>	Inositol trisphosphate
<b>Mb</b>	Myoglobin
<b><i>Ms</i> sGC-NT</b>	Truncated sGC from <i>Manduca sexta</i>
<b>nNOS</b>	Neuronal nitric oxide synthase
<b>NO</b>	Nitric oxide
<b>NMDA</b>	N-methyl-D-aspartate
<b>ODQ</b>	1H-[1,2,4]oxadiazolo[4,3-a]quinoxalin-1-one
<b>PDE</b>	Phosphodiesterase
<b>pGC</b>	Particulate guanylate cyclase
<b>PK</b>	Protein kinase
<b>sGC</b>	Soluble guanylate cyclase
<b>pGC</b>	Particulate guanylate cyclase
<b>SNP</b>	Sodium nitroprusside
<b>SOD</b>	Superoxide dismutase
<b>SPRi</b>	Surface Plasmon Resonance imaging
<b>SVD</b>	Singular value decomposition
<b>TEA</b>	Triethanolamine
<b>YC-1</b>	3-(5'-Hydroxymethyl-2'-furyl)-1-Benzylindazole (from Yung Chin Pharm.)
<b>2,3-BPG</b>	2,3-bisphosphoglyceric acid
<b>IHP</b>	Inositol hexakisphosphate
<b>WT-AXCP</b>	Wild type of Cytochrome <i>c'</i> from <i>Alcaligenes xylosoxidans</i>

## B – Principles of Surface plasmon resonance imaging

Surface Plasmon Resonance imaging (SPRi) is an optical detection process that occurs when a polarized light hits a dielectric covered by a metallic layer. A plasmon is a pseudo particle that is associated with a collective oscillation of electrons that is called plasmonic wave [1]. Under certain conditions (wavelength, polarization and incidence angle) free electrons at the surface absorb photons of incident light and convert them into surface plasmon waves [2]. The idea of SPRi technique is to detect interaction between molecules in a fluid environment by detecting perturbations of the plasmonic wave. The basic scheme is shown on Figure 1.

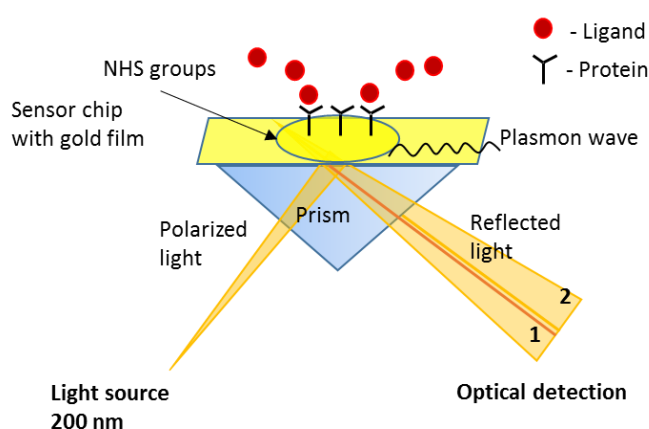
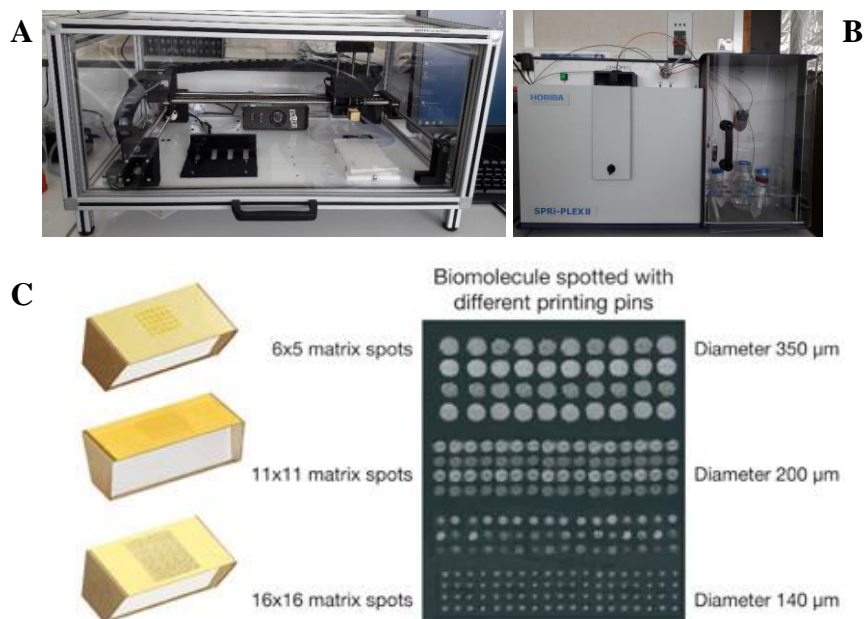


Figure 1. Surface plasmon resonance biochip.

As a collective oscillation of electrons at surface of the glass prism, plasmons can be perturbed. Perturbations at the gold surface of the biochip, such as an interaction between probe molecules immobilized on the chip and captured target molecules, induce a modification of resonance conditions which induce a change in reflectivity which can be measured (Figure 4A). The wave that enters inside the metal is an evanescent wave which exponentially decays with distance [3] and disappears within the first 100 nm of the surface. This is the reason why the prism is covered with a thin layer. For our experiment we used biochip from Horiba company consist of a glass prism coated with a thin gold layer.

The SPRi setup consists of SPRi-Arrayer system for spotting proteins on the prism (Figure 2A) and SPR imaging system for detection of binding (Figure 2B). SPRi-Arrayer is a programmable automatic apparatus with a metal-ceramic capillary needle (500  $\mu\text{m}$  internal diameter) to spot the surface of the bioship with proteins (Figure 2C). The SPRi-Biochip surface must be functionalized to immobilize proteins with chemistry chosen according to the nature of the molecules to be spotted. In our experiments, we used CS surface chemistry, which possesses amine function ( $\text{NH}_2$  group). Grafting functionalized groups on the surface is

based on the high affinity of sulfur atoms in polyoxyethylene molecules with gold. Free carboxylic acid functions of polyoxyethylene are then activated by N-Hydroxysuccinimide (NHS): 1-ethyl-3-(3-dimethylaminopropyl) carbodiimide solution. Activated carboxylic acids can then react with free amine functions of the protein to create amide functions. The time of protein fixation on the surface is 16 hours. After this step, we soaked the prism in a blocking solution for 15 min to deactivate the remaining reactive groups of the surface chemistry and to reduce non-specific binding.



**Figure 2.** SPRi-Array system for spotting proteins on prism (A). SPR imaging system for detection of ligand – receptor binding (B). Image of the SPRi-Biochip surface after different size of proteins spotting (C).

When the prism is ready, we introduced the biochip into a SPRi-Plex imager (Figure 2B) and a computer-controlled camera acquires images of the prism surface showing the spots of proteins using the acquisition program SPRiView (Figure 2C). The program averages the kinetics from all spots of the same protein that were selected, having the same concentration. The mirror is then moved to the working angle at the point of the highest gradient and fixed at that position (vertical line in Figure 3).

Then, the biochip surface was equilibrated in place with running buffer (TEA 10 mM, NaCl 5 mM, DMSO 2.5 %, pH = 7.4) having the same composition as the buffer containing the analyte to be injected. This technique is very well suited for large molecular weight (> 5 kDa) but we used it for the first time at the detection limit of about 0.5 kDa.

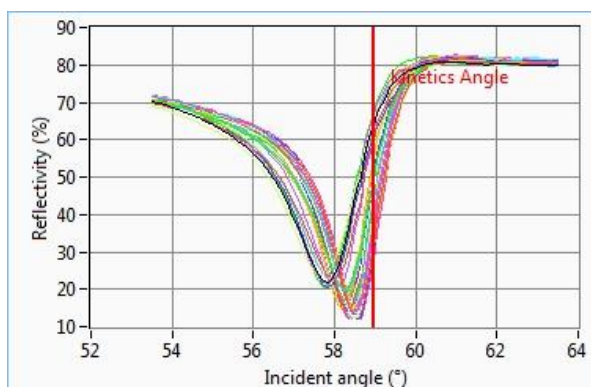


**Figure 3.** Plasmon curves of each spot of proteins and kinetics angle (58.97°).

When the sample solution enters the flow cell, binding of molecules to be detected occurs. This induces a shift of the plasmon curves and a variation of reflectivity (Figure 4A). The kinetic curves show the variations of reflectivity versus time. When the flow cell is washed with running buffer, the ligand-analyte complex dissociates. This again induces a back shift of the plasmon curves and a variation of reflectivity. When the ligand-analyte complex is fully dissociated, the plasmon curves and the kinetic curves return to the initial state.

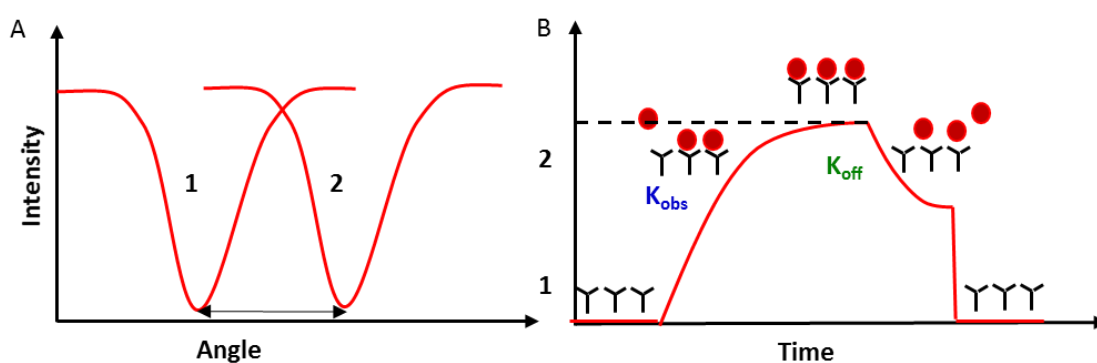


**Figure 4.** Changes of plasmon curves on the gold surface of prism with unbinding (1) and binding (2) protein-ligand complex (A). Kinetics of protein-ligand binding (B).

The parameter of interest is the affinity represented by the dissociation constant  $K_D$  and obtained in SPR by the ratio of dissociation and association rates:

$$K_D = [R][L] / [RL] = k_{off} / k_{on} \quad [2]$$

Where  $[R]$  is the concentration of the receptor,  $[L]$  is the concentration of the ligand and  $[RL]$  is the concentration of the receptor-ligand complex,  $k_{off}$  is the dissociation rate and  $k_{on}$  is the association rate (Figure 4B):

$$k_{on} = k_{obs} / C_i$$

where  $k_{obs}$  is the observed rate constant of association,  $C_i$  is the injected analyte concentration.

## C – Principles and methods of time-resolved absorption spectroscopy

Transient spectroscopy allows to probe and characterize the electronic and structural properties of short-lived transient states of photochemically/photophysically excited molecules. The principle of the time-resolved pump-probe experiment is to perturb a system, then to measure a spectrum at a defined time to evaluate the consequence of the perturbation. Using a visible light pulse, the perturbation always occurs through electronic excitation which, in our case, leads to the breaking of the bond between the heme iron and the diatomic ligand and thus to release it. The system ligand/protein is put into a non-equilibrium state and the measurement takes place during the relaxation dynamics. Reaching back the equilibrium of the sample may take place in several steps in picosecond to nanosecond or even second time-range. These changes are monitored at different time delays and probed with a low-energy second light pulse to measure the evolving spectrum. In our case the structural transitions observed are changes of coordination ( $6c \leftrightarrow 5c$  or  $5c\text{-XO} \leftrightarrow 4c \leftrightarrow 5c\text{-His}$ ) or change of redox state ( $\text{Fe}^{2+} \leftrightarrow \text{Fe}^{+3}$ ) of the heme iron.

Our measurements were performed with the pump-probe laser system previously described in [4]. The source of the ultra-short pulse ( $< 100$  fs) is a dye laser pumped by a continuous wave Argon ion laser (2.5 W) providing pulses at 620 nm at a repetition rate of 95 MHz. These pulses are amplified by a YAG laser at 30 Hz, and the amplified pulse train is split into two beams used for pumping and probing the sample [5]. In a typical pump-probe experiment, the delayed probe pulse is used to measure the difference of absorbance ( $\Delta A$ ) induced by the perturbation triggered with the pump pulse:

$$\Delta A(t) = A(t) - A_0 = A_{(\text{after dissociation})} - A_{(\text{before dissociation})}$$

Measuring the evolution of  $\Delta A$  as a function of time delays allows us to identify structural changes and quantify their kinetics. The experimental setup for Transient Absorption measurements is shown in Figure 5.

All experiments were carried out at 20 °C. The equilibrium absorption spectra of the samples were verified before and after time-resolved experiments using a spectrophotometer Shimadzu 1701. The quartz cell (Hellma) with a 1-mm optical path length was used for steady state and transient spectra experiment. The working range for this set-up was  $0.3 < OD < 0.8$ . Myoglobin (Mb) was used as a standard in its CO-liganded form to align the delay line and to adjust the collinearity and overlap between the pump and probe beams. The pump pulse, centered at 564 nm with duration of  $\sim 50$  fs, is used to photodissociate NO, CO or O<sub>2</sub> that was previously bound to the protein. A probe pulse with a broad spectral range (375 – 600 nm) is used to measure the TA spectrum after a controlled time delay between the two pulses. Both beams are focused to a spot of  $\sim 30 - 50$   $\mu\text{m}$  and spatially overlapped in the sample cell, which is continuously moving perpendicularly to the beams to renew sample between laser shots at 30 Hz. After going through the sample cell, the probe pulse is directed into a spectrometer at

the exit of which a CCD detector allows to record transient absorption spectra and the reference spectrum of the pulse before it went through the sample.

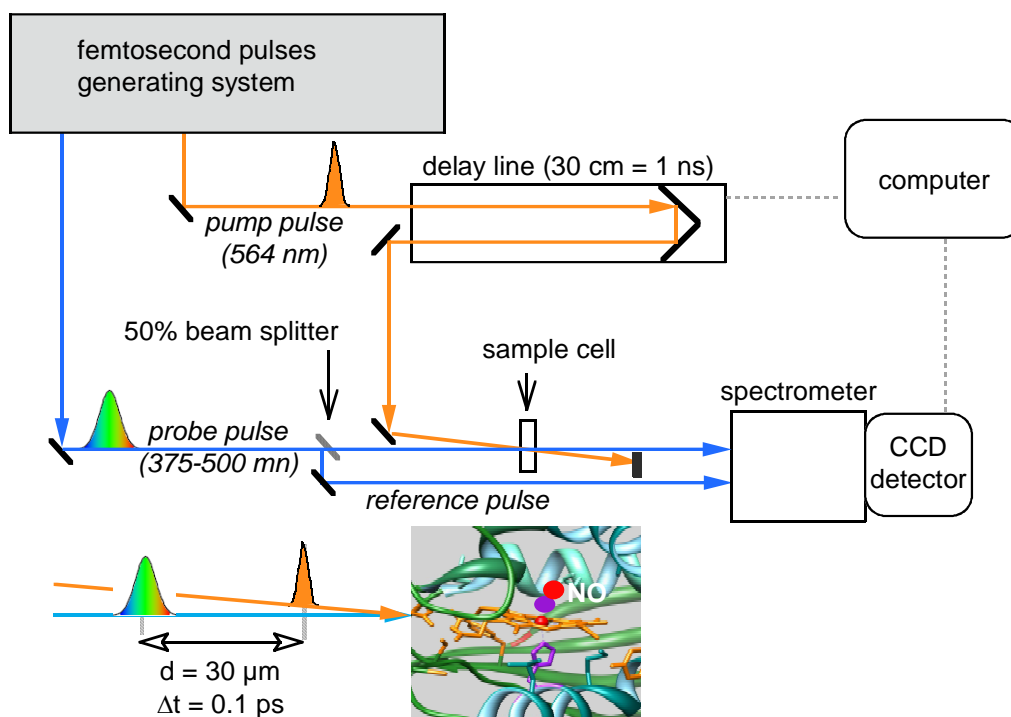


**Figure 5.** Scheme of the transient absorption spectroscopy experiment setup. Time delay from 0.1 ps to 5 ns. Excitation pulse at 564 nm, broad spectrum from 375 to 600 nm.

Since we recorded a series (40 to 60) of transient spectra (375 – 600 nm) at different time delays, the result consists of a matrix of differential absorption as a function of time and wavelength. The measurement of transient absorption data and the control of delay line were done by the same software whereas analysis of data was performed by Matlab using correction of distortion due to GVD and singular value decomposition (SVD).

### 1 – Correction of distortion in early time transient spectra

To understand the activation heme sensors, we need to identify the structural events induced by the detachment of a diatomic ligand (NO, O<sub>2</sub>, CO) from the heme in time range from 0.1 ps to 5 ns. During this time, diatomic ligand rebinding to the heme, internal side-chain rebinding, photo-induced oxidation or reduction, vibrational relaxation occur. In the time-range 1-20 ps, the spectra of these processes overlap and their rigorous identification requires a mathematical analysis of the data matrix. Due to the short duration and wide spectral range (375-600 nm) of the probe pulse, Group Velocity Dispersion (GVD) occurs in the numerous optical elements of the system, even if there is a pair of prisms for partially correcting it. Thus, the spectral components of the probe pulse after penetrating the sample

have different velocities and as a result, they arrive at the CCD at the different times, with maximal retardation in the range 1 – 3 ps between wavelengths contained in the pulse. This GVD results in distortion of the transient spectra and the data matrix must be corrected if the purpose is to identify a transient species having a short lifetime.

The GVD detection method we used consists of two steps:

1. Detection of the distortion: detect the curved time-zero line.
2. Modifying the time-wavelength matrix in order to recover a linear time-zero line.

The procedure implemented in Matlab by Shao Yifeng (LOB, Ecole Polytechnique, Master2, 2012) is described below. It enables automatic detection of the GVD thanks to the presence of peak artifacts at time zero in the transient spectrum, which are produced when the pump and probe pulses cross in time and space in the sample. The time-wavelength matrix of time-resolved transient spectroscopy can be viewed as an image. The absorbance at a certain wavelength and time in the matrix determines the brightness of each pixel in this image. The problem of detecting GVD in the data matrix then becomes detecting the discontinuity of image brightness – a typical edge detection problem. Thus, we can apply image convolution to identify the location of points at which the brightness changes abruptly, corresponding to the elements in the distorted spectra at time-zero. Most generally, the convolution of two functions is defined as follows:

$$(f * g)(x, y) = \sum_{v=y-h}^{y+h} \sum_{u=x-w}^{x+w} f(u, v)g(x-u, y-v)$$

where  $f(x, y)$  is a function that represents the image, and  $g(x, y)$  represents the kernel. In the formula,  $2w+1$  and  $2h+1$  are the width and height of the kernel respectively. The kernel  $g(x, y)$  is defined over points  $[-w, w] \times [-h, h]$ . To convolute the image, the formula is evaluated point by point in the image. To detect the edge, the Sobel operator is used as the kernel:

$$g(x, y) = \begin{bmatrix} -1 & 0 & +1 \\ -2 & 0 & +2 \\ -1 & 0 & +1 \end{bmatrix}$$

The aforementioned convolution is applied twice (which corresponds to the second derivative  $d^2/dt^2$ ) and the absolute value of obtained time-wavelength matrix is taken.

Once the maximum is determined for each wavelength (i.e. for each row in the time-wavelength matrix), the set of values after the maximum constitutes a new smaller time-wavelength matrix. Figure 7 shows an example of the correction of distortion of data matrix obtained from measurement of  $O_2$  dynamics in *Tt* H-NOX at 20 °C in short time scale (up to 200 ps) and long time range (up to 5 ns).

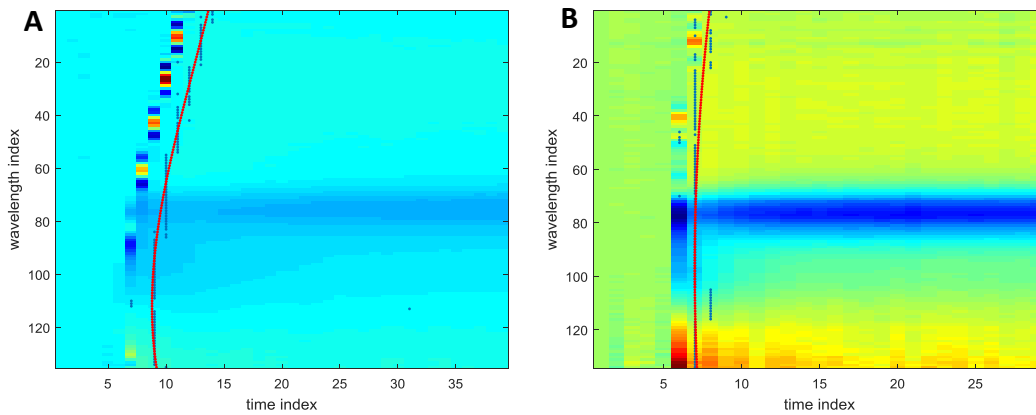


**Figure 6.** Correction of spectra distortion obtained from measurement of O<sub>2</sub> dynamics in *Tt* H-NOX at 20 °C. Data were fitted using interpolation by a polynomial of the third degree. Data was recorded up to 200 ps (A) and 5 ns (B).

In these data files, several time frames are present. Typically there is a high-resolution time frame 0 – 20 ps with 200 points and low-resolution time frame 20 – 200 ps with 20 points. In this case, the operation above is performed only on the first high-resolution time frame, which is then concatenated with the unmodified low-resolution time frame (Figure 8). In fact, while GVD is propagated along the entire spectrum, its maximal effect on data distortion extends essentially to time constants in the 5 – 20 ps range. Thus, in the time range up to 5 ns we decided to keep the low-resolution time frame unmodified in order to avoid an unnecessary manipulation of the raw experimental data.

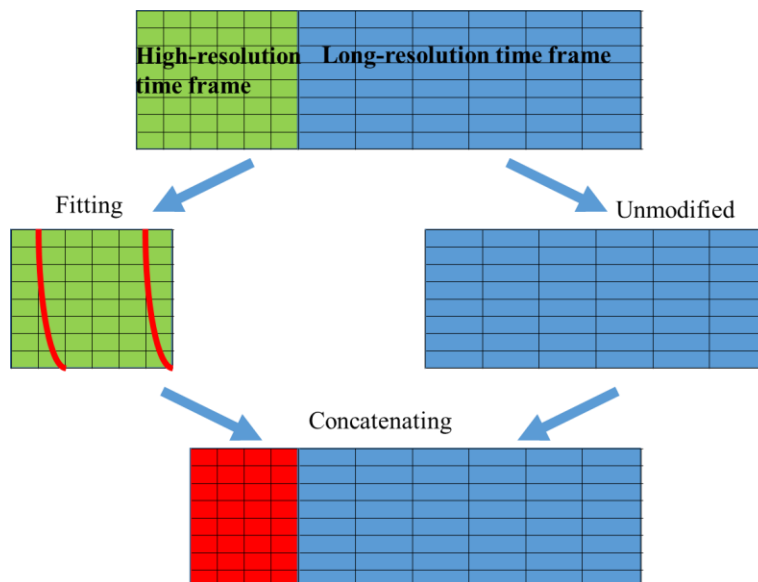


Figure 7. Scheme for correction of the distortion of data matrix

## 2 – Analysis of data matrix by singular value decomposition

Singular Value Decomposition (SVD) analysis of a matrix is a well-known mathematical method [6] to study the evolution of a physical quantity as function of two others, especially useful for dynamical processes. It allows us to efficiently separate the individual spectral components and their kinetics within the data matrix. In our system the successive transient spectra build up a two-dimensional matrix of induced absorbance  $A(\lambda, t)$  as a function of wavelength  $\lambda$  of the probe pulse and time  $t$  after excitation. The matrix  $\Delta A(\lambda, t)$  can be decomposed into:

$$\Delta A(\lambda, t) = \Delta A^{\text{SVD}}(\lambda) \times S \times K^{\text{SVD}}(t) \quad [5]$$

where  $\Delta A^{\text{SVD}}(\lambda)$  contains the spectral component matrix,  $S$  is the diagonal singular value, and  $K^{\text{SVD}}(t)$  is the matrix containing the associated kinetics. This procedure allows to separate the spectral components and their kinetic evolution together with reducing the time-correlated noise components contained in the raw data.

Normally, two or three SVD components were taken into account in our experiments because they are associated with chemically significant spectra and kinetics. The rest of the singular values typically represents correlated noise (essentially instability of the lasers and drift of the alignment). The kinetic components  $K^{\text{SVD}}(t)$  were fitted with a multi-exponential function, where the minimal number of components was determined iteratively. The decay associated spectra for each individual exponential process can be calculated to separate populations of proteins species which behave differently and to separate the elementary structural steps of relaxation after photodissociation of the ligand [5].

Importantly, SVD can be used to discover a hidden spectral component which is difficult to detect otherwise (see Section 4 in CHAPTER IV).

## D – Molecular dynamics simulation – CHARMM

The dynamics simulation program CHARMM (Chemistry at HARvard Molecular Mechanics) focuses on macromolecules of biological interest, including proteins, peptides, lipids, nucleic acids, carbohydrates [7]. The specialist in molecular dynamics calculations in our laboratory, Jean-Christophe Lambry used this program to visualize the differences in the heme domain of human sGC bound with NO, CO, and BAY41-2272 to (see results in CHAPTER IV). The simulation procedure comprises several steps.

The first step is the preparation of 3D structure of protein obtained from the Protein Data Bank website in PDB format. If the crystal structure does not exist, we calculated protein tertiary structure using the sequence of a known similar structure of protein using MODELLER program. It allows to use the coordinates of atoms of a homologous protein

template to build the 3D structure of an unknown protein by performing "mutations" *in silico*. In our case, we used the structure provided by Laleh Alisaraie (School of Pharmacy, Memorial University of Newfoundland, Canada) described in the study [8] of BAY 41-2272 binding site modulation. The model of a three-dimensional structure of the H-NOX domain of  $\beta$  subunit in human sGC is based on the template of H-NOX domain from *Nostoc sp* (2O0C.pdb).

The second step is to add water molecules box with ions around the protein to create a realistic environment. Since protein charge is unequal, we add ions to neutralize system to have global neutral charge. This procedure increases the number of total atoms of the system, leading to long times of calculations. Then we increased the temperature of system (assigning speed to each atom) up to 300 K during several picoseconds to stabilize the protein.

The third step is to minimize the energy of the system. The general form of the potential energy function used in CHARMM for macromolecular simulations is based on fixed point charges and is calculated using the equation below.

$$\begin{aligned}
 U_{CHARMM} = & \sum_{bonds} K_b(b - b_0)^2 + \sum_{angles} K_\theta(\theta - \theta_0)^2 + \sum_{dihedrals} K_\phi[1 + \cos(n\phi - \delta)] \\
 & + \sum_{impropers} K_\omega(\omega - \omega_0)^2 + \sum_{Urey-Bradley} K_{UB}(S - S_0)^2 + \sum_{residues} U_{CMAP}(\phi, \psi) \\
 & + \sum_{non-bonded-pairs} \left[ \epsilon_{ij} \left[ \left( \frac{R_{min,ij}}{r_{ij}} \right)^{12} - 2 \left( \frac{R_{min,ij}}{r_{ij}} \right)^6 \right] + \left( \frac{q_i q_j}{4\pi\epsilon_0\epsilon r_{ij}} \right) \right] \quad [7]
 \end{aligned}$$

Where the potential energy ( $U_{CHARMM}$ ) is a sum over individual terms representing the internal and non-bonded contributions as a function of the atomic coordinates. Internal terms include bond ( $b$ ), valence angle ( $\theta$ ), dihedral angle ( $\phi$ ), improper angle ( $\omega$ ), Urey-Bradley (UB,  $S$ ) and backbone torsional correction (CMAP,  $\phi$ ,  $\psi$ ) contributions. The parameters  $K_b$ ,  $K_\phi$ ,  $K_{UB}$ ,  $K_\theta$  and  $K_\omega$  are the respective force constants and the variables with the subscript 0 are the respective equilibrium values. The detailed explanation of the formula is presented in reference [7].

The calculation is performed by integration of Newton equations of atomic motion as function of time. The potential energy  $U$  is calculated for each atom (it depends on the positions of other interacting atoms) to calculate its velocity. A new position is calculated after 1 fs from this velocity. Having completed this step for every atom, the potential energy is again calculated with the new positions of all atoms. Because the basic time step is 1 fs, millions of integration of this step are necessary to have a few ns simulation time.

We modeled heme domain in several coordinated states: 5c – His, 6c – His with CO, 5c heme with NO, 5-c heme with CO. In each case in the presence of CO BAY412272 is

bound to the protein. For different coordinated-heme states, energy minimization was calculated separately. To visualize the calculated structures, we used program Chimera or Pymol.

## E – Bibliography

1. Zeng, S.; Baillargeat, D.; Ho, H. P.; Yong, K. T. Nanomaterials enhanced surface plasmon resonance for biological and chemical sensing applications. *Chem Soc Rev* **2014**, 43, 3426-52.
  2. Green, R. J.; Frazier, R. A.; Shakesheff, K. M.; Davies, M. C.; Roberts, C. J.; Tendler, S. J. Surface plasmon resonance analysis of dynamic biological interactions with biomaterials. *Biomaterials* **2000**, 21, 1823-35.
  3. Puiu, M.; Bala, C. SPR and SPR Imaging: Recent Trends in Developing Nanodevices for Detection and Real-Time Monitoring of Biomolecular Events. *Sensors (Basel, Switzerland)* **2016**, 16, 870.
  4. Martin, J.-L.; Vos, M. H. Femtosecond measurements of geminate recombination in heme proteins. *Methods in Enzymology*. **1994**, 232, 416-430.
  5. Yoo, B.-K. Investigation of the mechanisms of regulations, activation, and deactivation of Guanylate Cyclase, the endogenous NO-receptor, and NO-sensors. Ecole Polytechnique X, 2010.
  6. Vandegriff, K. D.; Shrager, R. I. Hemoglobin-oxygen equilibrium binding: Rapid-scanning spectrophotometry and singular value decomposition. *Methods in Enzymology*. **1994**, 232, 460-485.
  7. Brooks, B. R.; Brooks, C. L.; MacKerell, A. D.; Nilsson, L.; Petrella, R. J.; Roux, B.; Won, Y.; Archontis, G.; Bartels, C.; Boresch, S.; Caflisch, A.; Caves, L.; Cui, Q.; Dinner, A. R.; Feig, M.; Fischer, S.; Gao, J.; Hodoscek, M.; Im, W.; Kuczera, K.; Lazaridis, T.; Ma, J.; Ovchinnikov, V.; Paci, E.; Pastor, R. W.; Post, C. B.; Pu, J. Z.; Schaefer, M.; Tidor, B.; Venable, R. M.; Woodcock, H. L.; Wu, X.; Yang, W.; York, D. M.; Karplus, M. CHARMM: The Biomolecular Simulation Program. *Journal of computational chemistry* **2009**, 30, 1545-1614.
  8. Alisaraie, L.; Fu, Y.; Tuszynski, J. A. Dynamic Change of Heme Environment in Soluble Guanylate Cyclase and Complexation of NO-Independent Drug Agents with H-NOX Domain. *Chemical Biology & Drug Design* **2013**, 81, 359-381.
-

**Title:** Regulation, activation, and deactivation of soluble guanylate cyclase and NO-sensors

**Keywords:** Soluble guanylate cyclase, signal transduction, nitric oxide, cyclic GMP, allostery, inhibitors of guanylate cyclase, transient absorption spectroscopy.

**Abstract:** This thesis is devoted to the regulation of soluble guanylate cyclase (sGC), the endogenous nitric oxide (NO) receptor in mammals involved in signal transduction. The enzyme is activated by the binding of NO to its heme and catalyzes the formation of cGMP from GTP. While sGC is present in many mammalian cells, the homologous bacterial domain (H-NOX) is involved in NO detection and metabolism regulation. An important objective was to find sGC inhibitors to slow down tumor progression.

The screening of natural compounds from a chemical library, tested on purified sGC activity, revealed six active inhibitors ( $IC_{50} = 0.2 - 1 \mu M$ ). Together with two agents for photodynamic therapy (hypericin and hypocrellin) we demonstrated that these inhibitors are allosteric modulators which bind neither to the heme nor to the catalytic and activator sites, revealing a new class of pharmacological compounds targeting the NO/cGMP signaling pathway.

The structural transition induced in sGC by stimulator riociguat in synergy with CO was studied by transient absorption spectroscopy to demonstrate coordination changes of the heme. Two different activation states of sGC with CO

6c-heme and 5c-heme exist simultaneously in the presence of the stimulator which induces the breaking of the heme Fe-His bond, as does the sGC natural effector NO. In addition, the effect of isoliquiritigenin, which is sold as a sGC activator, was shown to be actually an inhibitor of sGC.

The dynamics of the ligands CO, NO and  $O_2$  were measured over 12 orders of magnitude in time in wild type and mutant of a bacterial NO transporter (AXCP). The single mutation Leu16Ala increased  $10^8$ -fold the CO affinity,  $\sim 10^6$ -fold the NO affinity and makes this protein reactive to  $O_2$ . In the case of CO and NO, whose affinities for L16A-AXCP are the largest ever measured, the bimolecular rebinding was absolutely not detectable. Molecular dynamic simulations demonstrated that dissociated CO is constrained to stay within 4   from  $Fe^{2+}$  by Ala16, contrarily to wild-type Leu16.

The dynamics of  $O_2$  in Tt-H-NOX proteins measured by transient absorption spectroscopy confirmed the hypothesis that Tt-H-NOX may not be a NO-sensor stricto sensu but a redox sensor. The properties of the Tt-H-NOX protein are not compatible with the role a mere NO-carrier.

